



HAL
open science

Flow-induced deformations and stress reduction by flexibility

Tristan Leclercq

► **To cite this version:**

Tristan Leclercq. Flow-induced deformations and stress reduction by flexibility. Mechanics [physics]. Université Paris Saclay (COMUE), 2018. English. NNT : 2018SACLX006 . tel-01713253

HAL Id: tel-01713253

<https://pastel.hal.science/tel-01713253>

Submitted on 20 Feb 2018

HAL is a multi-disciplinary open access archive for the deposit and dissemination of scientific research documents, whether they are published or not. The documents may come from teaching and research institutions in France or abroad, or from public or private research centers.

L'archive ouverte pluridisciplinaire **HAL**, est destinée au dépôt et à la diffusion de documents scientifiques de niveau recherche, publiés ou non, émanant des établissements d'enseignement et de recherche français ou étrangers, des laboratoires publics ou privés.

NNT : 2018SACLX006

THÈSE DE DOCTORAT DE
L'UNIVERSITÉ PARIS-SACLAY PRÉPARÉE À
L'ÉCOLE POLYTECHNIQUE

ÉCOLE DOCTORALE N° 579
Sciences mécaniques et énergétiques, matériaux et géosciences

SPÉCIALITÉ DE DOCTORAT : MÉCANIQUE DES FLUIDES

Tristan LECLERCQ

Flow-induced deformations and stress reduction by flexibility*

***Déformations induites par l'écoulement
et réduction d'efforts par la flexibilité**

Thèse soutenue à Palaiseau le 10 janvier 2018 devant le jury composé de

M. Christophe Eloy	Rapporteur	Centrale Marseille (IRPHE)
M. Ramiro Godoy-Diana	Rapporteur	École Supérieure de Physique et de Chimie Industrielle (PMMH)
M. Didier Clouteau	Président	CentraleSupélec (MSSMat)
M. Rémi Bourguet	Examineur	Institut de Mécanique des Fluides de Toulouse
M. Emmanuel de Langre	Directeur de thèse	École polytechnique (LadHyX)

Remerciements

La première personne que je voudrais remercier au terme de ces 1165 jours de thèse, c'est évidemment Emmanuel. Dans une aventure d'aussi longue haleine, il y a inévitablement des moments de doute, où la motivation s'affaisse et les perspectives se brouillent. A chacune de ces occasions, je suis ressorti de mes entretiens avec Emmanuel avec une vision claire et une confiance absolue que mes directions étaient les bonnes. L'intérêt contagieux qu'il porte aux questions scientifiques a constamment nourri ma motivation, et ses analyses éclairées ont su canaliser mes réflexions parfois divergentes. En m'incitant à plus d'offensivité dans l'affirmation de mes convictions, il a su m'aider à réorganiser, reformuler mes idées, sans les dénaturer sur le fond. Je lui dois d'être fier du résultat de trois années de recherche.

Je me dois bien sûr aussi de remercier Nigel, pour l'accueil et la disponibilité dont il m'a gratifié pendant les 7 mois de mon séjour à Cambridge. Ce fut un vrai plaisir de goûter aussi bien l'atmosphère chaleureuse et stimulante du CMS que les *free lunches at the pub* qui clôturent les réunions hebdomadaires du *wave group*.

Il n'y a pas de thèse sans laboratoire, et je veux exprimer ma gratitude à tous les membres du LadHyX, qui ont à coeur d'entretenir un climat de grande convivialité toujours appréciable, et de surcroît propice à la créativité scientifique. Merci notamment à Sébastien, de s'être intéressé à mes travaux et de m'avoir fait profiter de son expertise. A Pascal, Tonio et Romain, artisans de mes manips, et maîtres à penser pour l'expérimentateur qui sommeillait en moi. A Dany et Toai, à qui pas un crash de MatLab ou de LaTeX ne résiste. A Thérèse, Sandrine, Magali et Delphine, pour le soutien administratif si précieux qu'elles prodiguent avec efficacité et bonne humeur.

Au sein de l'écosystème ladhyxien, j'ai eu la chance d'habiter pendant la majeure partie de ma thèse un bureau au microclimat particulièrement clément. J'y ai rencontré des gens avec qui j'ai pris autant de plaisir à travailler sans m'en apercevoir qu'à digresser en m'en apercevant. Merci donc à Océane, Julien, Guillaume, Gaétan, Léopold, Vincent, pour ces parties de balle aléatoire, exutoires salvateurs par lesquels nous épanchâmes nos frustrations numériques et théoriques, ainsi que pour ces débats passionnés mais non moins aléatoires, que déclenchent parfois dans le cerveau du chercheur en mal de problématiques nouvelles les affirmations les plus anodines. Merci également à Arnaud-Eric Dampierre, grand gourou de la concaténation de fichiers pdf et bâtisseur avant-gardiste, d'avoir partagé pendant mes derniers mois, son bureau, mes Princes de Lu, et un amour immodéré commun pour le soda en canette. Je n'oublie évidemment pas tous les membres du labo, permanents ou éphémères, que je ne peux citer ici, mais avec qui j'ai partagé tant de cafés ou de boissons de toutes natures. Merci à tous.

Je voudrais enfin avoir une pensée particulière pour ceux qui, au-delà de la thèse, m'accompagnent au quotidien. Merci à mes parents et à mes frères, dont la confiance et le soutien m'ont toujours porté, bien avant que le mot "thèse" n'intègre mon vocabulaire. Un grand merci à Mathieu, qui a tout autant préparé le pot de thèse que le futur

docteur, ainsi qu'à Soledad, coloc' en or massif aux vertus exhilarantes dignes de celles du planteur qu'elle prépare. Un immense merci à Marine enfin, de m'avoir accompagné pendant les derniers mois de cette thèse, de s'être autant intéressée, et d'avoir partagé avec moi des moments d'évasion si doux et nécessaires.

Résumé

Au travers du processus d'évolution, les espèces végétales développent préférentiellement au fil des générations des traits qui améliorent leur aptitude à faire face aux challenges environnementaux qui se présentent à elles. En particulier, la flexibilité des individus est positivement corrélée avec l'intensité des chargements fluides dans les différents habitats. En effet, la déformation des structures flexibles exposées à des écoulements permet classiquement, dans le régime statique, de réduire la traînée à laquelle elles sont soumises. Dans le domaine de la biomécanique, cette déformation d'éléments végétaux flexibles conduisant à une réduction du chargement enduré est désignée par le terme de 'reconfiguration' pour souligner le caractère avantageux de ce processus adaptatif.

Dans le cadre d'une démarche de bioinspiration, l'objectif de cette thèse est d'appréhender les différents mécanismes physiques qui sous-tendent le processus de reconfiguration, par l'étude de systèmes modèles théoriques. Des extensions de la théorie classique de reconfiguration statique sont proposées pour évaluer l'impact de différents effets jusqu'à lors négligés dans la littérature. Dans un souci de simplicité, nous nous concentrons dans cette thèse sur le cas de structures élancées, encastrées-libres, et transverses à l'écoulement. La plupart des résultats présentés sont issus de simulations numériques basées sur des modèles simplifiés d'interactions fluide-structure. Sont analysés successivement, dans les différents chapitres, les effets de la variabilité spatiale du système fluide-structure, ainsi que l'impact de la dynamique provenant au choix de l'instationnarité de l'écoulement de base, d'un couplage fluide-structure conduisant à une instabilité de flottement, ou de vibrations induites par vortex.

Dans le cas d'un système non-uniforme, nous montrons que la loi d'évolution de la traînée avec la vitesse de l'écoulement dépend de la distribution spatiale des propriétés du système fluide-structure à l'échelle d'une longueur de courbure localisée à proximité du bord encastré. Par ailleurs, la faible sensibilité de cette loi d'évolution vis-à-vis des détails des variations spatiales du système constitue un élément d'explication à la grande homogénéité des lois de traînée mesurées dans la nature. Dans le cas d'un écoulement oscillant, nous mettons en lumière l'existence de différents régimes cinématiques de déformation selon l'amplitude et la fréquence de l'écoulement. La réduction des efforts par reconfiguration est généralement préservée dans ce cadre dynamique, à l'exception de possibles situations de résonance du système dans le régime des très faibles amplitudes. Les lois d'évolution de l'effort maximal en fonction des propriétés de l'écoulement dépendent par ailleurs du régime cinématique. L'étude de l'instabilité de flottement montre de plus que l'apparition d'une dynamique spontanée n'augmente généralement pas suffisamment la traînée sur le système pour contrebalancer le bénéfice apporté par la déformation statique sous-jacente. De rares et courts épisodes d'accroissement exceptionnel des efforts peuvent survenir dans le cas de structures lourdes et peu élancées, susceptibles de présenter une dynamique chaotique. Enfin, nous montrons de plus que la reconfiguration présente l'avantage supplémentaire de permettre la réduction des vibrations induites par vortex qui accroissent la traînée sur le système.

Ainsi, dans cette thèse, nous montrons que l'aptitude des structures flexibles à

réduire le chargement imposé par l'écoulement est préservée en présence de non-uniformités ou de dynamique, à condition que le design de la structure soit tel que la traînée résistive domine les forces inertielles. Les structures légères et élancées sont à ce titre les mieux adaptées pour limiter les risques d'origine inertielle. De plus, l'efficacité de la réduction du chargement par reconfiguration élastique dépend faiblement de la distribution spatiale des propriétés du système. Finalement, la réduction des efforts résulte toujours, indépendamment du régime de reconfiguration, de la concentration de la déformation sur une longueur caractéristique inférieure à la longueur réelle de la structure.

Contents

1	Introduction	1
1.1	Motivations	2
1.1.1	Bioinspiration: flexibility as a strategy for surviving the mechanical loads in flow-dominated environments	2
1.1.2	Other motivations	3
1.2	The mechanism of elastic reconfiguration	4
1.2.1	Reconfiguration in steady flow	5
1.2.2	Sources of dynamics in steady flow	10
1.2.3	Reconfiguration in time-dependent flows	14
1.3	Organization of the present thesis	17
2	Static reconfiguration of spatially variable flow-structure systems	19
2.1	Model	21
2.2	Drag reduction in a self-similar framework	24
2.2.1	Asymptotic Vogel exponent	24
2.2.2	Bending length	26
2.3	Applications	27
2.3.1	Numerical method	27
2.3.2	A uniform beam in a shear flow	28
2.3.3	A uniform beam in a Blasius boundary layer	29
2.3.4	A non-uniform beam in a uniform flow	34
2.4	Discussion	38
2.4.1	Implications for the Vogel exponents of realistic systems	38
2.4.2	On the robustness of the results	39
2.4.3	On the limits of the model	41
2.5	Conclusions	42
3	Dynamic reconfiguration in oscillatory flow	43
3.1	Model	45
3.1.1	Theory	45
3.1.2	Numerical resolution	48
3.2	Experiments and validation of the model	48
3.3	Kinematics	51
3.3.1	Small amplitude of flow oscillation	51
3.3.2	Large amplitude of flow oscillation	54
3.3.3	Summary of the kinematic regimes	56
3.4	Structural stress analysis	58
3.4.1	Stress reduction due to flexibility	58
3.4.2	Rigid case	58

3.4.3	Small amplitude of flow oscillation	59
3.4.4	Large amplitude of flow oscillation	61
3.5	Discussion	63
3.5.1	Stress alleviation due to flexibility and bending length	63
3.5.2	Consequences in terms of growth pattern of aquatic flexible plants	64
3.5.3	Remarks on previous work about the convective regime	65
3.5.4	Limits and extensions of the model	66
3.6	Conclusion	66
4	Flutter of reconfiguring structures	69
4.1	Specific background elements about flutter	71
4.2	Model	71
4.3	Stability of the static reconfiguration	74
4.4	Post-critical kinematics	77
4.4.1	Kinematic regimes	78
4.4.2	Influence of the slenderness and mass ratio	79
4.5	Drag reduction in the post-critical regime	81
4.6	Conclusion	86
5	Reduction of the vortex-induced vibrations by reconfiguration	89
5.1	Specific background elements about vortex-induced vibrations	91
5.2	Model	93
5.2.1	Theoretical modeling	93
5.2.2	Governing equations	95
5.2.3	On the governing parameters	97
5.3	Numerical results	98
5.3.1	Wake excitation bandwidth and inhibition of single mode lock-in	98
5.3.2	Localization of the excitation and VIV mitigation	101
5.3.3	Influence of the reactive force	103
5.4	Discussion and conclusion	109
6	Conclusion	111
6.1	Contributions	111
6.2	Perspectives	113
Appendix A Nomenclature for Chapter 2		115
Appendix B Simplification of the reactive force for inextensible structures		117
Appendix C Scaling laws for the tensile stress		119
Appendix D Influence of the slenderness on the static reconfiguration		121

Appendix E Comparison of the stability thresholds of Chapter 4 with the axial configuration	123
Appendix F Details on the model of Chapter 5	125
F.1 Derivation of the governing equations	125
F.1.1 Details about the structural model	125
F.1.2 Linearization of the structural model	126
F.1.3 Linearization of the fluid forces	126
F.1.4 Governing equations	127
F.2 Validity of the linearization	127
Appendix G Linear analysis for the transverse vibrations	129
G.1 Linear stability analysis for the coupled wake-structure system	129
G.2 Thresholds for the transverse flutter instability	129

Chapter 1

Introduction

The process of natural selection described by Charles Darwin is believed to have led to the differentiation of species based on their ability to survive and thrive in varying environments (Darwin, 1859). Through the adaptive process of evolution, the different species most likely developed traits that enhance their fitness to the challenges they face as they grow. Building on that assumption, the process of bioinspiration aims at transposing the design principles that have proved appropriate responses to given environmental challenges to the design of man-made structures facing similar constraints. With this in mind, arises first the need to identify the traits responsible for the particular fitness of given species to a specific constraint and to understand the physical mechanisms underlying their efficiency.

Among the many traits that may affect the differential survivorship of plants, the flexibility of the individuals is positively correlated to the magnitude of the flow-induced forces in their habitat (Usherwood et al., 1997; Miler et al., 2012). As in the fable of *Le chêne et le roseau* (*The Oak and the Reed*) by Jean de la Fontaine, flexible plants able to deform in response to the flow appear better suited to resist the large mechanical constraints due to flow-induced forces. This observation is inconsistent with the usual strategy adopted in engineering, where structures exposed to large fluid loads are usually stiffened in order to minimize their deformation. Of course, the design of an engineered structure has to be in accordance with specifications much more diverse than the sole ability not to break, but the same holds for the plants that also have to accommodate their biological needs. Hence, to the very least, there should be room for improvement and innovation if we prove able to understand the process and the limits of the mechanisms that make flexibility an evolutionary advantage for plants living in flow-dominated habitats. Besides, knowledge about the plant-flow interactions is of paramount importance in many fields such as agronomy, ecology, biology, land management, or even video processing (de Langre, 2008).

Plenty of work has already been carried on over the past decades, some of which will be detailed in the subsequent pages of this introduction. Yet, given the diversity of situations and the complexity of the flow-structure interactions in the field, much remains to be done. The purpose of this work is to provide insight regarding the influence of flexibility on the internal stresses in structures deformed in flows, in situations more complex than the overly idealized cases studied thus far. In particular, we analyse possible limitations of the existing theories to assess whether flexibility is unconditionally advantageous or if there are situations in which it might become detrimental to the structural integrity.

In this introductory chapter, we first detail some of the motivations that have led to

the study of plant-flow interactions, and in particular to the specific role of flexibility in these interactions. We then present a review of the state of the art regarding the response of flexible structures in fluid flows.

1.1 Motivations

1.1.1 Bioinspiration: flexibility as a strategy for surviving the mechanical loads in flow-dominated environments

Plants living in flow-dominated habitats have to cope with the mechanical loads to ensure their survival. In the perspective of designing sustainable, robust structures able to withstand large flow-induced forces, we may be interested in the solutions that evolution has brought to best accommodate this problem.

First, it is important to emphasize that the fluid forces are not necessarily the only mechanical loads plants have to withstand. In fact, terrestrial plants are usually subject to loads due to gravity greater than those due to the surrounding air. Growing stiff notably appears as a necessary condition to avoid buckling under their own weight (Usherwood et al., 1997; Ennos, 1999). On the other hand, water plants may rely on buoyancy to avoid gravity loads, but the larger density of water compared to air makes the fluid loadings absolutely dominant in aquatic environments.

Besides, it should be noted that survival does not necessarily mean avoiding breakage. On the contrary, some species such as the feather boa kelp *Egregia menziesii* may take advantage of the weakness of their tissue to avoid uprooting by self-pruning during the most extreme events such as winter storms (Demes et al., 2013). The ability to sacrifice some fronds in order to reduce the overall force on the root system acts as a kind of “*mechanical fuse*” (Usherwood et al., 1997) that may prevent the whole plant from being dislodged (Krumhansl et al., 2015). The details of this mechanism have been theoretically analysed in Lopez et al. (2011) and Lopez et al. (2014). For some coral species, flow-induced breakage may even constitute the main mechanism of reproduction by dispersing broken-off pieces that survive on their own and settle somewhere else (Highsmith, 1982). But in the case of *Egregia menziesii*, self-thinning comes at the expense of the reproductive output (Demes et al., 2013), and the weakness of its tissues results from a trade-off between the necessity to survive and other considerations.

In fact, the morphology and tissue properties of the plants are meant to accommodate not only the mechanical loads, but also the biological needs such as light interception, nutrient, carbon and oxygen uptake or reproductive efficiency (Puijalon et al., 2005; Bal et al., 2011). Generally speaking, growing large is beneficial in terms of these biological considerations (Denny et al., 1985; Krumhansl et al., 2015; Bal et al., 2011), but this comes at the cost of greater flow-induced forces that endanger the individuals.

To cope with the fluid forces while keeping the ability to reach large sizes, kelps grow either strong tissues able to endure large stress levels, or flexible blades that provide the ability to deform substantially to reduce the drag in a given flow (Starko and Martone,

2016). Breaking strength and flexibility furthermore appear to be negatively correlated, which suggests that drag avoidance and tolerance are two incompatible strategies in nature that both lead to a greater chance of surviving large hydrodynamic loads.

The potential that flexibility bears for reducing the drag on plants with relatively weak tissues is now believed to be one of the key factors that allow them to thrive in flow-dominated habitats (Harder et al., 2004). Thus, understanding the mechanisms responsible for alleviating the drag on flexible plant elements is undoubtedly of interest from a bioinspired perspective.

1.1.2 Other motivations

Apart from possible applications in bioinspired design, knowledge about the plant-flow interactions has been sought for many other reasons in diverse scientific communities.

In the agricultural sector, the effects of the wind on biomass production for the food or wood industries may be the cause of massive economic losses. The damages on cereal crops are responsible each year for productivity losses that may amount up to 30% of the harvest (Berry et al., 2004). Similarly, the violent storms that swept through France in December 1999 have caused the destruction of about 140 million cubic meters of wood (Birost et al., 2000), which represents about 3 times the average annual usage.

In biology, the wind-induced motion of leaves is believed to hinder foliage destruction due to herbivory (Yamazaki, 2011), to enhance water holding in the fog (Merriam, 1973), and to alter the photosynthesis and gaseous exchanges at the scale of the leaves (Clark et al., 2000; Roden and Pearcy, 1993) and the light shedding at the scale of the canopy (Pearcy, 1990; Roden, 2003). On a longer time-scale, the mechanical perception of the stresses induced in the plant structure results in a selective biomass allocation during the growth called thigmomorphogenesis. Eventually, this process improves the morphological and mechanical fitness of the plant to its environment (Jaffe, 1973; Moulia et al., 2011). For instance, the branches of the well-named ‘flag tree’ shown on Figure 1.1(a) grow in the direction of the wind. Koehl and Alberte (1988) also reported that the giant kelps *Nereocystis luetkeana* feature large ruffled blades in calm water environments and thin flat blades in fast flows (see Figure 1.1(b)). This intra-specific phenotypical difference most likely stems from different adaptive growth patterns in response to the flow-induced loads in the two types of habitat.

In ecology, the depletion of the macrophyte population due to the currents in freshwater lakes may have dramatic consequences on the stability of the ecosystem (Carpenter and Lodge, 1986) and the quality of the water (Van den Berg et al., 1998; Albertoni et al., 2014). Moreover, the aquatic vegetation opposes a resistance to the flow that affects the transport of the sediments and nutrients, or the erosion of river banks and foreshores. In coastal ecosystems such as salt marshes, mangrove forests or reed swamps, the flow dissipation due to vegetative resistance reduces the intensity of the waves and protect the shores from being too severely impacted (Anderson et al., 2011; Vuik et al.,

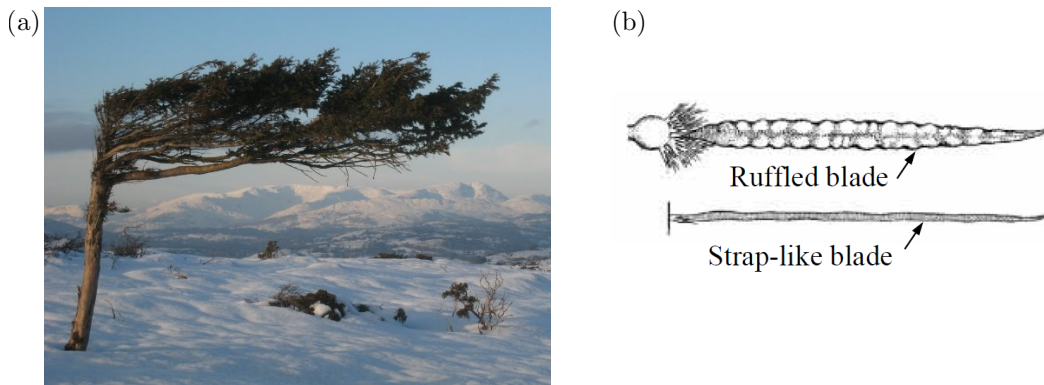


Figure 1.1: Examples of thigmomorphogenesis. (a) Flag tree with its branches aligned with the direction of the wind, from WEB01. (b) Ruffled and strap-like blades of *Nereocystis luetkeana* depending on the magnitude of the flow in their habitat, from Koehl (1999).

2016). The efficiency of the wave attenuation is obviously highly dependent on the standing biomass on the foreshore, so that flow-induced breakage of the vegetation may substantially increase the impact of the wave loads on the shorelines or the flood defense structures (Vuik et al., 2017). Similarly, riparian and floodplain vegetation are increasingly seen as a potential protection against flooding that is both efficient and sustainable. To this day, most available models of vegetated flow-resistance lack the consideration of some critical plant characteristics such as their ability to deform due to their flexibility (Anderson et al., 2011; Aberle and Järvelä, 2013). Some improvements have been made recently to remedy this flaw (Whittaker et al., 2013, 2015; Luhar and Nepf, 2013; Luhar et al., 2017), based on new progress made in the understanding of the mechanical behaviour of flexible model systems in fluid flows, but much remain to be done.

More generally, the determination of the key factors influencing the deformation of plant elements in different types of fluid flows, the magnitude of the fluid forces that are imposed on them, and the risk of breakage or uprooting they are subjected to all find applications in the domains cited above. In order to further deepen our knowledge of the plant-flow interactions, refined mechanical analyses of coupled flow-structure model systems are necessary. In the following section, we present some of the existing theories and results.

1.2 The mechanism of elastic reconfiguration

The process of elastic deformation resulting in an alleviation of the drag force on a flexible structure is usually referred to as ‘reconfiguration’. This term was introduced by Vogel (1984) in the field of biomechanics in order to emphasize the adaptive nature of

the deformation: “*Shape becomes a function of speed, and the scaling of drag with speed assumes unusual interest. Indeed the word ‘reconfiguration’ may be more appropriate than ‘deformation’ — we suspect specific adaptation and the latter carries some pathological odor of disfunction.*” Depending on the features of the flow and the structure, the mechanisms involved in this phenomenon may vary. We first focus on the case of a static deformation in a steady flow.

1.2.1 Reconfiguration in steady flow

According to observations made in Vogel (1984); Koehl (1984); Koehl and Alberte (1988); Vogel (1989); Boller and Carrington (2006), the mechanisms by which reconfiguration affects the intensity of the fluid loads in a steady flow are manifold. The two most well-documented effects are the frontal area reduction and the streamlining of the shape. Indeed, the pressure drag force on a rigid object in a steady flow classically reads

$$F = \frac{1}{2}\rho C_D A_f U^2 \quad (1.1)$$

where ρ is the density of the fluid, A_f is the frontal area of the object (projected on the plane normal to the flow), U the characteristic velocity of the flow through the frontal area, and C_D a drag coefficient (Taylor, 1952). The drag coefficient of rigid objects depends essentially on the Reynolds number R_e and on the shape of the object. However, the Reynolds number on macroscopic plants in flows fast enough to deform them is typically large enough ($R_e \sim 10^5 - 10^7$, see Harder et al., 2004) so that the Reynolds-related variations are negligible and C_D is essentially a shape-dependent quantity. The large value of the Reynolds number, and the geometry of the plants generally facing the flow more than being aligned with it further justifies that friction drag should be negligible compared to pressure drag. In the case of a flexible structure, the shape of the object varies with the flow velocity, as illustrated on Figure 1.2 in the cases of a tulip tree leaf and a red alder tree.

As a consequence, both the frontal area A_f and the drag coefficient C_D are functions of the flow velocity U . In most cases, reconfiguration results in a reduction of the frontal area. This is clearly visible in the case of the red alder tree on Figure 1.2(b). Besides, the deformation of the plant generally leads to a more streamlined shape that allows a better pressure recovery in its wake, so that the drag coefficient is lowered as well. For instance, the experimental results of Boller and Carrington (2006), displayed on Figure 1.3, clearly show a reduction of both the frontal area and the drag coefficient of the algae *Chondrus crispus* as the water velocity increases. Thus, overall, the drag force on a deforming plant does not increase quadratically with the flow velocity, but with a different scaling

$$F \propto U^{2+\nu} \quad (1.2)$$

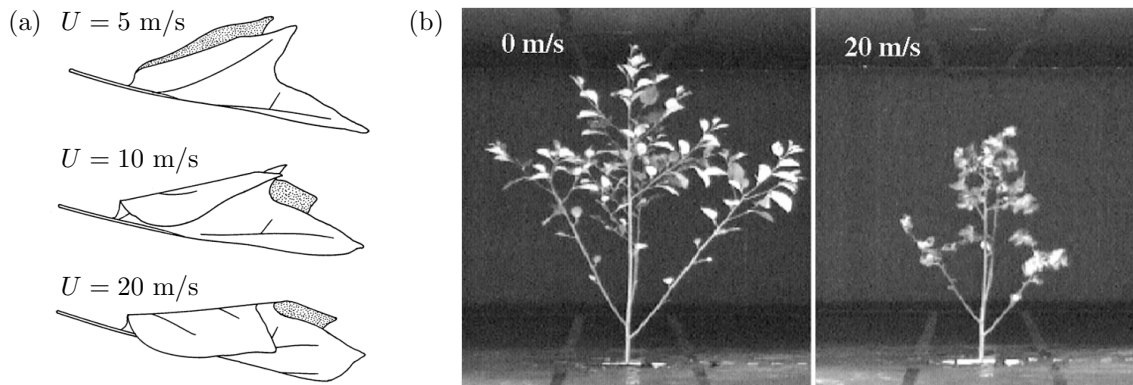


Figure 1.2: (a) Rolling-up reconfiguration of a tulip tree leaf (side view, air flow from left to right), from Vogel (1989) (b) Bending reconfiguration of a red alder tree (front view, air flow from front to back of the page), from Vollsinger et al. (2005)

where the so-called Vogel exponent ν , first introduced in Vogel (1984), includes the dependency on the flow velocity of the frontal area and drag coefficient. In most cases, it takes negative values so that the drag increases subquadratically due to the effects of the deformation. The effects of the deformation are not necessarily the same at low and large velocities, so that the Vogel exponent is not necessarily a constant value throughout the whole range of flow velocities.

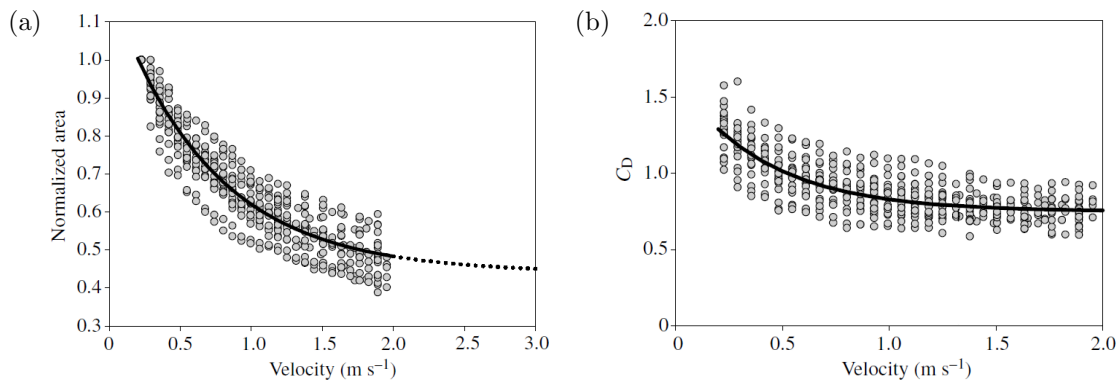


Figure 1.3: Variations with the flow velocity of (a) the frontal area normalized by the frontal area at rest and (b) the drag coefficient, for algae *Chondrus crispus* in a water flume, from Boller and Carrington (2006).

The first study to provide theoretical predictions of the drag reduction by elastic reconfiguration on a model system was that of Alben et al. (2002, 2004). The authors considered an elastic one dimensional fibre in an inviscid two dimensional flow, both experimentally and numerically (see Figure 1.4(a)). Their model for the drag predicts

a transition from the classical rigid-body U^2 law to a new $U^{4/3}$ scaling law at large flow velocities (see Figure 1.4(b)), corresponding to a Vogel exponent in the asymptotic regime (when the deformation is significant) $\nu_\infty = -2/3$.

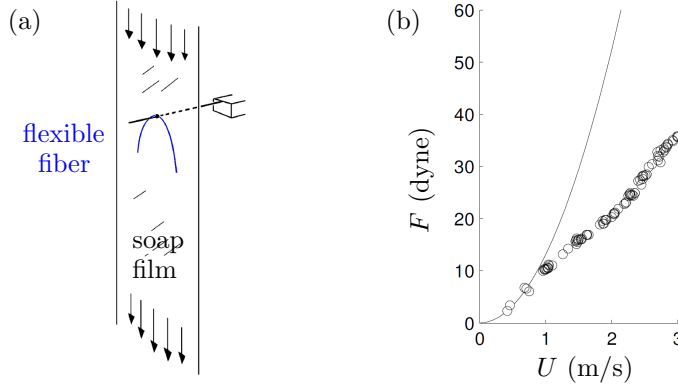


Figure 1.4: (a) Experimental setup of Alben et al. (2004) and (b) evolution of the drag force on the flexible fibre as a function of the velocity of the soap film.

Their study also revealed the importance of a single control parameter, which they call the elasto-hydrodynamical number. This quantity is the square root of the more commonly used Cauchy number C_Y (Tickner and Sacks, 1969; Chakrabarti, 2002; de Langre, 2008) that scales the competing effects of fluid loading to the elastic restoring force. When the Cauchy number is small $C_Y < 1$, deformation of the object is negligible. On the other hand, when $C_Y > 1$, the drag on the structure is significant enough to substantially deform it and we expect the scaling of the drag to deviate from the quadratic law. In the case of slender structures bending under the effects of a transverse flow, the Cauchy number reads

$$C_Y = \frac{\rho U^2 W L^3}{2EI} \quad (1.3)$$

where W is the width of structure in the direction transverse to the flow, L its length, and EI its bending stiffness (E the Young's modulus of the material and I the area moment of inertia of the cross-section). Subsequently, the study of Gosselin et al. (2010) considered the reconfiguration of two dimensional plates clamped at the centre in a wind tunnel (see Figure 1.5). To isolate the contribution of flexibility to the velocity-drag law throughout the whole range of flow velocities, the authors defined the reconfiguration number \mathcal{R} as the drag on the flexible structure normalized by that on a geometrically similar but rigid structure

$$\mathcal{R} = \frac{F}{F_{rigid}} \propto U^\nu. \quad (1.4)$$

As the Cauchy number is proportional to the flow velocity squared $C_Y \propto U^2$, the Vogel exponent can be inferred from the slope of the loglog plot $\mathcal{R}(C_Y)$ according to

$$\nu = 2 \frac{\partial \log \mathcal{R}}{\partial \log C_Y}. \quad (1.5)$$

A schematic view of the correspondence between the different representations of the velocity-drag relationship is shown on Figure 1.6 in arbitrary units. In this particular case, the Vogel exponent asymptotically goes to -1 for large Cauchy numbers, so that the velocity-drag law goes from quadratic to linear. The work of Gosselin et al. (2010) showed that variations in the drag coefficient of the cross-sections of the plates due to blockage effects in the wind tunnel prevented the data from different plates to collapse on a single curve. The proper definition of the Cauchy number should consequently include the cross-section drag coefficient $\widetilde{C}_Y = C_D C_Y$. The model used in this study further leads to an asymptotic Vogel exponent $\nu_\infty = -2/3$ similar to that found by Alben et al. (2004).

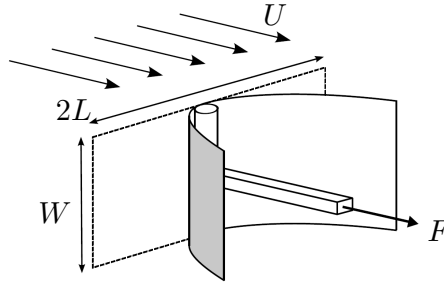


Figure 1.5: Experimental setup of Gosselin et al. (2010): a rectangular plate is clamped in the middle in a transverse flow of velocity U .

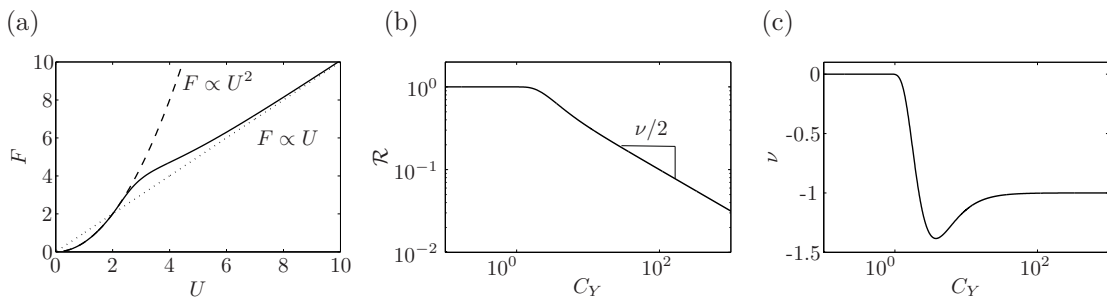


Figure 1.6: Schematic view of the loading-drag relationship in the different parameter spaces (arbitrary units). U : reference flow velocity, F : drag force, C_Y : Cauchy number, \mathcal{R} : reconfiguration number, and ν : Vogel exponent.

Reconfiguration may also occur through other modes of deformations. In order to explain the drag reduction due to the rolling up of daffodil leaves originally observed by

Vogel (1989) and shown on Figure 1.2(a), Schouveiler and Boudaoud (2006) obtained theoretical and experimental estimates of the asymptotic Vogel exponent for circular plastic sheets cut along a radius (experimental setup shown on Figure 1.7). They found a drag scaling as $U^{2/3}$, while a theoretical and numerical study by Alben (2010) on the same system concludes that the drag should increase as U^1 . From the assumption that the scaling of drag reduction results from the loss of one typical length scale, de Langre et al. (2012) showed that the Vogel exponent of any structure made of beams and plates (such as most plants) should exhibit approximately the same behaviour. By a simple dimensional analysis, they recovered the classical $-2/3$ Vogel exponent found by Alben et al. (2004) and Gosselin et al. (2010) in the asymptotic regime. They further claimed that non-linearity in the material constitutive law should have little impact on the scaling of drag. Subsequently, the work of Luhar and Nepf (2011) additionally proved that the effects of gravity or buoyancy should not significantly alter the aforementioned results as long as the flow is the dominant source of loading on the structure. On the other hand, the results of Zhu and Peskin (2007) and Zhu (2008) regarding the reconfiguration of 1D fiber in 2D flows at low Reynolds number concluded that viscosity mitigates the benefits of reconfiguration. Their study showed a variation of the asymptotic Vogel exponent from $-2/3$ at $R_e = 800$ to approximately 0 at $R_e = 10$.

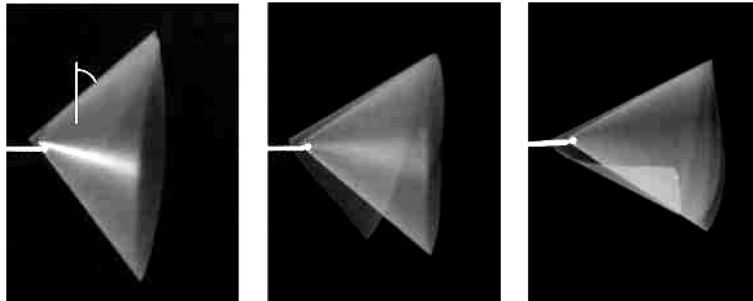


Figure 1.7: Experimental setup of Schouveiler and Boudaoud (2006): a circular plastic sheet cut along a radius rolls up into a cone as the flow velocity (from left to right) is increased, from left to right.

All these studies considered individual elements plunged in a uniform flow so that the reference velocity U that appears in the expression of the drag (1.1) is not affected by the deformation. However, when plants form bundles as is the case for instance for the giant bull kelp *Nereocystis luetkeana*, a reduction of the drag due to the reduction of the flow velocity inside the bundle was reported in Koehl and Alberte (1988); Koehl et al. (2008). The flow impinging on the inner blades may thus be slowed down due to a reduction of the porosity of the bundle as the blades clump together under the effect of the flow. In this particular case, the drag force is of a different nature as it stems from the friction on the blades aligned with the flow, but similar sheltering effects may cause the alleviation of the pressure drag as well. In that regard, the work of Gosselin

and de Langre (2011) found that the Vogel exponent of a poroelastic system made of beams decreases from $-2/3$ when the beams are far enough to be considered isolated to -1 when they shelter each other. The recent study of Barsu et al. (2016) also reported the existence of sheltering effects in laterally confined two dimensional canopies, when the spacing is small enough so that the downstream blades feel the influence of the recirculating flow in the wake of the upstream blades.

Finally, the reference velocity may be affected by the deformation even in the case of isolated elements, if the flow is non-uniform. This eventuality is suggested in Koehl (1984), in the case where deflection might allow a structure to dive and encounter the lower velocity of the boundary layer close to the substratum. We may also imagine that a non-uniform distribution of the structural properties may lead to variations in the deformation behaviour possibly leading to different scalings of the drag force with the flow velocity. **The influence of non-uniformities in the free-stream or in the structure have nonetheless never been theoretically accounted for in full.** The properties of the flows and plants in the field are very unlikely to be uniformly distributed, and a range of models is clearly missing to fill the gap between the idealized cases studied thus far and the more complex natural configurations.

In spite of the large diversity of the plant-flow systems, it is quite remarkable to see how robust the mechanism of drag reduction by elastic reconfiguration appears to be. A plethora of experimental measurements of Vogel exponents of plants or model systems can be found in the literature, and the vast majority of them indicate that the drag on flexible systems of almost any type grow close to linearly with respect to the flow velocity, $\nu \sim -1$ (de Langre, 2008). For instance, experiments on multiple species of pines in wind-tunnels presented in Vogel (1984) or Rudnicki et al. (2004) conclude to an approximately linear velocity-drag relation. Wilson et al. (2010) measured the hydrodynamic drag over full-scale trees towed in a water tank and also reported a linear increase of the drag. A similar conclusion was drawn by Sand-Jensen (2003) for freshwater macrophytes and strap-like plastic blades in water. Finally, the extensive lists of Vogel exponents for marine or aerial species of varying morphologies and sizes provided in Harder et al. (2004) or de Langre et al. (2012) display values between 0 and -1.3 , generally close to -1 . None of the geometrical properties of the structure, the nature of the fluid, or the mode of deformation appear to play a critical role in this mechanism. **This remarkable uniformity of the Vogel exponents with respect to the properties of the particular flow-structure systems remains so far unexplained.**

1.2.2 Sources of dynamics in steady flow

Whether they explicitly mention it or not, most of the studies mentionned thus far have focused on the static or averaged deformation and drag of plants or structures in steady currents. The dynamic deformation of whole canopies in response to the Kelvin-Helmoltz instability of the flow at their surface has received attention for some time

(Inoue, 1955; Py et al., 2006; de Langre, 2008; Ackerman and Okubo, 1993; Ghisalberti and Nepf, 2002; Okamoto and Nezu, 2009), but only little work has been devoted to the flapping motion of individual plant elements in steady flows and the impact it may have on the internal stress they have to bear. Such dynamics may arise on top of the static deformation, in response to the turbulence in the free-stream, from coupling with the vorticity wake of the object, or from fluid-structure instabilities (Blevins, 1990; Païdoussis, 1998; Païdoussis et al., 2010).

The work of Siniscalchi and Nikora (2012) and Denny (1994) has brought to light the close relation between the upstream turbulence and the variations of the drag force on water-swept organisms. However, further results in Siniscalchi and Nikora (2013) underline that the dynamic deformation of these plants is not related to turbulence but most likely stems from a flag-like flutter instability. Based on the work of Lighthill (1960); Barrett et al. (1999); Dong and Lu (2005) regarding the reduction of drag in fish-like locomotion, the authors of Siniscalchi and Nikora (2013) suggest that this regular, large-amplitude dynamic deformation might similarly improve the drag reduction ability of these plants. On the other hand, based on the work of Chang and Moretti (2002); Moretti (2003); Morris-Thomas and Steen (2009) about the drag of fluttering flags, the authors also mention the potential for drag enhancement that this instability may bear. Similar fluttering motion have also been reported in Koehl and Alberte (1988) and Koehl et al. (2008) for the giant bull kelp *Nereocystis luetkeana*, as well as in Usherwood et al. (1997) for some aquatic buttercup species. All these studies suggest that the inertial forces associated with the flapping motion should most likely enhance the drag and potentially endanger the plants. **However, none of them have assessed the actual impact of flutter on the drag or internal stress inside the plants. Whether flutter would help alleviating the loads, would counteract the drag reduction due to reconfiguration, or would even fully offset the benefits of reconfiguration and enhance the drag compared to a rigid structure remains an open question.** More background elements regarding the problem of flutter will be provided in Chapter 4.

Regarding the coupling of the structure with the vorticity wake, two different types of interactions are observed depending on the geometry of the system.

First, in the case of the planar bending of large plates, equivalent to the one-dimensional fibre bending in a two-dimensional flow studied by Alben et al. (2002, 2004) (voir Figure 1.4), vortex shedding may occur at the tips of the fiber. If this effect was neglected in the model of Alben et al. (2004), it has subsequently been accounted for. In the case of low Reynolds number $R_e \in [80, 300]$, the numerical simulations of Zhu (2007) show that the coupling between the fibre and its wake is responsible for small oscillations of the fibre about its mean position. The drag force similarly oscillates about its mean value. The features of the wake furthermore depends on the Reynolds number (see Figure 1.8), and the dynamics of the structure is affected accordingly. The transition of the asymptotic Vogel exponent (for the average drag) from

0 at low R_e to $-2/3$ at $R_e = 800$ shown in Zhu (2008) accounts for the coupling with the wake. However, the variation of the scaling of the drag force is most likely due to the switch of dominant fluid loading from skin friction to pressure drag and the effects of the wake-induced dynamics are most likely secondary. Additional results presented in Miller et al. (2012) show that the amplitude of the vortex-induced vibrations are enhanced if the fibre is attached at its center to a flexible tether instead of a rigid one.

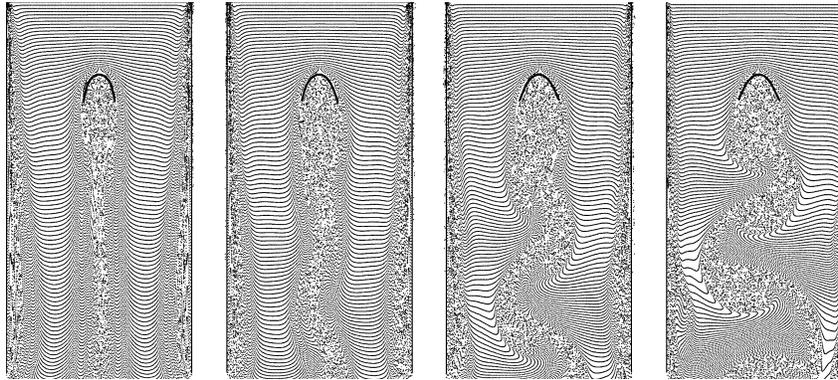


Figure 1.8: Flow past a flexible fibre at varying Reynolds number (a) $R_e = 82.5$, (a) $R_e = 165$, (a) $R_e = 330$ (a) $R_e = 660$, for a fixed Cauchy number, from Zhu (2007).

In the large Reynolds number situation of Alben et al. (2004), the numerical study of Yang and Liu (2016) concluded to the existence of four different bending modes displayed on Figure 1.9, essentially depending on the value of the Cauchy number. As the two deflecting branches of the fibre get closer to each other, the stability of the U-shaped mode considered by Alben et al. (2004) is lost and alternate vortex shedding forces the structure into slight oscillations. When the gap between the branches closes further, flapping is enhanced until the two branches finally come together in a stable closed shape. The scaling of the drag found in Alben et al. (2004) or Gosselin et al. (2010) is valid in the stable U-shaped mode, but Yang et al. (2014) explains that the effect of the dynamics in the flapping mode increases the drag substantially. Finally, the closed mode exhibits a quadratic drag increase because its shape remains unchanged as the velocity increases further.

The other configuration in which the effect of vortex shedding may impact the dynamics is that of elongated structures that are thin in the direction transverse to the flow. In this situation, the structure may locally be considered infinite in the axial direction and the fluid-structure interactions in neighbouring cross-sections along the span may be considered independent. As a consequence, vortex shedding from the tip of the structure in the direction of the free-stream is of negligible influence, but the vorticity shed locally in the wake of each cross-section may induce structural vibrations (see Figure 1.10). Indeed, the wake behind a cylindrical object destabilizes at large Reynolds number, and forms a Von-Karman street in which vortices of alternating signs

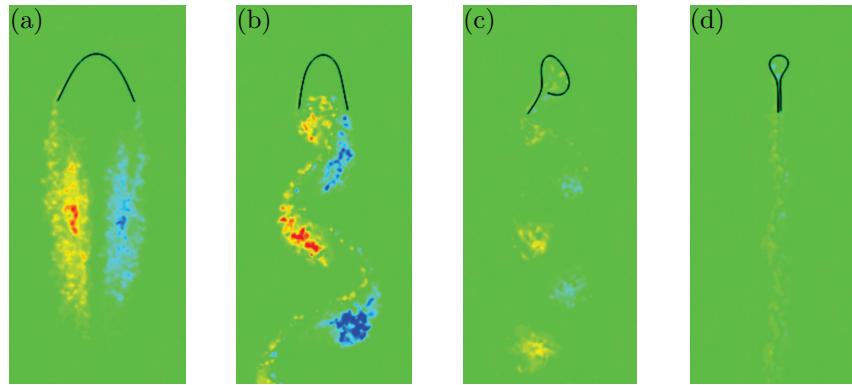


Figure 1.9: Bending modes found by Yang and Liu (2016): (a) stable U-shaped mode, (b) slight swing, (c) violent flapping, (d) closed mode.

are shed with a natural frequency $f_w = S_t U/D$, where U is the velocity of the free-stream, D the diameter of the cylinder and the Strouhal number S_t is typically of the order of 0.2 for circular cross-sections (Blevins, 1990). This results in an oscillating lift that forces the structure into a transverse motion of self-limited amplitude comparable to the transverse dimension of the object D . The evolutions of the frequency and amplitude of the oscillations of a flexibly mounted cylinder of natural frequency f_s is displayed on Figure 1.11 as functions of the reduced velocity $U_R = S_t U/f_s D = f_w/f_s$. When the wake frequency is far away from the natural frequency of the structure, the structure responds at the wake frequency f_w with a very small amplitude. On the other hand, when the natural frequencies of the wake and the structure are close to each other $U_R \sim 1$, the vibrations and vortex shedding both occur at a frequency f that deviates from the Strouhal law $f = f_w$. This phenomenon is classically referred to as *frequency lock-in* and stems from a strong bilateral coupling between the structure and its wake (Williamson and Govardhan, 2004; de Langre, 2006). In the range of flow velocities where that happens, the amplitude of the oscillations is enhanced due to the extended resonance in the system. In the more complex case of elongated flexible cables, the interaction between the structure and the distributed forcing by the wake along the span is made much more complex due to the multiplicity of the natural frequencies of the structure and the possible spanwise non-uniformity of the flow (see for instance King, 1995; Trim et al., 2005; Facchinetti et al., 2004b; Mathelin and de Langre, 2005). Additional background elements regarding the problem of the vortex-induced vibrations will be provided in Chapter 5.

Flexible elongated cylindrical structures, whether natural or man-made, are liable to such vortex-induced vibrations even when they are deflected under the effect of the flow. The VIVs have been a prominent subject of research for many years, mostly because of the threat they constitute for civil and marine engineering structures such as buildings, power transmission lines, marine risers, towing cables, or mooring lines. In the case of a structure heavily deflected under the effect of the flow, one might argue that the

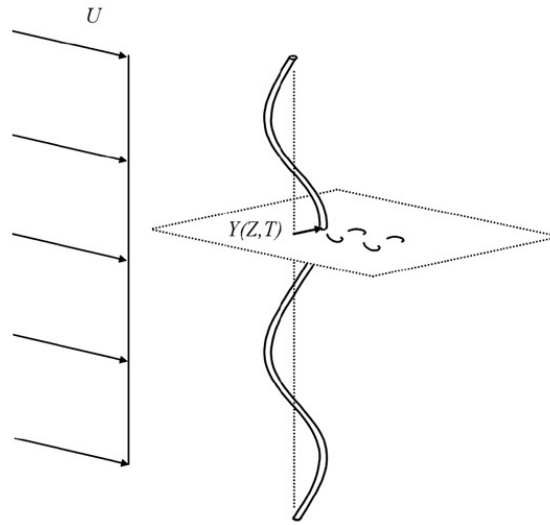


Figure 1.10: Vortex-induced vibration of a cable in transverse flow, from Violette et al. (2010). The wake vortices alternatively shed in the plane of the cross-sections force the structure into transverse oscillations.

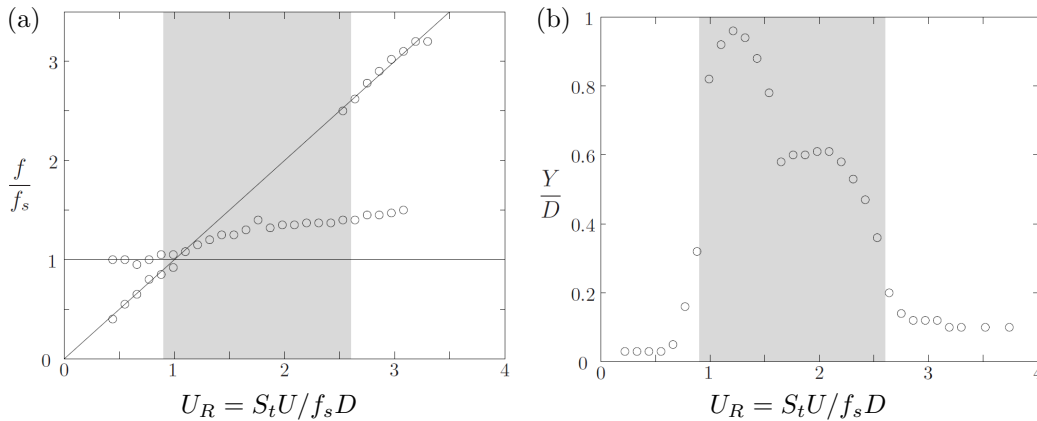


Figure 1.11: Lock-in of a flexibly mounted, rigid circular cylinder, from Khalak and Williamson (1997). Evolution of (a) the frequency f of the VIVs normalized by the natural frequency f_s of the solid oscillator, and (b) the amplitude of vibrations Y normalized by the diameter of the cylinder D , as functions of the reduced velocity $U_R = S_t U / f_s D$. The grey zone corresponds to lock-in.

additional stress due to the VIVs is negligible, as the amplitude of the vibration scales with the diameter of the structure D when the amplitude of the static in-line deflection is comparable to its length $L \gg D$. However, the VIVs are the source of a fast cyclic load that may be the cause of fatigue fracture after the repetition of a large number of cycles, even though the amplitude of the load itself is small. Besides, the drag coeffi-

cient of transversely vibrating cylinders is magnified by an amplitude-dependent factor (Vandiver, 1983; Blevins, 1990; Chaplin et al., 2005), due to a larger apparent exposure to the flow. The onset of VIVs may thus be responsible for a drag force up to twice as large, in comparison to a structure that does not vibrate. **Correctly predicting the VIVs of immersed structures is therefore of paramount importance in order to accurately assess their operating lifespans and risks of breakage. The features of the VIVs, and particularly their amplitude, are surely affected by the in-line deformation of the cylinder. No study has nonetheless explicitly accounted for this effect thus far.**

1.2.3 Reconfiguration in time-dependent flows

Compared to all the literature on the mechanisms of reconfiguration in steady flow presented above, relatively little work has been done regarding the consequences of the elastic deformations of flexible structures in time-dependent flows. Yet, as mentioned in Section 1.1, this question is of paramount importance for the prediction of wave-energy dissipation over coastal ecosystems, as well as for the understanding of the evolutionary trade-offs that have led the near-shore kelps to reach such large sizes.

In fact, it is not even clear whether or not flexibility should systematically result in an alleviation of the fluid loads in such circumstances, owing to the different nature of the fluid forces. In the formulation of Morison et al. (1950), the force on a rigid object in an oscillatory flow is the sum of the drag force (1.1) and an additional fluid inertial force (Blevins, 1990; Gaylord et al., 1994)

$$F_a = \rho V \dot{U} + C_m \rho V \dot{U} \quad (1.6)$$

The first term, often referred to as ‘virtual buoyancy’ (Koehl, 1984), is due to the pressure gradient induced by the absolute acceleration of the fluid \dot{U} . It is equivalent to the Archimedes force, only the acceleration of gravity is replaced by that of the fluid. It is proportional to the displaced mass of fluid ρV where V is the volume of the object. The second term, called ‘added mass force’, arises from the potential pressure field due to the relative acceleration of the fluid and the object. As for the drag coefficient in (1.1), the added mass coefficient C_m is of order $O(1)$ and depends on the shape of the object and on the Reynolds number. In an oscillatory flow of peak velocity U and frequency f , both coefficients also depend on an additional parameter called the Keulegan-Carpenter number $K_C = U/Wf$ (Keulegan and Carpenter, 1958), that compares the typical excursion of the fluid particles over one cycle U/f to the typical size of the object in the direction transverse to the flow W .

Koehl (1984) pointed out that the fluid acceleration forces in an oscillatory flow, proportional to the volume of the plant when the drag is only proportional to its frontal area, may be the dominant load that large organisms have to withstand. The author thus suggests that the mechanical loads may set the upper size limit of organisms in wave-swept habitats (see also Denny et al., 1985). However, the very large sizes reached

by giant kelps seems to indicate that the morphology of these algae must be finely tuned in order to overcome this limitation.

In fact, Koehl (1984) further suggests that flexible organisms may be able to reduce the fluid loads by moving with the water, thus reducing the magnitude of the relative flow. This mechanism of “going with the flow” (as worded in Gaylord et al. (1994)) should nonetheless have a drag-reducing effect only if the kelp is long enough not to reach the end of its tether during the wave-cycle. Otherwise, the momentum of the algae may impose large inertial forces when it reaches the end of its course. Hence, Koehl (1984) is actually suspecting that two possible dynamic regimes may exist, delimited by a condition on the length of the structure relative to the maximum excursion of the fluid particles: one in which the structure “goes with the flow” and reduces the hydrodynamic loads, and the other in which the structure may have to withstand large inertial forces. In the first regime, the total drag should furthermore become independent of the actual structure length, provided that it is large enough.

Different mechanical models have subsequently been proposed to replicate the motion of real macroalgae with different types of mechanical properties under the action of waves. Two such models are schematically shown on Figure 1.12 (for more details, see Friedland and Denny (1995) for fully submerged flexible plants, Utter and Denny (1996); Denny and Cowen (1997) for algae larger than the water depth, and Gaylord and Denny (1997) for stipitate kelps). Overall, the results of these simulations support Koehl’s predictions of a regime where the force is reduced, for structures larger than the wave excursion, as well as the potential for excessive swaying motion leading to increased forces when this criterion is not met. The results of Denny and Cowen (1997) further indicate that juvenile *Nereocystis luetkeana* would not be able to withstand the hydrodynamic loads when they grow if they maintained the same aspect ratio through isometric growth. Slenderness thus also appears as a factor affecting the intensity of the flow-induced loads.

In order to better characterize the different dynamic regimes, Denny et al. (1998) analysed the dynamic behaviour of simple unidimensional heuristic models subjected to the hydrodynamic forces in an oscillatory flow. This work highlighted the importance of an additional parameter, the ‘jerk number’ that basically compares inertial and drag forces. For high jerk numbers, resonances between the flow and the structure were found responsible for peak forces when the frequency of the flow was close to the natural frequency of the solid oscillator. On the other hand, drag reduction was observed only at low jerk numbers and far away from resonance frequencies.

This series of studies is very insightful and provides many leads regarding possible key factors and parameters influencing the magnitude of the flow-induced forces on flexible systems. However, the variety and the complexity of the systems considered, and the diversity of the models used in these papers make it hard to draw general conclusions from them. Besides, a proper analysis of the mechanisms ruling the different regimes and of the precise role of the different parameters involved, as well as the various scalings of the total force on the structure depending on them are still missing from those studies.

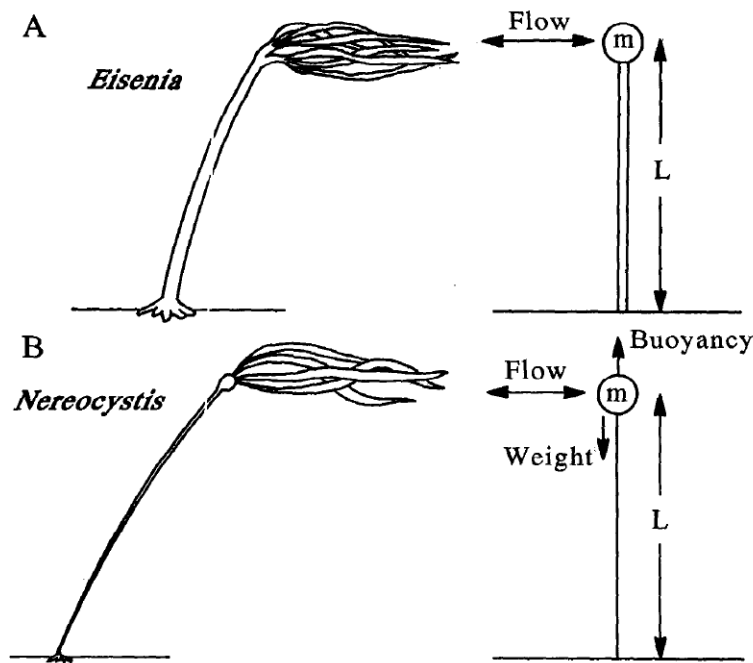


Figure 1.12: Examples of models used in the numerical work of Mark Denny: A. cantilever beam model with lumped mass at the top, for the modelling of the bending deformation of the stipitate kelp *Eisenia arboarea*. B. Spring-chain model with lumped mass at the top, for the modelling of the tensile deformation of *Nereocystis luetkeana*, from Denny et al. (1998).

Some of these issues were recently addressed in Luhar and Nepf (2016). Their work suggests, based on experimental results, that the drag on deformable structures may be expressed as that on a rigid structure with an effective length corresponding to the part of the actual structure over which significant relative fluid motion occurs. A scaling of this effective length with the flexibility was provided, with the aim to provide a tool to account for the deformability of near-bed organisms in the models of wave-energy dissipation (see also Luhar et al., 2017). But the work of Luhar and Nepf (2016) focuses on the specific case where the amplitude of the flow is at most of the order of the length of the structure. They do not investigate either the dynamic interactions (such as possible resonance effects) due to high frequency loading. Besides, for particular values of the parameters, Luhar and Nepf (2016) notice an increase of the total drag force compared to the rigid case that is still not fully understood. **Thus, in order to identify and understand the different mechanisms involved in the deformation and modulation of the drag and internal stress of flexible structures in oscillatory flow, a systematic analysis exploring the space of parameters is still required.**

1.3 Organization of the present thesis

From the presentation of the existing work on reconfiguration detailed in this introduction, we see that many of its aspects remain unexplored or poorly understood. The static reconfiguration of simple model systems in steady, uniform flows has been extensively analysed, and the main mechanisms enabling the fluid load to be reduced in this simple case are quite understood. But actual plants or even engineered structures in the field are likely to present more complex geometries and material properties, to be exposed to non-uniform, unsteady flows, and to undergo some dynamics due to some sort of coupling with the flow. It seems nonetheless that the ability to deform should still lead to a reduction of the fluid loads, at least in the range of parameters that characterizes natural systems, otherwise flexibility would likely not be as widespread among the live organisms in flow-dominated habitats. We thus claim that:

“The alleviation of the internal stress by elastic reconfiguration of flexible structures subjected to fluid flows is a robust phenomenon with respect to both the possible non-uniformities of the flow-structure system, and the dynamics that may arise from various physical origins.”

In the following chapters, we discuss this assertion, the physical mechanisms underpinning it, and also its domain of validity. In order to simplify the analysis and provide general conclusions, we choose in the whole manuscript the same model system of a slender, cantilever structure, clamped perpendicular to the flow. Most of the results presented rely on numerical simulations of the behaviour of such systems, based on suitable reduced order models depending on the situation considered. The technical details regarding these models are referred to the first pages of each chapter.

To defend this thesis, we propose to analyse, in the following chapters, the respective influence of different phenomena. The effect of the spatial variability of the flow-structure system is discussed in Chapter 2, while the scaling of the internal stresses due to the flow-induced dynamic reconfiguration in an oscillatory flow is addressed in Chapter 3. Then, Chapter 4 focuses on the consequences of a self-induced fluttering motion on the expected benefits of reconfiguration in terms of drag reduction, while Chapter 5 analyses the impact of the reconfiguration on the severity of the vortex-induced vibrations of circular cylinders. Finally, Chapter 6 summarizes the findings of this thesis and offers some perspectives for future work.

Chapter 2

Static reconfiguration of spatially variable flow-structure systems

Preamble

The mechanisms and scalings of drag reduction by static reconfiguration are well-known in the idealized case of a uniform flow-structure system. Actual plants or man-made structures and the flow they are plunged in are on the other hand very likely to show some spatial variability. In this first chapter, we address the question of the influence of such non-uniformities on the scaling of the drag with the flow velocity, through a dimensional analysis and numerical simulations based on a reduced order modelling of the problem.

In order to simplify the analysis and provide general conclusions, we restrict our study to the simple model geometry of a cantilever slender beam, clamped perpendicular to a unidirectional and steady flow. Our model accounts for most possible non-uniformities in the flow or structural properties, but it neglects the additional effects of viscosity, unsteadiness in the wake or in the background flow, or other external forces such as gravity. This configuration is the most commonly used in theoretical studies on drag reduction by reconfiguration (see for instance Alben et al., 2004; Gosselin et al., 2010; Luhar and Nepf, 2011, 2016), which provides us with reference points and validation cases. In accordance with what is classically done in the context of static reconfiguration, we characterize the drag reduction through the use of the Vogel exponent ν such that the total drag force scales with the flow velocity as $F \propto U^{2+\nu}$. In some aspects, the results presented in this chapter generalize the findings of Gosselin et al. (2010), de Langre et al. (2012) and Luhar and Nepf (2011).

After providing an analytical expression for the asymptotic Vogel exponent (for large deflections) of idealized systems with self-similar variations of their spatial properties, we discuss the practical applicability of this expression for realistic systems. We also analyse the weak sensitivity of the asymptotic Vogel exponent with respect to the spatial variability of the system in realistic ranges, which provides an explanation to the rather reduced scattering of the Vogel exponents measured on very diverse systems around the value -1 .

The results presented in this chapter have been published in the Journal of Fluids and Structures. The paper (Leclercq and de Langre, 2016) is attached at the end of the thesis. Compared to the present chapter, the paper includes an additional introduction and a comparison of the results for the asymptotic Vogel exponent in shear flow with preliminary results obtained in Henriquez and Barrero-Gil (2014). Apart from a few notations, the rest of the content is similar.

Contents

2.1	Model	21
2.2	Drag reduction in a self-similar framework	24
2.2.1	Asymptotic Vogel exponent	24
2.2.2	Bending length	26
2.3	Applications	27
2.3.1	Numerical method	27
2.3.2	A uniform beam in a shear flow	28
2.3.3	A uniform beam in a Blasius boundary layer	29
2.3.4	A non-uniform beam in a uniform flow	34
2.4	Discussion	38
2.4.1	Implications for the Vogel exponents of realistic systems	38
2.4.2	On the robustness of the results	39
2.4.3	On the limits of the model	41
2.5	Conclusions	42

2.1 Model

The model used in this chapter is represented in Fig. 2.1, and a nomenclature of the main variables used throughout this chapter is given in Appendix A. The elastic body is a cantilever beam of length L bending in the xz -plane. The width W , thickness D and material stiffness may all vary with the curvilinear coordinate s . The height $z(s)$ and curvature $\kappa(s)$ are related to the local angle of the beam with the vertical axis $\theta(s)$ by the kinematic relationships

$$z = \int_0^s \cos \theta(s') ds' \quad , \quad \kappa = \frac{\partial \theta}{\partial s}. \quad (2.1)$$

We assume a rather general form of the constitutive law relating the internal bending moment M to the curvature κ

$$M(s, \kappa) = b(s)g(\kappa), \quad (2.2)$$

where $b(s)$ is a local coefficient that accounts for the local stiffness and geometry, while $g(\kappa)$ is characteristic of the material constitutive law, which we take to be uniform on the beam. For instance, in the case of linear elasticity, $g(\kappa) = \kappa$ and $b(s) = EI(s)$ is the local bending stiffness of the beam. Under the assumption that the local radius of curvature $1/\kappa$ remains large compared to the thickness D ($\kappa D \ll 1$), Kirchoff's equations for rods (see for instance Audoly and Pomeau, 2010) relates the internal shear force Q to the internal bending moment M by

$$Q = -\frac{\partial M}{\partial s}. \quad (2.3)$$

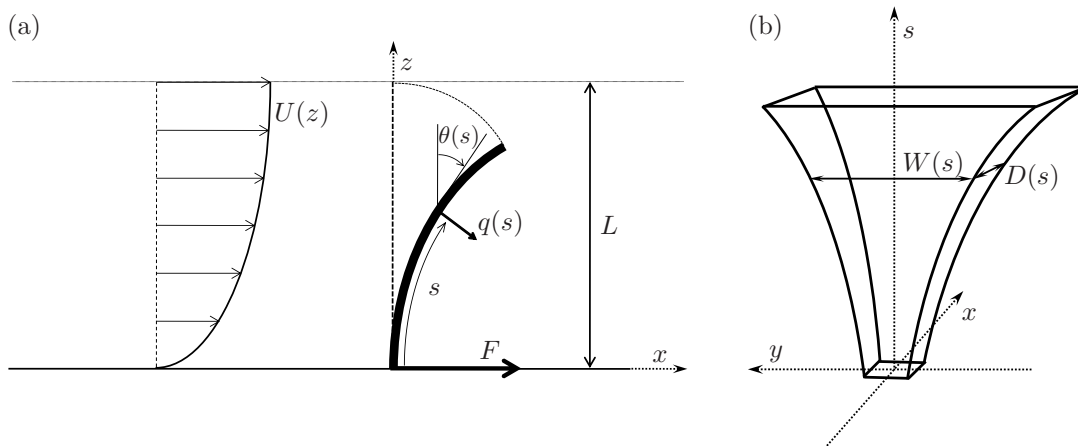


Figure 2.1: Description of the system. (a) Side view of the beam bending in the flow. (b) Front view of the unbent structure.

We further assume that the structure is subject to a horizontal flow $U(z)$ of a fluid of density $\rho(z)$. Both U and ρ may vary with the vertical coordinate z , Fig. 2.1(a) only

displaying a velocity profile $U(z)$ for clarity. We restrict our study to large Reynolds numbers, so that viscosity effects are neglected. The local fluid force q is then purely normal. In the case of uniform flow, it is usually considered that the normal fluid force include one term due to the so-called “reactive force” ($\sim \rho U^2 W^2 \kappa$ in the steady limit of the model of Lighthill (1971) (see also Candelier et al., 2011)) and one other term due to flow separation (“resistive force” $\sim \rho U^2 W$ in the model of Taylor (1952)). Thus, the resistive force is dominant in the slender body assumption $\kappa W \ll 1$. We assume that this is still the case for our vertically varying flow, and so we take q as purely resistive and independent of the body curvature. We assume a somewhat general form

$$q(s, z, \theta) = p(z)w(s)c(\theta), \quad (2.4)$$

where $p(z)$ accounts for the local dynamic pressure due to the undisturbed background flow at height z on the beam, $w(s)$ is a shape coefficient that accounts for the interactions of the normal flow with the local cross-section, and $c(\theta)$ is a projection term due to the local angle of the cross-section with respect to the background flow. It is not always obvious that the s - and θ -dependency can be decoupled, as the structure of the boundary layer and of the recirculating flow downstream will be modified by the angle of incidence. However, it is usually considered that to the first order, the resistive normal force only depends on the interaction between the cross-section and the flow in a plane normal to it, hence the expression chosen. The most classical example of such model is the resistive pressure drag derived by Taylor (1952): $q = 1/2\rho C_D W U_n^2$ where ρ is the fluid density, W the local width of the structure, $U_n = U \cos \theta$ the normal projection of the local flow velocity, and C_D a drag coefficient that accounts for the shape of the local cross-section. Specifically, Taylor’s model is equivalent to considering

$$p(z) = \frac{1}{2}\rho(z)U^2(z) \quad , \quad w(s) = C_D(s)W(s) \quad , \quad c(\theta) = \cos^2 \theta \quad . \quad (2.5)$$

Note that the model chosen here only gives an approximation of the exact loading. In particular, the modifications of the flow caused by the structure itself are neglected. However, the close similarity of the results obtained, on the one hand by Gosselin et al. (2010) with the present model, and on the other hand by Alben et al. (2002, 2004) who computed the pressure force distribution on the actual structure using a much more complex algorithm, indicates that the exact form of the force has little impact on the asymptotic scaling of the drag. Unless otherwise stated, $c(\theta) = \cos^2 \theta$ is used everywhere in the remaining of this chapter. The framework of the present chapter includes the study of the influence of the still unspecified form of $p(z) \propto U^2(z)$, $w(s)$, $b(s)$ and $g(\kappa)$. Note that the dynamic pressure due to the background flow at a given point in space does not depend on the position of the structure, so $p(z)$ only depends on the cartesian coordinate z (assuming the flow is invariant in the x -direction). On the other hand, the elasticity factor $b(s)$ and the cross-section shape coefficient $w(s)$ are structural properties that are specific to a given location along the beam span s , even though the cartesian coordinates (x, z) of that physical point change as the beam bends. The internal bending moment $M(s)$ depends on the curvilinear coordinate s

explicitly via the local stiffness factor $b(s)$, but also implicitly via the the local value of the curvature $\kappa(s)$ in the material constitutive law $g(\kappa)$.

Following Luhar and Nepf (2011), the local equilibrium at a given point s^* between the local internal shear force and the normal fluid loads yields the governing equation

$$\left. \frac{\partial M}{\partial s} \right|_{s^*} = - \int_{s^*}^L q(s) \cos(\theta(s) - \theta(s^*)) ds \quad (2.6)$$

where the force-free boundary condition $Q = 0$ at the free end $s = L$ has been used. Non-dimensionalizing this equation yields one governing parameter called the Cauchy number

$$C_Y = \frac{q_0 L}{M_0/L} \sim \frac{\text{typical external fluid load}}{\text{typical elastic restoring force}}, \quad (2.7)$$

considering that q_0 and M_0 are the orders of magnitude of the fluid load q and internal moment M in equation (2.6). Besides, the total drag of the beam reads

$$F = \int_0^L q(s) \cos(\theta(s)) ds. \quad (2.8)$$

The focus of this chapter is the scaling of the drag force, F , with the velocity of the flow. In the case of a flow that may not be uniform, we have to choose a reference velocity U_0 that scales the velocity at any point in the flow field. We are then interested in the variations of the Vogel exponent ν such that F scales as $U_0^{2+\nu}$. At large Reynolds number and in the limit of a rigid structure, the drag force is expected to grow as U_0^2 . Following Gosselin et al. (2010), to isolate the contribution of flexibility to the velocity-drag law, we define the reconfiguration number

$$\mathcal{R} = \frac{F}{F_{rigid}}, \quad (2.9)$$

so that $\mathcal{R} \propto U_0^\nu$. The actual governing parameter being the Cauchy number, we will prefer to work in the $C_Y - \mathcal{R}$ space rather than the $U_0 - F$ space. The Cauchy number being proportional to the typical fluid load $q_0 \propto U_0^2$, the local Vogel exponent can be computed directly in the $C_Y - \mathcal{R}$ space as

$$\nu = 2 \frac{\partial \log \mathcal{R}}{\partial \log C_Y}. \quad (2.10)$$

In the remaining of this chapter, unless otherwise stated, the Cauchy number is always defined based on the flow and structural properties at the tip of the upright beam.

2.2 Drag reduction in a self-similar framework

2.2.1 Asymptotic Vogel exponent

First, we further assume that the pressure, cross-section shape and stiffness parameters $p(z)$, $w(s)$ and $b(s)$ can be expressed as power functions of their respective arguments, namely

$$p(z) = p_0 \left(\frac{z}{L}\right)^\mu, \quad w(s) = w_0 \left(\frac{s}{L}\right)^\gamma, \quad b(s) = b_0 \left(\frac{s}{L}\right)^\beta. \quad (2.11)$$

Note that, although these power-law formulations of the structural parameters w and b may recall those of Lopez et al. (2011) for a slender cone, or those of Lopez et al. (2014) for a tree-like structure, they actually describe quite different distributions because the curvilinear coordinate s used in these studies was defined from the free tip towards the floor instead of the other way around here. We also assume that the material constitutive law may differ from linear elasticity by considering a more general dependency on curvature, still in the form of a power law

$$g(\kappa) = \kappa^\alpha. \quad (2.12)$$

Substituting (2.11), (2.12) and the particular form $c(\theta) = \cos^2 \theta$ into (2.6), the equilibrium equation reads

$$\frac{\partial}{\partial s} (s^\beta \kappa^\alpha) \Big|_{s^*} = -C_Y \int_{s^*}^1 \left(\int_0^s \cos \theta(s') ds' \right)^\mu s^\gamma \cos^2(\theta) \cos(\theta - \theta^*) ds, \quad (2.13)$$

where all the space variables have been made non-dimensional using the beam length L , and the Cauchy number C_Y has been defined as

$$C_Y = \frac{p_0 w_0 L}{b_0 L^{-1-\alpha}}. \quad (2.14)$$

From (2.8), the total drag force on the beam in this framework reads

$$F = p_0 w_0 L \int_0^1 \left(\int_0^s \cos \theta(s') ds' \right)^\mu s^\gamma \cos^3(\theta) ds. \quad (2.15)$$

We further assume that the drag is bounded by that on a rigid structure, namely

$$F_{rigid} = p_0 w_0 L \int_0^1 s^{\mu+\gamma} ds = \frac{p_0 w_0 L}{1 + \mu + \gamma}. \quad (2.16)$$

For this quantity to be finite, it is required that $\mu + \gamma > -1$. Using (2.9), (2.15) and (2.16), the reconfiguration number now reads

$$\mathcal{R} = \left(1 + \mu + \gamma\right) \int_0^1 \left(\int_0^s \cos \theta(s') ds' \right)^\mu s^\gamma \cos^3(\theta) ds. \quad (2.17)$$

Within this framework, the asymptotic Vogel exponent for large Cauchy numbers, noted ν_∞ , can now be inferred from a dimensional analysis that accounts for the particular power-like form of the flow and structural parameters. The flow pressure p , the cross-section shape coefficient w and the bending stiffness b are characterized by their respective invariants

$$\begin{aligned} I_p &= \frac{p(z)}{z^\mu} = \frac{p_0}{L^\mu} \quad [\text{kg.m}^{-1-\mu}.\text{s}^{-2}], \\ I_w &= \frac{w(s)}{s^\gamma} = \frac{w_0}{L^\gamma} \quad [\text{m}^{1-\gamma}], \\ I_b &= \frac{b(s)}{s^\beta} = \frac{b_0}{L^\beta} \quad [\text{kg.m}^{2+\alpha-\beta}.\text{s}^{-2}]. \end{aligned} \quad (2.18)$$

The Vaschy-Buckingham theorem predicts three non-dimensional figures which we choose to be the non-dimensional drag force, the Cauchy number and the aspect ratio

$$\tilde{F} = \frac{F}{I_p I_w L^{1+\mu+\gamma}}, \quad C_Y = \frac{I_p I_w L^{1+\mu+\gamma}}{I_b L^{-1-\alpha+\beta}}, \quad \Lambda = \frac{L}{w_0}. \quad (2.19)$$

Following Gosselin et al. (2010), we disregard the effect of the aspect ratio Λ . This assumption is actually valid for elongated structures $\Lambda \gg 1$, as will be discussed in Chapter 3 and more specifically in Appendix D. The problem now reduces to finding the relationship between \tilde{F} and C_Y , or equivalently to determining the function \mathcal{G} such that

$$F = I_p I_w L^{1+\mu+\gamma} \mathcal{G} \left(\frac{I_p I_w}{I_b} L^{2+\mu+\gamma+\alpha-\beta} \right). \quad (2.20)$$

For highly bent structures, Gosselin et al. (2010) demonstrated that the drag no longer depends on the beam length L . Hence, function \mathcal{G} must be taken as a power function $\mathcal{G}(C_Y) \propto C_Y^\varphi$ that cancels the overall exponent of L in (2.20), meaning

$$\left(1 + \mu + \gamma \right) + \varphi \left(2 + \mu + \gamma + \alpha - \beta \right) = 0. \quad (2.21)$$

Consequently, the asymptotic drag force scales as

$$F \propto \frac{(I_p I_w)^{1+\varphi}}{I_b^\varphi} \quad \text{with} \quad \varphi = -\frac{1 + \mu + \gamma}{2 + \mu + \gamma + \alpha - \beta}. \quad (2.22)$$

We are interested in the scaling of the drag force with the velocity U_0 , which only appears in the flow pressure invariant through $I_p \propto p_0 \propto U_0^2$. Therefore, F scales as $U_0^{2+2\varphi}$ and the asymptotic Vogel exponent naturally appears as $\nu_\infty = 2\varphi$. Ultimately,

$$\nu_\infty = -2 \frac{1 + \mu + \gamma}{2 + \mu + \gamma + \alpha - \beta}. \quad (2.23)$$

For a uniform, linearly elastic, rectangular plate bending in a uniform flow, $(\alpha, \beta, \gamma, \mu) = (1, 0, 0, 0)$, so that $\nu_\infty = -2/3$, which is consistent with Alben et al. (2002, 2004) and Gosselin et al. (2010). In the case of a non-linear stress-strain relationship $\sigma \propto \varepsilon^{1/N}$ considered in de Langre et al. (2012), we get $\alpha = 1/N$ in our model, and so we recover the asymptotic result $\nu_\infty = -(2N)/(2N + 1)$.

2.2.2 Bending length

If it is well-known that the effects of flexibility are negligible below $C_Y \sim 1$, no study has ever predicted the threshold above which the Vogel exponent should finally reach its asymptotic value. This threshold can however be estimated by looking at the global balance of forces on the beam. Assuming that the beam length L loses its relevance when the beam is highly bent implies that there must exist a smaller region of length ℓ , function of the level of loading only, on which all the significant interactions between the beam and the flow concentrate. This inner region is thus responsible for the dominant contribution to the drag, and show large curvature responsible for the balancing force. Assuming that the contribution of the region $s > \ell$ to the drag is negligible, (2.15) gives the dominant contribution to the drag as

$$F \sim p_0 w_0 L \ell^{1+\mu+\gamma}. \quad (2.24)$$

On the other hand, using (2.3), (2.2), (2.11) and (2.12), the internal shear force at the base can be roughly estimated as

$$Q(0) \sim b_0 \ell^\beta (L\ell)^{-1-\alpha} = b_0 L^{-1-\alpha} \ell^{-1-\alpha+\beta}. \quad (2.25)$$

Balancing these two quantities yields

$$\ell^{-(2+\mu+\gamma+\alpha-\beta)} \sim \frac{p_0 w_0 L}{b_0 L^{-1-\alpha}}, \quad (2.26)$$

which is the Cauchy number defined in equation (2.14). We now choose the specific value of ℓ as follows

$$\ell = C_Y^{-\frac{1}{2+\mu+\gamma+\alpha-\beta}}. \quad (2.27)$$

This analysis highlights the emergence of an intrinsic characteristic length ℓ that characterizes the region of the beam on which the interactions governing its behaviour concentrate. If ℓ is larger than 1 (or equivalently $C_Y < 1$), the flow interacts with the beam on its whole length and the structural behaviour is close to that of a rigid beam. On the other hand, if $\ell \ll 1$, then the interactions in the region of length ℓ dominate the behaviour of the beam, and so the asymptotic regime is reached. This regime, where the Vogel exponent given by (2.10) has become constant, should thus be expected to be obtained above a threshold that is expressed in terms of some critical

value of ℓ instead of C_Y . Depending on the exponent of the power law relating ℓ to C_Y , the gap between the onset of significant bending ($C_Y = 1$) and the convergence of the asymptotic regime ($\ell \ll 1$) might cover a wider or smaller range of loadings. This analysis is consistent with the dimensional analysis above. Indeed, injecting (2.27) into (2.24) and using the fact that the pressure of reference p_0 and the Cauchy number C_Y both scale as U_0^2 easily yields

$$F \sim U_0^{2-2\frac{1+\mu+\gamma}{2+\mu+\gamma+\alpha-\beta}}, \quad (2.28)$$

and so the asymptotic Vogel exponent given by equation (2.23) is obviously recovered.

Note that the choice of expression (2.27) to define ℓ is somewhat arbitrary, as no actual ‘‘bending length’’ can be uniquely defined on the physical system. (2.27) essentially represents a scaling of the Cauchy number that transforms a ratio of forces into the ratio of some characteristic bending length over the length of the beam. As such, it gives a different interpretation of the Cauchy number, but it does not correspond to a physical quantity that can be easily measured or obtained as the output of a numerical simulation.

2.3 Applications

2.3.1 Numerical method

To check the validity of our equation (2.23) for the asymptotic Vogel exponent as well as the predicted threshold discussed above, we numerically compute the Vogel exponent in different cases by solving (2.13). To solve the integrodifferential equation, we use a first order centred finite difference scheme with the discrete boundary conditions $\theta_1 = 0$, $\theta_{N+1} - \theta_N = 0$ (Thomas, 1995). The integrals are computed by the trapezoidal rule. The resulting non-linear system of equations is solved using a pseudo-Newton solver (so-called method of Broyden, see Broyden 1965). The beam is discretized with $N = 30$ panels. For $C_Y \leq 1$, the beam bends very little, so we use a uniform mesh. When the beam reconfigures significantly, we have seen that its curvature tends to concentrate in a small region of characteristic non-dimensional length ℓ near the clamped edge. In order to model the curved region with accuracy when $C_Y \geq 1$, we use a non-uniform mesh $s_k = (k/(N+1))^\chi$ with $\chi = \log \ell / \log 2$ so that $s_{((N+1)/2)} = \ell$, meaning that half of the points are in the curved region $s \leq \ell$. This mesh scales with the characteristic bending length in the curved region, and so it is not necessary to increase the number of points to maintain a good accuracy when the beam is highly bent. Convergence was checked on a few cases by measuring the relative error on the asymptotic Vogel exponent. On all the cases tested, doubling the number of points changed the value of the asymptotic Vogel exponent by less than 0.1%.

2.3.2 A uniform beam in a shear flow

One first situation that is of particular interest is the case of reconfiguration in a sheared flow. This situation is observed for instance for aquatic organisms in underwater boundary layers or within canopies. We consider a plate of constant width W and cross-section drag coefficient C_D , made of a linearly elastic material of uniform bending stiffness EI , deforming in a flow of uniform density ρ with a sheared velocity profile

$$U = U_0 \left(\frac{z}{L} \right)^{\mu/2}. \quad (2.29)$$

Assuming Taylor's model for the local fluid load, the parameters of the model specifically read

$$p(z) = \frac{1}{2} \rho U_0^2 \left(\frac{z}{L} \right)^\mu, \quad w(s) = C_D W, \quad c(\theta) = \cos^2 \theta, \quad b(s) = EI, \quad g(\kappa) = \kappa, \quad (2.30)$$

which corresponds to a constitutive law, stiffness and cross-section shape exponents respectively $(\alpha, \beta, \gamma) = (1, 0, 0)$ with the shear exponent μ being the only varying parameter. Hence, from (2.23), the theoretical asymptotic Vogel exponent is predicted as

$$\nu_\infty = -2 \frac{1 + \mu}{3 + \mu}. \quad (2.31)$$

In the case of a uniform flow $\mu = 0$, we recover the classical $\nu_\infty = -2/3$ of Gosselin et al. (2010). From (2.27), the characteristic bending length reads here

$$\ell = C_Y^{-\frac{1}{3+\mu}} \quad (2.32)$$

To numerically confirm these predictions, we solve the non-dimensional governing equation (2.13) that reads in this specific case,

$$\left. \frac{\partial^2 \theta}{\partial s^2} \right|_{s^*} = -C_Y \int_{s^*}^1 \left(\int_0^s \cos \theta(s') ds' \right)^\mu \cos^2 \theta(s) \cos(\theta(s) - \theta(s^*)) ds, \quad (2.33)$$

with the Cauchy number

$$C_Y = \frac{\rho U_0^2 C_D W L^3}{2EI}. \quad (2.34)$$

Fig. 2.2 shows the results of the computational approach. On Fig. 2.2(a), the deflection of the beam for increasing loads is shown in the case of a linear flow $\mu/2 = 1$. As expected, significant bending is observed when $C_Y > 1$. The evolution of the reconfiguration number and of the Vogel exponent on Figs 2.2b and 2.2c stresses the existence of two asymptotic regimes. At low Cauchy numbers, the structure behaves as a rigid beam

so the Vogel exponent is null no matter the flow profile. At very large Cauchy numbers however, the Vogel exponent converges towards a constant that depends on the shear exponent μ . We re-plot on Fig. 2.3 the evolution of the Vogel exponent as a function of the characteristic bending length ℓ given by (2.32) instead of the Cauchy number C_Y . In the three cases displayed, the Vogel exponent was within 2% of the asymptotic value for $\ell < 0.2$. This confirms that the threshold for the asymptotic regime is well expressed, for any value of the parameter μ , in terms of the same critical value of ℓ .

2.3.3 A uniform beam in a Blasius boundary layer

The particular power-like form of the pressure, cross-section shape and stiffness distributions $p(z)$, $w(s)$, $b(s)$, as well as the constitutive law $g(\kappa)$, is a necessary assumption for the theoretical derivation of the asymptotic expression (2.23) that may appear like a strong limitation of the model above. It seems however that the actual scope of applicability of (2.23) encompasses a much wider range of practical situations. For highly bent structure, the curvature tends to concentrate in a small “inner” region $s < \ell$ near the clamped edge. As explained in Alben et al. (2002, 2004), the “outer” portion of the system located above ℓ “sits” in the wake created by the deflection of the incident flow heading to the inner region upstream, and so it only endures very little fluid loading. Consequently, the outer domain only has negligible influence on the overall shape and drag of the structure, and only the spatial dependency of the flow and structural parameters inside the inner domain is actually relevant to the modelling of the system. The whole theory above should thus remain valid as long as power function approximations can accurately model these parameters at the scale of ℓ only, and not necessarily at the scale of the whole beam length.

To better understand the implications above, we consider the reconfiguration of a non-tapered, elastic, homogeneous beam, in a Blasius boundary layer. In this case, all the structural parameters are spatially invariant, but the flow exhibits a more intricate shear profile than a simple power-law fit in z . For the sake of clarity, all the space variables have been normalized by the length of the beam, or equivalently $L = 1$. In the model of Blasius, the vertical velocity is negligible and the horizontal velocity is expressed as

$$U(x, z) = U_\infty f'(\eta). \quad (2.35)$$

with the similarity variable $\eta = z\sqrt{R_e^L/x}$, the Reynolds number based on the length of the beam and outer flow velocity R_e^L , and f the solution of the Blasius boundary layer equations

$$2f''' + ff'' = 0 \quad , \quad f(0) = f'(0) = 0 \quad , \quad f(\eta) \xrightarrow{\eta \rightarrow \infty} 1. \quad (2.36)$$

The resulting flow profile, shown on Fig. 2.4(a) for a fixed value of x , is characterized by a smooth transition from a linear increase with slope $U_\infty/L_B(x)$ near the wall saturating

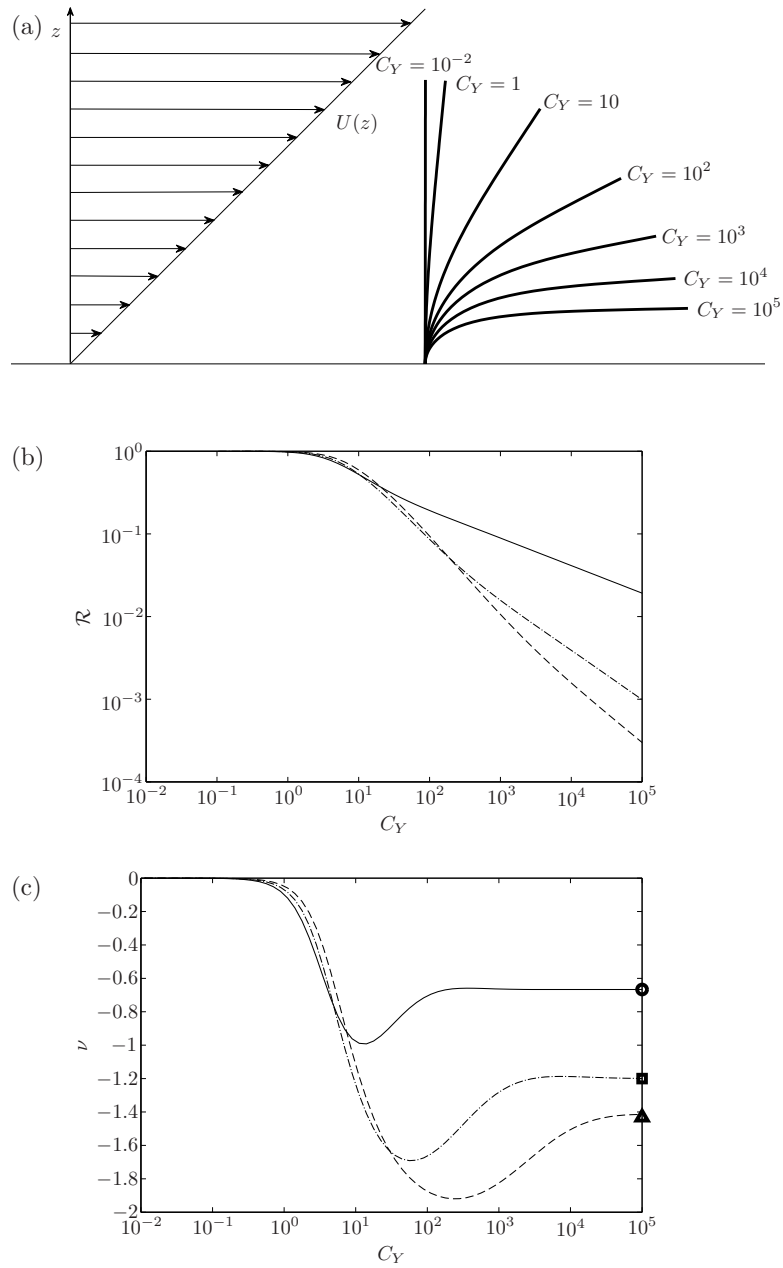


Figure 2.2: A uniform beam in a shear flow. (a) Deformation of the beam in a linear flow profile $\mu/2 = 1$. (b) and (c) Reconfiguration number \mathcal{R} and Vogel exponent ν as functions of the Cauchy number C_Y : uniform flow profile $\mu/2 = 0$ (—), linear flow profile $\mu/2 = 1$ (-·-), quadratic flow profile $\mu/2 = 2$ (- - -). Asymptotic Vogel exponent predicted by equation (2.23), uniform flow profile $\mu/2 = 0$ (\circ), linear flow profile $\mu/2 = 1$ (\square), quadratic flow profile $\mu/2 = 2$ (\triangle).

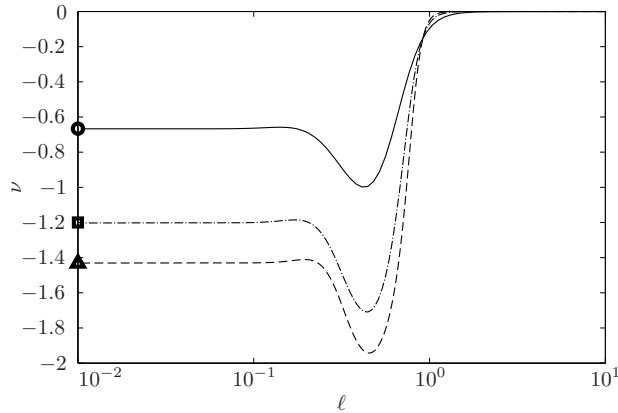


Figure 2.3: A uniform beam in a shear flow. Variation of the Vogel exponent in the $\ell - \nu$ space, uniform flow profile $\mu/2 = 0$ (—), linear flow profile $\mu/2 = 1$ (- · -), quadratic flow profile $\mu/2 = 2$ (- - -). Asymptotic Vogel exponent predicted by equation (2.23), uniform flow profile $\mu/2 = 0$ (○), linear flow profile $\mu/2 = 1$ (□), quadratic flow profile $\mu/2 = 2$ (△).

to a uniform magnitude U_∞ far from it. The two domains are roughly delimited, at each location x , by the dimensionless characteristic length scale

$$L_B(x) = \frac{1}{f''(0)} \sqrt{\frac{x}{Re^L}}, \quad (2.37)$$

such that,

$$U(x, z) \sim U_\infty \text{ for } z \gg L_B(x) \text{ and } U(x, z) \sim \frac{U_\infty}{L_B(x)} z \text{ for } z \ll L_B(x). \quad (2.38)$$

The approach presented in this chapter is based on the assumption that the flow is invariant in the x -direction, and so the x -dependency of the Blasius flow inside the boundary layer would a priori prevent (2.23) to be valid. However, the region of space swept by the deforming beam extends at most one beam length downstream of its anchorage point x_0 (see Fig. 2.4(b)). If the structure is placed far enough from the origin of the boundary layer ($x_0 \gg 1$), then $L_B(x) \sim L_B(x_0)$ anywhere in the vicinity of the beam, and so the flow can be considered locally horizontally invariant. The coexistence of the two flow regimes along the vertical axis makes room for two different characteristic velocities according to (2.38): $U_0 = U_\infty$ in the uniform domain, and $U_0 = U_\infty/L_B$ in the linear domain. Two Cauchy numbers can subsequently be defined according to (2.14): $C_{Y,uni}$ is based on the uniform outer flow velocity $U_0 = U_\infty$, while $C_{Y,lin} = C_{Y,uni}/L_B^2$ is based on the inner characteristic velocity $U_0 = U_\infty/L_B$. Fig. 2.5(a) displays the evolution of the Vogel exponent as the loading increases, for several fixed values of $L_B \leq 1$. The parameter chosen to describe the fluid loading is the Cauchy number based on the uniform outer flow, $C_{Y,uni}$.

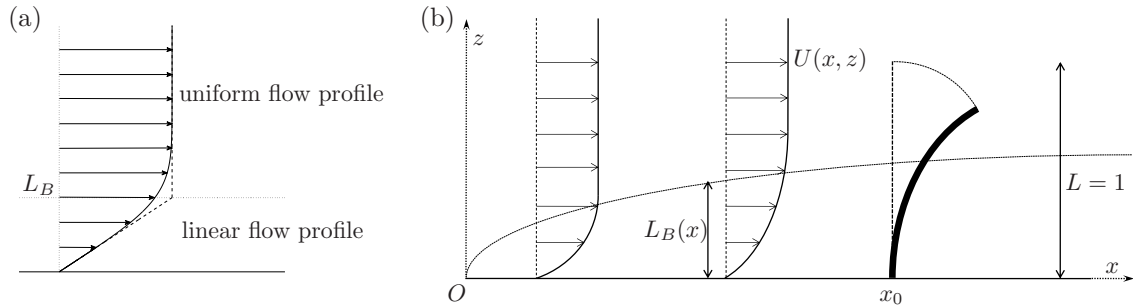


Figure 2.4: Description of the reconfiguration in a Blasius boundary layer. (a) Blasius profile $U(x, z)$ at a fixed x . (b) Beam deforming in a Blasius boundary layer.

Evidently, if $L_B \geq 1$, then the beam lies entirely in a linearly sheared flow even when it stands upright. This situation is strictly equivalent to the shear flow case studied in Section 2.3.2 with pressure shear exponent $\mu = 2$, if the Cauchy number C_Y is identified with the linear flow Cauchy number $C_{Y,lin}$. For $L_B = 1$, $C_{Y,lin} = C_{Y,uni}$ and the evolution of the Vogel exponent shown on Fig. 2.5(a), is very similar to the curve obtained for a linear velocity profile in Fig. 2.2(c).

On the other hand, structures reconfiguring in boundary layers smaller than their lengths ($L_B < 1$) experience much more intricate behaviours. Fig. 2.5(b) shows a zoom on the near-wall region of a beam reconfiguring in a Blasius boundary layer a hundred times smaller than its size ($L_B = 10^{-2}$). This plot should be analysed jointly with the corresponding curve in 2.5a. When the Cauchy number is small, the linear flow region is much smaller than the portion of the beam that experiences significant bending. The inner domain $s < \ell$ is mostly subjected to the uniform flow $U = U_\infty$, and the influence of the linear flow on the very bottom of the beam is negligible. Consequently, the evolution of the Vogel exponent for $C_{Y,uni} < 10^2$ is very similar to that obtained for a uniform flow on Fig. 2.2(c). As the loading increases, the beam bends more and more and as a result the linear flow covers an increasing portion of the inner region. It follows that the Vogel exponent decreases for $C_{Y,uni} > 10^2$. Asymptotically, when the bending region is fully confined inside the boundary layer, the Vogel exponent catches up with the asymptotic value characteristic of linear shear, $\nu_\infty = -6/5$. The same analysis remains valid for other boundary layers smaller than the beam $L_B < 1$. If the loading increases enough, the beam will always eventually dive entirely inside the boundary layer and the Vogel exponent will asymptotically reach the theoretical value predicted for a linear flow profile. But the threshold above which this asymptotic regime is reached depends on the thickness of the boundary layer L_B . The larger L_B , the sooner the shear flow will dominate. Precisely, the relative impacts of the uniform and linear flow regions can be estimated by comparing the thickness of the boundary layer L_B to the size of the bending region ℓ . However, the expression of ℓ depends on which of the uniform or linear flow dominates. In the uniform outer flow, (2.27) yields $\ell_{uni} = C_{Y,uni}^{-1/3}$, while in the linear region it would predict $\ell_{lin} = C_{Y,lin}^{-1/5} = L_B^{2/5} C_{Y,uni}^{-1/5} = L_B^{2/5} \ell_{uni}^{3/5}$. At the threshold

between the two regimes, $\ell_{uni} = \ell_{lin} = L_B$, which also yields $C_{Y,uni} = L_B^{-3}$. Note that this threshold specifically sets the lower bound (in terms of the Cauchy number) to the purely linear flow approximation, but the purely uniform flow approximation loses its validity for much smaller loads. Indeed, for ℓ smaller but close to L_B , the region of the beam that concentrates the interaction with the flow is already confined inside the boundary layer so that the influence of the uniform domain above totally vanishes. Conversely, for $\ell > L_B$, the influence of the linear domain never strictly vanishes, and its influence becomes negligible only for $\ell \gg L_B$. This result is consistent with the thresholds for convergence towards the linear regime observed for the different cases on Fig. 2.5(a). For L_B equal to 10^{-1} , 10^{-2} and 10^{-3} , the Vogel exponent was within 2.5% of its expected asymptotic value $\nu_\infty = -6/5$ for $C_{Y,uni}$ respectively superior to $10^{2.9}$, $10^{5.85}$ and $10^{8.8}$. If the thickness of the boundary layer L_B is small enough, the influence of the linear region may remain negligible for loadings large enough to permit convergence of the Vogel exponent in the uniform domain, before it reaches the linear domain. This is observed for instance on Fig. 2.5(a), where the Vogel exponent for $L_B = 10^{-3}$ displays a plateau around the asymptotic uniform flow Vogel exponent $\nu = -2/3$ for $C_{Y,uni} \sim 10^2 - 10^5$, before switching to the asymptotic linear flow Vogel exponent $\nu_\infty = -6/5$ above $C_{Y,uni} \sim L_B^{-3} = 10^9$. On the other hand, for thicker boundary layers ($L_B \geq 10^{-2}$), the influence of the linear domain may not be neglected for loadings large enough to reach convergence in the uniform domain. For $L_B = 10^{-1}$, convergence to the asymptotic regime is approximately concomitant with the switch from uniform to linear flow regime. The small hump around $C_{Y,uni} = 10^2$ illustrates the successive dominance of the uniform flow that tends to bring the Vogel exponent closer to $\nu = -2/3$ as the asymptotic regime approaches, soon overcome by the linear flow whose influence is to decrease it to $\nu = -6/5$. When $L_B = 1$, the linear flow region dominates as soon as reconfiguration occurs, so the early effects of the uniform domain are not even noticeable on Fig. 2.5(a).

This example shows that our approach based on self-similarity actually provides understanding of the behaviour of much more complex configurations. Strictly speaking, there will always be an asymptotic regime, should it be reached for extremely large Cauchy numbers. Indeed, as the structure bends, curvature always concentrate in a region of characteristic length ℓ that gets smaller and smaller, so that it eventually gets small enough for all the parameters to be well-approximated by power laws at its scale. Thus, the actual asymptotic Vogel exponent is given by (2.23) using the exponents of the first order in the power law expansions of the structural and flow parameters at the foot of the beam. Yet, the threshold above which these power law approximations all hold may be too large to be ever reached in practice. In this case, intermediate asymptotic regimes may arise on whole ranges of Cauchy numbers. We may conclude that convergence of the Vogel exponent towards a constant independant of the loading may occur if the bending length ℓ is either much larger or much smaller than any of the other characteristic length scales involved.

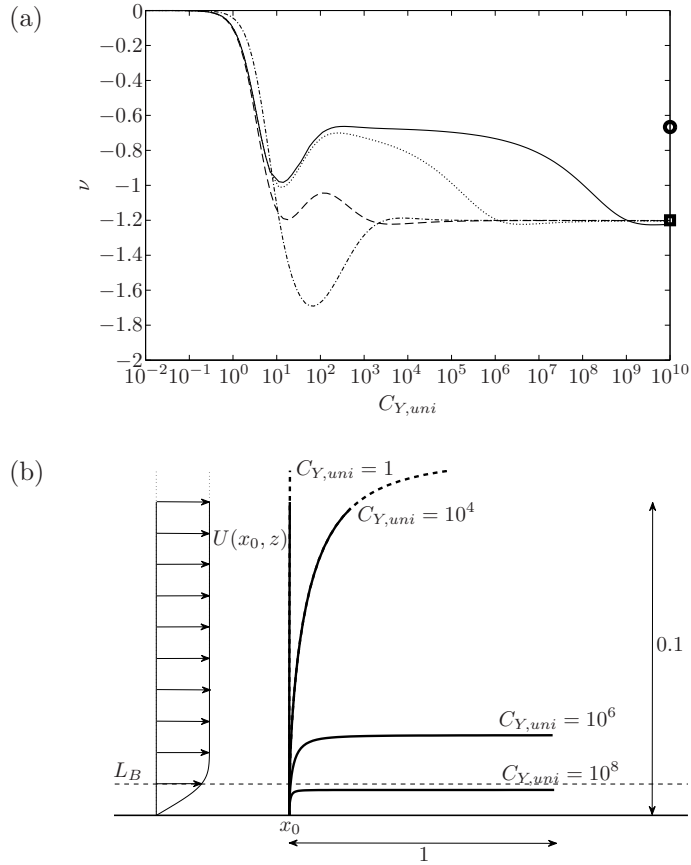


Figure 2.5: Reconfiguration in a Blasius boundary layer, anchorage point $x_0 = 10^7$. (a) Vogel exponent ν as a function of the Cauchy number $C_{Y,uni}$, $L_B = 10^{-3}$ (—), $L_B = 10^{-2}$ (⋯), $L_B = 10^{-1}$ (---), $L_B = 1$ (-·-). Asymptotic Vogel exponent predicted by equation (2.23), uniform flow profile (o), linear flow profile (□). (b) Zoom near the clamped edge of a beam bending in a Blasius boundary layer, $L_B = 10^{-2}$.

2.3.4 A non-uniform beam in a uniform flow

To further check the validity of the asymptotic expression (2.23), we compared it to the numerically computed asymptotic Vogel exponent in some other cases involving variations of the material constitutive law, material stiffness or structural cross-section shape. To make sure that the asymptotic regime was reached in the numerical simulations, a large enough value of the Cauchy number ($C_Y = 10^5$) was chosen so that the characteristic bending length ℓ would be inferior to 0.1 in all cases. The results are shown on Table 2.1, along with the corresponding ℓ -value. Agreement is excellent in all the cases considered.

A more intricate example is that of a linearly tapered beam of increasing width W ,

System	α	β	γ	μ	theoretical ν_∞ (2.23)	numerical ν at $C_Y = 10^5$	ℓ -value (2.27) at $C_Y = 10^5$
benchmark case	1	0	0	0	-2/3	-0.6681	0.02
elastoplastic behaviour	0.5	0	0	0	-0.8	-0.8013	0.01
rigid base	1	-1	0	0	-0.5	-0.5006	0.06
linear width	1	0	1	0	-1	-1.0024	0.06

Table 2.1: Comparison of the theoretical and numerically computed Vogel exponents for varying systems

namely

$$W(s) = W_1 + (W_0 - W_1)s, \quad (2.39)$$

as shown on Fig. 2.6. In most cases, we would then expect the bending stiffness to also vary, but to highlight the effect of the cross-flow area alone, we assume here that the variations of the cross-sectional shape and elastic modulus are chosen such that the bending stiffness remains uniform. Consistently with (2.14), we define the Cauchy number as in equation (2.34) using the width at the tip W_0 as characteristic width. Note that the case $W_0 - W_1 = 0$ corresponds to the constant width problem $\gamma = 0$, while the case $W_1 = 0$ corresponds to the linear width problem $\gamma = 1$. We define the characteristic length δ as shown on Fig. 2.6, such that $W(-\delta) = 0$:

$$\delta = \frac{W_1}{W_0 - W_1}. \quad (2.40)$$

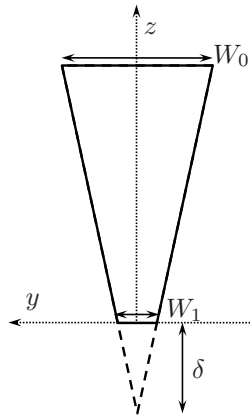


Figure 2.6: Tapered beam

This quantity can be seen as the length on which the width must vary to significantly deviate from W_1 due to the given slope. Notably, the relative gap between $W(s)$ and W_1 can be expressed as

$$\frac{W(s) - W_1}{W_1} = \frac{s}{\delta}. \quad (2.41)$$

In other words, the quantity δ is a measure of the length of validity of the uniform width approximation, as L_B was characteristic of the length of validity of the linear flow approximation in the Blasius boundary layer. Hence, the evolution of the computed Vogel exponents shown on Fig. 2.7 for several values of δ and for increasing Cauchy numbers may be explained in a similar fashion. The Vogel exponent converges at large Cauchy numbers towards the theoretical value $\nu_\infty = -2/3$, consistently with the first order W_1 in the power function expansion (2.39). For $\delta > 1$, the Vogel exponent deviates very little from that of a beam of uniform width ($\delta = \infty$). Conversely, for very small δ such as 10^{-3} , the structure behaves as a beam of linear width, long enough to exhibit an intermediate asymptotic regime $\nu = -1$ on a broad range of loadings. Structures with intermediate δ -values show an earlier shift from linear-like to uniform-like behaviour that do not allow intermediate convergence of the Vogel exponent. Finally, it should be noted that the characteristic bending lengths reads here $\ell = C_Y^{-1/4}$ in the linear width regime. Hence, the threshold between the two regimes, $\ell/\delta = 1$, reads in this case $C_Y \sim \delta^{-4}$. Contrary to the case of reconfiguration in a boundary layer, this threshold here must be thought of as a reference load around which both the uniform and linear terms of the width (2.39) influence the behaviour of the beam equally. It is not a critical load above or under which one of the two regimes loses all influence. This is so because, while the two flow domains of the boundary layer were spatially separated (above and below L_B), the two terms of $W(s)$ coexist everywhere, including at the clamped edge. If each term can be neglected, respectively far above or far below the threshold $C_Y = \delta^{-4}$, none of them can be ignored in the transition range around this value. This is consistent with the evolutions displayed on Fig. 2.7. At $C_Y = \delta^{-4}$, the Vogel exponent is equal to -0.79 for all three values $\delta = 10^{-1}$, 10^{-2} and 10^{-3} .

One may wonder what would happen if the width was decreasing from base to tip instead of increasing. In this case, $\delta < -1$ means that the effects of the slope are only noticeable near the tip, but never near the base where the finite value dominates in any case. In other words, the effects of taper may slightly affect the Vogel exponent for low Cauchy numbers, but the drag rapidly resembles that of a beam of constant width W_1 as soon as bending is significant. These expectations are confirmed by numerical simulations, not shown.

These results shed light on the apparent contradiction between the two asymptotic Vogel exponents for a disk cut along many radii derived respectively by numerical computations ($\nu_\infty = -2/3$) and by dimensional analysis ($\nu_\infty = -1$) in Gosselin et al. (2010). In the latter, it was assumed that because the inner radius R_i was 4 to 6 times smaller than the exterior radius the small width at the base $W_1 \propto R_i$ could be neglected. However, because the bending stiffness EI , proportional to the width W , cannot vanish at the base, it was assumed that the inner radius still influenced the drag through its finite contribution to the characteristic bending stiffness at the base. Consequently,

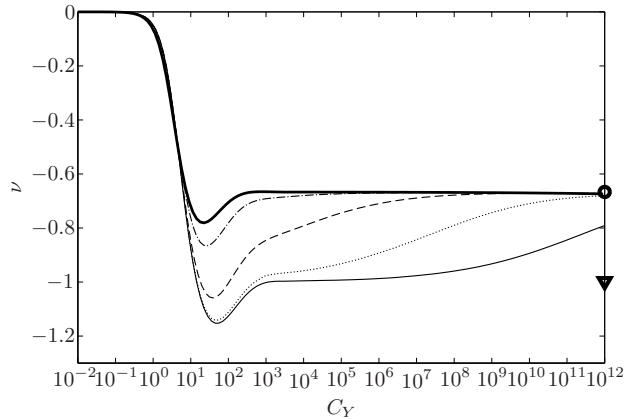


Figure 2.7: Vogel exponent ν of a tapered beam for increasing Cauchy numbers C_Y , $\delta = 10^{-3}$ (—), $\delta = 10^{-2}$ (\cdots), $\delta = 10^{-1}$ (---), $\delta = 1$ (-·-), $\delta = +\infty$ (thick —). Asymptotic Vogel exponent predicted by equation (2.23), constant width (\circ), linear width (∇).

their analysis corresponds to the case of a purely linear increase of the width from 0 at the base ($\gamma = 1$), on a beam with a non-vanishing bending stiffness ($\beta = 0$), hence the predicted Vogel exponent $\nu_\infty = -1$. However Fig. 2.7 clearly shows that for δ as small as 10^{-1} , we do not see a plateau at $\nu = -1$ before the effects of the actually non-vanishing width are observed. The two taper ratios considered in Gosselin et al. (2010), $\delta = 0.22$ and 0.32 are even larger, and so the assumption of negligible base width does not hold there. A Vogel exponent of $-2/3$ is in fact to be expected, and that was indeed the result of their numerical computations. Note that the experimental results in Gosselin et al. (2010) do not match either $\nu = -2/3$ nor $\nu = -1$, neither for the cut-disk nor for the single rectangular plate. The largest Cauchy number considered in the experiments barely exceeded 10^2 , so it is very likely that the asymptotic regime was simply not reached. However, the close values of the Vogel exponents computed in both cases ($\nu = -1.3$ for the cut-disk and $\nu = -1.4$ for the rectangular plate) may indicate that the cut-disk behaves similarly to the rectangular plate, consistently with our expectations.

It should also be noted that the influence of other types of tapering was also addressed by Lopez (2012), for slender cones and tree-like structures with rectangular cross-sections (see also Lopez et al. (2014)). It was found in both cases that taper had no influence on the scaling of drag, as numerical computations all yielded the same asymptotic Vogel exponent $\nu_\infty = -2/3$. As a matter of fact, as the vertical axis used in these studies was reversed with respect to ours, both the cross-flow width and the thickness of the beam would reach finite values at the clamped edge for any of the geometries considered. Consequently, according to the present study, the drag experienced by such structures in the limit of large loadings scales as that on a beam of uniform properties $(\alpha, \beta, \gamma, \mu) = (1, 0, 0, 0)$. According to equation (2.23), this indeed

yields $\nu_\infty = -2/3$.

2.4 Discussion

2.4.1 Implications for the Vogel exponents of realistic systems

Equation (2.23) gives the Vogel exponent for large Cauchy numbers in the general case as a function of the exponents α (constitutive law $g(\kappa)$), β (stiffness distribution $b(s)$), γ (cross-section shape distribution $w(s)$), μ (pressure distribution $p(z)$). Interestingly, (2.23) can also be written in a simpler form

$$\nu_\infty = -\frac{2}{1 + \psi/\phi} \quad (2.42)$$

that highlights the influence of only two parameters: on the one hand, a *geometrical* parameter $\phi = 1 + \mu + \gamma$ that accounts for the distribution of fluid loading on the structure, and on the other hand, a *material* parameter $\psi = 1 + \alpha - \beta$ that characterizes the restoring stresses.

In practice, the ranges accessible to the exponents α , β , γ and μ are bounded by limitations of multiple kinds. First, considering the rigid-body force a limiting value, the finiteness of the drag force mathematically requires that $\gamma + \mu > -1$ (see Section 2.2). But in fact, neither the structural cross-section nor the flow profile of actual systems can possibly diverge at $s = 0$, so γ and μ must actually be both positive or null in practice. Moreover, to ensure that the structural stress vanishes for zero curvature, the exponent α of the material constitutive law $g(\kappa)$ has to be strictly positive. Finally, the bending moment at the base cannot vanish when a loading exists. If the stiffness at the base $b(0)$ was null, the curvature there would need to be infinite and the resulting discontinuity in the angle θ across the boundary $s = 0$ would make the problem ill-posed. The minimum energy solution would obviously be the straight horizontal beam, which experiences neither drag nor internal stress. To eliminate this case, $b(0)$ must be different from 0, so the exponent β of the self-similar stiffness function $b(s)$ must be negative or null. Note that a system with zero-stiffness at the base would essentially revert to a pin joint free to rotate, with a Neumann boundary condition at $s = 0$. This would define a different system that falls out of the scope of this study, and that would experience zero drag no matter the magnitude of the fluid loading. Consequently, the lower physically admissible boundaries for the geometrical and material parameters of our system are $\psi > 1$ and $\phi \geq 1$.

Moreover, practical considerations further set upper boundaries to the typical values expected for these parameters. First, the vast majority of actual structures have finite width, and only quite exotic systems would exhibit cross-sections increasing more than linearly. It also seems unlikely that an actual flow would show more than linear shear, so we may reasonably expect the geometrical parameter ϕ to remain approximately below 3 in most cases. Besides, the constitutive law of most elastic materials should

not deviate much from linearity ($\alpha = 1$). Even the extreme case of perfect plasticity may be represented by taking $\alpha = 0$, as noted by de Langre et al. (2012), and a larger value $\alpha = 2$ would already be a very strong exponent. Besides, continuous structures generally show rather smooth variations of their stiffness, so that the magnitude of the exponent of the stiffness distribution, $|\beta|$, should really not deviate much at all from 0. Nonetheless, the use of the present model with $\beta \neq 0$ might constitute a valid approach to handle the overall behaviour of compound or branched structures such as trees. Indeed, the drag of such structure is the sum of the individual drag forces on each of its constitutive elements: trunk, branches, leaves. The relative contribution of each term is proportional to the projected area of each element. If we model the structure as an equivalent beam with local stiffness based on the weighted mean of the individual elements at a given height, we would expect the equivalent stiffness to decrease by several orders of magnitude from bottom (trunk) to top (leaves). At this point, the validity of this modelling is purely speculative and further investigations should be carried on to analyse its relevance. In any case, the variations corresponding to $\beta = -1$ seems already quite sharp, and we do not expect the material parameter ψ to exceed 3 by much in general.

Considering all these limitations, we may now estimate the expected range of variation of the Vogel exponent. The isovalues of the asymptotic Vogel exponent ν_∞ predicted by (2.42) are displayed on Fig. 2.8. They clearly indicate that, in these typical ranges of the geometrical and material parameters $\phi \in [1, 3]$ and $\psi \in [1, 3]$, ν_∞ may approximately vary between $-1/2$ and $-4/3$ at most. To illustrate the diversity of situations included in this rather narrow parameter space domain, a few practical configurations are marked with crosses on (2.42). Case A is the benchmark case of Alben et al. (2002, 2004) and Gosselin et al. (2010), where all is homogeneous and the constitutive law is linear: $(\alpha, \beta, \gamma, \mu) = (1, 0, 0, 0)$. Case B is the linear flow case shown on Fig. 2.2(a): $(\alpha, \beta, \gamma, \mu) = (1, 0, 0, 2)$. Case C would correspond to a uniform, perfectly plastic beam, in a uniform flow: $(\alpha, \beta, \gamma, \mu) = (0, 0, 0, 0)$. Finally, case D would characterize a system with either $(\alpha, \beta, \gamma, \mu) = (2, 0, 0, 0)$ (non-linear constitutive law $g(\kappa) = \kappa^2$) or $(\alpha, \beta, \gamma, \mu) = (1, -1, 0, 0)$ (global model of a tree with infinite stiffness at the base and flexible branches). Overall, we expect that in most situations of practical interest, the Vogel exponent at large Cauchy numbers will not deviate much from -1 . This is consistent with observations on plants, as discussed in the Introduction. Case E will be discussed in Section 2.4.3.

2.4.2 On the robustness of the results

The use of the equation (2.23) to predict the asymptotic Vogel exponent of a given system relies on the ability to fit a power-law on the spatial distributions of the structural and flow parameters, at least at the scale of the typical length on which significant bending is observed. This requirement may appear as a very limiting factor, because some parameters may exhibit complex variations, and because accurate assessment of the exponents might be challenging. However these two apparent issues might not be

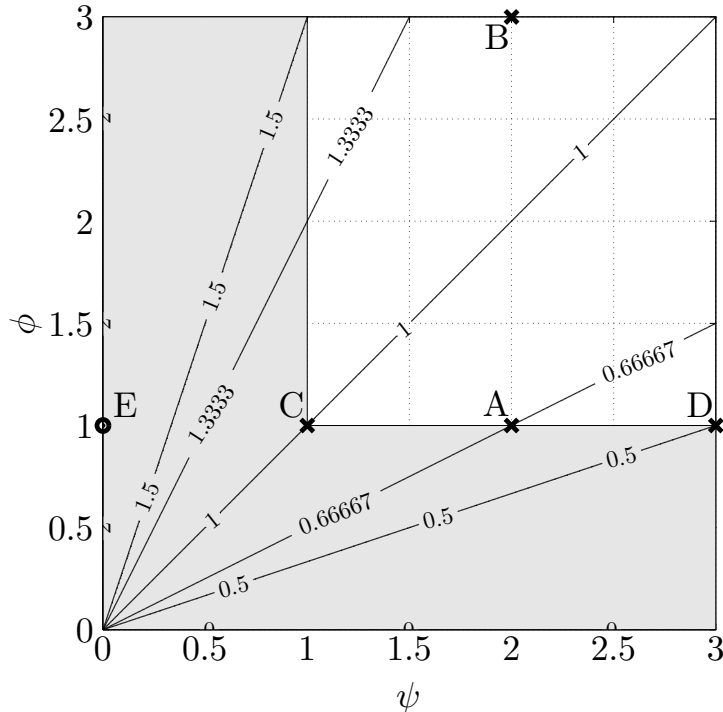


Figure 2.8: Absolute value of the Vogel exponent in the reduced parameter space $\psi - \phi$. The domain shaded in grey corresponds to non-physical ranges. Practical cases: A,B,C,D,E (see text for the details).

as problematic as one might expect.

First, it follows from Sections 2.3.3 and 2.3.4 that discrepancies between the actual distributions of the parameters and their best power-law approximations affects very little the validity of the analytical estimation of the Vogel exponent by (2.23). For instance, it is striking that a beam with taper ratio as large as 10, or even close to 100, still does not exhibit any intermediate plateau similar to the asymptotic regime of a linearly tapered one. In fact, drag reduction on a beam with taper ratio of order 10 is very similar to that of a beam of constant width equal to the base width. Similarly, a structure in a Blasius boundary layer of thickness one order of magnitude smaller than its size is well described, as far as the asymptotic scaling of drag is concerned, by a beam entirely inside the boundary layer. In other words, the ability of (2.23) to provide accurate estimation of the Vogel exponent of actual systems seems very robust with respect to the accuracy of the self-similar fit of the system parameters. Crude power-law fits at the scale of the bending length are likely to yield rather good results.

Second, the consequences of poor estimations of the exponents of the flow and structural parameter distributions α , β , γ , μ also appear limited. It is noticeable on Fig. 2.8 that the asymptotic Vogel exponent ν_∞ does not vary much in the domain

under consideration. The larger the geometrical and material parameters ϕ and/or ψ , the less sensitive the Vogel exponent becomes to small variations of the parameters. As already noted in de Langre et al. (2012), in the case of a uniform beam in a uniform flow, a quadratic material constitutive law (case D on Fig. 2.8) is expected to lead to a Vogel exponent of -0.5 , which differs very little from the $-2/3$ exponent characteristic of linear elasticity (case A). Similarly, changing a linearly elastic, uniform beam from a linearly sheared flow (case B, $\mu = 2$ so $\phi = 3$) to an environment with half less shear ($\mu = 1$ so $\phi = 2$) would only reduce the Vogel exponent from $-6/5$ to -1 . Hence, the estimation of the asymptotic Vogel exponent given by (2.23) is expected to be also robust with respect to the possible errors made in estimating the fitting exponents.

To conclude, it may be said that the prediction of the Vogel exponent using equation (2.23) is quite robust with regards to the parameters of the model.

2.4.3 On the limits of the model

The whole theory derived in this chapter is based on assumptions of three different levels.

First, assumptions have been made regarding the way the action of the flow on the deforming structure is handled. The choice of the simplified form for the local fluid loading (2.4) has already been discussed in Section 2.1. As to the specific form of the projection term in the fluid loading distribution $c(\theta) = \cos^2 \theta$ used all along the present study following Taylor (1952), alternative admissible forms $c(\theta) = \cos^n \theta$ with $n \geq 1$ were numerically tested, and did not lead to any significant alteration of the results.

Second, the study is limited to the influence of the steady background flow at large Reynolds number, in an otherwise force-free environment. Namely, other effects such as gravity, viscosity, vortex shedding or dynamic effects have been neglected here. Depending on the situation, these additional forces may impact the Vogel exponent of natural systems and explain some of the scattering noted in the measurements performed on actual biological or man-made systems. Yet, consistently with the results of Luhar and Nepf (2011) and Zhu (2008), we do not expect that the present results will be largely affected by the effects of gravity or viscosity. The field of dynamics however still requires further investigations (see Kim and Gharib (2011) or Luhar and Nepf (2016)).

Third, as to the type of system chosen, we have considered exclusively the reconfiguration of flexible cantilever beams in cross-flow. Equation (2.23) might actually remain valid for a broader range of systems, if the mechanism of reconfiguration is resemblant enough to the axial bending considered here. Formula (2.42) directly embodies the competition between the fluid loading, characterized by the geometrical parameter ϕ , and the structural restoring force, characterized by the material parameter ψ . All along this chapter, we have considered the restoring force to be the internal elastic bending force, but it might very well be of a different nature. For instance, Barois and de Langre (2013) showed that a ribbon with a weight at one end exhibits a constant drag. In that case, the fluid loading is of the same nature as in the present study, but the restoring

force is the constant axial tension due to the weight. For such system, the material parameter is $\psi = 0$ because there is no length scale associated with the restoring force. It lies out of the admissible range defined earlier, and equation (2.42) yields an asymptotic Vogel exponent $\nu_\infty = -2$ (case E on Fig. 2.8). This does indeed correspond to a constant drag. Conversely, there does not seem to be any obvious analogy between the present study and the rolling up of sheets cut along one radius treated by Schouveiler and Boudaoud (2006) and Alben (2010). In their case, drag reduction is the result of a more complex three dimensional bending process that does not resemble the mechanism considered here.

Finally, it should be noted that the approach used here may easily be adapted to assess the asymptotic effect of elastic reconfiguration on other physical quantities such as the torque at the base of the structure. After some straightforward calculations, the analytical expression found for the Vogel exponent is similar to (2.42) except that the geometrical and material parameters ϕ and ψ must be respectively replaced by $1 + \phi$ and $1 + \psi$.

2.5 Conclusions

To conclude, we may say that this work provides a framework for the understanding of the typical values of Vogel exponents observed in nature. It was shown that the scaling of drag with respect to the flow velocity, in the limits of large loadings, mostly depends on the best power-law approximation of the flow and structural parameters distributions at the scale of the length on which significant bending occurs. An analytical formula relating the asymptotic Vogel exponent to the fitting exponents was derived in equation (2.23), and the sensitivity of this expression with respect to the accuracy of the modelling was shown to be weak.

More importantly, the application of equation (2.23) to a variety of actual systems highlighted the fact that scattering of the Vogel exponents due to non-uniformities in the structural or flow distributions is expected to remain small. Consistently with experimental observations, the predicted Vogel exponents for large loadings always lie around -1 . Consequently, the scaling of the drag on bending beams appears as a characteristic of the mechanism of elastic reconfiguration that depends only to a very limited extent on the actual features of the system.

For the sake of consistency with previous work on the subject, the results presented in this chapter are relative to the total drag on the structure, not to the internal stress generated inside it. However, the results of the next chapter incidentally prove that the reconfiguration number used here also represents the ratio of the maximum shear stress in the deformed and rigid structure, so that the results regarding the reduction of the total drag force are equivalently valid for the maximum shear stress in the structure. Besides, the results of the next chapter also prove that the scalings of both the tensile and shear stress (compared to the rigid case) can be expressed in

terms of the bending length, so that the results of this chapter regarding the scaling of the bending length readily provides the scaling laws for the internal stresses. The present study is however limited to quasi-static configurations. The dynamic effects arising from possible couplings between the structure and the flow are investigated in the following chapters.

Chapter 3

Dynamic reconfiguration in oscillatory flow

Preamble

In the preceding chapter, we have provided an extension of the theory of reconfiguration to the case of spatially varying flow-structure systems. In the following chapter, we present another extension, this time for the case of uniform flexible structures exposed to a uniform, but oscillatory flow. As detailed in the general introduction of this thesis, in spite of the diversity of studies that have tackled this problem, a systematic characterization of the different regimes of flow-structure interaction is still missing. We thus intend to elucidate the nature of the dynamical response of flexible structures, depending in particular on the amplitude and frequency of the oscillatory flow, and to provide the scaling laws for the maximum internal stress generated in the structure in the different regimes, depending on the relevant parameters.

We consider in this chapter a model system very similar to that used in Chapter 2, a cantilever slender beam, clamped perpendicular to the flow. However, contrary to Chapter 2, we further restrict this study to neutrally buoyant flat plates with infinitely small thickness in the direction of the flow. We do so in order to neglect the structural inertia in the balance of forces, so that the dynamics of the structures in our analysis results exclusively from the forcing by the flow. This configuration is furthermore realistic in regard to the features of the macroalgae that endure the oscillatory flow due to the passing waves in the field. Compared to Chapter 2, the governing equation is modified owing to the inclusion in the balance of forces of additional fluid forces due to the unsteadiness of the interaction.

Contrary to the previous chapter, we do not make use of the Vogel exponent in the following work to characterize the drag reduction. Indeed, because of the time-variability of the flow, the (maximum) total hydrodynamic force on a rigid structure does not necessarily scale with the flow velocity squared. The very concept of Vogel exponent is consequently ill-defined in the context of an oscillatory flow. We may on the other hand still define reconfiguration numbers to compare directly the maximum forces generated respectively in a flexible and a rigid structure. In this chapter, we do not define the reconfiguration number based on the total drag force on the structure as in Chapter 2, but based on the spatio-temporal maximum of the internal stress in the structure. Besides, we define two different such quantities, to evaluate respectively the modulations of the tensile and shear stress compared to the rigid configuration.

After introducing the theoretical model and the numerical method we chose to reproduce the dynamics of the system, we present an experimental setup used for visualizing the actual deformation of blades in oscillatory forced motion and to validate the model. We then identify four different kinematic regimes for varying ranges of the forcing amplitude and frequency, before discussing the resulting flexibility-induced scalings of the structural stresses and the different mechanisms underpinning them. We notably prove that flexibility always leads to a reduction of the internal stresses, as long as the resistive drag dominates over the inertial forces.

The findings of this chapter have been published in the Journal of Fluid Mechanics. The paper (Leclercq and de Langre, 2018a) is attached at the end of the thesis. Compared to the present chapter, it includes an additional introduction, but the rest of the content is similar.

Contents

3.1 Model	45
3.1.1 Theory	45
3.1.2 Numerical resolution	48
3.2 Experiments and validation of the model	48
3.3 Kinematics	51
3.3.1 Small amplitude of flow oscillation	51
3.3.2 Large amplitude of flow oscillation	54
3.3.3 Summary of the kinematic regimes	56
3.4 Structural stress analysis	58
3.4.1 Stress reduction due to flexibility	58
3.4.2 Rigid case	58
3.4.3 Small amplitude of flow oscillation	59
3.4.4 Large amplitude of flow oscillation	61
3.5 Discussion	63
3.5.1 Stress alleviation due to flexibility and bending length	63
3.5.2 Consequences in terms of growth pattern of aquatic flexible plants	64
3.5.3 Remarks on previous work about the convective regime	65
3.5.4 Limits and extensions of the model	66
3.6 Conclusion	66

3.1 Model

3.1.1 Theory

In this chapter, we consider a neutrally buoyant, cantilever beam of length L , width W and thickness D , placed perpendicular to a uniform oscillatory flow of velocity $\mathbf{U}(t) = A\Omega \sin(\Omega t) \mathbf{e}_x$ in a fluid of density ρ (see Figure 3.1). The amplitude A corresponds to the maximal horizontal excursion of the fluid particles over one cycle, while Ω is the angular frequency of the oscillations.

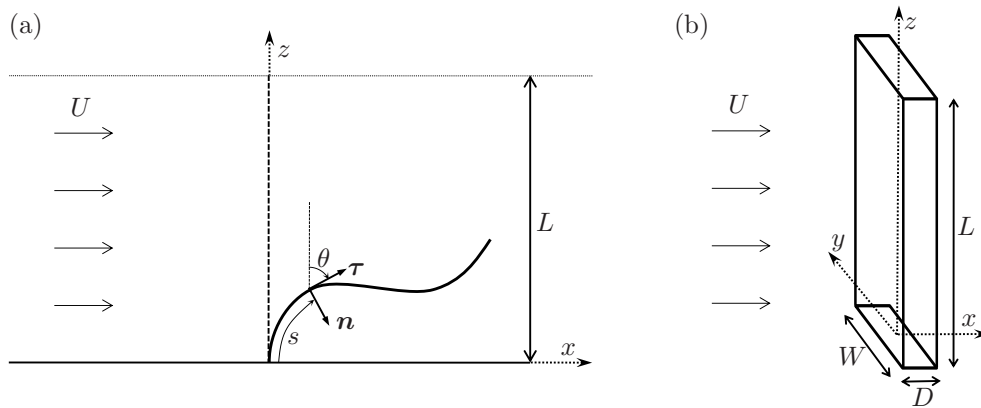


Figure 3.1: (a) Side view of the bending structure. (b) Dimensions of the undeformed blade.

We assume the thickness of the plate is small compared to its width ($D \ll W$) so that deflection under the effect of the flow is confined in the xz -plane. We also assume the structure is slender ($L \gg W$) so we can model it as a two-dimensional inextensible Euler-Bernoulli beam of bending stiffness EI and mass per unit length m (see Audoly and Pomeau, 2010). The curvilinear coordinate s represents the distance from the clamped edge along the span, and we use the prime symbol $(\cdot)'$ to denote differentiation with respect to s . Hereafter, θ is the local angle of the tangent $\boldsymbol{\tau} = \mathbf{r}'$ with the vertical axis \mathbf{e}_z , where $\mathbf{r} = x(s, t)\mathbf{e}_x + z(s, t)\mathbf{e}_z$ is the position vector. Following Audoly and Pomeau (2010), the dynamic equilibrium reads

$$m\ddot{\mathbf{r}} = \mathbf{F}' + \mathbf{q} \quad (3.1)$$

where \mathbf{q} is the external load per unit length on the structure, $\mathbf{F} = T\boldsymbol{\tau} + Q\mathbf{n}$ is the internal force vector, with T the tension and Q the shear force, and the overdot stands for time derivation. The internal bending moment M is related to the local curvature $\kappa = \theta'$ by $M = EI\kappa$, and the shear force Q is given by $Q = -M' = -EI\kappa'$. Clamping implies $x = z = \theta = 0$ at $s = 0$, while the free tip condition reads $T = M = Q = 0$ at $s = L$.

Because the structure is neutrally buoyant, its density is also ρ and gravity and buoyancy forces cancel each other. We assume large Reynolds number so that friction forces are negligible. Following Eloy et al. (2012); Singh et al. (2012b); Michelin and Doaré (2013); Piñeirua et al. (2017) we model the effect of the relative flow as a combination of two external loads distributed along the span. First, the resistive drag (Taylor, 1952)

$$\mathbf{q}_d = -1/2\rho C_D W |U_n| U_n \mathbf{n} \quad (3.2)$$

due to the pressure in the wake is purely normal. It is proportional to the square of the normal component U_n of the relative velocity $\mathbf{U}_{rel} = U_\tau \boldsymbol{\tau} + U_n \mathbf{n} = \dot{\mathbf{r}} - \mathbf{U}$. The drag coefficient C_D depends on the geometry of the cross-section and is typically of order $O(1)$. In pure sinusoidal flow, it slightly varies with the frequency through the Keulegan-Carpenter number $K_C = U/Wf = 2\pi A/W$ (Keulegan and Carpenter, 1958). But in the case of a deformable body, the relative flow varies along the span and is not purely sinusoidal because of the motion of the structure itself. The exact value of C_D is however not critical here so we will simply use the value for steady flows. We will also assume a rectangular cross-section so we will use $C_D = 2$. The second force component is the reactive (or added mass) force (Lighthill, 1971; Candelier et al., 2011)

$$\mathbf{q}_{am} = -m_a \left[\partial_t (U_n \mathbf{n}) - \partial_s (U_n U_\tau \mathbf{n}) + \frac{1}{2} \partial_s (U_n^2 \boldsymbol{\tau}) \right] \quad (3.3)$$

where the added mass is given by $m_a = \rho\pi W^2/4$. This expression involves the normal component but also the tangential component U_τ of the relative velocity. In the case of an inextensible beam, this force becomes purely normal and its expression may be simplified in

$$\mathbf{q}_{am} = -m_a \left[\left(\ddot{\mathbf{r}} - \dot{\mathbf{U}} \right) \cdot \mathbf{n} - 2\dot{\theta} U_\tau + \kappa \left(U_\tau^2 - \frac{1}{2} U_n^2 \right) \right] \mathbf{n}. \quad (3.4)$$

as explained in Appendix B. Finally, because the fluid itself is accelerated, a third force component has to be considered, called the virtual buoyancy force (Blevins, 1990)

$$\mathbf{q}_{vb} = m_d \dot{\mathbf{U}}. \quad (3.5)$$

This term is due to the pressure gradient induced by the acceleration of the fluid. It is equivalent to the Archimedes force, only the acceleration of gravity is replaced by the acceleration of the fluid. It is proportional to the displaced mass per unit length $m_d = \rho W D$. We have assumed so far that the structure is fixed in an oscillating fluid. If the clamped edge of the structure was set into a forced horizontal motion of velocity $\mathbf{U}_f = U_f \mathbf{e}_x$, then the equilibrium equation in the frame of the structure Eq. (3.1) would include an additional load due to the inertial pseudo-force $\mathbf{q}_i = -m \dot{\mathbf{U}}_f$. For a neutrally buoyant structure the displaced mass is equal to the structural mass ($m_d = m$), so this inertial force has the same expression as the virtual buoyancy term Eq. (3.5) if $U_f = -U$. Thus, oscillating a plate in a still fluid is actually equivalent to having a

fixed structure in an oscillating flow, providing that the structure has the same density as the fluid.

In the following, we will only consider very thin blades $D \ll W$ (equivalently $m = m_d \ll m_a$) so that we may neglect the structural inertia and the virtual buoyancy. The dynamic equilibrium Eq. (3.1) then reads

$$\left[T + \frac{1}{2}EI\kappa^2 \right]' \boldsymbol{\tau} + \left[\kappa T - EI\kappa'' \right] \mathbf{n} + \mathbf{q}_d + \mathbf{q}_{am} = 0. \quad (3.6)$$

After projection on the tangential and normal directions and elimination of the unknown tension T , we finally obtain a single differential equation for the kinematic variables κ , θ , \mathbf{r}

$$EI \left[\kappa'' + \frac{1}{2}\kappa^3 \right] + \frac{1}{2}\rho C_D W |U_n| U_n + m_a \left[\ddot{\mathbf{r}} \cdot \mathbf{n} + \kappa \left(U_\tau^2 - \frac{1}{2}U_n^2 \right) - 2\dot{\theta}U_\tau - \Omega^2 A \cos \theta \cos(\Omega t) \right] = 0. \quad (3.7)$$

We non-dimensionalize all the variables using the length of the structure L and the scale of the natural period of the structure in small-amplitude oscillations in the fluid $T_s = L^2 \sqrt{m_a/EI}$. We finally obtain, in non-dimensional form

$$\kappa'' + \frac{1}{2}\kappa^3 + \lambda |U_n| U_n + \ddot{\mathbf{r}} \cdot \mathbf{n} + \kappa \left(U_\tau^2 - \frac{1}{2}U_n^2 \right) - 2\dot{\theta}U_\tau - \omega^2 \alpha \cos \theta \cos(\omega t) = 0 \quad (3.8)$$

with boundary conditions $\mathbf{r} = 0$ and $\theta = 0$ at the clamped edge $s = 0$ and $\kappa = \kappa' = 0$ at the free tip $s = 1$, and the tangential and normal relative velocities $U_\tau = \dot{\mathbf{r}} \cdot \boldsymbol{\tau} - \alpha \omega \sin(\omega t) \sin \theta$ and $U_n = \dot{\mathbf{r}} \cdot \mathbf{n} - \alpha \omega \sin(\omega t) \cos \theta$. This system is ruled by three non-dimensional parameters that are

$$\alpha = \frac{A}{L}, \quad \omega = \Omega T_s, \quad \lambda = \frac{\rho C_D W L}{2m_a} = \left(\frac{2}{\pi} C_D \right) \frac{L}{W}. \quad (3.9)$$

The first two parameters α and ω respectively scale the amplitude and frequency of the background flow to the length and natural frequency of the structure, while $\lambda = O(L/W)$ is mostly a slenderness parameter specific to the structure alone. Because our model is only valid for slender structures, we are restricted to $\lambda \gg 1$. Note that, when studying the influence of flexibility on the loads endured by a structure, the classical non-dimensional parameter that describes the competition between the fluid loading stemming from the resistive drag and the elastic restoring force is the Cauchy number C_Y (Tickner and Sacks, 1969; Chakrabarti, 2002; de Langre, 2008). Following the definition of Gosselin et al. (2010) in the case of the static reconfiguration of cantilever beams, we may here define a Cauchy number based on the maximum velocity of the flow ($A\Omega$) as $C_Y = \rho C_D W L^3 (A\Omega)^2 / EI = \lambda \alpha^2 \omega^2$. In the governing equation (3.8),

given the scaling of the normal relative velocity component $U_n = O(\alpha\omega)$, the resistive drag term $\lambda|U_n|U_n$ directly scales as $\lambda\alpha^2\omega^2 = C_Y$ owing to the choice of characteristic length and time chosen for normalization.

3.1.2 Numerical resolution

We numerically solve Eq. (3.8) along with the boundary conditions using a time-stepping scheme. The one-dimensional structure is discretized using the Gauss-Lobatto distribution $s_k = \frac{1}{2} \left(1 - \cos\left(\frac{k-1}{N-1}\pi\right) \right)$ with $N = 100$ points. The curvilinear derivatives and integrals are computed respectively by Chebyshev collocation and the Clenshaw-Curtis quadrature formulae. We evaluate the time-derivatives at time t_n with implicit second order accurate finite differences with 10^3 time steps per forcing cycle in most cases. The time step is reduced further to maintain good accuracy when a smaller time scale is involved in Sections 3.3.2 and 3.4.4. At each time step, we solve the boundary value problem in $\kappa_n(s)$ with a pseudo-Newton solver (method of Broyden (1965)). The computations are carried on until a limit cycle is found.

3.2 Experiments and validation of the model

We conducted experiments to visualize the actual kinematics of slender blades in an oscillatory flow and validate our model. The setup of the experiment is depicted on Figure 3.2.

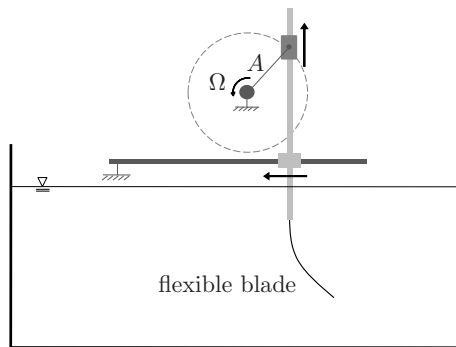


Figure 3.2: Schematic view of the experimental setup.

The flexible object is made of a rectangular piece of $20 \text{ cm} \times 2 \text{ cm}$ (so that $\lambda = 12.7$) and bending stiffness $EI = 1.68 \times 10^{-4} \text{ N.m}^2$ that was cut out of a plastic document cover of thickness 0.49 mm and density 895 kg.m^{-3} . This plate has a mass per unit length $m = 8.72 \times 10^{-3} \text{ kg.m}^{-1}$ and added mass per unit length $m_a = 3.14 \times 10^{-1} \text{ kg.m}^{-1}$, so that $m/m_a = 2.8 \times 10^{-2}$. In order to get the desired relative flow, we forced the clamped edge of the blade into an oscillatory translation of opposite velocity $-\mathbf{U}(t)$

and analysed the dynamic deformation of the structure in the oscillating frame. The flexible structure is clamped at the bottom of a vertical rigid rod and fully immersed in a rectangular water tank of horizontal dimensions 58 cm \times 35 cm and 48 cm of water depth. The rod crossing the free-surface is streamlined in the direction of the motion in order to induce as little perturbation as possible in the fluid. The forcing motion is obtained through a DC motor driving an arm of length A in rotation. The speed of rotation Ω is tuned by changing the voltage at the terminals of the motor. The arm is attached to a carriage freely translating on a vertical rail, which in turn is fixed on another carriage sliding on an horizontal rail. The mounting rod is linked to the latter carriage so that it is driven into the desired sinusoidal translation of amplitude A and angular frequency Ω as the arm rotates. The amplitude A could be varied continuously between 5.4 cm ($\alpha = 0.27$) and 13 cm ($\alpha = 0.65$), and the frequency between 0.21 Hz ($\omega = 2.3$) and 1.08 Hz ($\omega = 12.0$). The motion of the whole structure is filmed with a fixed camera in front of the tank at 100 fps and the position and deformation of the blade through time is extracted from each frame. The deformation in the oscillating frame is then phase-averaged over a minimum of 10 cycles to get a unique cycle representative of the whole run.

The results for three different amplitudes and frequencies spanning the experimental domain are shown on Figure 3.3. In this range of forcing parameters, we notice a diversity of behaviours. For a given frequency ratio ω , the maximum deflection of the blade increases with the amplitude of the forcing α . However, the horizontal excursion of the structure is obviously limited by its own length, so the amplitude of the motion has to saturate when α is increased even more. Besides, the maximum deflection is clearly increasing with the forcing frequency for the largest forcing amplitude $\alpha = 0.65$, but this is much less obvious for the smallest amplitude $\alpha = 0.27$. On the other hand, for any given forcing amplitude α , the dynamics of the deformation is greatly affected when the forcing frequency is increased. For the smallest frequency ratio $\omega = 2.3$, the tip follows the same trajectory during both half-cycles and remains close to the unit circle. The motion of the whole blade is therefore approximately in phase, and curvature is concentrated near the clamped edge while the rest of the beam remains straight. This deforming shape is similar to the static reconfiguration that occurs in steady flow (Gosselin et al., 2010). Conversely, when the frequency is increased, the tip follows a figure-of-eight trajectory and we notice curvature waves propagating along the span in the course of the cycle indicating an increasing spanwise phase-shift. This indicates a highly dynamic response that cannot be considered quasi-steady a priori. Besides, the propagation of curvature waves may induce large loads anywhere along the span and not restricted to the clamping point.

In order to validate the numerical model of Section 3.1, we also compared these experimental observations to the output of the numerical simulations. As shown on Figure 3.4(a), the numerical results for the amplitude of deflection at the tip X_{tip} match very closely the experimental measurements. The snapshots displayed on Figure 3.4(b) for two cases at the boundaries of our experimental domain (indicated on Figure

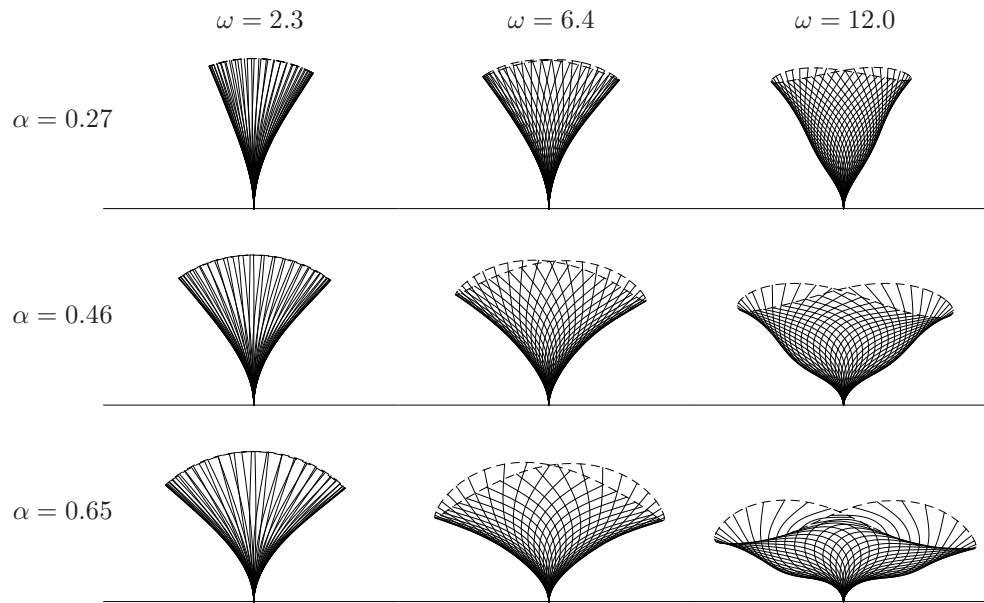


Figure 3.3: Phase-averaged experimental oscillation cycle for varying amplitudes α and frequencies ω . Snapshots of the structural shape (—) and tip trajectory (--).

3.4(a)) also show very good agreement between the observations and the simulations. Additional experimental validation of the model for smaller forcing amplitudes can be found in Piñeira et al. (2017).

These results confirm the validity of our model, and we will therefore use it in the following to systematically explore the parameter space within and beyond the experimentally accessible range.

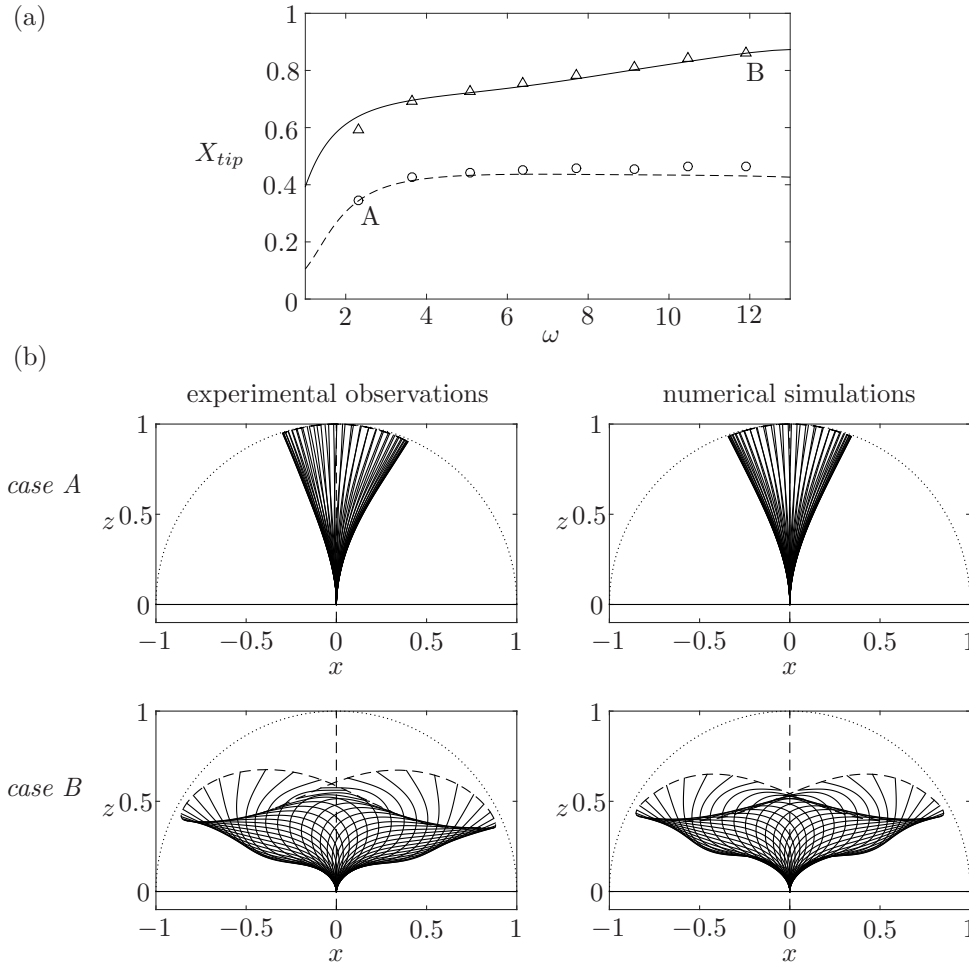


Figure 3.4: Comparison between experimental observations and numerical simulations. (a) Amplitude of the deflection at the tip against the frequency ratio, for $\alpha = 0.27$ (numerical $--$, experimental \circ), $\alpha = 0.65$ (numerical $—$, experimental \triangle). (b) Deformed shape found experimentally (left) and numerically (right), in case A (top, $\alpha = 0.27$, $\omega = 2.3$) and case B (bottom, $\alpha = 0.65$, $\omega = 12.0$).

3.3 Kinematics

3.3.1 Small amplitude of flow oscillation

Let's first consider the situation where the amplitude of forcing is small ($\alpha \ll 1$). The excursion of the fluid particles being small compared to the length of the blade, we may also assume that the deflection remains small as well $|x(s, t)| \ll 1$. Neglecting all the geometrical non-linearities in Eq. (3.8) thus yields the small-amplitude equation

$$x^{(4)} + \ddot{x} = \alpha\omega^2 \cos(\omega t) - \lambda |\dot{x} - \alpha\omega \sin(\omega t)| (\dot{x} - \alpha\omega \sin(\omega t)) \quad (3.10)$$

with boundary conditions $x = x' = 0$ at $s = 0$ and $x'' = x''' = 0$ at $s = 1$. Eq. (3.10) is the standard cantilever beam linear oscillator, forced on the right-hand side by the fluid inertia and the resistive drag. Note that only the non-linearities of geometrical nature have been removed but the quadratic relative velocity term of the resistive drag has been retained at this point. Indeed, the slenderness parameter λ that scales this term is large and the order of magnitude of the whole resistive drag term depends as much on the scaling of λ as it depends on that of α . Besides, no assumption has been made regarding the characteristic time scale for the variations of x , and there is no reason to presume that \dot{x} should be small compared to the free-stream velocity based on the sole assumption that x is small.

If the period of the forcing is large compared to the characteristic response time of the structure ($\omega < 1$), we may assume that the structure is in static equilibrium with the fluid forcing at all times. Consequently, we may neglect the velocity and acceleration of the structure and Eq. (3.10) reduces to the small-amplitude static equation

$$x^{(4)} = \alpha\omega^2 \left[\cos(\omega t) + (\lambda\alpha) |\sin(\omega t)| \sin(\omega t) \right] \quad (3.11)$$

The left-hand side of this equation now involves only the linearized stiffness force, while the fluid forcing on the right-hand side is the same as that a perfectly rigid blade would endure.

On the other hand, if the forcing varies with a period comparable to the characteristic structural response time or faster ($\omega > 1$), we may then assume that the amplitude and the frequency of the response will scale as those of the forcing, as is usually the case for linear oscillators (see for instance Blevins, 1990). We thus define the rescaled deflection and time $\tilde{x} = x/\alpha$, $\tilde{t} = \omega t$, so that the small-amplitude equation (3.10) can be written

$$\frac{1}{\omega^2} \tilde{x}^{(4)} + \tilde{x} = \cos(\tilde{t}) - K_C |\dot{\tilde{x}} - \sin(\tilde{t})| (\dot{\tilde{x}} - \sin(\tilde{t})) \quad (3.12)$$

which now only depends on two parameters: the frequency parameter ω and a new amplitude parameter $K_C = \lambda\alpha = (2C_D/\pi)A/W$ that compares the fluid particles excursion to the width instead of the length of the blade. This parameter is a problem-specific formulation of the classical Keulegan-Carpenter number that compares the respective magnitudes of the drag and the fluid inertial forces. When K_C is small, the fluid inertia dominates over drag and vice versa.

Let's first look at the asymptotic limit of infinitely small amplitude of the forcing $K_C \rightarrow 0$. The non-linear drag term can be neglected and Eq. (3.12) then simply describes a linear oscillator with sinusoidal forcing due to the fluid inertial term. It can be solved analytically and the solution is

$$\tilde{x}(s, \tilde{t}) = 2 \sum_{m=0}^{+\infty} \frac{\sigma_m}{k_m} \frac{\omega^2}{k_m^4 - \omega^2} X_m(s) \cos \tilde{t} \quad (3.13)$$

with the wavenumbers k_m satisfying $\cos k_m \cosh k_m + 1 = 0$, the classical cantilever beam modes $X_m(s) = [\cosh(k_m s) - \cos(k_m s)] - \sigma_m [\sinh(k_m s) - \sin(k_m s)]$ and $\sigma_m = (\sinh k_m - \sin k_m) / (\cosh k_m + \cos k_m)$ (see Weaver et al., 1990).

Figure 3.5(a) compares the amplitude of the maximum deflection for different values of K_C , and for the asymptotic solution Eq. (3.13), as a function of ω . This analytical solution is in good agreement with the model predictions for any $K_C \leq 1$, and it shows that the system behaves as a high-pass filter in this range of the parameter space. As the frequency increases, successive beam modes are excited and resonances occur when the frequency of the forcing matches one of the natural modes of the structure $\omega = k_m^2$. For finite but small K_C , drag acts as a damping term that saturates the amplitude of the resonances but does not seem to affect significantly the modal shape of the deforming structure. The deformation of the beam close to the first three resonances ($\omega_1 = 3.5$, $\omega_2 = 22.0$, $\omega_3 = 61.7$) for $K_C = 10^{-2}$ on Figure 3.5(b) is indeed similar to the corresponding beam modes X_1 , X_2 , X_3 involved in the asymptotic solution Eq. (3.13). Note that when K_C is close to 1, the non-linear drag term is also responsible for a drift of the resonance frequencies that has been studied in Arellano Castro et al. (2014). This effect is not obvious on Figure 3.5(a) because of the very strong attenuation of the resonance peak for $K_C = 1$, but is more visible in the structural stress analysis of Figure 3.9(a).

On the other hand, if we increase the fluid particles excursion beyond the width of the structure ($K_C \gg 1$), a change in physical behaviour occurs. Drag becomes the dominant term in Eq. (3.12). The leading order solution now is $\tilde{x}(s, \tilde{t}) = \cos \tilde{t}$, which amounts to considering that the structure is convected exactly with the fluid particles. Therefore, we may call this regime the convective regime. This solution is however incompatible with the boundary condition at the clamped edge $\tilde{x}(0, \tilde{t}) = 0$, so an elastic boundary layer develops close to the clamping point. The relative magnitude of the terms in Eq. (3.12) suggests that the thickness of the boundary layer scales as $\delta = (K_C \omega^2)^{-1/4}$. Rescaling the curvilinear coordinate $\hat{s} = s/\delta$ in Eq. (3.12) provides the leading order equation for the inner solution

$$\partial_{\hat{s}}^4 \tilde{x} = |\tilde{x} - \sin(\tilde{t})| (\tilde{x} - \sin(\tilde{t})) \quad (3.14)$$

with boundary conditions $\tilde{x} = \partial_{\hat{s}} \tilde{x} = 0$ at $\hat{s} = 0$ and $\partial_{\hat{s}}^2 \tilde{x} = \partial_{\hat{s}}^3 \tilde{x} = 0$ at $\hat{s} = 1/\delta$.

The dynamic deformation of the structure displayed on Figure 3.5(c) for $K_C = 10^2$ for the same values of frequency ratios as on Figure 3.5(b) clearly shows the concentration of the curvature close to the clamped edge and the passive convection of the main part of the structure. The resonances previously observed in the modal regime on Figure 3.5(a) are now completely damped out when $K_C = 10^2$. Compared to the case $K_C = 1$, this curve is shifted one decade to the left as the proper scaling parameter is

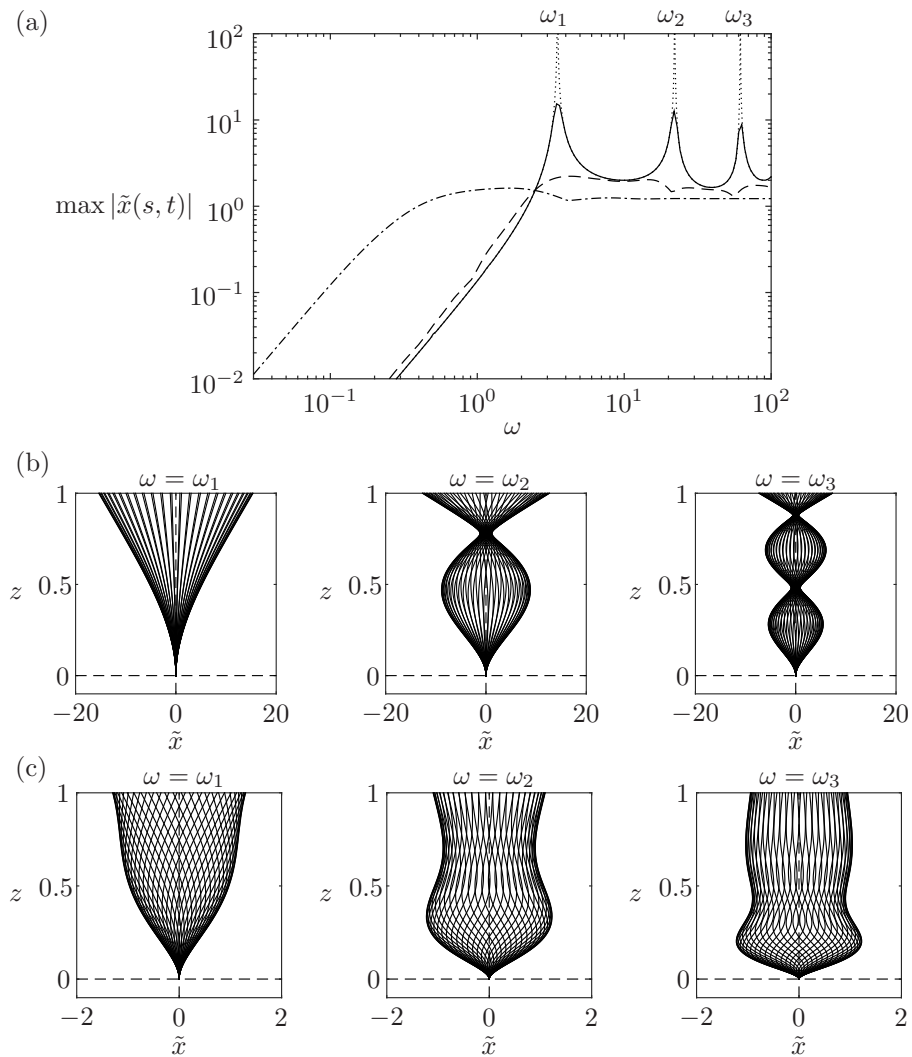


Figure 3.5: (a) Amplitude of the maximum scaled deflection obtained with Eq. (3.12) against the frequency ratio. $K_C = 10^{-2}$ (—), $K_C = 10^0$ (---), $K_C = 10^2$ (-·-·). Analytical solution for $K_C \rightarrow 0$ (· · · ·). (b) Snapshots of the beam over one cycle obtained with Eq. (3.12) for $K_C = 10^{-2}$ (modal regime) and for $\omega = \omega_1$ (resonance of mode 1), $\omega = \omega_2$ (resonance of mode 2), $\omega = \omega_3$ (resonance of mode 3). (c) Same as (b) but with $K_C = 10^2$ (convective regime).

now $\sqrt{K_C} \omega$ instead of ω , and $\sqrt{K_C} = 10$ for $K_C = 10^2$. The scaling of the boundary layer thickness δ is similar to that of the effective length of Luhar and Nepf (2016), as it is based on the equilibrium between the same forces. A similar problem had also been considered in Mullarney and Henderson (2010). In the case of a wave-like flow, the authors neglected the quadratic non-linearity in order to get an analytical solution.

3.3.2 Large amplitude of flow oscillation

In the convective regime discussed above, the structure is purely convected with the fluid particles on most of its span over the whole cycle. But when the amplitude becomes larger than the length of the structure, geometric saturation of the deflection occurs because the structure cannot extend further than its own length. The deflection is now of order $x = O(1)$ and so we cannot neglect the geometrical non-linearities of Eq. (3.8) anymore. The slenderness λ becomes the relevant parameter to compare drag to the fluid inertial forces in lieu of the Keulegan-Carpenter number K_C . Because we only consider elongated structures $\lambda \gg 1$ in this study, drag will always be the dominant term in the large-amplitude regime.

The dynamic deformations obtained with Eq. (3.8) in two cases with similar amplitude $\alpha = 10^2$ and slenderness $\lambda = 12.7$ but different frequencies are compared on Figure 3.6 with 100 snapshots per cycle with constant time interval. In the small frequency case (a), the deformation looks quasi-static. Transition from one side to the other is slow (many snapshots distributed from left to right) and the curvature is essentially concentrated near the clamped edge during the whole cycle. On the other hand, in the larger frequency case (b), the structure switches sides very fast (few snapshots visible in the center while many are superimposed on the sides) and curvature waves propagate very quickly along the span during reversal. Therefore, the cycle may be decomposed into two steps: first, a fast reversal period during which the structure switches from one side to the other immediately after flow reversal, followed by a longer period of quasi-static adaptation to the increasing magnitude of the drag. Because the dominant drag force $\lambda|U_n|U_n \propto \lambda\alpha^2\omega^2$ is proportional to ω^2 , the maximum drag is larger in the large frequency case on Figure 3.6, which explains why the maximum deflection is enhanced.

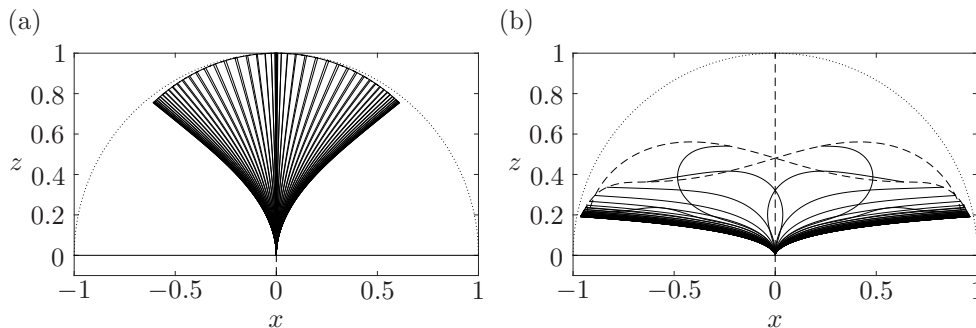


Figure 3.6: Snapshots of the deforming structure over one cycle (—) and tip trajectory (---) obtained with Eq. (3.8) for $\lambda = 12.7$, $\alpha = 10^2$. (a) $\omega = 10^{-2}$, (b) $\omega = 1$.

To estimate the time scale of reversal T_r , let's assume that shortly before flow reversal, the structure is fully reconfigured on one side $x(s = 1, t = 0) = -1$. At flow reversal $t = 0$, drag starts pushing the structure to the other side. Let's assume that the blade is purely convected until it is fully reconfigured on the other side at the end of the reversal time $x(s = 1, t = T_r) = 1$. In that case, we may write

$$2 = x_{tip}(T_r) - x_{tip}(0) = \int_0^{T_r} \alpha \omega \sin(\omega t) dt \simeq \int_0^{T_r} \alpha \omega^2 t dt = \frac{1}{2} \alpha (\omega T_r)^2 \quad (3.15)$$

where the linearization holds owing to the fact that reversal occurs on a time scale much smaller than the period of the cycle ($\omega T_r \ll 2\pi$). We finally obtain $T_r = 2/(\omega\sqrt{\alpha})$. This expression of the reversal time is normalized by the scale of the natural period of the structure. It is more relevant than ω to assess the quasi-steady nature of the deformation in the large-amplitude regime because it compares only the time scale on which structural motion is significant (instead of the whole cycle period) to the characteristic structural response time. Indeed, on Figure 3.6(a), the large reversal time $T_r = 20$ allows the structure to be in quasi-static equilibrium with the fluid loading at all times. Conversely, on Figure 3.6(b) the small reversal time $T_r = 0.2$ is responsible for the propagation of curvature waves during reversal. Hence, when $T_r \gg 1$, the structure is in static equilibrium with the fluid forces during the whole cycle, while the quasi-static character of the deformation is lost during the fast reversal when $T_r \ll 1$.

A zoom on the trajectory of the tip around flow reversal in the case of Figure 3.6(b) shown on Figure 3.7 (solid line) confirms that reversal occurs approximately between $t/T_r = 0$ and $t/T_r = 1$. When the slenderness parameter is increased (broken lines, $\lambda = 127$), the time scale of the dynamics remains unchanged. The same graphs for the same T_r but for a smaller or a larger amplitude ($\alpha = 10$ and $\alpha = 10^3$ respectively), not shown here, are practically indistinguishable from that on Figure 3.7. This result confirms that the amplitude and frequency parameters influence the kinematics of the reversal exclusively through the combined parameter T_r . Besides, because the structural mass was neglected, no dynamic excitation possibly resulting from the violent reversal is allowed to persist after T_r .

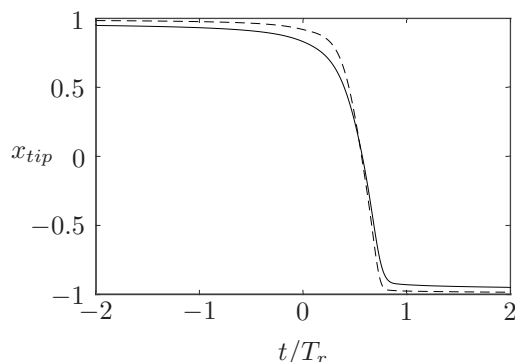


Figure 3.7: Horizontal displacement of the tip during flow reversal against the rescaled time t/T_r , for $\alpha = 10^2$, $T_r = 0.2$ ($\omega = 1$) and $\lambda = 12.7$ (—), $\lambda = 127$ (---).

3.3.3 Summary of the kinematic regimes

So far we have found that depending on the amplitude and frequency of the oscillating flow with respect to the dimensions and natural frequencies of the blade, four different kinematic regimes may exist. Their respective locations in the parameter space are summarized on Figure 3.8.

First, if the amplitude is much smaller than the length of the blade ($\alpha \ll 1$ or equivalently $A \ll L$) and the frequency of the flow smaller than that of the structure ($\omega < 1$ or equivalently $\Omega < 1/T_s$), the structure is in static equilibrium with the fluid forces at all times. On the other hand, if the frequency is now comparable or larger than the characteristic structural frequency ($\omega > 1$ or equivalently $\Omega > 1/T_s$), the kinematics further depends on the ratio of the amplitude of the flow to the width of the structure. If the amplitude is much smaller than the width of the blade ($A \ll W$, or equivalently $K_C = \lambda\alpha \ll 1$), the structure behaves as a linear oscillator and we are in the modal regime. If the amplitude is large compared to the width, but small compared to the length ($W \ll A \ll L$, or equivalently $K_C = \lambda\alpha \gg 1$ and $\alpha \ll 1$), an elastic boundary layer develops close to the clamped edge in which all the curvature is confined, while the rest of the structure is passively convected with the fluid particles. This convective regime occurs because of the saturation of the drag term in the small-amplitude equation (3.10).

Now, if the amplitude is increased further and becomes larger than the length of the blade ($A \gg L$ or equivalently $\alpha \gg 1$), the convection of the blade by the fluid is limited to its own length and the blade deformation is subject to geometric saturation. The convection process is therefore limited in time to a short reversal period, right after flow reversal, and during which the blade switches side at the speed of the fluid particles, followed by a longer period of quasi-static adaptation to the increasing magnitude of the drag force. If reversal occurs on a longer time scale than the characteristic structural response time ($T_r \sim 1/(\omega\sqrt{\alpha}) \gg 1$), the structure has time to reach the static equilibrium with the fluid forces at all time. Conversely, if reversal is faster than the characteristic time of the structure ($T_r \sim 1/(\omega\sqrt{\alpha}) \ll 1$), the quasi-static nature of the large-amplitude structural response is lost during the short time needed for reversal.

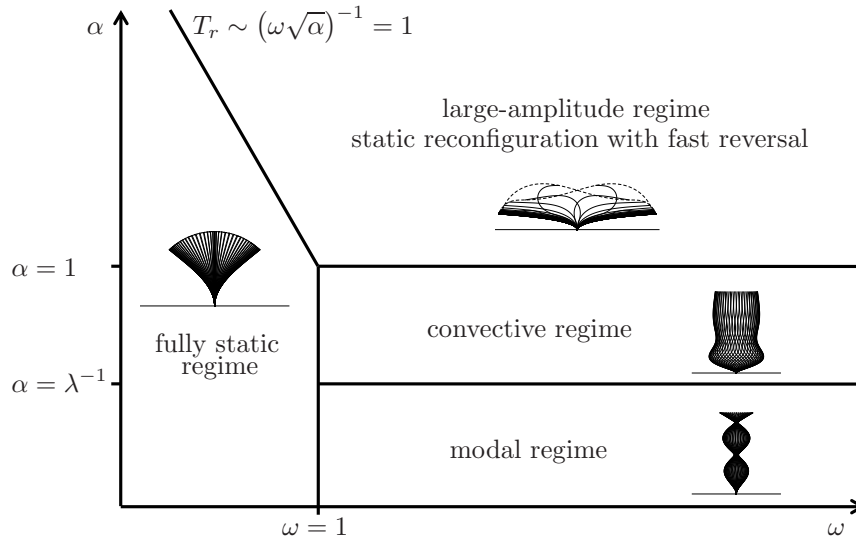


Figure 3.8: Schematic view of the kinematic regimes in the amplitude-frequency space.

3.4 Structural stress analysis

3.4.1 Stress reduction due to flexibility

Depending on the kinematic regime, we expect that the consequences of flexibility in terms of magnitude and repartition of the internal stresses will vary. Our main interest is to assess whether flexibility makes a blade more or less likely to break in a given flow. Structural failure may occur when, at a given time t , the stress due to the loads exceeds a given threshold called the breaking strength, at some location within the structure. For an Euler-Bernoulli beam in two dimensional bending, the stress tensor may essentially be reduced to two components, the tensile (or compressive) stress σ_τ and the shear stress σ_n . Both quantities vary along the span but also within the cross-section. The maximum tensile stress is reached at the edges of the cross-section and depends linearly on the internal bending moment $\sigma_\tau \propto MD/I \propto M/WD^2$. Conversely, the shear stress reaches its maximum on the neutral axis and it is proportional to the internal shear force $\sigma_n \propto Q/WD$. Thus, following the dedicated terminology of Gosselin et al. (2010), we may define two reconfiguration numbers

$$\mathcal{R}_\tau = \frac{\max |M(s, t)|}{\max |M_{rigid}(s, t)|}, \quad \mathcal{R}_n = \frac{\max |Q(s, t)|}{\max |Q_{rigid}(s, t)|} \quad (3.16)$$

that compare the maximum stresses endured over a cycle at any point along the structure to the maximum value the same structure would have to endure if it were rigid. The reconfiguration numbers are smaller than one if the flexibility is beneficial in terms of internal stresses, and larger than unity if it is detrimental.

Our shear reconfiguration number \mathcal{R}_n is equivalent to the reconfiguration number

defined in Gosselin et al. (2010) and used in Chapter 2, in the static case. Their definition is based on the total drag $Q(s=0)$ instead of the maximum of the shear force $\max|Q|$, but the shear force is in fact maximum at the clamped edge in their case so it is equal to the total drag. Our \mathcal{R}_n is also quite similar to the effective length defined by Luhar and Nepf (2016), only the latter was based on the RMS value of the total drag $Q(s=0)$ instead of the spatio-temporal maximum of Q . This is so because the goal of Luhar and Nepf (2016) was to provide insight about how flexibility affects energy dissipation in the background flow, while our focus is the ability of the structure to withstand the fluid loads. For the sake of simplicity, in the rest of this chapter we will only present results about the shear stress σ_n and shear reconfiguration number \mathcal{R}_n . The results about the tensile stress are actually quite similar and will be provided in Appendix C.

3.4.2 Rigid case

In the case of a perfectly rigid structure, the combination of the external fluid forces Eqs. (3.2) and (3.4) results in a span-invariant, purely horizontal load

$$q_{rigid}(t) = \alpha\omega^2 \left[\cos(\omega t) + (\lambda\alpha) |\sin(\omega t)| \sin(\omega t) \right] \quad (3.17)$$

that also reads, in terms of the Cauchy number ($C_Y = \lambda\alpha^2\omega^2$) and Keulegan-Carpenter number ($K_C = \lambda\alpha$)

$$q_{rigid}(t) = \frac{C_Y}{K_C} \left[\cos(\omega t) + K_C |\sin(\omega t)| \sin(\omega t) \right]. \quad (3.18)$$

The first term is an inertia term, proportional to the flow acceleration, while the second term is the resistive drag force proportional to the velocity squared. Integration from the free tip provides the internal bending moment and shear force

$$M_{rigid}(s, t) = -\frac{1}{2}q_{rigid}(t)(1-s)^2, \quad Q_{rigid}(s, t) = -q_{rigid}(t)(1-s) \quad (3.19)$$

that are maximum at the clamped edge and $\max|M_{rigid}(s, t)| = \frac{1}{2}\max|Q_{rigid}(s, t)| = \frac{1}{2}\max|q_{rigid}(t)|$ with

$$\max|q_{rigid}(t)| = \frac{C_Y}{K_C} \text{ if } K_C \leq \frac{1}{2} ; \quad C_Y \left(1 + \frac{1}{4K_C^2}\right) \text{ if } K_C \geq \frac{1}{2}. \quad (3.20)$$

3.4.3 Small amplitude of flow oscillation

As for the kinematics, let's first consider the case where the amplitude of forcing is small compared to the length of the structure ($\alpha \ll 1$). Depending on the value of the Keulegan-Carpenter number K_C , the system will be in the modal or convective regime.

The variations of the shear reconfiguration number with the frequency ratio are shown on Figure 3.9(a) for different values of K_C in the modal regime. Because the system behaves as a high-pass filter, the blade remains rigid in the quasi-static limit $\omega < 1$ and so there is no drag reduction in this regime $\mathcal{R}_n \sim 1$. For larger frequencies, the reconfiguration number decreases overall but peaks at the successive resonances. The magnitude of the peaks is mitigated when the Keulegan-Carpenter number is increased due to damping by the drag term. The resonance frequencies are decreased as well owing to the non-linearity of the drag term, as explained in Arellano Castro et al. (2014). But when K_C is small enough, the reconfiguration number may even exceed unity close to the first resonances. In these particular cases, flexibility may therefore be responsible for a magnification of the shear stress. Apart from the resonances, the slope of the overall decay may be estimated by a scaling argument. Far from the resonances, the amplitude of the deflection is of the order of the fluid particles excursion $x = O(\alpha)$. The non-dimensional shear force $Q = \kappa'$, is thus of order $O(\alpha \times k^3)$ with the wavenumber of the dominant mode $k \sim \sqrt{\omega}$, while the rigid shear force is of order $O(C_Y/K_C) = O(\alpha\omega^2)$ according to Eq. (3.20). Thus, the shear reconfiguration number is $\mathcal{R}_n \sim k^{-1} \sim \omega^{-1/2}$, which is consistent with the slope observed on Figure 3.9(a).

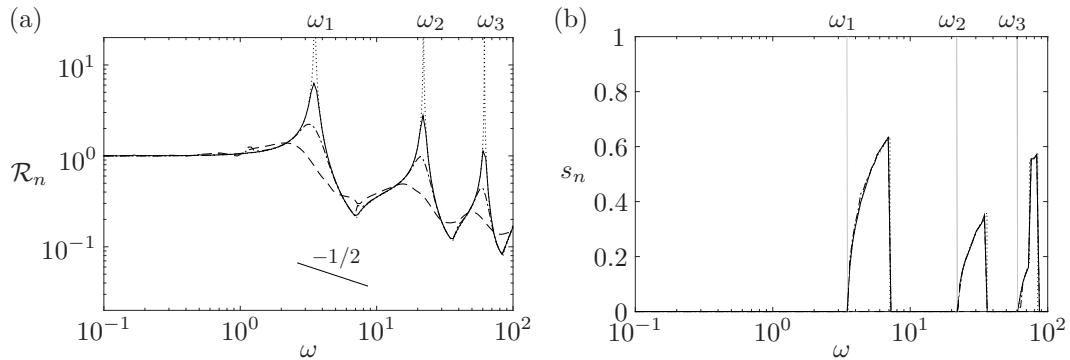


Figure 3.9: Shear reconfiguration number (a) and location of maximum shear stress along the span (b), in the modal regime, against the frequency ratio, for $K_C = 10^{-2}$ (—), $K_C = 10^{-1}$ (- · -), $K_C = 10^0$ (- - -), and analytical solution for $K_C \rightarrow 0$ (· · · ·).

As shown on Figure 3.9(b), the location s_n along the span of the blade where the maximum shear stress $\max(\sigma_n)$ is reached varies with the frequency. In the rigid domain $\omega < 1$ the maximum stress remains at the clamped edge, until the first resonance is reached. After ω_1 , the maximum stress starts moving from the clamped edge towards the free tip as \mathcal{R}_n decreases, before suddenly going back to the clamping point as \mathcal{R}_n starts increasing again, until the second resonance is attained. Similarly, after ω_2 , the locus moves again as \mathcal{R}_n decreases and then comes back as \mathcal{R}_n starts increasing towards the next resonance, and so on. This trajectory of the most solicited spot is independent of K_C , except close to the transition towards the convective regime. Indeed, for $K_C = 1$, the maximum shear stress remains at the clamping point for any value of the frequency

ratio.

In the convective regime $K_C > 1$, we have shown that all the curvature concentrates within an elastic boundary layer of typical size $\delta = (K_C \omega^2)^{-1/4}$ close to the attachment point. Consequently, the location of the maximum stress is always located at the clamping point in the convective regime. Besides, the variations of the shear reconfiguration number \mathcal{R}_n , displayed as a function of the frequency ratio on Figure 3.10(a), all collapse on the same curve when replotted as a function of $K_C \omega^2$ on Figure 3.10(b). Even the transition case $K_C = 1$ also follows the same trend on average, but still exhibits some variations and small resonances due to the persistent modal nature of the response. When $K_C \omega^2 < 1$, the scale of the boundary layer exceeds the length of the structure so the blade behaves rigidly and $\mathcal{R}_n \sim 1$. Conversely when $K_C \omega^2 > 1$, the motion allowed by the flexibility is responsible for an alleviation of the internal shear stress. We may estimate the slope of the asymptotic decay by a similar argument as in the modal regime. Assuming that the characteristic bending length scales as the boundary layer thickness δ , we now have $Q \sim O(\alpha \times \delta^{-3})$ and the rigid shear force of order $O(C_Y) = O(\alpha \delta^{-4})$. We thus obtain $\mathcal{R}_n \sim \delta \sim (K_C \omega^2)^{-1/4}$, in agreement with Figure 3.10(b). Note that, as illustrated on Fig. 3.10(a), reconfiguration in the elastic boundary layer occurs even in the quasi-static regime $\omega < 1$ provided that $K_C \omega^2 > 1$. Indeed, in this particular case, the rigid force q_{rigid} that appears on the right-hand side of the small-amplitude static equation (3.11) would actually lead to static deformations exceeding the excursion of the fluid particles. This is not possible in this drag-dominated regime as only strong inertial forces can cause the structure to overshoot the fluid particles. The drag term of Eq. (3.12) thus ensures the limitation of the structural excursion to that of the fluid particles, while only the elastic boundary layer that develops close to the clamped edge actually satisfies the quasi-static equilibrium between the elasticity forces and the drag (which amounts to neglecting the \ddot{x} terms in the boundary layer equation (3.14)). Consequently, the scaling of the drag associated with reconfiguration in the elastic boundary layer remains valid in this domain as well.

3.4.4 Large amplitude of flow oscillation

In the large-amplitude regime ($\alpha > 1$), we have proven that significant structural motion may only occur during a short period of time T_r following flow reversal ($\omega t = 0$). During that time, the flow magnitude is close to zero and the drag force is at its minimum. Drag being the dominant term of the equation, we expect the largest stress to be experienced when it is at its maximum around $\omega t = \pm\pi/2$, at a time where the structure is in quasi-static equilibrium with the flow forces. Besides, the flow acceleration cancels out when the flow magnitude is maximum so that, at the time where the stress peaks, Eq. (3.8) reduces to the static equation

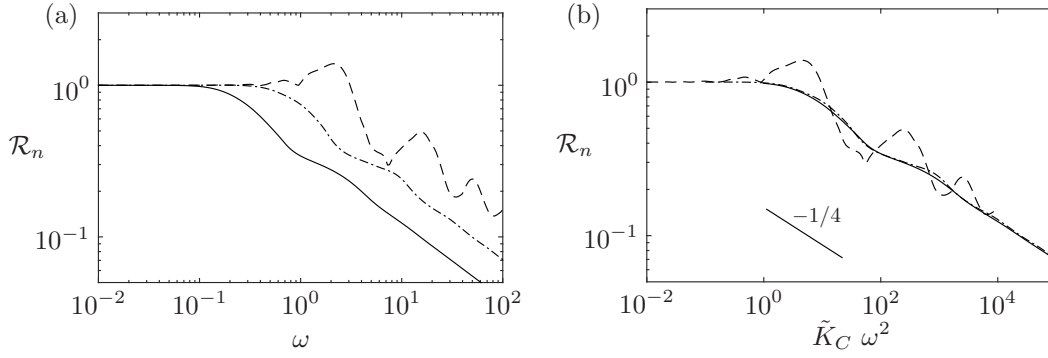


Figure 3.10: Shear reconfiguration number in the convective regime against (a) the frequency ratio ω , (b) the rescaled parameter $K_C \omega^2$, for $K_C = 10^0$ (---), $K_C = 10^1$ (-·-), $K_C = 10^2$ (—).

$$\kappa'' + \frac{1}{2}\kappa^3 - C_Y \left[|\cos \theta| \cos \theta - \frac{1}{\lambda} \kappa \left(\sin^2 \theta - \frac{1}{2} \cos^2 \theta \right) \right] = 0. \quad (3.21)$$

In the quasi-static part of the cycle, the amplitude and frequency parameter influence the shape of the structure and the internal stress only through the Cauchy number $C_Y = \lambda \alpha^2 \omega^2$. Consequently, the evolution of the shear reconfiguration number shown on Figure 3.11(a) as a function of the frequency ratio ω (for $\lambda = 12.7$) collapse very well on the static curve obtained with Eq. (3.21) when replotted as a function of the Cauchy number on Figure 3.11(b). The curves are perfectly superimposed for $\alpha = 10$, but even for α as small as 1, agreement is already very good. When the Cauchy number is inferior to 1, deflection is negligible so Eq. (3.21) actually reduces to the small-amplitude static equation (3.11). In this limit, even though the amplitude of the forcing is large $\alpha > 1$, we actually recover the small-amplitude static regime in which the structure experiences the same amount of stress as if it were rigid $\mathcal{R}_n \sim 1$.

On the other hand, when the Cauchy number is large $C_Y > 1$, the stress is much reduced. In the limit where drag dominates over the added mass corrective term (limit of infinite slenderness $\lambda \rightarrow \infty$), the static equation (3.21) has a self-similar structure. The scaling of the terms of the equation provides the length of the self-similar boundary layer $\ell_s = C_Y^{-1/3}$ within which all the curvature concentrates. Consequently we may here again estimate the asymptotic behaviour of the shear reconfiguration number by a scaling argument. In this case, the saturated angle θ is of order $O(1)$ so the shear force $Q = \kappa' \sim O(1 \times \ell_s^{-2})$. The rigid shear force is of order $O(C_Y) = O(\ell_s^{-3})$ so we get $\mathcal{R}_n \sim \ell_s \sim C_Y^{-1/3}$. The slope on Figure 3.11(b) is close but differ slightly from that estimation. The analysis of Appendix D shows that this discrepancy is due to the rather small value of $\lambda = 12.7$. For any larger slenderness, the asymptotic scaling provided here matches very well the numerical results. Note that this bending length is similar to that previously found by Gosselin et al. (2010) who neglected the cubic term in curvature in their governing equation, as well as that found by Alben et al. (2004)

for the case of a 2D plate (opposite limit of infinite width). The extended validity of this static bending length to the case of large-amplitude unsteady flows was moreover suggested in Luhar and Nepf (2016).

Note finally that this analysis is independent of the magnitude of the reversal time T_r . The key point of this analysis lies in the fact that even if significant dynamics may be involved during reversal when $T_r \gg 1$, the maximum stress is endured at a time when the structure is in static equilibrium with the fluid forces. This remains obviously true when $T_r \ll 1$ and static equilibrium is enforced at all times.

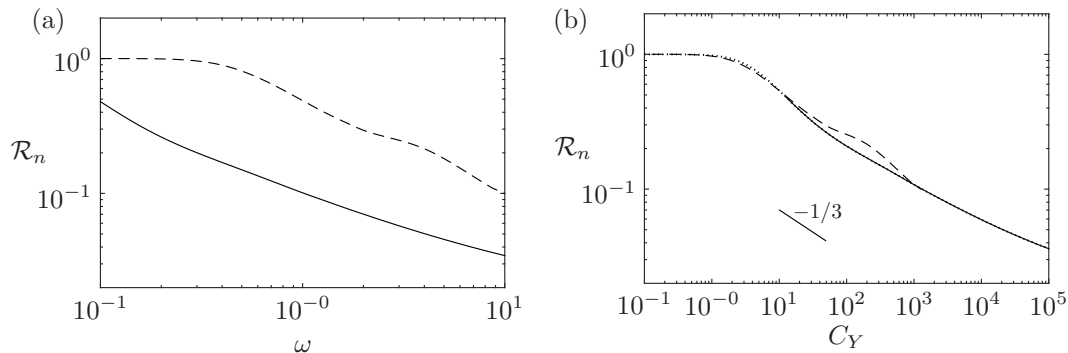


Figure 3.11: Shear reconfiguration number in the large-amplitude regime for $\lambda = 12.7$, against (a) the frequency ratio ω , (b) the Cauchy number C_Y , for $\alpha = 10^0$ (---), $\alpha = 10^1$ (—). Static solution obtained with Eq. (3.21) (⋯⋯, on (b) only).

3.5 Discussion

3.5.1 Stress alleviation due to flexibility and bending length

Depending on the values of the amplitude and frequency of the oscillating flow, we have identified four distinct kinematic regimes summarized on Figure 3.8. In each regime, the consequences of the flexibility on the magnitude of the internal stress are different. The varying scalings of the shear reconfiguration number \mathcal{R}_n depending on the amplitude and frequency of the flow are schematically displayed on Figure 3.12.

As long as the forcing is dominated by the inertial forces (in the modal regime $A \ll W$), there exists a risk of resonance if the frequency of the flow matches one of the natural frequencies of the structure. This is a case where the dynamical motion allowed by the flexibility may be responsible for a magnification of the internal stress. However, this is also the region in the parameter space where the loading is the lowest and so this is unlikely to cause any severe damage. Far from the resonances and in all other cases, flexibility always alleviates the magnitude of the internal stress.

The general scaling of the reconfiguration numbers is related to some characteristic bending length ℓ_b such that $\mathcal{R}_n \sim \ell_b$ and $\mathcal{R}_\tau \sim \ell_b^2$ (see Appendix C), but the scaling of that very bending length depends on the reconfiguration regime. In the modal

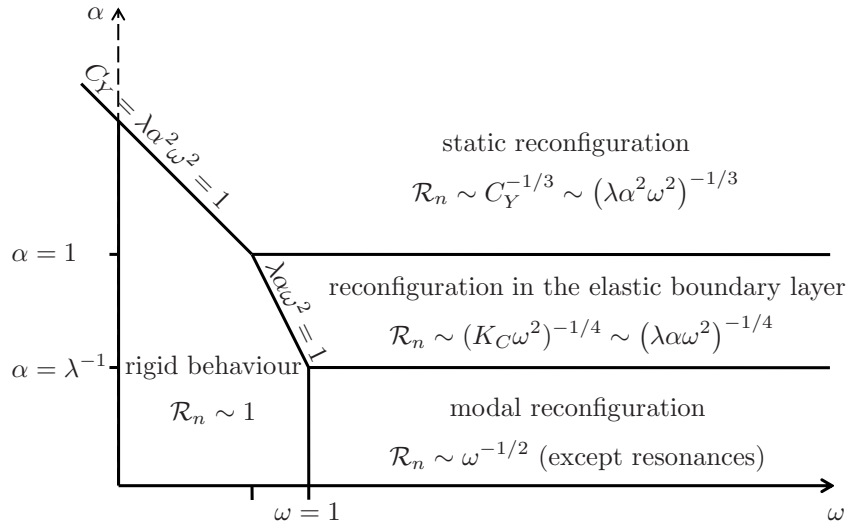


Figure 3.12: Schematic view of the reconfiguration regimes in the amplitude-frequency space.

regime ($A \ll W$), the bending length is proportional to the wavelength of the dominant mode that varies as $\ell_b = k^{-1} = \omega^{-1/2}$. In the convective regime ($W \ll A \ll L$), curvature is confined in the elastic boundary layer so naturally $\ell_b = \delta = (\lambda\alpha)^{-1/4}\omega^{-1/2}$. The characteristic bending length varies continuously between the two small-amplitude regimes as their expressions are similar at the transition when $K_C = \lambda\alpha = 1$. On the other hand, in the large-amplitude regime ($A \gg L$) the bending length transitions to $\ell_b = \ell_s = C_Y^{-1/3} = (\lambda\alpha^2\omega^2)^{-1/3}$. The boundary of the rigid domain with the three different reconfiguration regimes is nonetheless continuous as illustrated on Fig. 3.12.

3.5.2 Consequences in terms of growth pattern of aquatic flexible plants

In any of the three reconfiguration regimes, the reconfiguration numbers scale in dimensional form with the length of the blade as $\mathcal{R}_n \sim L^{-1}$ and $\mathcal{R}_\tau \sim L^{-2}$. Given the scalings of the rigid loads and of the internal stresses in Section 3.4.1, we thus obtain the cancellation of the dependency of the dimensional forces and internal stresses on the actual length of the blade $\sigma_n \propto Q \sim L^0$ and $\sigma_\tau \propto M \sim L^0$. This loss of relevance of the true length of the structure in aid of a smaller characteristic bending length was already pointed out in the steady case (see de Langre et al., 2012) and remains valid in the oscillatory case. Consequently, it does not seem as if there is any mechanical limit to size in wave-swept flexible kelps, as long as growth is concentrated in the axial direction.

But real plants grow according to more complex allometric patterns (Gaylord and Denny, 1997; Denny and Cowen, 1997). Following the growth of a plant in the vari-

ables of Figure 3.12 amounts to decreasing α from the top. In the static reconfiguration regime, the internal stresses σ_n and σ_τ are both independent of any of the three dimensions D , W , L and so growth does not affect the magnitude of the stresses in a given environment, no matter the allometry of the plant. When the structure reaches the convective regime ($L \geq A$), the stresses become decreasing functions of the thickness D but remain independent of W and L . One might think that a growth pattern favouring thickness would be advantageous, but this is only so for thin plates $D < W$ for which the elastic effects are confined in the plane of the flow. A thicker structure might experience 3D deformations that would considerably complexify the dynamics. Finally, in the modal regime ($W \geq A$), the stresses now start increasing with the width W , and the risk of resonances may enhance the stresses even more depending on the frequency of the flow. It thus appears detrimental for a flexible plant to grow in width in excess of the fluid particle excursion.

These remarks come as complementary answers to the work of Koehl (1984) and especially Denny et al. (1985), Gaylord et al. (1994) and Denny (1999). Koehl (1984) first noted that “flexibility in combination with great length provides a mechanism of avoiding bearing large forces in habitats subjected to oscillating flow”, in comparison to rigid organisms that need to remain small. However the question of whether there might be size limits imposed on wave-swept flexible organisms due to the oscillatory fluid loading has never received a definitive answer. Our results indicate that for slender, neutrally buoyant blades, the hydrodynamic loads do limit the width, but put no constraints on the axial growth.

3.5.3 Remarks on previous work about the convective regime

Most aquatic plants are close to neutrally buoyant and the horizontal amplitude of the passing waves is typically much larger than the width if not the length of these plants (see Gaylord et al., 1994; Gaylord and Denny, 1997; Denny and Cowen, 1997). Thus it seems that plants growing larger than the fluid particles excursion are likely to remain in the convective regime in order to avoid large flow-induced stresses. The work of Mullarney and Henderson (2010) and Luhar and Nepf (2016) has focused mainly on this convective regime. The latter show on their Figure 11 that their effective length (analogous to our normal reconfiguration number \mathcal{R}_n) seems to scale as $(C_Y/\alpha)^{-1/4} = (\lambda\alpha\omega^2)^{-1/4} = \delta$. This result is consistent with the scaling of the elastic boundary layer that develops in the convective regime, and indeed almost all the experimental cases of Luhar and Nepf (2016) were obtained within the appropriate range $\alpha \leq 1$ and $K_C \geq 1$ (more precisely $0.06 \leq \alpha \leq 1.32$ and $0.76 \leq K_C \leq 4.2$). However, because the slenderness parameter of their blades is rather low (between $\lambda = 3.2$ and $\lambda = 12.7$), α and K_C are quite close to each other and consequently most of their points are very close to either one of the boundaries of that regime. Some particular points in that study show an increase of the load compared to the rigid case. The authors suggested that this might result from an interaction between the blade and the vortex shed at the tip. But these points are characterized by a rather small amplitude $\alpha = O(10^{-1})$

and Keulegan-Carpenter number $K_C \sim 0.7 - 1.2$, and forcing frequencies close to the resonance frequency $\omega \sim 1-5$. For instance, the largest load was obtained for ($\alpha = 0.12$, $K_C = 0.76$ and $\omega = 2.30$). It is thus a possibility that the load enhancement is simply the consequence of a resonance of the impinging wave with the first natural mode of the structure, due to the persistent modal nature of the dynamic response for such values of the parameters. Conversely, other points obtained for $\alpha = O(1)$ seem to collapse quite well with the others. We have shown that for such high values of the amplitude parameter, at least when $\lambda = 12.7$, the reconfiguration number should be close to its static equivalent. But if very slender structures exhibit a clear asymptotic regime $\mathcal{R}_n \sim C_Y^{-1/3}$, decreasing the slenderness below $O(10)$ mitigates the efficiency of the reconfiguration and increases the slope so that it may be difficult to know the difference with the scaling of the convective regime.

3.5.4 Limits and extensions of the model

In all this study we have focused exclusively on the case of an infinitely thin, neutrally buoyant blade. These two assumptions have allowed us to neglect both the displaced mass and the structural mass. In practice however, aquatic plants are not strictly speaking of the same density as the water and their thickness might not be negligible.

First, if the thickness of the neutrally buoyant blade is not negligible anymore, we need to consider the inertial and virtual buoyancy forces. These forces might be responsible for additional inertial effects in the large-amplitude regime, such as persistent oscillations following the quick reversal with $T_r < 1$, or a flutter instability similar to that observed on axial flags. The effects of such flapping motion is discussed in detail in the next chapter. The dynamics induced would then be responsible for additional loads that may challenge the findings of that study. However, we expect the consequences to remain marginal, as damping by the drag term would still dominate. This is even more so as the slenderness is increased and for infinite slenderness, we do not expect any significant discrepancy with the present work. Besides, the small-amplitude regimes would not be affected in any way as equation (3.10) would remain the same, providing that the characteristic time of the structure used for non-dimensionalization is redefined to account for the structural mass $T_s = L^2 \sqrt{(m_a + m)/EI}$.

If the structure is now lighter than the fluid, then its inertia is even more negligible. Buoyancy may still modify our results, but this effect should become negligible as soon as the fluid loading is dominant as explained in Luhar and Nepf (2011) and Luhar and Nepf (2016).

On the other hand, if the structure is much denser than the fluid, some more complicated dynamical effects might come into play due to the large structural inertia possibly overcoming even drag. We do not expect the conclusions of the present work to hold in that case.

3.6 Conclusion

The work presented in this chapter provides a dynamical extension of the theory of reconfiguration to the case of oscillatory flow. Focusing on neutrally buoyant cantilever slender blades, we proved that flexibility is always favourable to reducing the internal stresses as long as drag dominates the fluid inertial forces. In fact, drag appears as the motor of reconfiguration. In large-amplitude oscillations (or equivalently in steady flow), drag is responsible for the static deflection that reduces the stress. In small-amplitude oscillations, it is also the saturation of the drag term that forces the passive convection of the structure with the fluid particles if the Keulegan-Carpenter number is large. Even in the less favourable case of small Keulegan-Carpenter numbers, it is the small drag term that saturates the resonances that occur due to the fluid inertia, even when the structural inertia is negligible. We also expect that drag would saturate flutter-like oscillations that might occur if the structural mass were not negligible, thus limiting the enhancement of the internal stresses to a bearable extent (see Chapter 4 for more details).

As in the static case, we have shown that dynamic reconfiguration results in the concentration of the stresses on a short bending length near the clamped edge, only the scaling of that bending length varies depending on the dynamic regime. Besides, the scaling of the bending length in the static regime also depends on the spatial variability of the system, and the scaling of the bending length depending on the intensity of the non-uniformities was provided earlier in Chapter 2.

Note that the dependency of the internal stresses on the actual length of the structure disappears in the reconfiguration regimes, so there does not seem to be any mechanical limitation to the axial growth of plants living in wave-swept environment due to the hydrodynamic loads. However, in order to avoid deleterious inertial effects, it seems preferable to keep a width much smaller than the excursion of the fluid particles. In other words, if there is no limitations to growth in itself, there is an incentive to grow slender based on mechanical considerations. Of course, the actual growth pattern of aquatic plants also involves other aspects such as the optimization of its biological functions that we do not take into account here.

Finally, only the inertia of the fluid has been accounted for in this work. We expect the inclusion of significant structural inertia should considerably modify the results of the present work. Even in the case of a uniform and steady flow, we anticipate that the inclusion of the structural inertia in the balance of forces may result in a dynamic instability. This effect is investigated in the next chapter.

Chapter 4

Flutter of reconfiguring structures

Preamble

In Chapter 3, the inertia of the structure was neglected based on the assumption that it was flat and neutrally buoyant. The dynamics of the structure was consequently entirely due to the unsteadiness of the free-stream itself. In this chapter, we relax this assumption in order to investigate the possible dynamic coupling that may arise between the flow and the structure, and the consequences it may have on the drag of the structure.

As explained in the introductory chapter, most existing studies on reconfiguration in steady flows assume a static structural deflection, but the flow-structure coupling may be the source of a dynamic motion similar to that observed on flags flapping in the wind, in a time-varying or even in a steady free-stream. The very occurrence of dynamics induces inertial loads on the structure, and one may wonder whether flexibility is associated with lower or larger drag in that case, compared to a rigid structure that does not reconfigure but does not flap either.

As in the whole thesis, we still consider in this chapter the model system of a cantilever slender beam clamped transverse to the flow, and perform numerical simulations based on reduced order models. In order to relax the assumption on the structural mass, we do not make additional assumptions regarding the geometry of the cross-section or the density of the structure anymore. For the sake of simplicity, we limit this study to the self-induced, two-dimensional dynamics of structures that reconfigure in a uniform and steady background flow.

As in Chapter 2, the results are presented in terms of the modulation of the total drag force to remain consistent with previous work on reconfiguration in steady free-streams. Note however that here again, the maximum shear stress in the structure is located at the clamped edge and balances the total drag force, so that the results for the drag displayed in this chapter are equivalently valid for the internal shear stress. Besides, due to the absence of asymptotic regime for the drag in the limit of large deflections when flutter occurs, the concept of Vogel exponent does not seem relevant in this context so we directly discuss the variations of the reconfiguration number.

After a short introduction to provide some specific background elements regarding the problem of flutter, we present the model and important parameters used throughout the study. We then discuss the domain of stability of the static reconfiguration, the post-critical flapping behaviour of the deflected structure, and finally the consequences of flexibility in terms of total drag modulation when reconfiguration and flutter are both considered. We finally conclude that the additional drag due to the flapping motion

does mitigate the benefits of reconfiguration, but only rarely offsets the drag reduction it provides. Isolated and brief snapping events may transiently raise the drag above that of a rigid structure in the particular case of heavy, moderately slender beams. But apart from these short peak events, the drag force remains otherwise significantly reduced in comparison with a rigid structure.

The results presented in this chapter have been published in the Proceedings of the Royal Society of London A: Mathematical, Physical and Engineering Sciences. The paper (Leclercq et al., 2018) is attached at the end of the thesis. Compared to the present chapter, the paper includes a slightly more furnished introduction, and more details about the model that have already been provided in the previous chapter. The rest of the content is similar.

Contents

4.1	Specific background elements about flutter	71
4.2	Model	71
4.3	Stability of the static reconfiguration	74
4.4	Post-critical kinematics	77
4.4.1	Kinematic regimes	78
4.4.2	Influence of the slenderness and mass ratio	79
4.5	Drag reduction in the post-critical regime	81
4.6	Conclusion	86

4.1 Specific background elements about flutter

The flapping of flags in the wind illustrates that structures parallel to the flow are prone to self-induced dynamic oscillations (Kornecki et al., 1976; Huang, 1995; Watanabe et al., 2002; Connell and Yue, 2007; Michelin et al., 2008; Shelley and Zhang, 2011). This flag flutter instability results from the competition between the destabilizing aerodynamic pressure forces and the stabilizing rigidity of the structure, so slender structures in axial flow are liable to it as well (Datta and Gottenberg, 1975; Yadykin et al., 2001; Païdoussis et al., 2002; Semler et al., 2002; Lemaitre et al., 2005; de Langre et al., 2007). A few authors have tried and assessed the drag of such structures theoretically (Moretti, 2003), numerically (Yadykin et al., 2001), and experimentally (Fairthorne, 1930; Hoerner, 1965; Taneda, 1968; Carruthers and Filippone, 2005; Morris-Thomas and Steen, 2009; Wilk and Skuta, 2009; Virost et al., 2013). All these studies prove that the onset of flutter is associated with a large increase of the drag force, whose magnitude is strongly correlated to the periodicity and the envelope of the flutter mode.

Cantilever structures that bend in a transverse flow become more and more aligned with it, so that the flow about sufficiently deflected beams becomes mostly axial. If reconfiguration is known to have a drag-lowering effect that protects the structural integrity, the possible fluttering of highly reconfigured beams may on the other hand be responsible for a magnification of the drag possibly leading to damage or breakage. In the literature, the small-amplitude vibrations of a naturally curved rod in a flow has been considered in Ni et al. (2014), as well as the flapping dynamics of plates clamped in axial flow at their trailing edge instead of their leading edge (the so-called inverted flag problem (Gurugubelli and Jaiman, 2015; Tang et al., 2015; Sader et al., 2016)), and the flow-induced instability of filaments clamped at their trailing edge but deflected by gravity (Schouveiler et al., 2005). However, very little is known about the self-induced dynamics of structures passively bending under the effect of the flow, and even less about whether the resulting drag force is overall enhanced or reduced. The goal of this work is thus to determine if, and to what extent, the occurrence of flutter may impair the drag reduction abilities of flexible structures in transverse flow compared to rigid ones. We will focus on the case of cantilever, elongated beams of arbitrary but uniform cross-section.

4.2 Model

We consider the problem depicted on Figure 4.1. A structure of length L , width W , thickness D and mass per unit length m is clamped perpendicular to a uniform and steady flow of velocity U of a fluid of density ρ . As in the previous chapters, we still assume the structure may only bend in the xz -plane, and we model it as a two dimensional Euler-Bernoulli beam (Audoly and Pomeau, 2010).

To model the dynamic behaviour of the structure in the flow, we use the same reduced order models for the structure and for the fluid forces as in Chapter 3. We

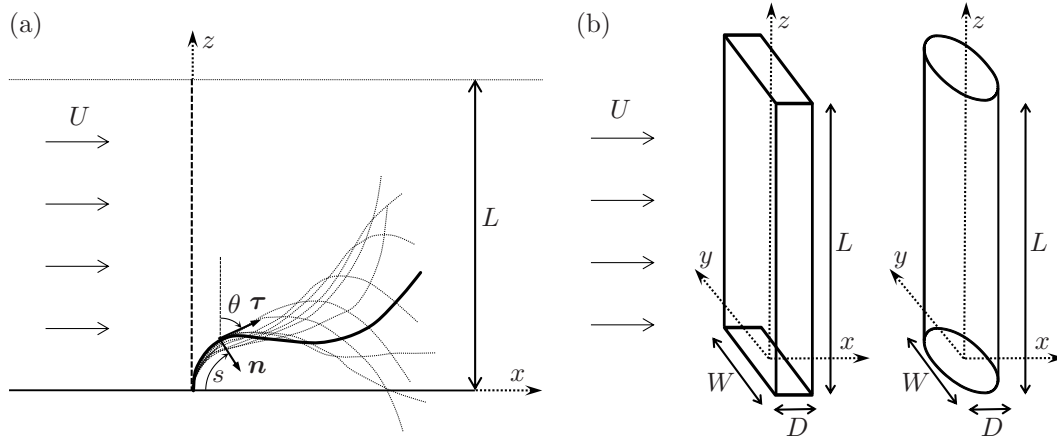


Figure 4.1: (a) Side view of the deforming structure. (b) Examples of geometries of two undeformed structures with different cross-section shapes.

disregard the influence of gravity and buoyancy forces in this problem, and we restrict our study to large Reynolds numbers so that friction drag is neglected (see de Langre et al., 2007, for more details about the effect of friction on the flutter instability). Besides, because the flow in this chapter is steady, the virtual buoyancy force (3.5) does not contribute to the balance of forces. Thus, the external forcing by the fluid reduces, as in Chapter 3, to the combination of the resistive drag \mathbf{q}_d given in equation (3.2) and reactive force \mathbf{q}_{am} given in equation (3.4). However, we do not make any assumption regarding the mass of the structure, so we cannot neglect the inertia of the structure on the left hand-side of the dynamic equilibrium equation (3.1) anymore. The governing equation (3.6) supplemented with the inertial term now reads

$$m\ddot{\mathbf{r}} = \left[T + \frac{1}{2}EI\kappa^2 \right]' \boldsymbol{\tau} + \left[\kappa T - EI\kappa'' \right] \mathbf{n} + \mathbf{q}_{am} + \mathbf{q}_d. \quad (4.1)$$

This model is consistent with previous work on flutter of slender beams in axial flow. The expression (3.4) (from Lighthill, 1971; Candelier et al., 2011) for the reactive term \mathbf{q}_{am} has been extensively used in the literature for the linear stability analysis of straight beams in axial flow (Païdoussis, 1998; Lemaitre et al., 2005; de Langre et al., 2007). Indeed, as emphasized in Eloy et al. (2007) and Singh et al. (2012a), it is the potential component of the flow that is driving the instability. Moreover, when studying the large-amplitude post-critical oscillations, an additional resistive contribution \mathbf{q}_d associated with flow separation in the plane of the cross-sections has proved necessary to avoid unrealistically large flapping amplitude (Singh et al., 2012a). The semi-empirical formulation (3.2) of Taylor (1952) is unambiguously used in the literature as flapping amplitude-limiting term in flutter studies such as Eloy et al. (2012), Singh et al. (2012a), Singh et al. (2012b) or Michelin and Doaré (2013). Besides, in our case, the beam is statically deflected by the effect of the cross-flow before it starts fluttering. The reactive term \mathbf{q}_{am} vanishes on a straight and motionless beam, so the resistive contribution \mathbf{q}_d

is essential to bend the beam into a configuration prone to flutter.

After projection on the tangential and normal directions and elimination of the unknown tension T , Eq. (4.1) finally yields a single integro-differential equation on the kinematic variables κ , θ , \mathbf{r}

$$(m + m_a)\ddot{\mathbf{r}} \cdot \mathbf{n} - m\kappa \int_L^s \ddot{\mathbf{r}} \cdot \boldsymbol{\tau} + EI \left[\kappa'' + \frac{1}{2}\kappa^3 \right] + m_a \left[\kappa \left(U_\tau^2 - \frac{1}{2}U_n^2 \right) - 2\dot{\theta}U_\tau \right] + \frac{1}{2}\rho C_D W |U_n|U_n = 0. \quad (4.2)$$

As in Chapter 3 and following Païdoussis (1998) and de Langre et al. (2007), we non-dimensionalize all the variables using the length of the structure L and the scale of the natural period of the structure in small-amplitude oscillations in the fluid $T_s = L^2\sqrt{(m + m_a)/EI}$. We finally obtain, in non-dimensional form

$$\ddot{\mathbf{r}} \cdot \mathbf{n} - (1 - \beta)\kappa \int_1^s \ddot{\mathbf{r}} \cdot \boldsymbol{\tau} + \kappa'' + \frac{1}{2}\kappa^3 + \beta \left[\kappa \left(U_\tau^2 - \frac{1}{2}U_n^2 \right) - 2\dot{\theta}U_\tau \right] + \beta\lambda|U_n|U_n = 0 \quad (4.3)$$

with the inextensibility condition $\mathbf{r}' = \boldsymbol{\tau}$, the boundary conditions $\mathbf{r} = 0$, $\theta = 0$ at the clamped edge $s = 0$ and $\kappa = \kappa' = 0$ at the free tip $s = 1$. The non-dimensional relative velocity is given by $U_\tau\boldsymbol{\tau} + U_n\mathbf{n} = \dot{\mathbf{r}} - u/\sqrt{\beta}\mathbf{e}_x$. This system is ruled by three non-dimensional parameters that are

$$\beta = \frac{m_a}{m_a + m}, \quad u = UL\sqrt{\frac{m_a}{EI}}, \quad \lambda = \frac{\rho C_D W L}{2m_a} = \left(\frac{2}{\pi}C_D \right) \frac{L}{W}. \quad (4.4)$$

The mass ratio β represents the amount of fluid inertia within the total inertia of the system. It takes values between 0 and 1. For instance, $\beta \rightarrow 0$ for a very dense structure, $\beta = 0.5$ for a neutrally buoyant cylinder with circular cross-section, and $\beta \rightarrow 1$ for very thin plates ($D \ll W$). Note for instance that the assumption of small structural mass $m \ll m_a$ made in Chapter 3 is equivalent to taking $\beta = 1$. The reduced velocity u compares the relative magnitude of the fluid inertial (or reactive) load to the internal elasticity forces. Both are classically used in studies about the flutter of slender beams in axial flow, as in Païdoussis (1998) or de Langre et al. (2007), while the third parameter $\lambda = O(L/W)$ is the same slenderness parameter as in Chapter 3. It can be seen as the ratio of the resistive drag to the reactive force. Because our model is only valid for elongated structures, we are restricted to $\lambda \gg 1$.

As already mentioned, the flutter instability results from the competition between the destabilizing effect of the reactive force and the stabilizing effect of the rigidity of the structure. The reduced velocity u is therefore the natural parameter that governs this

phenomenon. On the other hand, the static reconfiguration of the beam is primarily due to the resistive drag overcoming the bending stiffness of the structure. The classical non-dimensional parameter that compares these two forces is the Cauchy number C_Y (Tickner and Sacks, 1969; Chakrabarti, 2002; de Langre, 2008). In the case of a slender structure bending in transverse flow, we define the Cauchy number following Gosselin et al. (2010) as $C_Y = \rho C_D W L^3 U^2 / 2EI$. These two non-dimensional parameters are redundant as they both provide scaling of the flow velocity with respect to the structural stiffness. They are related via the slenderness parameter by $C_Y = \lambda u^2$. However, the Cauchy number is more relevant to describe reconfiguration while the reduced velocity is more relevant to discuss features of the flutter instability.

4.3 Stability of the static reconfiguration

In order to discuss the joint effect of flutter and reconfiguration, we first need to identify the domain in which flutter may happen, and that in which the structure will reconfigure without flapping. To do so, let's first look for the stationary equilibrium solutions of the governing equation (4.3). Removing all unsteady terms in Eq. (4.3) yields the static equation

$$\kappa'' + \frac{1}{2}\kappa^3 + \frac{C_Y}{\lambda} \left(\sin^2 \theta - \frac{1}{2} \cos^2 \theta \right) \kappa - C_Y \cos^2 \theta = 0 \quad (4.5)$$

with boundary conditions $\theta = 0$ at $s = 0$ and $\kappa = \kappa' = 0$ at $s = 1$. This equation is independent of the mass ratio β , and depends exclusively on the Cauchy number C_Y and the slenderness parameter λ . It is similar to the large-amplitude static equation (3.21) found in Chapter 3. In the limit of infinite slenderness $\lambda \rightarrow +\infty$, we recover the model of (Gosselin et al., 2010), used in Chapter 2, based on the equilibrium between the elastic forces and the resistive drag to describe static reconfiguration. In Chapter 3 and particularly in Appendix D, we have proved that the static contribution of the reactive force $O(C_Y/\lambda)$ is negligible as soon as the slenderness $\lambda \gtrsim 10$ so that the known results for the reconfiguration in steady flow remain valid for slender structures, regardless of their actual aspect ratio, as long as the deflection remains static. However, by analogy with beams in axial flow, we expect the static shape solution of Eq. (4.5) to become unstable to some flutter instability as the flow velocity exceeds some threshold and the structure aligns with the flow.

To determine the stability threshold, we make use of Lyapunov's indirect method as advocated in Dupuis and Rousselet (1992) and applied in Lundgren et al. (1979) regarding the stability of cantilever fluid-conveying pipes with an inclined terminal nozzle. Namely, for each value of the parameters, we perform a global linear stability analysis of the dynamic governing equation (4.3) with the corresponding boundary conditions, about the stationary equilibrium solution of Eq. (4.5) for that particular set of parameters. Thus, we expand the instantaneous position vector and angle θ as

$$\mathbf{r}(s, t) = \mathbf{r}_0(s) + \xi(s, t) \boldsymbol{\tau}_0(s) + \eta(s, t) \mathbf{n}_0(s) \quad , \quad \theta(s, t) = \theta_0(s) + \delta\theta(s, t) \quad (4.6)$$

where the subscript $_0$ refers to quantities related to the stationary solution, and ξ , η and $\delta\theta$ are small-amplitude time-dependent perturbations of the same order. At the linear order, the tangential and normal vectors read

$$\boldsymbol{\tau}(s, t) = \boldsymbol{\tau}_0(s) + \delta\theta(s, t) \mathbf{n}_0(s) \quad , \quad \mathbf{n}(s, t) = \mathbf{n}_0(s) - \delta\theta(s, t) \boldsymbol{\tau}_0(s). \quad (4.7)$$

Linearisation of the inextensibility condition $\mathbf{r}' = \boldsymbol{\tau}$ provides two relations between the small variables

$$\xi' - \kappa_0 \eta = 0 \quad , \quad \delta\theta = \eta' + \kappa_0 \xi. \quad (4.8)$$

Making use of the boundary condition $\xi = 0$ at $s = 0$, we may rewrite the tangential perturbation as

$$\xi = \int_0^s \kappa_0 \eta. \quad (4.9)$$

Finally, injecting the expansion (4.6) in Eq. (4.3) and making use of (4.7), (4.8), (4.9), we obtain the governing equation for the small-amplitude normal perturbation

$$\begin{aligned} & \ddot{\eta} - (1 - \beta)\kappa_0 \int_1^s \int_0^s \kappa_0 \ddot{\eta} \\ & + 2u\sqrt{\beta} \left[S_0 \dot{\eta}' + \left(\frac{1}{2}\kappa_0 + \lambda \right) C_0 \dot{\eta} \right] \\ & + \left(\left[u^2 \left(S_0^2 - \frac{1}{2}C_0^2 \right) + \frac{5}{2}\kappa_0^2 \right] \eta' \right)' \\ & + \eta^{(4)} + \left[\frac{3}{2}(\kappa_0^2)'' + \kappa_0^4 \right] \eta \\ & + 2\lambda u^2 C_0 \left[S_0 \eta' + \frac{1}{2}C_0 \kappa_0 \eta \right] = 0 \end{aligned} \quad (4.10)$$

where the notations $C_0 = \cos \theta_0$ and $S_0 = \sin \theta_0$ have been used for brevity, and with the boundary conditions $\eta = \eta' = 0$ at $s = 0$ and $\eta'' = \eta''' = 0$ at $s = 1$. This equation is consistent with previous work on slender beams in axial flow. Indeed, for $\theta_0(s) = \pi/2$ and $\kappa_0(s) = 0$ (structure parallel to the flow in the static equilibrium configuration), Eq. (4.10) reduces to

$$\ddot{\eta} + 2u\sqrt{\beta}\dot{\eta}' + u^2\eta'' + \eta^{(4)} = 0 \quad (4.11)$$

which is the classical small-amplitude flutter equation for an undamped beam in axial flow with no friction or gravity, used for instance in Païdoussis (1998), Lemaitre et al. (2005), or Païdoussis et al. (2002).

Following de Langre et al. (2007), we then assume a perturbation of the form $\eta(s, t) = \phi(s)e^{i\omega t}$ so that Eq. (4.10) turns into the quadratic eigenvalue problem

$$\begin{aligned}
 & -\omega^2 \left[\phi - (1 - \beta)\kappa_0 \int_1^s \int_0^s \kappa_0 \phi \right] + 2iu\sqrt{\beta}\omega \left[S_0\phi' + \left(\frac{1}{2}\kappa_0 + \lambda \right) C_0\phi \right] \\
 & + \phi^{(4)} + \left(\left[u^2(S_0^2 - \frac{1}{2}C_0^2) + \frac{5}{2}\kappa_0^2 \right] \phi' \right)' + 2\lambda u^2 C_0 S_0 \phi' + \left[\frac{3}{2}(\kappa_0^2)'' + \kappa_0^4 + \lambda u^2 C_0^2 \kappa_0 \right] \phi = 0
 \end{aligned} \tag{4.12}$$

with the boundary conditions $\phi = \phi' = 0$ at $s = 0$ and $\phi'' = \phi''' = 0$ at $s = 1$.

To solve this numerically, the beam is discretized using $N = 100$ Gauss-Lobatto points $s_k = \frac{1}{2}(1 - \cos((k-1)/(N-1)\pi))$, and the derivatives and integrals are computed respectively by Chebyshev collocation and using the Clenshaw-Curtis quadrature formulae. For a given slenderness λ and mass ratio β , we first compute the static solution of Eq. (4.5) iteratively by increasing the Cauchy number from the upright case $C_Y = 0$. After each increment, we solve Eq. (4.5) with a pseudo-Newton solver (method of citepbroyden1965) using the solution at the previous step as initial guess. Then, for each value of C_Y (equivalently of u), we compute the eigenmodes $\phi(s)$ and eigenfrequencies ω by solving Eq. (4.12) with the MatLab function `quadeig` (Hammarling et al., 2013). To check convergence of the results with respect to the mesh, computations with twice the number of points $N = 200$ were conducted and led to no significant modification of the results. For instance, the static angle at the tip of the structure $\theta_0(s=1)$ (solution of Eq. (4.5)) varied by less than 10^{-10} for any Cauchy number C_Y between 10^{-1} and 10^5 and for the three values of λ considered ($10, 10^2$ or 10^3).

The stability thresholds are shown on Figure 4.2 in the $\beta-u$ plane for different values of the slenderness λ . Similarly to the axial case, the critical velocity increases with the mass ratio so making the structure heavier or the fluid lighter has a destabilizing effect. For instance, a given structure is much more likely to flap in air than in water, and neutrally buoyant structures are always stable if they are close to flat ($\beta \rightarrow 1$, situation of Chapter 3) while they lose stability between around $u \sim 16$ and 21 if they have a circular cross-section ($\beta = 0.5$). For a given mass ratio, the critical velocity depends very little on the slenderness. Therefore, it is indeed the relative magnitude of the reactive fluid force and the structural stiffness that sets the onset of flutter regardless of the magnitude of the resistive drag.

On the other hand, the same stability thresholds re-drawn in terms of the Cauchy number on Figure 4.3 are obviously shifted with respect to one another as $C_Y \propto \lambda$ for a given u . Consequently, the static equilibrium shapes at the critical velocity (also shown on Figure 4.3) are more and more deflected as slenderness is increased. Thus, we may deduce that the critical velocity does not depend on the preexisting curvature distribution in the static equilibrium shape. More importantly, we may conclude that elongation stabilizes reconfiguration. Indeed, the more slender a structure is, the larger its critical Cauchy number $C_{Y,c}$, and so the more it may reconfigure statically before

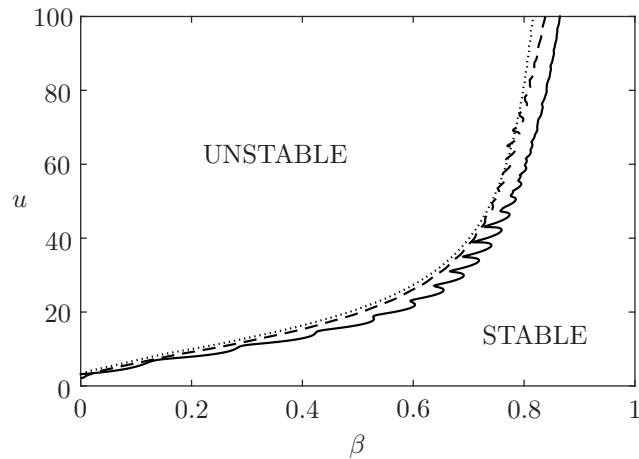


Figure 4.2: Critical velocity u_c as a function of the mass ratio β , for $\lambda = 10$ (—), $\lambda = 10^2$ (---), $\lambda = 10^3$ (···).

it loses stability and starts fluttering. Note finally that the critical Cauchy number is always much larger than 1. Consequently, flutter may only occur on highly reconfigured structures.

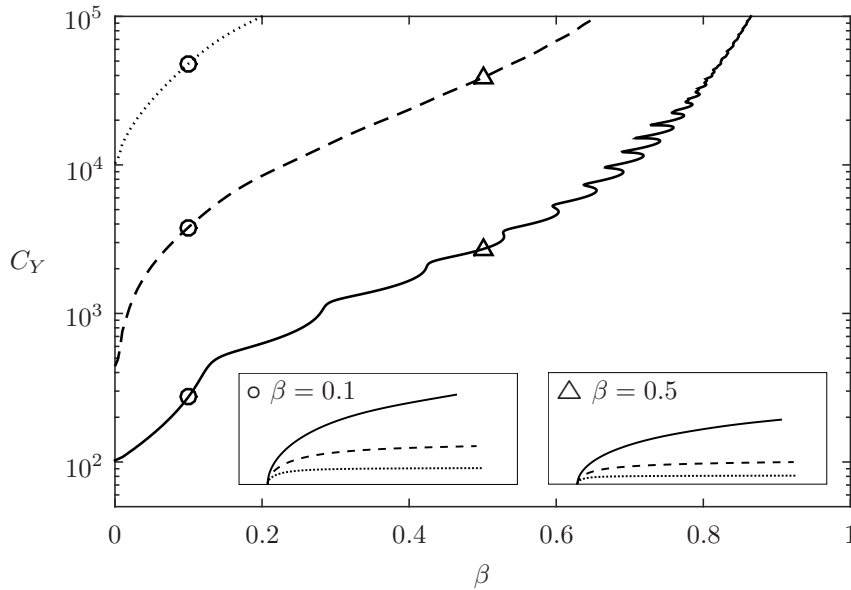


Figure 4.3: Critical Cauchy number $C_{Y,c}$ as a function of the mass ratio β and static equilibrium shape at the stability threshold for two specific values of the mass ratio, for $\lambda = 10$ (—), $\lambda = 10^2$ (---), $\lambda = 10^3$ (···).

Note that even for the most deflected cases (corresponding to $\lambda \rightarrow +\infty$) that are almost parallel to the flow, the critical velocity does not converge to that of slender beams in axial flow. This point is discussed in Appendix E.

4.4 Post-critical kinematics

When the stability threshold is exceeded, the static solution of Eq. (4.5) cannot physically exist anymore. The static reconfiguration models are not valid in the unstable domain and we ought to account for the self-triggered dynamics to properly assess the drag. In this Section, we start by analysing the kinematics that takes place in the post-critical regime in order to discuss its consequences in terms of drag in Section 4.5.

Hence, we now solve the full time-dependent non-linear equation (4.3) using a time-stepping method. The time derivatives are computed using implicit second order accurate finite differences. The time step is tuned for each case using the period T_{lin} and growth rate σ_{lin} of the most unstable eigenmode found in the linear stability analysis. It is chosen so that 100 iterations are performed over T_{lin} or $1/\sigma_{lin}$, whichever is the shortest. At $t = 0$, we combine a small contribution of the most unstable eigenmode to the static solution to initialize the system. Then, at each time step, the boundary value problem is solved with the pseudo-Newton solver used in the static case (Broyden, 1965). Computations are carried on a horizon such that $120 T_{lin}$ has passed, and the amplitude of the most unstable eigenmode would have had time to grow by a factor of 10^{10} in the linear framework, whichever lasts the longest.

4.4.1 Kinematic regimes

For the sake of clarity, let's first focus on the reference case of a neutrally buoyant circular cylinder ($\beta = 0.5$) with moderately large aspect ratio ($\lambda = 10$), before discussing the influence of varying slenderness or mass ratio in Sections 4.4.2. We analyse both the average and the extreme features of the dynamics, respectively through the standard deviation and the amplitude (defined as half of the peak-to-peak amplitude measured over the simulation horizon) of the tip vertical displacement on Figure 4.4. As is classical in flag flutter studies, three distinct regimes are identified depending on the value of u (Connell and Yue, 2007; Alben and Shelley, 2008; Alben, 2008; Michelin et al., 2008). Each regime is illustrated on Figure 4.4 for particular values of u in the thumbnails. Below the critical velocity $u_c = 16.5$, the structure is statically stable so the amplitude of flapping is null. Right above the stability threshold, periodic flapping takes place. The amplitude and standard deviation both sharply increase from zero, then decrease very slowly for increasing u . The bumpy shape of these curves is most likely associated with flapping mode switches (Alben, 2008; Michelin et al., 2008). The amplitude is continuous at the onset of the flutter, thus indicating that the instability is supercritical. Periodic flapping is observed until $u \sim 62.7$. Above that threshold, no limit cycle can be identified in most cases and the motion is generally either quasi-periodic or chaotic. In this non-periodic regime, the standard deviation of the tip displacement remains rather continuous and of the same order of magnitude as in the periodic regime. On the other hand, the amplitude of flapping measured over the simulation horizon is rather erratic, due to the random nature of the dynamics. Overall, our results indicate that

the amplitude jumps from being of the order of 0.12 to approximately 0.2. In fact, if the loss of periodicity preserves the flapping amplitude on average, it is also associated with the random occurrence of isolated, short, extreme events characterised by violent accelerations. These so-called “snapping events” have also been reported in the axial configuration (Connell and Yue, 2007; Alben and Shelley, 2008) and are known to be responsible for drag peaks probably at the origin of the tearing of flags (Virost et al., 2013). Note that, owing to the random occurrence of these peaks, their magnitude may actually depend on the horizon of the simulation. Longer simulations would allow more of the most extreme events to occur and would consequently lead most likely to a larger, and smoother amplitude. The precise features of the non-periodic dynamics such as its frequency spectrum or the probability distribution of the magnitude of the snapping events are however out of the scope of this article. Note also that regular flapping is still observed for some values of reduced velocity between $u \sim 72$ and $u \sim 93$, corresponding to the lower flapping amplitudes on Figure 4.4. These occurrences are disseminated among irregular flapping cases without a clear separation, so the boundary of the periodic regime drawn on Figure 4.4 is actually more of a threshold above which non-periodic motion is observed, but not exclusively.

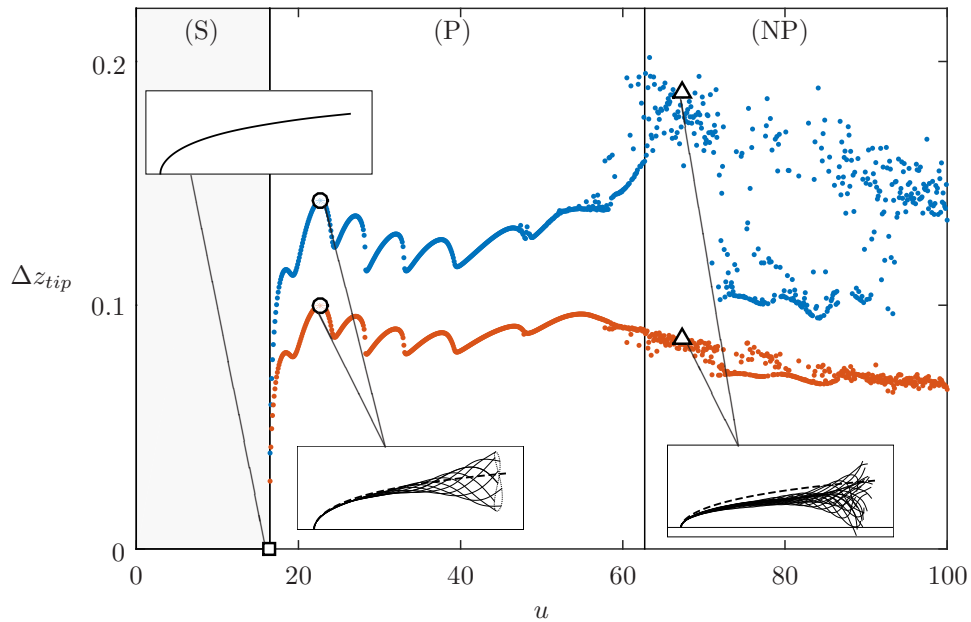


Figure 4.4: Vertical amplitude of flapping at the tip (blue) and standard deviation (orange) versus the reduced velocity u , for $\beta = 0.5$, $\lambda = 10$. Static regime (S), periodic regime (P) and non-periodic regime (NP). Examples of deformation modes are shown in the thumbnails for $u = 16.4$ (\square , static regime), $u = 22.7$ (\circ , periodic regime), $u = 67.3$ (\triangle , non-periodic regime). Static equilibrium shape superimposed (— —).

4.4.2 Influence of the slenderness and mass ratio

The kinematic regimes described above are affected if the slenderness or mass ratio are varied.

For instance, the same data as in Figure 4.4 is displayed on Figure 4.5 for a structure 100 times more elongated $\lambda = 10^3$. First, the order of magnitude of the non-dimensional amplitude of flapping is drastically decreased. Actually, it even seems that $\lambda \Delta z_{tip} = O(1)$ so that the dimensional amplitude of flapping would scale with the width of the structure, independently of its length. Similarly to the previous case, limit cycle flapping takes place above the critical velocity $u_c = 20.8$. But contrary to the previous case, the motion remains periodic for the whole range of reduced velocity tested. As u is increased, period multiplications and divisions successively take place, leading to more complex flapping dynamics illustrated in the thumbnail for $u = 78.0$ on Figure 4.5. The trajectory of the tip makes several loops within a single period of the system while it simply follows an eight-shaped trajectory in the simpler case $u = 59.0$. These flapping modes are elaborate but remain nonetheless regular and no snapping event is observed. Slenderness thus has a stabilizing effect on the non-linear dynamics as it saturates the flapping amplitude and prevents irregular motion to take place at large flow velocities.

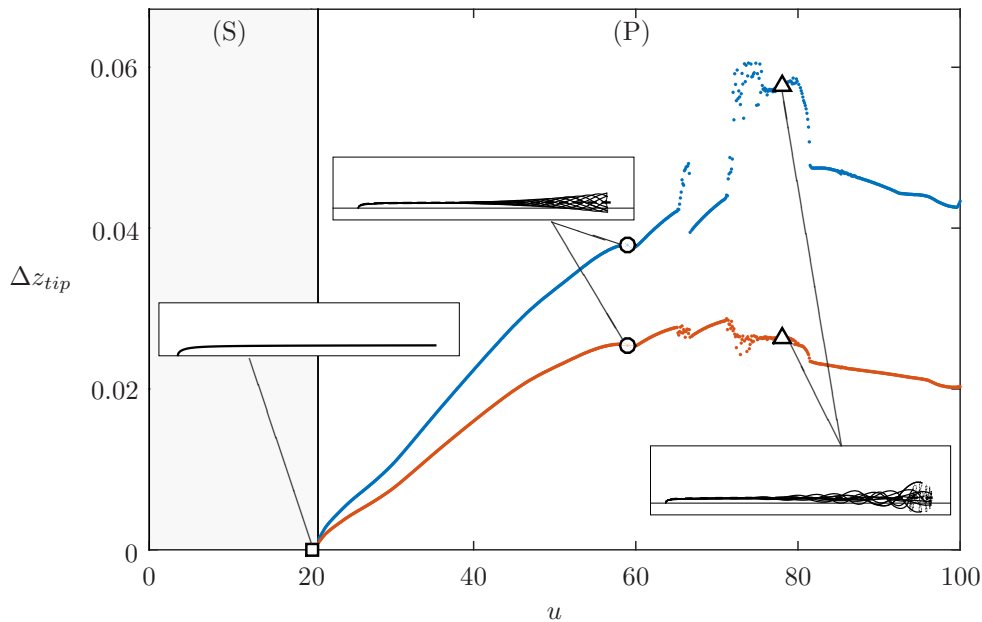


Figure 4.5: Vertical amplitude of flapping at the tip (blue) and standard deviation (orange) versus the reduced velocity u , for $\beta = 0.5$, $\lambda = 10^3$. Static regime (S) and periodic regime (P). Examples of deformation modes are shown in the thumbnails for $u = 20.0$ (\square , static regime), $u = 59.0$ (\circ , periodic regime), $u = 78.0$ (\triangle , periodic regime as well). Static equilibrium shape superimposed (— — —).

The mass ratio also has an influence on the post-critical dynamics. We show on

Figure 4.6 the case of a flat plate with smaller mass ratio $\beta = 0.1$, and moderate slenderness similar to the first situation $\lambda = 10$. Similarly to the reference case, periodic flapping is triggered right above the critical velocity $u_c = 5.24$ until periodicity is lost above some other threshold $u \sim 18.5$. The amplitude of flapping is however larger, and the domain of regular flapping is reduced. Thus, reducing the mass ratio has a destabilizing effect on the non-linear dynamics, as it enhances the flapping amplitude and favours the early transition towards irregular motion.

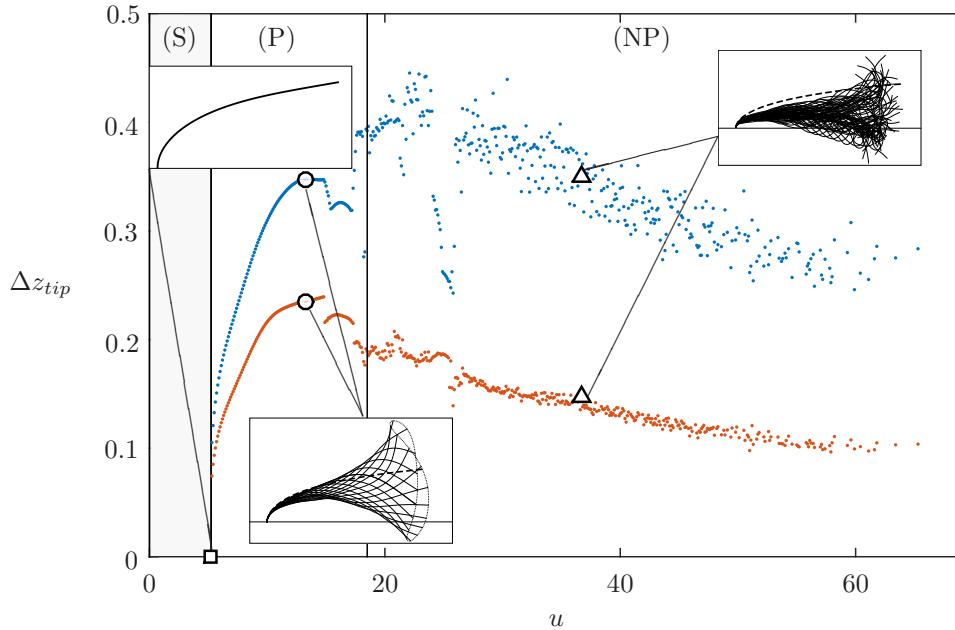


Figure 4.6: Vertical amplitude of flapping at the tip (blue) and standard deviation (orange) versus the reduced velocity u , for $\beta = 0.1$, $\lambda = 10$. Static regime (S), periodic regime (P) and non-periodic regime (NP). Examples of deformation modes are shown in the thumbnails for $u = 5.2$ (\square , static regime), $u = 13.2$ (\circ , periodic regime), $u = 36.7$ (\triangle , non-periodic regime). Static equilibrium shape superimposed (— —).

4.5 Drag reduction in the post-critical regime

The very occurrence of flutter, be it periodic or not, is known to be responsible for a significant additional drag force. Besides, its magnitude is strongly related to the amplitude of the flapping motion, but also to its regularity as the violent accelerations associated with snapping events are responsible for enhanced drag peaks (Viot et al., 2013). We thus expect the drag reduction abilities of the three structures introduced in Section 4.4 to be at least mitigated above the stability threshold. In this Section, we discuss the modulation of drag due to flexibility for the same three structures, based on the computational results of the previous Section, and in the light of the observations

regarding the post-critical kinematics.

In order to quantify drag reduction by reconfiguration, the reconfiguration number is defined in Gosselin et al. (2010) as the ratio of the drag force on the deflected structure to that on the similar but upright beam $\mathcal{R} = F/F_{rigid}$. The total drag force F is equal to the internal shear force at the base $Q(s=0) = -EI\kappa'(s=0)$, while the rigid drag is the integral of the resistive drag on the vertical structure of length L , $F_{rigid} = 1/2\rho C_D W L U^2$, so that the reconfiguration number reads in terms of the non-dimensional quantities $\mathcal{R} = -\kappa'(s=0)/C_Y$. When $\mathcal{R} < 1$, flexibility is responsible for lowering the drag, while it enhances it when $\mathcal{R} > 1$. Because the drag force F on the deflected structure is time-dependent when flutter occurs, we will focus in the following on the time-averaged and maximum values of \mathcal{R} . The variations of the maximum and average reconfiguration numbers are related respectively to that of the amplitude and standard deviation of flapping.

First, Figure 4.7 displays the variations of these two quantities with the Cauchy number C_Y in the reference case ($\beta = 0.5$, $\lambda = 10$), along with the corresponding static reconfiguration curve. The maximum and average reconfiguration numbers diverge from the static curve at the critical Cauchy number $C_{Y,c} = \lambda u_c^2 = 2.71 \times 10^3$, because of the triggering of flutter. Further increasing C_Y , the average reconfiguration number remains always larger than the static one. The self-induced dynamics is therefore responsible for an additional drag that significantly contributes to the total drag on average. However, the average reconfiguration number is decreasing with increasing C_Y so that a larger flexibility is still associated with an enhanced drag reduction above the stability threshold, on average. This trend carries on in the non-periodic regime as well as in the periodic regime. On the other hand, similarly to the flapping amplitude, the maximum drag sharply increases when periodicity is lost due to the occurrence of snapping events, as will be discussed in further details later in the low mass ratio case. But most importantly, the maximum reconfiguration number remains inferior to 1 for all values of C_Y . Therefore, no matter how large the flow velocity, the drag force remains at all times inferior to what it would be if the structure were rigid and standing upright. In other words, the additional drag due to flapping is not large enough in this case so as to completely offset the drag reduction due to reconfiguration.

This conclusion holds for more stable structures as well, such as the more slender structure ($\beta = 0.5$, $\lambda = 10^3$) of Section 4.4.2. In fact, we have shown in Section 4.4.2 that the amplitude of regular flapping is reduced compared to the reference case, so that the associated flutter-induced drag contribution is smaller. Besides, the results of Section 4.3 indicate that the instability is restricted to more deflected structures (the critical Cauchy number $C_{Y,c} = 4.33 \times 10^5$ is higher), associated with larger static drag. Consequently, the relative contribution of flutter-induced drag to the total drag is now almost negligible, and the reconfiguration numbers displayed on Figure 4.8 are almost superimposed on the static curve.

The situation of a less stable structure such as the low mass ratio plate ($\beta = 0.1$, $\lambda = 10$) of Section 4.4.2 is actually more intricate. As for the two previous cases, the average \mathcal{R} displayed on Figure 4.9 keeps decreasing slowly (or remains almost constant)

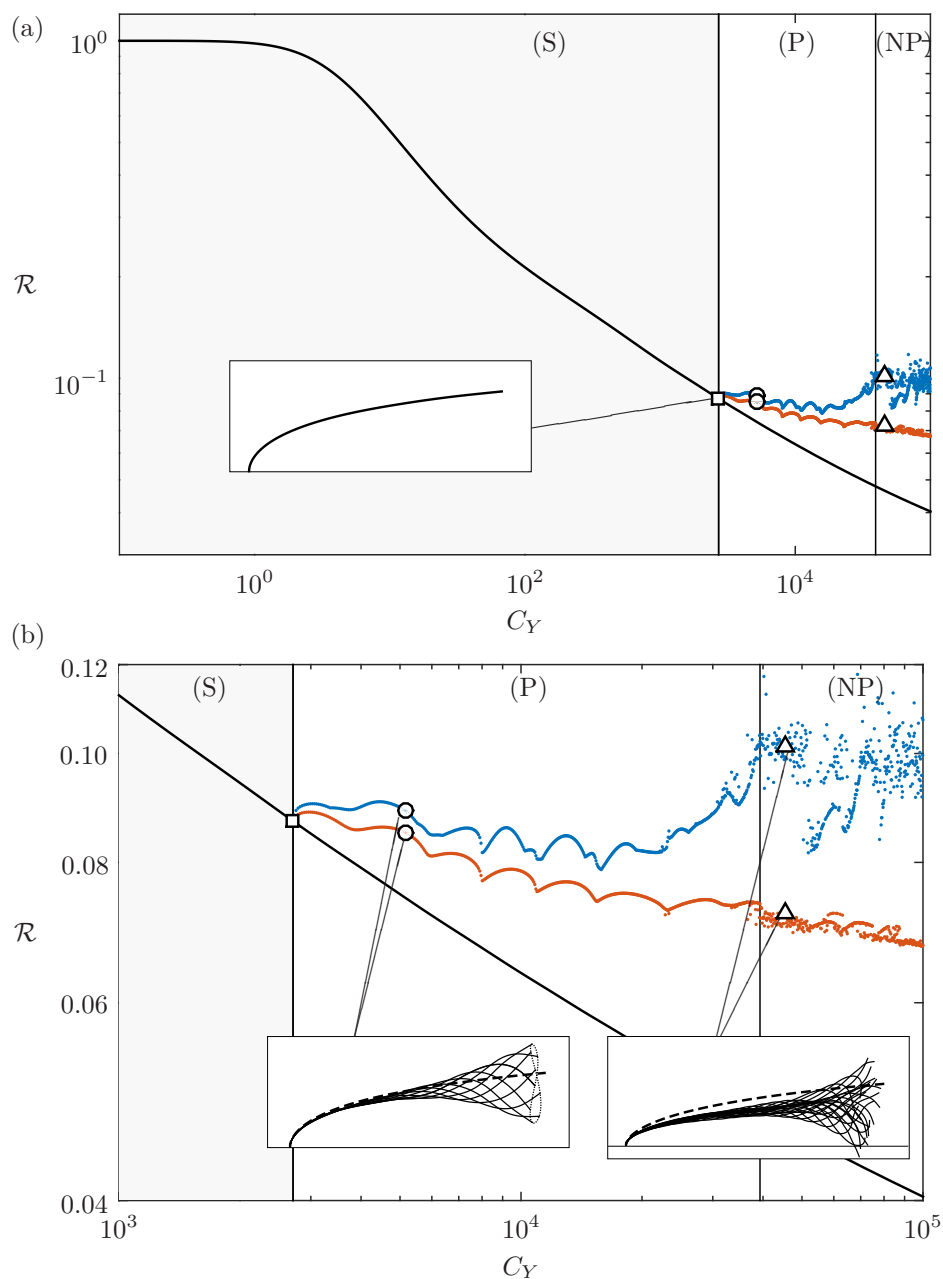


Figure 4.7: Reconfiguration number \mathcal{R} versus the Cauchy number C_Y , time average (orange) and maximum (blue), for $\beta = 0.5$, $\lambda = 10$. Static reconfiguration number (black). The same examples of deformation modes as in Figure 4.4 are shown in the thumbnails, corresponding respectively to $C_Y = 2.69 \times 10^3$ (\square , static regime), $C_Y = 5.15 \times 10^3$ (\circ , periodic regime), $C_Y = 4.53 \times 10^4$ (Δ , non-periodic regime). Static equilibrium shape superimposed (---). (b) is simply a zoom on the lower right corner of (a).

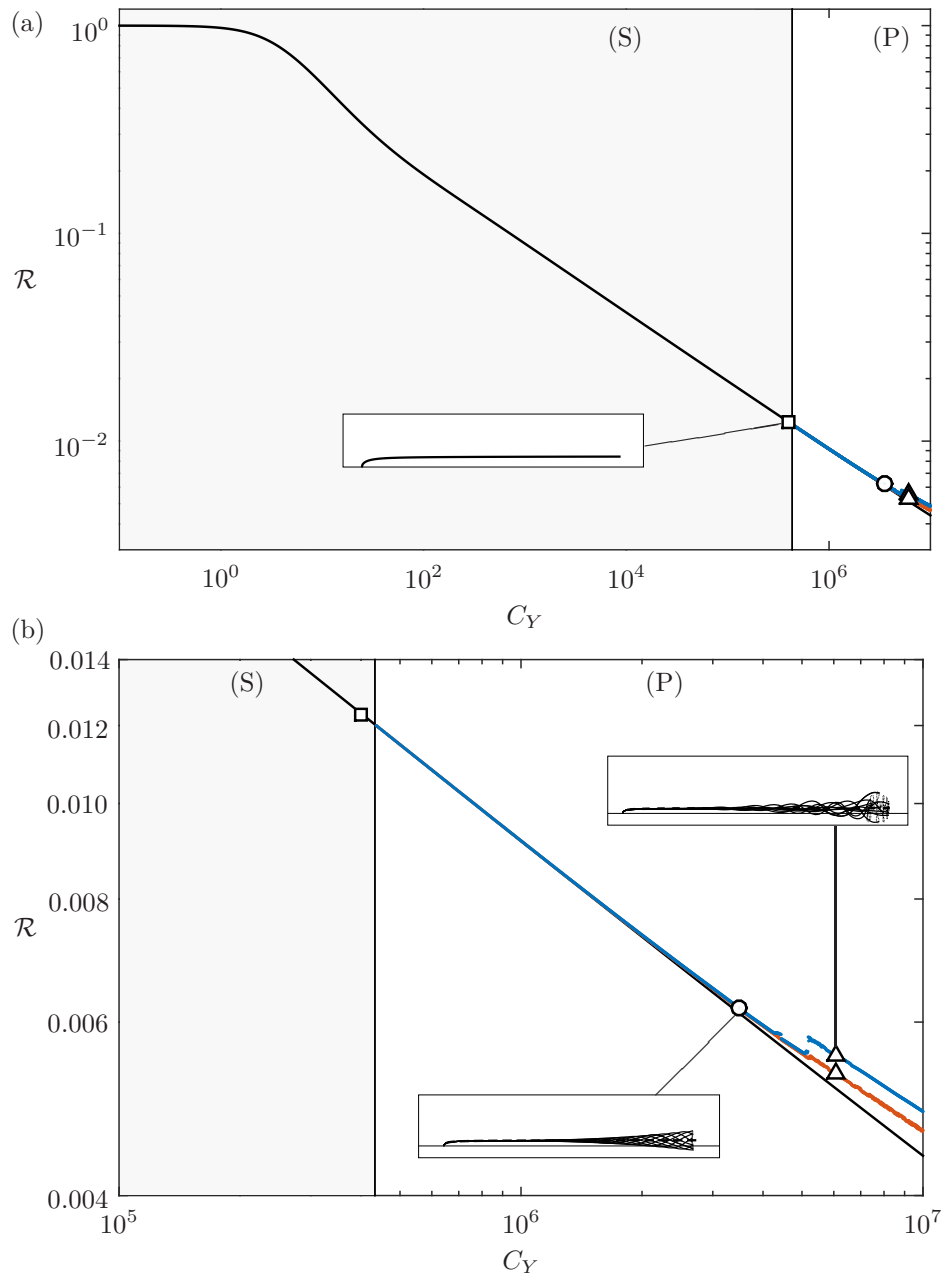


Figure 4.8: Reconfiguration number \mathcal{R} versus the Cauchy number C_Y , time average (orange) and maximum (blue), for $\beta = 0.5$, $\lambda = 10^3$. Static reconfiguration number (black). The same examples of deformation modes as in Figure 4.5 are shown in the thumbnails, corresponding respectively to $C_Y = 4.00 \times 10^5$ (\square , static regime), $C_Y = 3.48 \times 10^6$ (\circ , periodic regime), $C_Y = 6.08 \times 10^6$ (\triangle , periodic regime as well). Static equilibrium shape superimposed (---). (b) is simply a zoom on the lower right corner of (a).

above the stability threshold, regardless of the regularity of the flapping motion. Thus, a larger flexibility is still responsible for an alleviation (or at least no enhancement) of the drag on average even when flutter is triggered at an early stage of reconfiguration, when the amplitude of flapping is large, and in spite of the early loss of periodicity. On the other hand, the sharp increase of the flapping amplitude in the non-periodic regime may induce large enough flutter-induced drag forces so as to increase the total drag in excess of its static value. The maximum reconfiguration number raises above 1 in these cases, as for instance in the case $C_Y = 1.35 \times 10^4$ on Figure 4.9. The variations of \mathcal{R} through time for this case on Figure 4.10 confirm that this peak of drag is related to a very brief, rare, snapping event. If the peak value of the drag during one of those snapping events exceeds the largest load the structure may endure, flexibility may in this particular case and at this particular moment be responsible for structural failure. Nonetheless, the rareness and brevity of these events make their contribution negligible on average, and flexibility remains responsible for a large overall reduction of drag, at almost any moment, in spite of flapping.

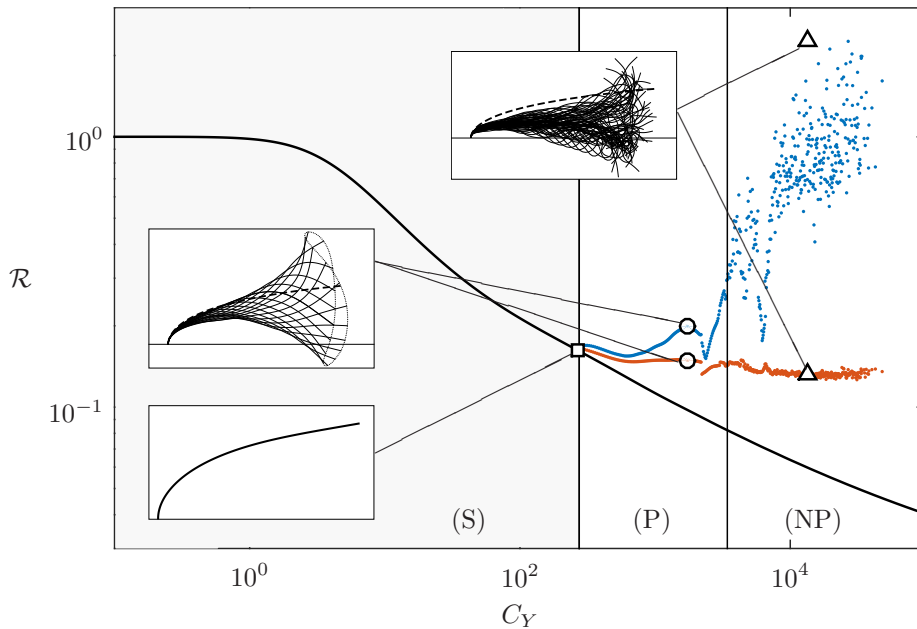


Figure 4.9: Reconfiguration number \mathcal{R} versus the Cauchy number C_Y , time average (orange) and maximum (blue), for $\beta = 0.1$, $\lambda = 10$. Static reconfiguration number (black). The same examples of deformation modes as in Figure 4.6 are shown in the thumbnails, corresponding respectively to $C_Y = 2.70 \times 10^2$ (\square , static regime), $C_Y = 1.74 \times 10^3$ (\circ , periodic regime), $C_Y = 1.35 \times 10^4$ (\triangle , non-periodic regime). Static equilibrium shape superimposed (---).

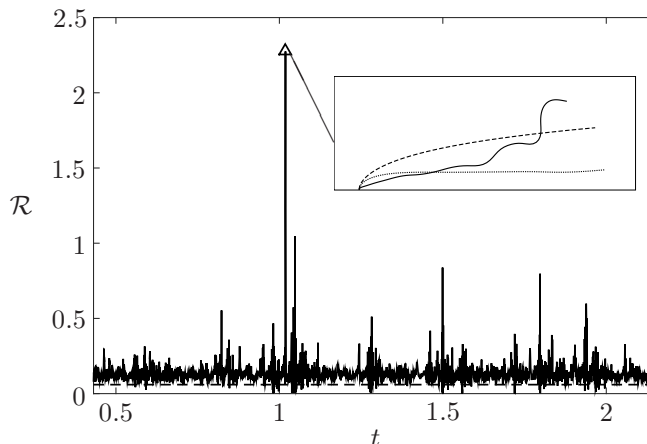


Figure 4.10: Time-series of the reconfiguration number in the non-periodic regime of case $\beta = 0.1$, $\lambda = 10$, $C_Y = 1.35 \times 10^4$ (equivalently $u = 36.7$) corresponding to the thumbnail shown on Figures 4.6 and 4.9. Level of the static reconfiguration number drawn for comparison (---). The time interval displayed corresponds to the whole simulation, apart from the transient regime. Largest snapping event at $t_{snap} = 1.019$ (\triangle). The shape of the structure at t_{snap} is shown in the thumbnail (—), along with the static shape (---) and the average shape ($\cdot \cdot \cdot$).

4.6 Conclusion

We have addressed the question of how flexibility may affect the drag of structures exposed to transverse flows, when the competing influences of reconfiguration and flutter are simultaneously considered. First, we performed a linear stability analysis to determine the domain in which dynamics comes into play. Then we performed non-linear simulations in the time domain to analyse how the occurrence of dynamics alters the total drag force in the post-critical domain.

We may finally draw the following conclusions. First, it appears that in spite of an additional flutter-induced drag contribution, the total drag of flexible structures is still reduced overall in comparison with rigid structures. Flutter may only occur when the structure reaches an advanced level of reconfiguration, so that the drag associated with the flapping motion is never large enough to fully offset the already significant reduction due to bending. Thus, flutter does not prevent drag reduction by reconfiguration.

However, the triggering of dynamics does lower the extent to which the drag of flexible structures is reduced, depending on the slenderness λ and mass ratio β of the structure. Increasing either of these parameters have a threefold stabilizing effect that tends to abate the flutter-induced contribution to drag. Firstly, both parameters are positively correlated with the stability threshold in terms of the Cauchy number $C_{Y,c}$, so the level of reconfiguration reachable before losing stability is enhanced when any of the two parameters is increased. Secondly, the amplitude of flapping is negatively correlated with β and λ , and so is the magnitude of the additional drag force. Thirdly,

both parameters have a regularizing effect on the post-critical dynamics in the sense that the larger β and λ , the larger the flow velocity may get before periodicity of the dynamics is lost. This last point is particularly important because when flapping is irregular, very large inertial forces may transiently raise the total drag in excess of the rigid value during short snapping events. In that case, flexibility may possibly be the cause of structural damage if the failure threshold is reached. But this situation may only happen for moderately slender, rather heavy structures, and only during rare and very brief occurrences. The order of magnitude of the drag remains otherwise comparable to its mean value, which is much reduced compared to the rigid case in any situation. Therefore, we may finally conclude that the ability of flexible structures to alleviate drag by reconfiguration, albeit lessened by the flapping motion, generally prevails nonetheless in spite of flutter.

Chapter 5

Reduction of the vortex-induced vibrations by reconfiguration

Preamble

So far in this thesis, we have successively considered the respective influences of the spatial variability of the system, the flow dynamics, and the self-induced dynamics on the magnitude of the flow-induced loads on flexible structures. As explained in the introductory chapter, structural dynamics may also arise due to the coupling of the structure with the vortices shed in its wake. In the case of the slender structures considered in this thesis, the interactions of the structure with the surrounding fluid are essentially local along the span, so that the effects of the wake are essentially caused by the vorticity shed in the plane of each cross-section. The vortices shed alternatively in this plane are responsible for an oscillating lift that forces the structure into transverse vibrations in the direction perpendicular to the direction of the static deflection. As mentioned in the introduction, the amplitude of the vortex-induced vibrations (VIVs) are known to scale with the diameter of the cylinder, while the large static deflection is typically of the order of its length. In the case of slender structures, the additional stress due to the VIVs is consequently likely to be small. The VIVs may nonetheless still have important consequences, because of the cyclic nature of the load that may lead to fatigue damage, but also through the magnification of the drag coefficient due to the transverse vibrations that may result in a significant increase of the drag. The point of view in this chapter is therefore slightly different from the other chapters. In the preceding chapters, the focus was on how the mechanism of reconfiguration might be affected when some additional effect (spatial variability of the system, flow-induced or self-induced dynamics) was accounted for. The aim of this chapter is conversely to assess the influence of the reconfiguration on the features of the VIVs, in order to determine whether and why the ability to reconfigure may alleviate or amplify the vibrations.

In this chapter, we still consider the same model geometry of a cantilever slender structure clamped perpendicular to the flow. However, we restrict this study to the case of a circular cross-section, and we relax the assumption of two-dimensional deformation to authorise the transverse vibrations due to the forcing by the wake.

First, we present some background elements about the specificities of the problem of the VIVs on a structure deformed by the flow, as well as a review of some existing work on the topic. We then explain how the model used throughout this thesis is adapted

to handle transverse VIVs as well. We finally discuss the consequences of the flow-induced deflection on the VIVs and identify the mechanisms at play, from the results of numerical simulations based on our reduced order modelling of the problem. We finally conclude that the primary effect of the flow-induced deflection is the inhibition of lock-in and the reduction of the vibration amplitude, as a result of the broadening of the wake excitation spectrum and of the localization of the energy transfer due to the variations induced in the normal flow profile. We also find that the curvature-induced tension is of negligible influence, but that the axial flow component may on the other hand significantly alter the dynamics owing to the destabilizing effect of the reactive force on the structural modes.

The findings of this chapter are currently being considered for publication in the *Journal of Fluids and Structures*. The paper (Leclercq and de Langre, 2018b), submitted to the journal and currently under review, is attached at the end of the thesis. Apart from a few wording differences, the paper is identical to the following chapter.

Contents

5.1	Specific background elements about vortex-induced vibrations	91
5.2	Model	93
5.2.1	Theoretical modeling	93
5.2.2	Governing equations	95
5.2.3	On the governing parameters	97
5.3	Numerical results	98
5.3.1	Wake excitation bandwidth and inhibition of single mode lock-in	98
5.3.2	Localization of the excitation and VIV mitigation	101
5.3.3	Influence of the reactive force	103
5.4	Discussion and conclusion	109

5.1 Specific background elements about vortex-induced vibrations

The vortex-induced vibrations (VIVs) of slender cylindrical structures has been a prominent subject of research for many years. Originally, a better understanding of this phenomenon was sought in the civil and marine engineering community mostly because of the damage it may cause on a number of flow-exposed structures such as buildings, power transmission lines, marine risers, towing cables, or mooring lines. For extensive reviews regarding VIVs, the reader is referred to Williamson and Govardhan (2004); Sarpkaya (2004); Williamson and Govardhan (2008); Bearman (2011); Wu et al. (2012). More recently, a renewed interest for the VIVs has arisen from the potential they bear as an alternative source of energy (Bernitsas et al., 2008).

The large majority of existing studies focus on the VIVs of straight cylinders in a variety of configurations: rigid or flexible, perpendicular to the flow or slanted, exposed to a uniform or a sheared flow. However, most of the off-shore flexible structures such as those cited above are actually greatly deformed in the direction of the flow under the effect of the free-stream. This configuration differs from the case of a straight cylinder on several aspects. First, the deflection in the plane of the free-stream of a cylinder is responsible for a curvature-induced tension inside the structure. The tensioning of the cylinder may affect its natural frequencies, and consequently its dynamic response to the wake excitation. Secondly, deflected structures are not locally perpendicular to the flow, which modifies the features of vortex shedding in the wake and the associated forces on the structure. Besides, a curved structure experiences a spanwise variation of its angle with the free-stream. Finally, the reconfiguration of the structure leads to a large axial component of the flow on the most inclined portion of the structure that may even become dominant when the deflection is significant. The consequences of some of these specificities have been individually studied, see for instance Srinil et al. (2009); Srinil (2010) for the structural effect of the curvature, Lucor and Karniadakis (2003); Facchinetti et al. (2004b); Franzini et al. (2009); Jain and Modarres-Sadeghi (2013); Bourguet et al. (2015) for the effect of the inclination, or Vandiver (1993); Chaplin et al. (2005); Trim et al. (2005); Lucor et al. (2006); Violette et al. (2010); Bourguet et al. (2013) for the effect of non-uniform normal flow profiles, but their combined effects may lead to a significant alteration of the wake-structure interaction that has not yet been fully investigated.

As a first step towards the understanding of VIVs of bent cylinders, Miliou et al. (2007) and de Vecchi et al. (2008) numerically explored the vortex shedding process in the wake of a rigid cylinder in the shape of a convex or concave quarter of a ring, when the structure is respectively fixed or forced into an oscillatory motion. Building on these results, Assi et al. (2014) and Seyed-Aghazadeh et al. (2015) experimentally investigated the free vibrations of similar structures and found that the amplitude of the oscillations is much reduced compared to the straight configuration. Two studies provided experimental observations regarding the VIVs of flexible structures about a

curvy shape: the experimental work of Zhu et al. (2016) considered the vibrations of a naturally concave-shaped cylinder subjected to a shear flow, while that of Morooka and Tsukada (2013) tested a model riser deformed in the shape of a concave catenary under the effect of a uniform free-stream. Finally, Bourguet et al. (2012) and Bourguet et al. (2015) numerically investigated the VIVs of tensioned flexible beams respectively exposed to a normal sheared flow and an inclined uniform flow. Both studies considered the influence of a small average in-line deformation and noted the transition from a mono-frequency to a multi-frequency response associated with a modification of the normal flow profile due to the bending. A reduction of the amplitude of the VIVs was also reported in Bourguet et al. (2015). At this point however, a theoretical study is still missing to clarify the consequences of flow-induced bending on the VIVs of slender cylinders in large deformations and identify the physical mechanisms at play. One may for instance wonder how the bending-induced shear in the normal flow might impact the vibration spectrum, whether lock-in may or may not still occur, or furthermore how the amplitude of vibration might be affected?

But the flow-induced bending of the structure may have even more dramatic consequences. Indeed, slender structures in axial flows are liable to a flutter instability (Datta and Gottenberg, 1975; Yadykin et al., 2001; Païdoussis et al., 2002; Semler et al., 2002). This self-induced dynamics results from the destabilizing effect of the inviscid pressure forces associated with the deformation of the structure in a free-stream with a significant axial component (Eloy et al., 2007; Singh et al., 2012a). When a cylinder deflects in a transverse flow, the increasing spanwise component of the free-stream may thus be the cause of such instability. More generally, the influence of the inviscid pressure forces on the structural modes may have consequences on the vortex-induced dynamics even in a domain of the parameter space where the system does not flutter.

The purpose of the present chapter is to provide an analysis of the small-amplitude vibrations of slender cylinders bent by the flow by means of reduced order models to identify the physical mechanisms at play. In particular, a formulation of the inviscid pressure forces based on Lighthill's large-amplitude elongated body theory (Lighthill, 1971) will be used to account for the destabilizing effect of the axial component of the free-stream. We will also make use of a wake oscillator to describe the lift resulting from vortex shedding. This class of models was originally derived to represent the dynamics of the free wake behind a fixed structure (Birkhoff and Zarantonello, 1957; Bishop and Hassan, 1964), and they have been proved able to capture some characteristic features of the vortex shedding mechanism, such as the formation of cells in shear flow (Noack et al., 1991; Mathelin and de Langre, 2005). Such models have also been proved useful in qualitatively describing the physics of VIVs when coupled with a structural oscillator (Hartlen and Currie, 1970; Skop and Balasubramanian, 1997; Balasubramanian et al., 2000; Mukundan et al., 2009; Srinil and Zanganeh, 2012), and they have been validated against experimental and numerical results (Violette et al., 2007). In this regard, the work of Facchinetti et al. (2004a) demonstrated that features such as the boundaries of the lock-in range, the amplitude of the vibrations or the phase between the structure and the wake are correctly predicted when a coupling term proportional to the structural

acceleration is used. The subsequent work of de Langre (2006) and Violette et al. (2010) further demonstrated that many features of the nonlinear limit-cycle dynamics can be interpreted through the linear analysis of the coupled wake-structure oscillators.

In Section 2, the model for the flow-structure interactions and its specific adaptations to the problem in question are detailed. The consequences of the flow-induced bending on the VIVs are then discussed in Section 3 based on the results of numerical simulations.

5.2 Model

5.2.1 Theoretical modeling

We consider the model system represented on Fig. 5.1. A circular cylinder of length L , diameter D and mass per unit length m is clamped perpendicular to a uniform and steady flow of velocity $U\mathbf{e}_x$ of a fluid of density ρ . As in the preceding chapters, we assume the cylinder is slender ($D \ll L$) and we model it as an inextensible Euler-Bernoulli beam of bending stiffness EI (see more details about the structural model in Appendix F.1.1). In this chapter we focus on the small-amplitude transverse oscillations so we consider that the structure is primarily deflected in the xz -plane under the effect of the flow into a leading order configuration $\mathbf{r}_0(s)$ (broken black line on Fig. 5.1, specifically shown on Fig. 5.1(c)). Vortex shedding in the wake of the bent structure is then responsible for an oscillatory lift force in the y -direction that induces small-amplitude transverse vibrations (solid grey line on Fig. 5.1, specifically shown on Fig. 5.1(d)) such that $\mathbf{r}(s, t) = \mathbf{r}_0(s) + Y(s, t)\mathbf{e}_y$.

Here again, we disregard the influence of gravity and buoyancy, and we restrict our study to large Reynolds number flows so that friction forces are neglected. Following Mukundan et al. (2009) and Violette et al. (2010), we model the effect of the fluid as the combination of three load distributions along the span $\mathbf{p} = \mathbf{p}_{am} + \mathbf{p}_d + \mathbf{p}_w$, where \mathbf{p}_{am} and \mathbf{p}_d are respectively the reactive and resistive terms used in the preceding chapters, and \mathbf{p}_w is the additional oscillating lift force due to the vorticity wake. The expressions of these forces involve the projections (U_τ, U_N) on the direction tangent to the structure and on the plane normal to it, of the relative velocity between the cylinder and the fluid $\mathbf{U}_{rel} = \dot{Y}\mathbf{e}_y - U\mathbf{e}_x = U_\tau\boldsymbol{\tau} + U_N\mathbf{N}$, where the overdot still stands for time differentiation. Note that, contrary to the previous chapters, the direction of the normal component of the flow is noted with an upper case \mathbf{N} . This is so to emphasize the difference with the lower case vector \mathbf{n} used in Appendix F.1, which is materially attached to the structure. The upper case vector \mathbf{N} is not materially attached to the structure, but is defined as the direction of the projection of the relative velocity \mathbf{U}_{rel} on the plane orthogonal to the axis of the structure $\boldsymbol{\tau}$. In the previous chapters where the deformation was contained in a plane, the two definitions were strictly equivalent, but the three dimensionality of the deformation in this chapter now creates a distinction between the two directions (see Appendix F.1).

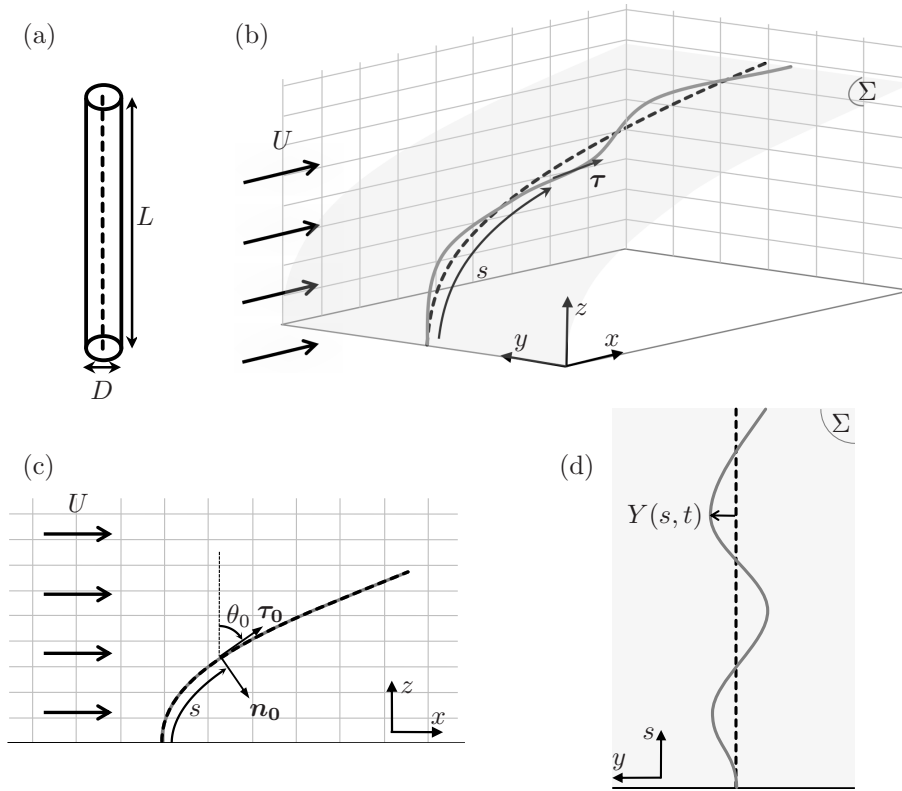


Figure 5.1: (a) Dimensions of the undeformed cylinder and centerline (broken line). (b) 3D view of the centerline of the vibrating cylinder, static deflection $\mathbf{r}_0(s)$ (broken black line), fully deformed shape $\mathbf{r}(s, t)$ (solid grey line). The π -plane in grey indicates the surface upon which the vibration occurs. (c) Projection of the deformation on the plane of static deflection (xz -plane). (d) Projection of the deformation on the surface of vibration (π -surface or sy -surface).

Firstly, in the case of an elongated body such as those considered in this study, the expression of the added mass force for large-amplitude 3D motions reads (Candelier et al., 2011)

$$\mathbf{p}_{am} = -m_a \left[\partial_t(U_N \mathbf{N}) - \partial_s(U_\tau U_N \mathbf{N}) + \frac{1}{2} \partial_s(U_N^2 \boldsymbol{\tau}) \right] \quad (5.1)$$

with the added mass $m_a = 1/4\rho\pi D^2$. This expression differs from the usual added mass force used in VIV studies because it is designed to account for the effects of the curvature as well as a large axial flow component. The additional terms thus introduced cancel in the specific case of a straight structure so this choice is nonetheless consistent with the usual expression used in previous works on the topic.

Secondly, in this three dimensional case, we express the resistive drag force following Taylor (1952) as

$$\mathbf{p}_d = -\frac{1}{2}\rho C_D D |U_N| U_N \mathbf{N} \quad (5.2)$$

with C_D the cross-section drag coefficient. Due to the transverse vibrations, this coefficient may be dynamically enhanced by an amplitude-dependent factor classically of the order of 2 (Vandiver, 1983; Blevins, 1990; Chaplin et al., 2005). The exact value of the drag coefficient should however have only a limited impact on the qualitative features of the VIVs. For the sake of simplicity, we hereafter take $C_D = 2$ for a vibrating cylinder (Blevins, 1990; Chaplin et al., 2005; Mathelin and de Langre, 2005). This term is responsible for the leading order static deflection of the beam in the xz -plane (see Gosselin et al. 2010 and previous chapters) and acts here also as hydrodynamic damping for the transverse vibrations.

Finally, following Antoine et al. (2016) the local effect of vortex shedding is modeled as an oscillating lift force orthogonal to the cylinder axis and to the component of the free-stream normal to the still cylinder

$$\mathbf{p}_w = \frac{1}{4}\rho C_L^0 D U^2 \cos^2 \theta_0 q \mathbf{e}_y \quad (5.3)$$

where the fixed cylinder lift coefficient C_L^0 is multiplied by a local magnification factor $q(s, t)$ that satisfies a nonlinear Van der Pol equation forced by the transverse acceleration of the structure

$$\ddot{q} + \varepsilon \left(2\pi \frac{S_t U}{D} \cos \theta_0 \right) (q^2 - 1) \dot{q} + \left(2\pi \frac{S_t U}{D} \cos \theta_0 \right)^2 q = A \frac{\ddot{Y}}{D}. \quad (5.4)$$

We assume in this study the classical values $S_t = 0.2$, $C_L^0 = 0.3$ in the sub-critical range $300 < R_e < 1.5 \times 10^5$ (Blevins, 1990; Facchinetti et al., 2004a). Following Facchinetti et al. (2004a), we further assume $A = 12$, $\varepsilon = 0.3$. Even though these parameters were derived from experiments on rigid cylinders, this approach was validated in the case of flexible structures in Facchinetti et al. (2004b) and Violette et al. (2007). It was then successfully used in subsequent theoretical studies (Mathelin and de Langre, 2005; Violette et al., 2010; Meng and Chen, 2012; Dai et al., 2013, 2014). No direct spanwise coupling between the wake oscillators is considered in Eq. (5.4) as the work of Mathelin and de Langre (2005) has demonstrated that the coupling with the structural oscillator is the main source of synchronisation in the wake. Similar observations have been reported by de Vecchi et al. (2008) from direct numerical simulations that showed parallel vortex shedding in the wake of a curved cylinder in forced oscillations, in contrast with the spanwise phase shift reported by Miliou et al. (2007) in the wake behind a fixed cylinder. Moreover, this local modeling is based on the so-called *independence principle* that states that the physics of vortex shedding is primarily governed by the component of the free-stream normal to the structure only (see Lucor and Karniadakis, 2003; Franzini et al., 2009; Jain and Modarres-Sadeghi, 2013). The work of Bourguet et al. (2015) has demonstrated the validity of that principle when applied locally at each location along the span in the case of the VIVs of flexible cylinders inclined at

60° of incidence. In this case, due to the in-line deformation of the structure, the local incidence of the cylinder could reach values as large as 75°. The local lift force (5.3) is thus taken quadratic in the locally normal projection of the free-stream velocity $U \cos \theta_0$ and the local natural shedding frequency that appears in (5.4) satisfies the Strouhal law expressed in terms of that normal component as well $f_w = S_t U \cos \theta_0 / D$ (Williamson, 1996; Facchinetti et al., 2004b).

Note that vortex shedding in the wake is also responsible for an oscillating drag term that creates slight temporal variations of the in-line deflection. Besides, recent studies have shown that the coupling between the in-line and transverse vibrations may considerably affect the transverse dynamics (Jauvtis and Williamson, 2003, 2004; Marcollo and Hinwood, 2006; Srinil and Zanganeh, 2012; Srinil et al., 2013). However, for the sake of simplicity and given the leading-order nature of the resistive drag term considered here, we choose to disregard the influence of the in-line fluctuations in this study.

5.2.2 Governing equations

We non-dimensionalize all variables but the transverse displacement using the length L of the cylinder as characteristic length, and the inverse of the natural shedding frequency on the undeformed straight cylinder $f_w^0 = S_t U / D$ as characteristic time scale. Because the amplitude of the VIVs classically scales with the diameter of the structure, we non-dimensionalize the transverse displacement Y using D instead of L . We also define the following non-dimensional parameters: the Cauchy number C_Y , the reduced velocity v , the aspect ratio Λ , the mass ratio β

$$C_Y = \frac{\rho C_D D U^2 L^3}{2EI} \quad , \quad v = \frac{S_t U}{D} L^2 \sqrt{\frac{m + m_a}{EI}} \quad , \quad \Lambda = \frac{L}{D} \quad , \quad \beta = \frac{m_a}{m + m_a} \quad (5.5)$$

and rescaled drag and lift coefficients $c_d = 2C_D / \pi$ and $c_l = C_L^0 / \pi$. This definition of the Cauchy number is classical in studies of the static deflection of slender structures (Gosselin et al., 2010; Hassani et al., 2016) and consistent with the previous chapters. Note that the reduced velocity used here is different from that used in Chapter 4. The present formulation is consistent with the classical definition used in VIV studies of systems with only one degree of freedom (see for instance Khalak and Williamson, 1999; Païdoussis et al., 2010), in the sense that it compares the characteristic scale of the natural period of the structure $T_s = L^2 \sqrt{(m + m_a) / EI}$ to the reference vortex shedding period $1 / f_w^0 = D / S_t U$. The mass ratio β is on the other hand similar to that used in Chapter 4, while the aspect ratio Λ is related to the slenderness parameter λ used in Chapters 3 and 4 by $\lambda = c_d \Lambda$. The proper linearization of the model presented in Section 5.2.1 is detailed in Appendix F.1, and its appropriateness for the modelling of VIVs is discussed in Appendix F.2. In terms of the non-dimensional variables, the governing equation for the leading order static deflection in the xz -plane then reads

$$\kappa_0'' + \frac{1}{2}\kappa_0^3 + \frac{C_Y}{c_d\Lambda} \left(S_0^2 - \frac{1}{2}C_0^2 \right) \kappa_0 - C_Y C_0^2 = 0 \quad (5.6)$$

where the prime notation stands for curvilinear differentiation, the notations $S_0 = \sin \theta_0$ and $C_0 = \cos \theta_0$ have been used for brevity, and with the curvature $\kappa_0 = \theta_0'$. The corresponding boundary conditions are $\theta_0 = 0$ at the clamped edge $s = 0$ and $\kappa_0 = \kappa_0' = 0$ at the free tip $s = 1$. This equation is the same as the large-amplitude equation (3.21) of Chapter 3 in the regime of static reconfiguration, and the static equilibrium equation (4.5) of Chapter 4. At the linear order, the equation for the non-dimensional transverse vibration $Y(s, t)$ is

$$\begin{aligned} v^2 \ddot{Y} + \frac{\beta v^2}{S_t \Lambda} \left[2S_0 \dot{Y}' + C_0 (\kappa_0 + c_d \Lambda) \dot{Y} \right] \\ + \left(\left[\frac{\beta v^2}{S_t^2 \Lambda^2} \left(S_0^2 + \frac{1}{2} C_0^2 \right) + \frac{3}{2} \kappa_0^2 \right] Y' \right)' + c_d \frac{\beta v^2}{S_t^2 \Lambda} C_0 S_0 Y' + Y^{(4)} = c_l \frac{\beta v^2}{S_t^2} C_0^2 q \end{aligned} \quad (5.7)$$

with $Y = Y' = 0$ at the clamped edge $s = 0$ and $Y'' = Y''' = 0$ at the free tip $s = 1$. The lift magnification factor $q(s, t)$ then satisfies the Van der Pol equation

$$\ddot{q} + \varepsilon (2\pi C_0) (q^2 - 1) \dot{q} + (2\pi C_0)^2 q = A \ddot{Y}. \quad (5.8)$$

5.2.3 On the governing parameters

Within the four non-dimensional parameters defined above (C_Y, v, Λ, β), only three are necessary to fully characterize the problem. In fact, for a given structure with a fixed mass and aspect ratios, the Cauchy number and the reduced velocity are redundant parameters that are related by $C_Y = (c_d \beta / S_t^2 \Lambda) v^2$. Both quantities scale the influence of the flow to the rigidity of the structure, but from different perspectives. The Cauchy number expresses the ratio between the leading order drag force and the restoring structural stiffness (Tickner and Sacks, 1969; Chakrabarti, 2002; de Langre, 2008). Consequently, it controls the level of static deflection in the xz -plane. For small $C_Y < 1$, deflection is negligible and the structure stands upright in the flow, while for $C_Y \gg 1$ the cylinder is highly deformed in the direction of the free-stream (Gosselin et al., 2010). On the other hand, the reduced velocity compares the natural shedding frequency f_w^0 (on the straight structure) to the scale of the natural period of the structure T_s , so it controls the dynamic behaviour of the coupled wake-structure system.

The mass ratio β represents the amount of fluid inertia within the total inertia of the system. We do not expect the precise value of β should significantly influence the qualitative features of the VIVs presented in this chapter. We also expect the influence of the gravity and buoyancy forces on the static deflection due to the flow to remain small (Luhar and Nepf, 2011). Thus, for the sake of simplicity, we restrict this study to the case of a neutrally buoyant cylinder $\beta = 0.5$. Finally, as was shown in Chapter

3 and 4, the aspect ratio $\Lambda = L/D$ scales the relative contributions of the resistive and reactive terms. In the case of slender structures $\Lambda \gg 1$ as those considered in this thesis, the contribution of the reactive force $O(C_Y/\Lambda)$ to the static equilibrium shape in Eq. (5.6) has been proved negligible (see Chapter 3 and Appendix D). On the other hand, Chapter 4 has proved that the reactive force may be responsible for triggering a large-amplitude flutter instability in the xz -plane. As will be shown in Section 5.3.3, the same flutter instability may also be initiated in the transverse y -direction, and its influence on the vortex-induced dynamics may be significant near the critical threshold when the deflection is large. Thus we may not neglect a priori the terms originating from the reactive force in Eq. (5.7).

Our main interest in this study is the effect of the flow-induced bending on the properties of the vortex-induced vibrations. In other words, we wish to compare the dynamics of structures with varying levels of deflection in the direction of the free-stream (varying Cauchy numbers C_Y), at a given reduced velocity v . However, as explained above, for a given fluid-structure system of fixed mass and aspect ratios (β, Λ) , the Cauchy number and the reduced velocity vary together as $C_Y \propto \beta v^2/\Lambda$. Therefore, increasing the Cauchy number *with a fixed reduced velocity* requires to change the structure to *lower* the aspect ratio Λ . This may seem counter-intuitive, as a lower aspect ratio is classically associated with lower deflections. Indeed, the Cauchy number is an increasing function of the aspect ratio $C_Y \propto \Lambda^3$ when the dimensional flow velocity, fluid density, and Young's modulus of the solid material are kept constant. In our case however, we allow these dimensional quantities to vary in order to keep the reduced velocity v constant instead, and consequently the Cauchy number becomes a decreasing function of the aspect ratio. In the limit of an infinitely slender structure $\Lambda \rightarrow +\infty$, the Cauchy number remains much smaller than 1 even for arbitrarily large reduced velocities. This asymptotic case is therefore equivalent to considering a structure that remains straight in the free-stream. For this benchmark case, the dynamic system (5.7)-(5.8) reduces to

$$v^2 \ddot{Y} + c_d \frac{\beta v^2}{S_t} \dot{Y} + Y^{(4)} = c_l \frac{\beta v^2}{S_t^2} q \quad (5.9)$$

$$\ddot{q} + \varepsilon (2\pi) (q^2 - 1) \dot{q} + (2\pi)^2 q = A \ddot{Y} \quad (5.10)$$

which is the standard system of equations for the modeling of VIVs by means of a wake oscillator, in the case of a straight slender cylinder with flexural stiffness and hydrodynamic damping (Mukundan et al., 2009).

5.3 Numerical results

In order to analyse the vibration behaviour, we solve the problem defined by equations (5.6),(5.7),(5.8) numerically. The beam is discretized using $N = 100$ Gauss-Lobatto

points $s_k = \frac{1}{2}(1 - \cos((k-1)/(N-1)\pi))$, and the curvilinear derivatives are computed by Chebyshev collocation. For a given aspect ratio Λ , we first compute the static solution of Eq. (5.6) iteratively by increasing the Cauchy number from the upright case $C_Y = 0$. After each increment, we solve Eq. (5.6) with a pseudo-Newton solver (method of Broyden, 1965) using the solution at the previous step as initial guess. Then, for each value of C_Y (corresponding to a given v), we solve the nonlinear system (5.7)-(5.8) using a time-stepping method, with time step $dt = 10^{-2}$. The time derivatives are computed using implicit second order accurate finite differences. At each time step, the nonlinear boundary value problem involving the unknown spanwise distributions (Y, q) is solved thanks to the pseudo-Newton solver. The simulations are run for 200 periods and the last 100 periods are considered for the analysis in order to cut the transient.

5.3.1 Wake excitation bandwidth and inhibition of single mode lock-in

First, we discuss the influence of the deflection on the modal content of the dynamics. To do so, we compare the vibrations of a structure that bends (finite aspect ratio $\Lambda = 10^3$) to that of a structure that remains straight ($\Lambda \rightarrow +\infty$), on the same range of reduced velocities. For the structure with finite aspect ratio $\Lambda = 10^3$, the variations of v within the range considered will be associated with variations in the Cauchy number $C_Y \propto v^2/\Lambda$ leading to varying levels of deflections. On the other hand, the infinitely slender cylinder will remain straight because the Cauchy number will remain asymptotically small in the same finite range of v . We recall here that the cylinder with the finite aspect ratio is the one that deflects while the infinitely slender one remains unbent because we compare the dynamics of the two structures *on the same range of reduced velocities* (see Section 5.2.3 for more details).

As explained in Section 5.2.1, the independence principle states that the natural frequency of vortex shedding $f_w(s)$ decreases along the span when the structure is deformed because of the projection of the free-stream on the normal direction $f_w(s)/f_w^0 = U_{n0}/U = \cos \theta_0(s)$. The deforming structure is therefore subjected to a forcing by the wake on a continuum of frequencies that broadens when the deflection is enhanced with increasing Cauchy numbers, as shown on Fig. 5.2.

The enrichment of the excitation spectrum significantly alters the modal content of the response. This is illustrated on Fig. 5.3 for the vibration spectrum and Fig. 5.4 for the spanwise localization of the vibration. In the straight case, the structure is subject to a forcing by the wake at a single frequency along the whole span. The frequency of the vibration remains close to the Strouhal law ($f \simeq 1$ on Fig. 5.3(a)), but slightly deviates to follow an evolution closer to that of the nearest structural mode. As v varies, lock-in with the successive structural modes occurs in turn and frequency discontinuities mark the transitions between consecutive lock-ins. This phenomenon is a well-known feature of the VIVs of flexible structures perpendicular to the flow (King, 1995; Chaplin et al., 2005; Violette et al., 2010). As expected, this behaviour remains unchanged for as long as the deflection is negligible ($C_Y < 1$ on Fig. 5.3(b)) in the case

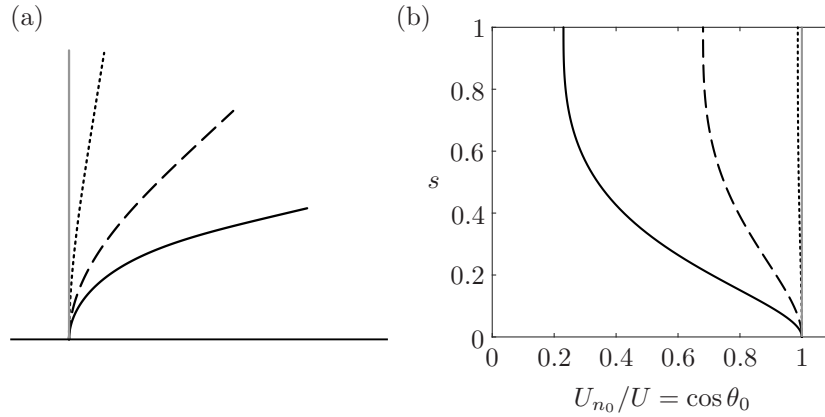


Figure 5.2: (a) Deflection in the xz -plane and (b) normal velocity profile normalized by the horizontal velocity, in the straight case (grey —), and in deflected cases $C_Y = 10^0$ ($\cdot \cdot \cdot$), $C_Y = 10^1$ ($- - -$), and $C_Y = 10^2$ (black —) for $\Lambda = 10^3$.

$\Lambda = 10^3$. However, at the early stages of reconfiguration ($C_Y \lesssim 10^1$ on Fig. 5.3(b)), the ranges of reduced velocities within which lock-in with a given mode occurs are slightly widened and increasingly shifted towards larger reduced velocities (see Table 5.1). For instance, lock-in with mode 4 persists on a slightly larger range $v \in [16.3, 29.9]$ when the structure is bent compared to $v \in [15.2, 27.0]$ when it is not. The modal shapes in both configurations remain on the other hand almost identical, as illustrated for $v = 19.8$ in Fig. 5.4(c), which proves that the curvature of the structure in the xz -plane only has a very limited impact on the eigenmodes.

Following the method of Violette et al. (2010), we may interpret these results by comparing the spectrum of the nonlinear dynamics to the frequencies of the eigenmodes found by a linear stability analysis (see Fig. 5.5). The details of the linear stability analysis can be found in Appendix G.1. The eigenmodes thus found can be classified in 3 distinct types. Firstly, a series of N unstable modes (where N is the number of discretization points s_k) with eigenvalues matching almost exactly the eigenvalues of the linearized wake oscillator without structural coupling $\omega_k \simeq \cos \theta_0(s_k)(2\pi\sqrt{1 - (\varepsilon/2)^2} - i\pi\varepsilon)$ are observed. They have no significant structural component ($\phi_k(s) \simeq 0$), and their wake components are localized respectively at each discretization point ($|\psi_k(s)| \simeq \delta(s - s_k)$ with δ the Dirac function). These modes thus correspond to the naturally unstable free wake modes. For the sake of clarity, the continuous spectrum of the free wake oscillator itself is represented in grey on Fig. 5.5(b) instead of the N individual eigenmodes spanning the area. Secondly, the modes in blue correspond closely to the eigenmodes of the structural equation (5.7) without coupling with the wake. These modes may thus be designated as the free structural modes. Finally, the four modes in black are coupled modes that each arise from lock-in with one of the structural modes. They are all unconditionally unstable and will be referred to as the lock-in modes. Following Violette et al. (2010), we expect lock-in with a given mode to persist in the nonlinear limit-cycle if the corresponding linear lock-in mode is the most unstable.

The comparison of the linear and nonlinear lock-in ranges in Table 5.1 confirms these findings and we may thus lean on the linear analysis to interpret the dynamics observed in the limit-cycle. In particular, as deflection increases, we notice on Fig. 5.5 that the broadening of the free wake spectrum allows the structural frequencies to remain within the excitation bandwidth on a larger range of reduced velocities. Lock-in with these modes may consequently occur on these larger ranges as well. Hence, it appears that the primary consequence of the deflection is the broadening of the free wake spectrum due to the increased shear in the normal component of the free-stream. At leading order, a bending structure in a uniform flow is therefore equivalent to a straight structure in a sheared flow whose profile varies, depending on the Cauchy number, according to that of the normal flow shown on Fig. 5.2(b).

	straight case (nonlinear)	bent case $\Lambda = 10^3$ (nonlinear)	bent case $\Lambda = 10^3$ (linear)
mode 1	0 – 2.3	0 – 2.3	0 – 2.16
mode 2	2.4 – 6.8	2.4 – 6.9	2.16 – 6.80
mode 3	6.9 – 15.1	7 – 16.2	6.80 – 15.86
mode 4	15.2 – 27.0	16.3 – 29.9	15.86 – 28.70

Table 5.1: Reduced velocity ranges for lock-in in the straight and bent cases (nonlinear and linear ranges).

When bending is more pronounced ($C_Y > 10^1$), not only one but several frequencies are involved in the spectrum of the nonlinear limit-cycle Fig. 5.3(b), and the localization of the transverse vibration significantly deviates from the single-mode shape on Fig. 5.4. Indeed, when the wake spectrum becomes large enough, several structural modes are excited simultaneously at different locations along the span (several structural modes appear within the wake excitation bandwidth on Fig. 5.5). Consequently, single mode lock-in is replaced by a multi-frequency response of the whole structure associated with the spatial fragmentation of the wake into multiple cells of locally uniform frequency. As illustrated on Fig. 5.6, the frequency within each wake cell matches that of the structural mode that is closest (in the frequency space) from the Strouhal law, so that it might be said that single mode lock-in is actually replaced by multiple occurrences of lock-in along the span. It is however noteworthy that the local wake dynamics is essentially monochromatic, while the structural dynamics involves comparable contributions from all the excited modes at any location along the span. Besides, the linear analysis shows that, past $v > 28.7$, the most unstable mode is not one of the coupled lock-in modes anymore, but is found instead within one of the free wake modes. No fifth coupled mode that would appear because of lock-in with the fifth structural mode is observed. It thus appears that the large shear in the normal flow hinders single mode lock-in, but leads to the simultaneous excitation of multiple structural modes that all participate in the dynamics.

We may finally conclude that bending primarily affects the dynamics through its influence on the component of the free-stream normal to the cylinder. More specifically,

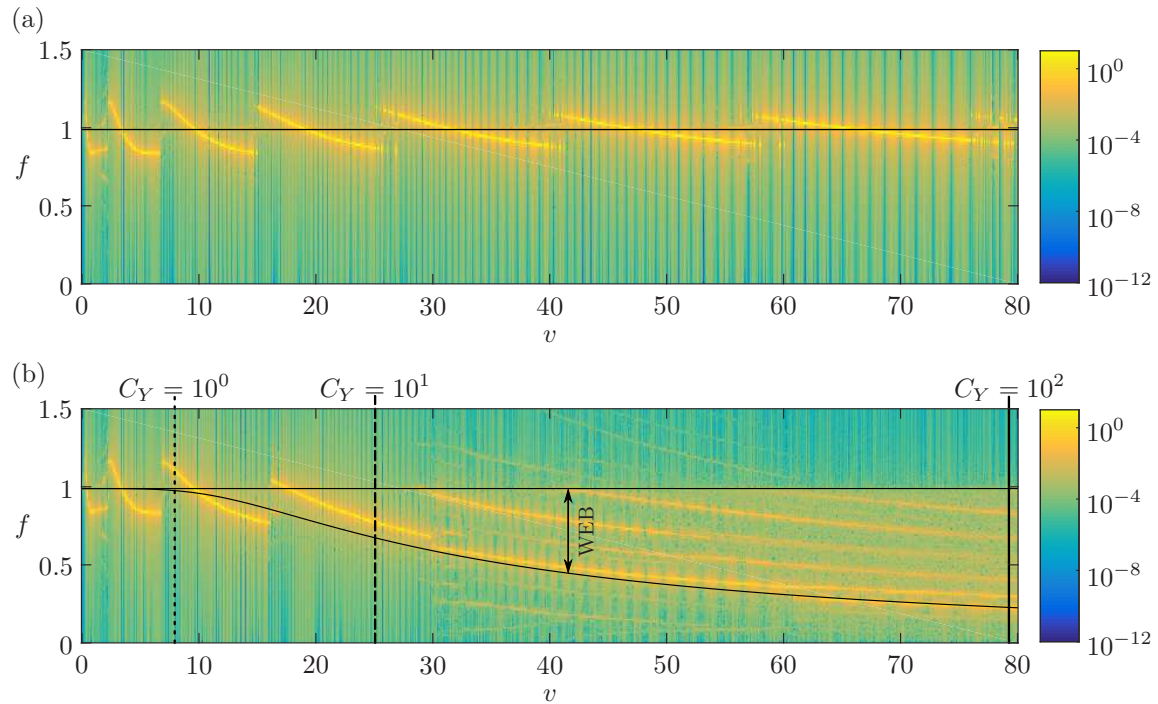


Figure 5.3: Comparison between the power spectral densities of the motion at the tip $Y(s = 1, t)$ in (a) the straight case and (b) the deflected case $\Lambda = 10^3$, for varying reduced velocities v . The natural wake excitation bandwidth (WEB) is superimposed. The particular values of the reduced velocity v corresponding to Fig. 5.2 are indicated as well.

the growing shear in the normal flow is responsible for broadening the wake spectrum. When the deflection remains moderate, the wake excitation bandwidth remains narrow enough so that single-mode lock-in still prevails, but on a slightly larger range of reduced frequencies. On the other hand, when the deflection is large, several structural modes may be simultaneously excited, leading to the inhibition of single mode lock-in replaced by a multi-frequency response to the broadband excitation. These conclusions are consistent with the observations of Bourguet et al. (2012), Bourguet et al. (2015) for a pinned-pinned cylinder experiencing small in-line deformations, as well as those of Vandiver (1993); Ge et al. (2011); Srinil (2011) for straight pinned-pinned cylinders in shear flow.

5.3.2 Localization of the excitation and VIV mitigation

As emphasized in the introduction, the experimental work of Assi et al. (2014) and Seyed-Aghazadeh et al. (2015) has shown that the amplitude of the vibrations of rigid cylinders is much reduced under the effect of the curvature. The same observation was made by Bourguet et al. (2015) regarding the VIVs of pinned-pinned flexible cylinders. Similarly, the works of Trim et al. (2005); Ge et al. (2011); Srinil (2011) have also

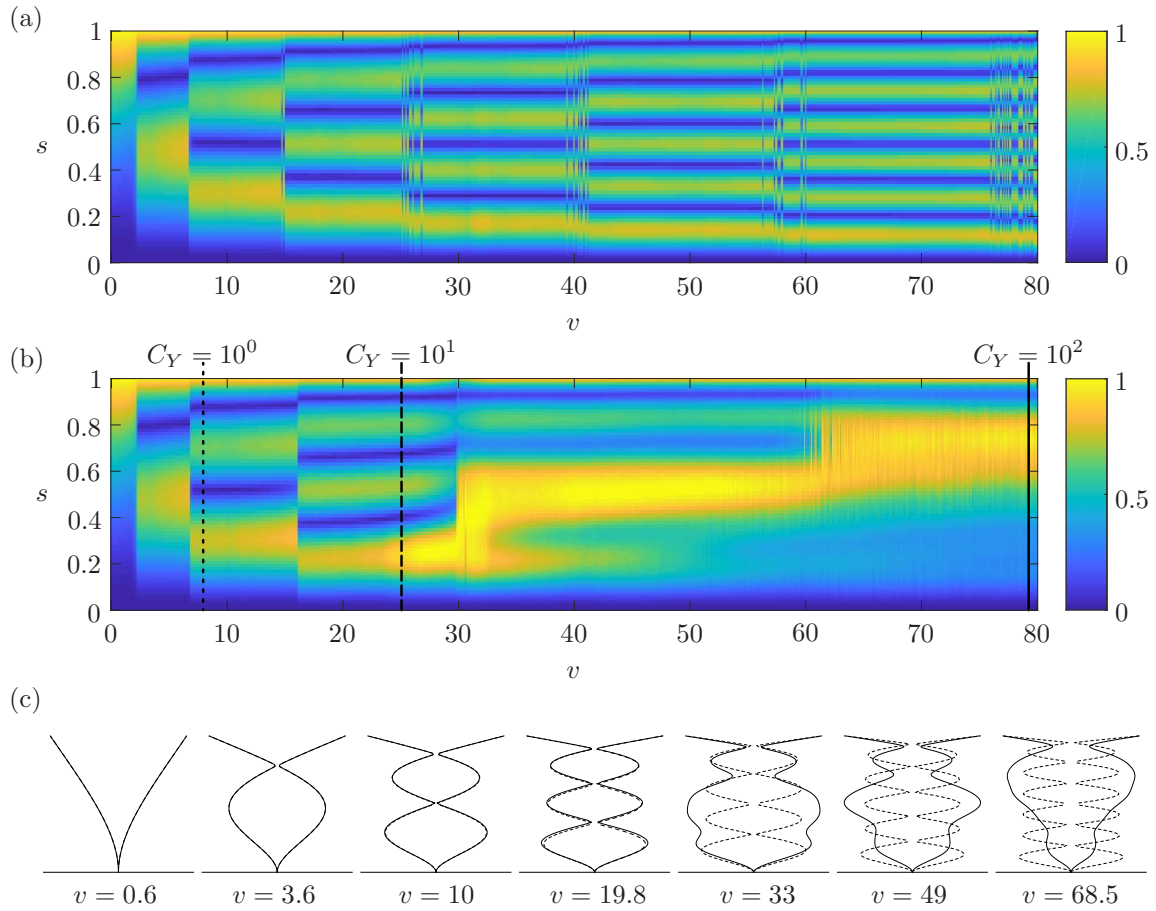


Figure 5.4: Comparison between the spanwise localizations of the transverse deformation in (a) the straight case and (b) the deflected case $\Lambda = 10^3$, for varying reduced velocities v . The colorplots show the temporal RMS of $Y(s, t)$, normalized to 1 along the span. The particular values of the reduced velocity v corresponding to Fig. 5.2 are indicated as well. (c) Comparison of the envelopes of the transverse deformation in the straight case (---) and deflected case $\Lambda = 10^3$ (—), for particular values of v corresponding to successive structural modes in the straight case.

shown that sheared incoming flows entailed lower structural responses than uniform flows. Our numerical simulations indicate that this observation holds true as well for flexible cantilever cylinders curved by the flow. Indeed, the amplitude of the VIVs of the deflecting cylinder ($\Lambda = 10^3$) reduces progressively on Fig. 5.7(a) compared to the straight case above the bending threshold $C_Y > 1$. For large deflections $C_Y > 10$, the amplitude settles around approximately 1/3 of the amplitude of the straight case.

We may explain this reduction of amplitude by considering the energy transferred to the structure from the wake oscillator. In non-dimensional form, the work of the oscillating lift force at a given location along the span reads $e = \dot{Y} \cdot q \cos^2 \theta_0$, so that the total energy E transferred to the structure over one cycle of oscillations is the temporal

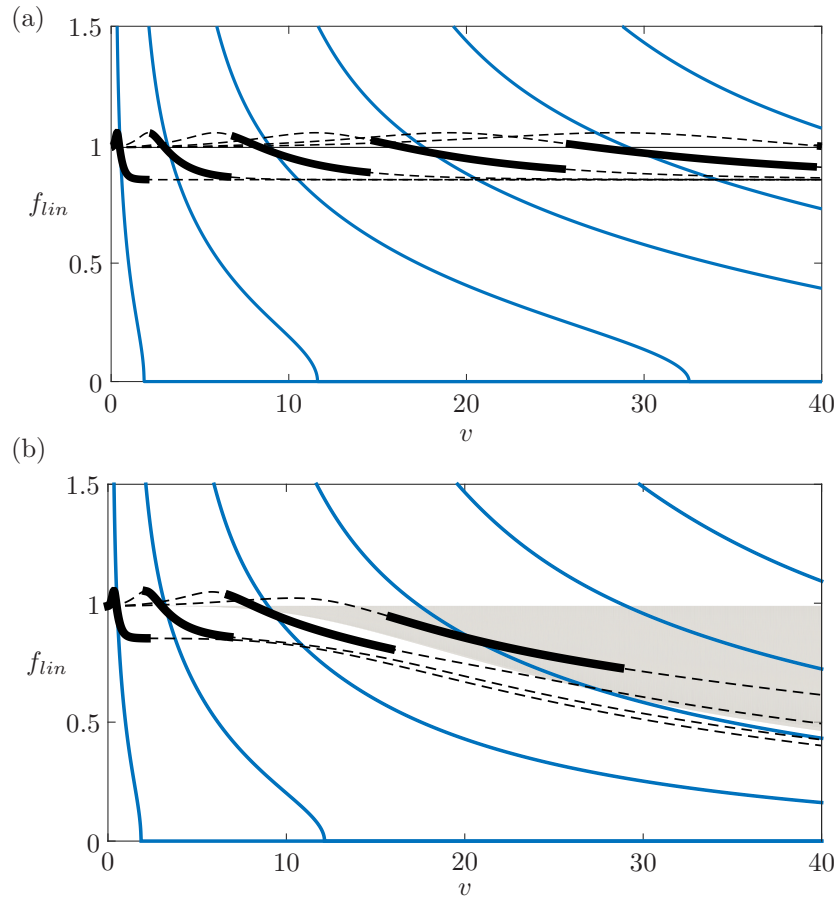


Figure 5.5: Evolution of the linear frequencies of the coupled wake-structure system with the reduced velocity v , for (a) the straight case and (b) the deflected case $\Lambda = 10^3$. The unconditionally unstable free wake spectrum is represented by the grey area. The structural modes in blue are always stable. The coupled modes, displayed in black, are always unstable. The most unstable mode for a given range of v is emphasized in bold.

mean of e , integrated over the whole span. The evolution of E with the reduced velocity on Fig. 5.7(b) proves that deflection drastically mitigates the transfer. A more detailed look at the spanwise distribution of the mean energy transfer on Fig. 5.8 indicates that the excitation by the wake, which is equally distributed in the straight case, concentrates around $s \sim 0.2$ as the deflection increases. This is actually quite intuitive, because the lift force varies with the square of the normal component of the free-stream $\propto \cos^2 \theta_0$. When deflection is important, only the small region close to the clamping point remains close enough to the vertical so as to significantly contribute to the excitation. As the Cauchy number increases and the cylinder bends more and more, the size of that region reduces progressively. The amount of energy transferred overall is consequently reduced, and the amplitude of the vibrations accordingly mitigated.

Note that the discontinuities observed in the straight and low-deflection cases on

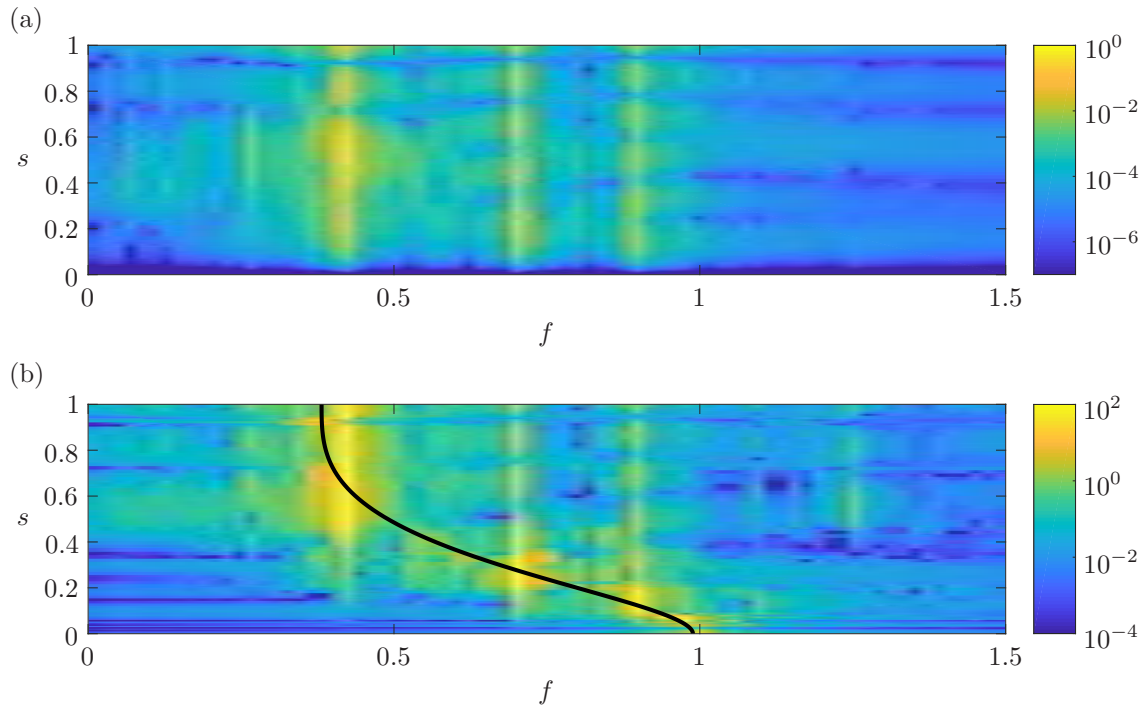


Figure 5.6: Spanwise distribution of power spectral density of (a) the structural motion Y and (b) the wake oscillator q , for $\Lambda = 10^3$ and $v = 49.0$. The natural shedding frequency $f_w^0(s)$ given by the Strouhal law is superimposed in (b) (—).

Fig. 5.7 correspond to mode switches. The disappearance of these jumps above $v > 30$ in the deflected case is consistent with the continuous evolution of the spectrum and vibration shape reported in Figs. 5.3(b) and 5.4(b) due to the inhibition of lock-in.

5.3.3 Influence of the reactive force

Finally, we discuss the influence of the large axial component of the free-stream when the structure is highly reconfigured. Indeed, as the flow velocity increases, the inclination of the structure switches from perpendicular to mostly parallel to the flow. As explained in Section 5.2.3, the level of deflection is controlled by the Cauchy number $C_Y \propto v^2/\Lambda$. We focus here on a case where the deflection increases more rapidly with the reduced velocity than before, that is to say a structure with a smaller aspect ratio $\Lambda = 10$.

At first, the amplitude of vibrations on Fig. 5.9(a) follows the same trend as in the previous case: below $C_Y < 1$, the effect of bending is unnoticeable, while it results in a constant amplitude much reduced compared to the straight case when bending is significant. The amplitude is even reduced as low as 1/10–th of the straight case. But conversely to the previous case, the vibrations start growing again slowly past $v \sim 20$ and they even exceed the amplitude of the straight case for $v \gtrsim 33.5$. Above some critical threshold $v \sim 35$, the amplitude finally grows continuously during the whole time of the simulation. The VIVs are by nature a self-initiated and self-limited

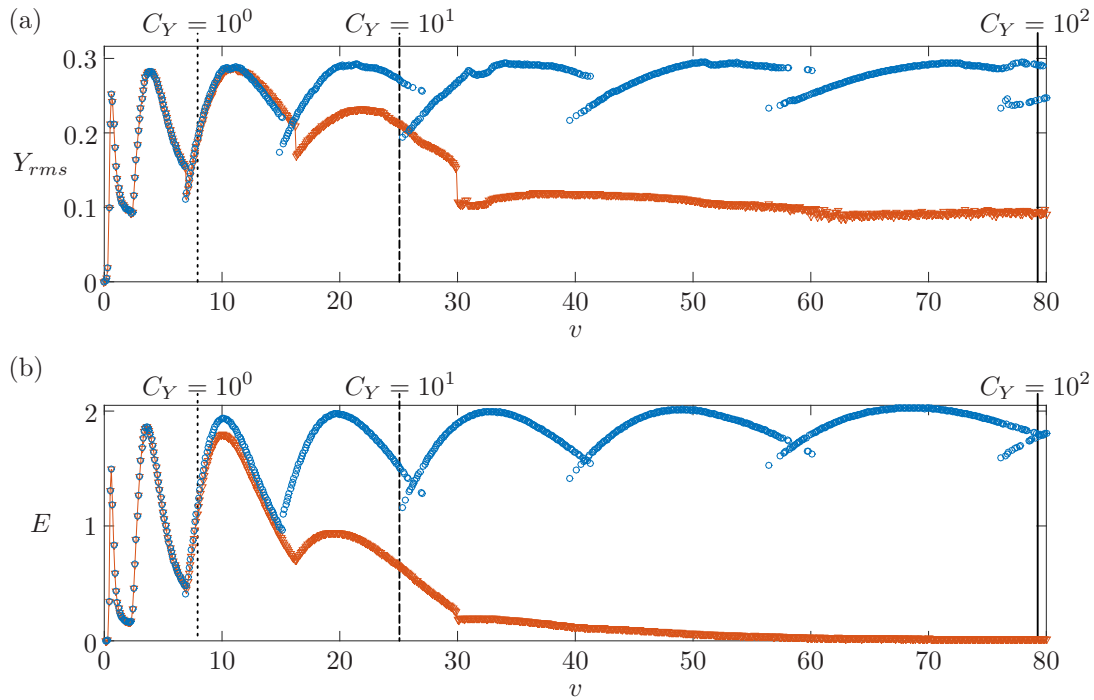


Figure 5.7: Comparison of (a) the RMS amplitude of vibration Y_{rms} and (b) the total energy transfer E from the wake to the structure, between the straight case (blue \circ) and the deflected case $\Lambda = 10^3$ (orange ∇) for varying reduced velocities v . The particular values of the reduced velocity v corresponding to Fig. 5.2 are indicated as well.

phenomenon. In the model, the onset of the VIVs is ensured by the negative damping of the Van der Pol wake oscillator when the amplitude of q is small, while the limitation of the amplitude is ensured by the nonlinear saturation of that same term. This unbounded growth is therefore not related to the VIVs, but is instead the consequence of the onset of a flutter instability caused by the destabilizing influence of the hydrodynamic reactive force on the large portion of the cylinder that is aligned with the free-stream (Eloy et al., 2007; Singh et al., 2012a).

This is confirmed by the results of the linear stability analysis presented on Fig. 5.9(b) and (c). Lock-in with structural mode 1 occurs for the smallest reduced velocities (the coupled linear mode is the most unstable as long as $v < 2.30$), when flow-induced bending is still small. When deflection becomes significant ($C_Y \gg 1$), several structural modes are simultaneously excited by the wake on Fig. 5.9(b) and lock-in is consequently hindered (no discontinuities on Fig. 5.9(a)). But in this case, one of the structural modes (mode 3) is progressively destabilized as v increases. Above $v \gtrsim 20$, the growth rate of this mode starts increasing on Fig. 5.9(c) until it finally becomes unstable at the critical threshold $v_c = 34.9$ (marked by the orange cross on Fig. 5.9(b) and (c)). If the effect of the curvature on the structural modes has been proved negligible in Section 5.3.1, these observations prove on the other hand that the influence of the reactive

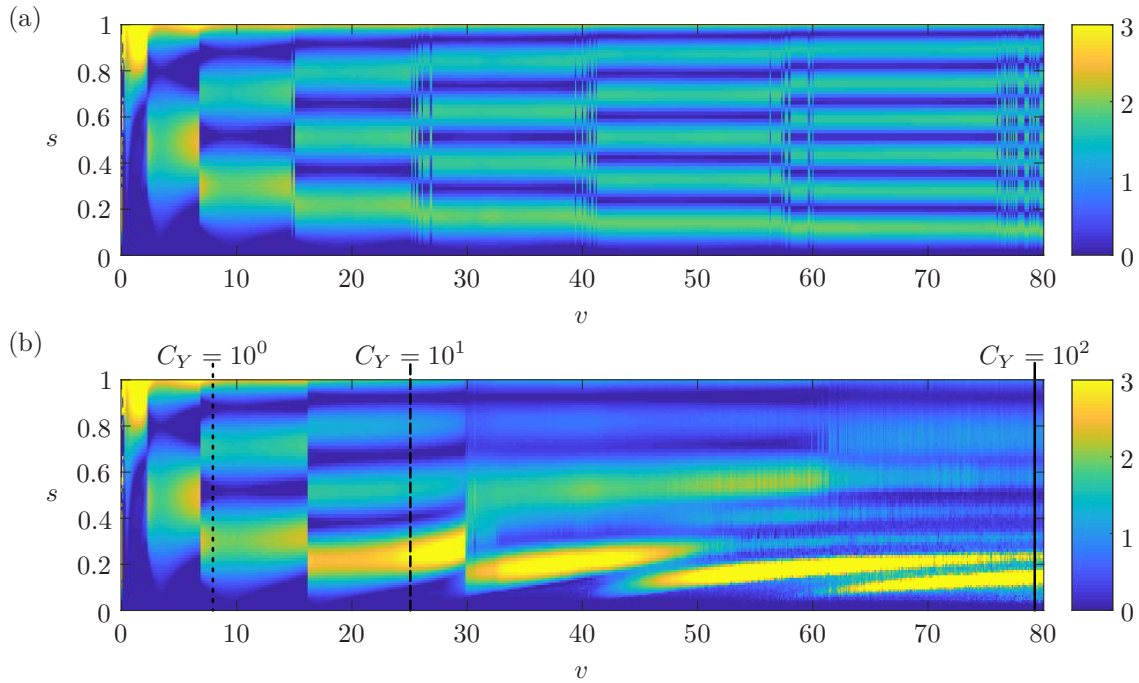


Figure 5.8: Comparison of the spanwise distributions of energy transfer from the wake to the structure between (a) the straight case and (b) the deflected case $\Lambda = 10^3$, for varying reduced velocities v . The colorplots show the mean work of the oscillating lift force $\langle e \rangle$ normalized by the total energy transfer E . The particular values of the reduced velocity v corresponding to Fig. 5.2 are indicated as well.

force may be very significant in the vicinity of the critical threshold. The progressive increase of the vibration amplitude from $v \sim 20$ until the actual onset of the instability $v_c = 34.9$ is indeed concomitant with the destabilization of structural mode 3. Hence, the larger vibration amplitudes observed in this range of reduced velocities are most likely attributable to the growing influence of the gradually destabilizing structural mode 3.

The flow-induced bending thus has competing consequences on the amplitude of the vibrations. On the one hand, we have shown in Section 5.3.2 that the shrinkage of the wake excitation zone considerably mitigates the VIVs. We demonstrate here that on the other hand, the reorientation of the structure in the direction of the free-stream may amplify the vibrations because of the destabilizing effect of the reactive force on the structural modes. This last effect becomes significant in the vicinity of the structural stability threshold. As explained in Appendix G.2, the structural stability threshold in terms of either the reduced velocity v or the Cauchy number C_Y is close to proportional to the aspect ratio Λ . More slender structures may consequently reach much higher modes and larger deflections before feeling the destabilizing influence of the reactive force.

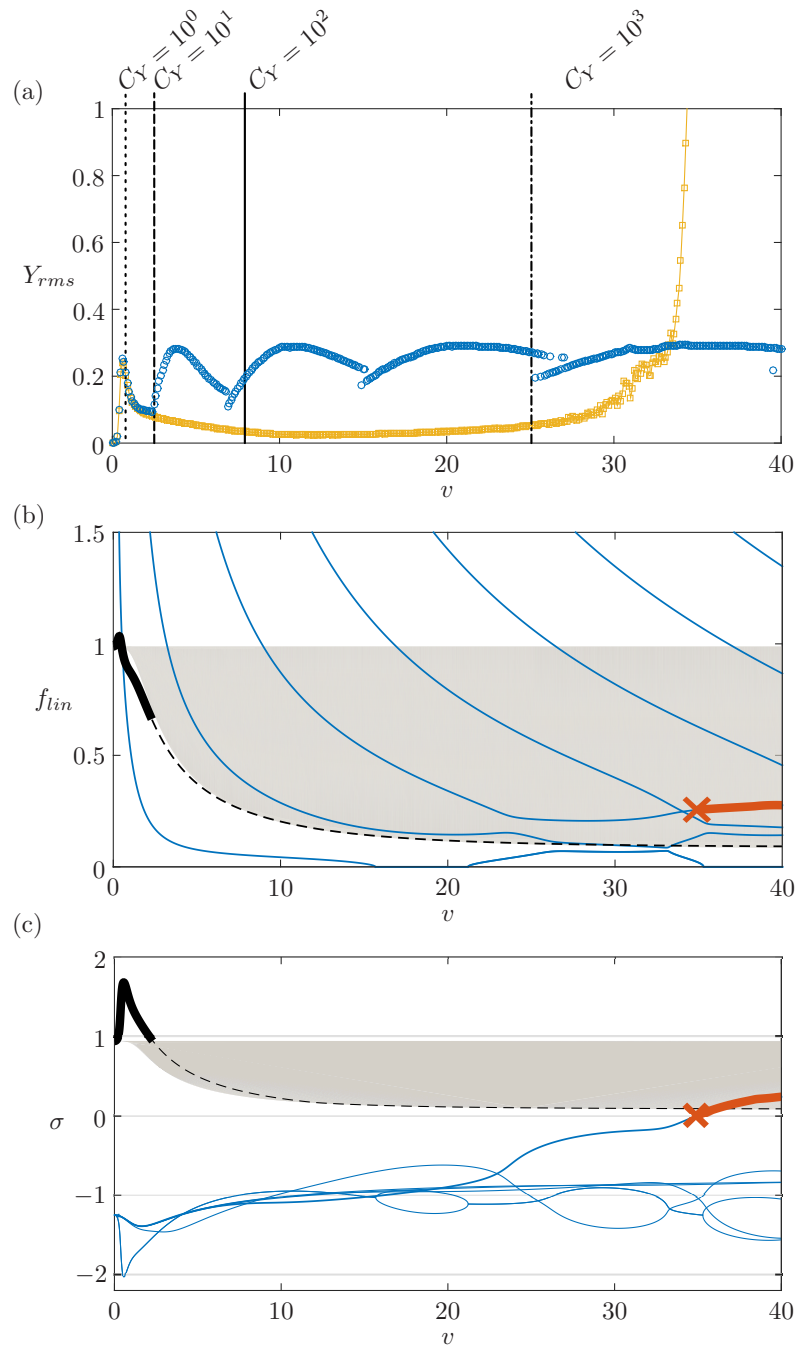


Figure 5.9: (a) Comparison of the RMS amplitude of vibration between the straight case (blue \circ) and the deflected case $\Lambda = 10$ (yellow \square). (b) and (c) Linear frequencies f_{lin} and growth rates σ of the coupled wake-structure system, for $\Lambda = 10$. The unconditionally unstable free wake spectrum is represented by the grey area. The structural modes are in blue when stable, and in bold orange when unstable. The orange cross marks the stability threshold for structural mode 3. The coupled mode, displayed in black, is always unstable. It is emphasized when it is the most unstable mode.

5.4 Discussion and conclusion

In this chapter, we have provided a qualitative analysis of the consequences of flow-induced bending on the vortex-induced dynamics of slender flexible cylinders based on reduced order models. Overall, the effects of the deflection may impact the features of the vibrations on two levels.

Firstly, the deformation of the cylinder changes the spanwise profile of the component of the free-stream normal to the structure. We have shown that the increasing non-uniformity of the normal flow leads to the spreading of the wake excitation spectrum and the localization of the energy transfer from the wake to the structure, owing to the independence principle. These two effects result in a strong mitigation of the amplitude of the vibrations coupled with the inhibition of single mode lock-in replaced by the simultaneous excitation of multiple structural modes. These mechanisms were indeed evidenced in several experimental and numerical studies about the VIVs of straight cylinders in shear incoming flow, such as Vandiver (1993); Trim et al. (2005); Srinil (2011); Ge et al. (2011); Bourguet et al. (2013) for instance. As any deformation of a straight cylinder in the direction of the free-stream would induce shear in the normal flow, we expect that these conclusions are independent of the initial structural configuration, boundary conditions, or the features of the in-plane deformation. For instance, similar observations have been reported by Bourguet et al. (2015) for a pinned-pinned cylinder initially inclined and slightly deformed by the flow. Similarly, the smaller amplitudes of vibrations reported in Assi et al. (2014) and Seyed-Aghazadeh et al. (2015) for rigid curved cylinders compared to straight ones is likely also the consequence of the difference in the normal flow profiles between the two configurations. The loss of harvesting efficiency reported in Antoine et al. (2016) when increasing the sag (and consequently the deformation) in the in-flow catenary configuration also results from the induced shear in the normal flow.

Secondly, the deformation of the structure is responsible for a modification of the structural modes resulting from both the flow-induced tension and the axial component of the flow through the reactive forcing term.

The effect of the tension is negligible in our case, but it should be noted that it may be of significant importance in other situations. Indeed, the structural frequencies depend on the total stiffness of the system, which can be decomposed in the natural bending stiffness EI specific to the structure, and an additional tension-induced stiffness. In our case, the structural tension $T = -1/2EI\kappa_0^2$ itself is the physical consequence of the structural stiffness EI , and so it is understandable that the influence of the tension-induced stiffness on the natural frequencies of the structure be small compared to that of the natural stiffness that originated it. However, in the rather common case of tensioned cables, the structural tension is either externally controlled or flow-induced but it is in any case independent of the usually small bending stiffness. Its influence on the structural frequencies and thus on the vortex-induced dynamics

may then be totally dominant (see for instance the study of Antoine et al., 2016), but this effect is out of the scope of the present work as the tension in this case is not related to the flow-induced deformation of the structure.

The effect of the axial flow component may on the other hand be dramatic in the configuration chosen in this chapter. When the deflection is very large, the axial flow may become the dominant component, and the added damping and stiffness stemming from the reactive forcing on the inclined portion of the cylinder may significantly alter the structural modes. Above some critical velocity threshold, the cylinder might undergo some large-amplitude oscillations originating from a flutter instability. It should be noted that only the transverse stability along the y -direction has been considered in this chapter, but flutter may also be initiated in the xz -plane, as was shown in Chapter 4. However, we do not expect the in-plane destabilization to have consequences on the vortex-induced dynamics below the stability threshold. Indeed, the geometrical linearization performed in Appendix F.1.2 results in the decoupling of the small-amplitude dynamics in the two directions. There should consequently be no interactions between the in-plane structural modes and the transverse vibrations as long as the amplitude of vibration remains small. On the other hand, we have shown that the progressive destabilization of the transverse structural modes may enhance the amplitude of the VIVs even in the stable domain. These conclusions may not easily be generalized to other structural configurations as the stability of the structural modes is highly dependent on the boundary conditions of the structure. The choice of the cantilever configuration in our work merely demonstrates the potentially large consequences the axial flow may bear through the reactive force, and neglecting the terms originating from it must only be done with great care. Nonetheless, we also found that the magnification of the vibrations due to the reactive force becomes significant for higher modes of vibrations and larger levels of deflection as the structure is made more slender. In this regard, it may thus be considered as a secondary effect that sets a limit to the strong abatement of the vortex-induced vibrations more commonly observed.

We may thus conclude that the primary consequence of flow-induced deformations on the vortex-induced dynamics of flexible cylinders is the hindrance of lock-in, replaced by a multi-frequency response of the structure, and the strong mitigation of the vibrations that rest on the modification of the spanwise profile of the normal component of the free-stream. Neglecting the in-line deformation when assessing the features of the VIVs should therefore generally result in an overestimation of the severity of the vibrations.

Chapter 6

Conclusion

6.1 Contributions

To conclude, we have shown in this thesis that the ability of flexible structures to reduce the magnitude of the flow-induced loads is preserved in many situations involving some spatial or temporal variability of the flow-structure system, provided that the design of the structure is such that drag dominates over the structural and fluid inertial forces.

In the case of a non-uniform system, we found that the scaling of the total drag with the flow velocity could be related to the spatial variability of the flow-structure system at the scale of a bending length located in the vicinity of the clamped edge. This indicates that, apart from the well-known mechanisms of frontal area reduction and streamlining, drag reduction by elastic reconfiguration may also rely on a third mechanism of localization of the flow-structure interaction in a small region at the scale of which the average properties of the system are more favourable. For instance, this may occur when a structure in a boundary layer flow dives into the region of lower flow velocity as it reconfigures.

Besides, we have derived an analytical expression relating the Vogel exponent in the limit of large deflections to the parameters that provide the best fit of the system properties as power functions of the spatial coordinates. Given the weak sensitivity of the Vogel exponent to all these parameters in the ranges accessible to realistic systems, we have concluded that the Vogel exponents of plants and model systems should never deviate much from -1 regardless of the precise features of the system. This conclusion is consistent with most experimental measurements performed either in the field or in the laboratory, and suggests that the mechanism of drag reduction by elastic reconfiguration is weakly sensitive to the spatial distribution of the system properties.

In the case where the background flow is oscillatory, we have shown that different regimes exist for the response of the structure, depending on the amplitude and frequency of the flow. Overall, the dynamic reconfiguration of flexible structures in oscillatory flow always results in the alleviation of the internal stresses, as long as the resistive drag is the dominant source of fluid loading. When the amplitude of the flow is smaller than the width of the structure, the fluid inertia dominates over the drag. In this regime, the structure essentially behaves as a linear oscillator and exhibit resonances responsible for a large magnification of the internal stress, when the frequency of the flow matches the natural frequencies of the structure. Apart from these resonances, the internal stress is reduced due to the shortening of the characteristic scale

of deformation from the whole length of the structure to the typical wavelength of the modal shape. On the other hand, when the amplitude of the flow is larger than the structural width, the resistive drag is the dominant source of fluid loading. As long as the amplitude remains smaller than the structural length, the internal stress in the structure is reduced by the concentration of the deformation in an elastic boundary layer close to the clamping point. The rest of the structure is passively convected with the flow particles thanks to the saturation of the drag term, which corresponds to the mechanism of “going with the flow” foreseen by Koehl (1984). When the amplitude of the flow is now larger than the length of the structure, drag still dominates over inertial forces on slender structures, but the passive convection of the structure is limited to its finite length. The deformation of the structure becomes quasi-static, apart from a swift reversal period, and the known results about static reconfiguration apply.

It appears from this systematic study that whatever the regime of reconfiguration, the reduction of the structural stress always results from the concentration of the deformation on a characteristic bending length smaller than the actual length of the structure. This loss of relevance of the actual size of the structure in aid of a smaller bending length had already been noted in the static regime in Gosselin et al. (2010) and used as the key assumption leading to different scaling laws for the drag on flexible structures in different situations in de Langre et al. (2012). Our work indicate that this mechanism appears to be the common feature to all (static or dynamic) regimes of reconfiguration, and the source of the alleviation of the load.

The dynamic flow-structure couplings that may occur when the structure has a significant inertia may however set some limitations to the benefits of reconfiguration. The spontaneous flapping dynamics that arises in steady flows is indeed responsible for additional loads on the structure that mitigate the efficiency of the drag reduction process. However, apart from some rare and brief snapping events during which very large peak forces may be recorded, the additional contribution due to the dynamics never offsets the significant drag reduction stemming from the static deflection.

Furthermore, the destabilization of the structure leading, first, to the triggering of flutter, and eventually, to the loss of regularity of the flapping dynamics, is dependent on the density and geometry of the structure. Heavier structures are naturally more prone to inertial forces, while slender structures are efficiently damped due to the dominance of drag over the added mass force. The mass and aspect ratio are consequently critical parameters in the evaluation of the disturbance brought about by inertial effects to the reconfiguration process. Our work indicates that a good design strategy in order to make flow-resistant flexible structures is to build light and slender structures. For that matter, these design instructions should seem reasonable from a biologist’s point of view, as they are consistent with the morphology of the macroalgae that have managed to grow to large sizes in flow-dominated habitats.

Finally, we have also demonstrated that the ability to statically deform under the effect of the flow has the added benefit of reducing the magnitude of the vortex-induced

vibrations. These vibrations are usually undesirable in engineering applications, because of the risks of fatigue damage associated with the cyclic nature of the load, and the magnification of the static drag that they bring about. Our study shows that the modification of the normal flow profile due to the reorientation of the structure broadens the wake excitation spectrum and localizes the energy transfer, thus inhibiting single mode lock-in and mitigating the amplitude of vibration. The abatement of the VIVs due to the deflection may however be thwarted by the destabilizing influence of the reactive added mass force on the transverse structural modes. This last effect is likely to depend on the boundary conditions imposed to the structure, and other configurations should be considered in order to draw general conclusions regarding the impact of the reactive force on the VIVs of deforming structures.

6.2 Perspectives

In this thesis, we have provided some extensions of the theory of reconfiguration to more realistic situations in contrast to the overly idealized cases considered thus far in the literature. But the configurations considered in this work are still simplified to a large extent. In particular, the choice of a cantilever beam clamped transverse to the flow limits the validity of the conclusions drawn here to structures that deform assuming a two dimensional flexion mode. For instance, some findings of Chapter 2 do not seem to be readily applicable to the rolling-up of plastic sheets of Schouveiler and Boudaoud (2006), probably because of the more complex three dimensional reconfiguration mechanism. Besides, we did not observe in Chapter 3 the “jerking” effect predicted by Koehl (1984), Denny and Cowen (1997), Denny et al. (1998), that would create large inertial forces when the structure reaches the end of its tether after the short reversal period. This, of course, is partly due to the fact that the structural inertia was neglected in the model. But the effect of the added mass that is virtually affected to the structure could still cause such inertial effects. We believe likely that we did not observe any jerking effect because of the reversal mechanism of bending structures, characterized by the propagation of a single curvature wave from the clamped edge to the free tip over the reversal time. The progressive reversal of the structure thus prevents any brutal deceleration at the end of the reversal. In the case of tensile structures, such as those considered in the aforementioned studies, the mass at the end of the chain-spring system is convected freely during the reversal, but the momentum acquired during this time may induce large tensioning effects in its tether when the mass brutally reaches the end of its course. When subjected to flows, the behaviour of systems with more complex deformation mechanisms remains to this day largely unexplored.

Besides, when considering the influence of the time-variability of the free-stream in Chapter 3, we have restricted our study to the particular case of a sinusoidally oscillating flow. But flexible benthic organisms are also subjected to brief, potentially larger loads, due for instance to the impingement of breaking waves (Gaylord et al., 2008; Jensen

and Denny, 2016). The response of flexible structures to such impulsive loads has been considered in a few situations (see for instance Gaylord et al., 2001; Kim and Gharib, 2011), but relatively few studies have analysed the potential that flexible structures bear in alleviating the large loads due to transient flow forces. Moreover, the actual variations of the flow in the field are likely to be more complex, involving non-linear random waves possibly combined with a steady current such as the Stoke's drift. A few studies have recently considered more complex and realistic time-variations of the flow (see for instance Gaylord et al., 2003; Henry et al., 2015). We believe the present thesis provides some insight regarding the behaviour of flexible structures in time-varying flows, but more work is undoubtedly necessary to understand the mechanisms of deformation and predict the magnitude of the loads imposed on such structures in transient or irregular flows. Besides, some interesting phenomena remain to be explored even in the simple case of a sinusoidally oscillating flow. Some results (not included in this thesis) of the experiments presented in Chapter 3 have for instance shown that the deformation of the structure is not necessarily symmetric. For some particular values of the forcing parameters, the structure has sometimes been seen oscillating about an average position that slowly drifted to one side. The impact on the internal stress of such large average deflection might be significant and certainly needs to be investigated.

Finally, we have demonstrated that flexibility was responsible for an alleviation of the loads, at the condition that the resistive drag was dominant over the inertial effects. Incidentally, we have also shown that inertial effects are generally responsible for destabilizing the structure and enhancing the loads it has to bear. In the perspective of harvesting energy from flows, it might be of use to investigate ways not to mitigate but to increase and control the flow-induced oscillations. We have already proven that resonances of a virtually massless structure may occur in an oscillatory flow, when the amplitude of the forcing is small compared to the width of the structure. The results of numerical simulations, not shown in this thesis, suggest that increasing the mass of the structure enhances the amplitude of its response. However, when the amplitude of the flow increases further than the structural length, the structure may exhibit erratic oscillations. Further investigations regarding the influence of the structural mass on the response of elastic structures in different types of flows may be useful in assessing the potential and the limits of using such structures as flow-energy harvesters. Besides, even in the bioinspired perspective of designing structures that best accommodate the flow-induced loads, it might not always be possible to lower the structural mass to the level required to avoid the inertial risks. A more detailed analysis of the consequences of inertial loads would therefore be of use in that regard as well.

Appendix A

Nomenclature for Chapter 2

$L, W(s), D(s)$	length, width and thickness of the beam
$EI(s)$	bending stiffness in the case of linear elasticity
$C_D(s)$	cross-section drag coefficient
$\rho(z)$	fluid density distribution
$U(z), U_0$	flow profile and reference velocity
$\theta(s), \kappa(s)$	inclination angle of the beam from the vertical axis and curvature
$M(s), M_0$	internal bending moment and reference value
$Q(s)$	internal shear force
$q(s), q_0$	local normal fluid load and reference value
$c(\theta)$	angular dependence of the normal fluid load
$g(\kappa), \alpha$	function and exponent associated with the material constitutive law
$b(s), b_0, \beta$	distribution, reference and exponent associated with the stiffness factor
$w(s), w_0, \gamma$	distribution, reference and exponent associated with the cross-section shape factor
$p(z), p_0, \mu$	distribution, reference and exponent associated with the pressure
ϕ, ψ	geometrical and material parameter
F, F_{rigid}	drag force on the flexible/rigid beam
\mathcal{R}	reconfiguration number
C_Y	Cauchy number
ν, ν_∞	local and asymptotic Vogel exponents
ℓ	characteristic non-dimensional bending length
L_B	characteristic non-dimensional boundary layer thickness
δ	characteristic non-dimensional tapering length

Appendix B

Simplification of the reactive force for inextensible structures

In the particular case of an inextensible structure, the reactive force (3.3) is purely normal and may be simplified in (3.4). Indeed, developing and sorting the terms in Eq. (3.3) yields

$$\mathbf{q}_{am} = -m_a \left[\left(\dot{U}_n - U'_n U_\tau - U_n U'_\tau + \frac{1}{2} \kappa U_n^2 \right) \mathbf{n} + \left(U'_n + \kappa U_\tau - \dot{\theta} \right) \boldsymbol{\tau} \right]. \quad (\text{B.1})$$

Differentiating the relative velocity equation $U_\tau \boldsymbol{\tau} + U_n \mathbf{n} = \dot{\mathbf{r}} - \mathbf{U}$ with respect to s and using the inextensibility condition $\mathbf{r}' = \boldsymbol{\tau}$ provides

$$(U'_\tau - \kappa U_n) \boldsymbol{\tau} + (U'_n + \kappa U_\tau) \mathbf{n} = \dot{\mathbf{r}}' = \dot{\boldsymbol{\tau}} = \dot{\theta} \mathbf{n}. \quad (\text{B.2})$$

so that the tangential component of Eq. (B.1) vanishes and $U'_\tau = \kappa U_n$ and $U'_n = \dot{\theta} - \kappa U_\tau$. Using these expressions, Eq. (B.1) further simplifies in

$$\mathbf{q}_{am} = -m_a \left[\dot{U}_n - \dot{\theta} U_\tau + \kappa \left(U_\tau^2 - \frac{1}{2} U_n^2 \right) \right] \mathbf{n}. \quad (\text{B.3})$$

Differentiating the relative velocity with respect to time now provides

$$\left(\dot{U}_\tau - \dot{\theta} U_n \right) \boldsymbol{\tau} + \left(\dot{U}_n + \dot{\theta} U_\tau \right) \mathbf{n} = \ddot{\mathbf{r}} - \dot{\mathbf{U}} \quad (\text{B.4})$$

so that projection on the normal vector gives $\dot{U}_n = \left(\ddot{\mathbf{r}} - \dot{\mathbf{U}} \right) \cdot \mathbf{n} - \dot{\theta} U_\tau$. Making use of that expression in Eq. (B.3) finally yields Eq. (3.4).

Appendix C

Scaling laws for the tensile stress

Similarly to the shear reconfiguration number considered in Chapter 3, the variations of the tensile reconfiguration number are displayed on Figure C.1(a) for the modal regime, along with the location of the maximum stress on Figure C.1(b). Figures C.1(c) and C.1(d) respectively show the results in the convective and large-amplitude (or static) regime. All the conclusions drawn about the shear reconfiguration number are still valid for the tensile number. The only noticeable difference is the asymptotic scaling for large loadings. Indeed, the non-dimensional bending moment $M = \kappa$ involves one less derivative in space than the shear force $Q = -\kappa'$ so that $M \sim Q \times l_b$, while the non-dimensional rigid load is unchanged. Therefore, $\mathcal{R}_\tau \sim \mathcal{R}_n \times l_b \sim l_b^2$. Finally, this provides $\mathcal{R}_\tau \sim \omega^{-1}$ in the modal regime, $\mathcal{R}_\tau \sim (K_C \omega^2)^{-1/2}$ in the convective regime and $\mathcal{R}_\tau \sim C_Y^{-2/3}$ in the large-amplitude (or static) regime, in agreement with the results shown on Figure C.1.

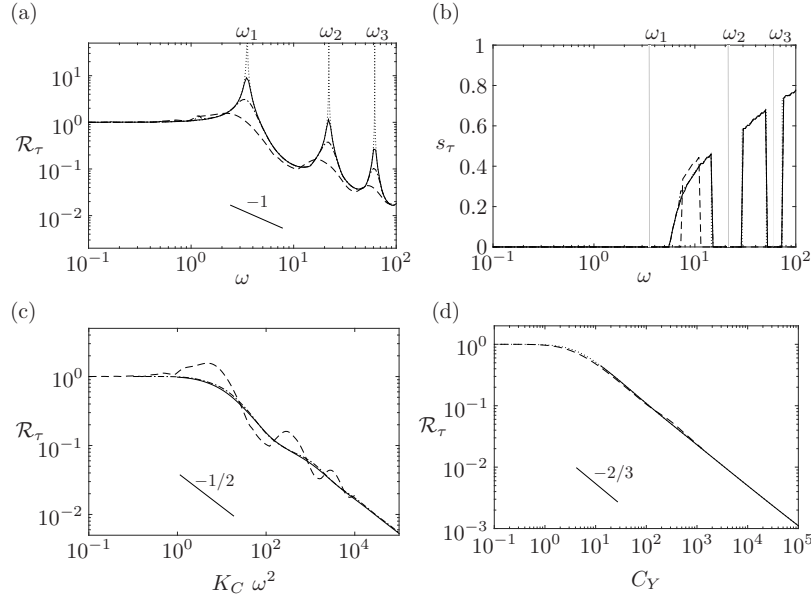


Figure C.1: (a) Tensile reconfiguration number and (b) location of maximum tensile stress along the span, in the modal regime, against the frequency ratio, for $K_C = 10^{-2}$ (—), $K_C = 10^{-1}$ (-·-·-), $K_C = 10^0$ (- - -), and analytical solution for $K_C \rightarrow 0$ (· · · ·). (c) Tensile reconfiguration number against $K_C \omega^2$ in the convective regime $K_C = 10^0$ (- - -), $K_C = 10^1$ (-·-·-), $K_C = 10^2$ (—). (d) Tensile reconfiguration number in the large-amplitude regime for $\lambda = 12.7$, against the Cauchy number C_Y for $\alpha = 10^0$ (- - -), $\alpha = 10^1$ (—), and static solution obtained with Eq. (3.21) (· · · ·).

Appendix D

Influence of the slenderness on the static reconfiguration

In the large-amplitude regime, most of the cycle is quasi-static and the system is well modeled by equation 3.21. The different static reconfiguration curves for varying slenderness parameters shown on Figure D.1 prove that the reconfiguration numbers converge on an asymptotic trend as the slenderness is increased. For any finite λ , the discrepancy with the asymptotic curve remains quite small for the shear stress, and almost completely imperceptible for the tensile stress. The asymptotic scaling provided in Section 3.4 can therefore be used even for moderately large slenderness.

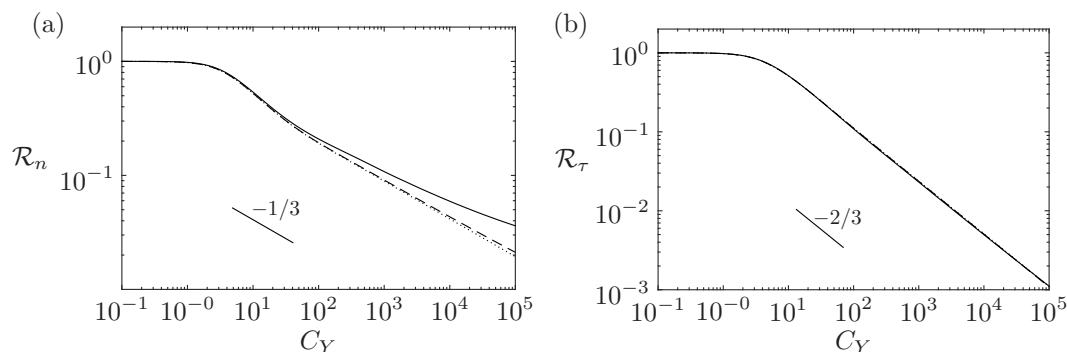


Figure D.1: Variations of the static reconfiguration numbers obtained with Eq. 3.21 ((a) shear, (b) tensile) as a function of the Cauchy number C_Y , for $\lambda = 12.7$ (—), $\lambda = 127$ (---), $\lambda = 1270$ (····).

Appendix E

Comparison of the stability thresholds of Chapter 4 with the axial configuration

For asymptotically large slenderness $\lambda \rightarrow +\infty$, the structure aligns with the flow and one might expect it to behave similarly to the classical axial configuration. However, Figure E.1 shows that the critical velocity for large slenderness does not converge to the threshold expected for an elongated beam in axial flow. In fact, even though $\theta_0 \rightarrow \pi/2$ almost everywhere, the product λC_0 remains of order $O(1)$ so that the contribution of the resistive drag remains significant even on the part of the structure that is nearly parallel to the flow. Consequently, in the limit of infinite slenderness, Eq. (4.10) actually reduces to the classical elongated small-amplitude equation in axial flow Eq. (4.11), but supplemented by the non-vanishing resistive drag contribution

$$\ddot{\eta} + 2u\sqrt{\beta}\dot{\eta}' + u^2\eta'' + \eta^{(4)} + 2\lambda C_0 (u\sqrt{\beta}\dot{\eta} + u^2\eta') = 0. \quad (\text{E.1})$$

The stability curve found for $\lambda = 10^3$ with this asymptotic equation on Figure E.1 is indistinguishable from that obtained with the full equation (4.10). Quite understandably, this persistent drag term introduces some additional damping that stabilizes the system compared to the axial configuration, as soon as $\beta \gtrsim 0.024$.

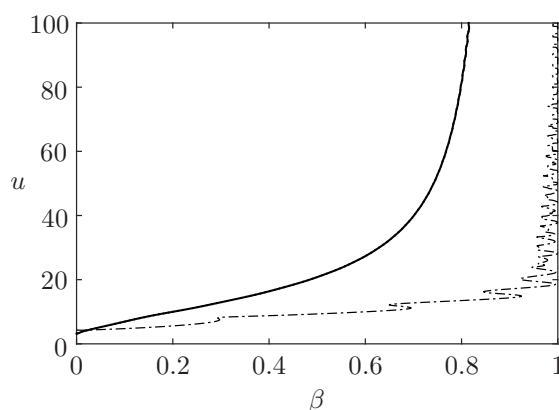


Figure E.1: Linear stability thresholds obtained with the full equation (4.10) for $\lambda = 10^3$ (\cdots), with the equation relative to the axial configuration (4.11) ($- \cdot -$), and with the asymptotic equation (E.1) for $\lambda = 10^3$ (---).

Appendix F

Details on the model of Chapter 5

F.1 Derivation of the governing equations

F.1.1 Details about the structural model

Following Audoly and Pomeau (2010), we define a local direct orthonormal frame $\mathbf{e}_{i=1,2,3} = (\mathbf{n}, \mathbf{w}, \boldsymbol{\tau})$, materially attached to the structure and such that $(\mathbf{n}, \mathbf{w}, \boldsymbol{\tau})|_{s=0} = (\mathbf{e}_x, \mathbf{e}_y, \mathbf{e}_z)$. We also define the Darboux vector $\boldsymbol{\Omega} = \kappa_n \mathbf{n} + \kappa_w \mathbf{w} + \gamma \boldsymbol{\tau}$ where κ_n and κ_w are the material curvatures and γ is the twist of the cylinder. By definition, the Darboux vector is such that $\mathbf{e}_i' = \boldsymbol{\Omega} \times \mathbf{e}_i$. For an Euler-Bernoulli beam of bending stiffness EI in both (\mathbf{n}, \mathbf{w}) -directions, torsional stiffness GJ , and subjected to an external force \mathbf{q} and no external torque, the Kirchhoff equations governing the dynamics of the structure read

$$m\ddot{\mathbf{r}} = \mathbf{F}' + \mathbf{q} \quad , \quad \mathbf{0} = \mathbf{M}' + \boldsymbol{\tau} \times \mathbf{F} \quad (\text{F.1})$$

with the internal force vector $\mathbf{F} = T\boldsymbol{\tau} + Q\mathbf{n} + P\mathbf{w}$ and the constitutive law for the internal bending moment $\mathbf{M} = GJ\gamma\boldsymbol{\tau} + EI\kappa_n\mathbf{n} + EI\kappa_w\mathbf{w}$. The inextensibility condition reads $\mathbf{r} = \boldsymbol{\tau}$, and for a cantilever beam, the boundary conditions read $\mathbf{r} = \mathbf{0}$ and $\mathbf{r}' = \mathbf{e}_z$ at the clamped edge $s = 0$, and $\mathbf{F} = \mathbf{M} = \mathbf{0}$ at the free end $s = L$. Using the second Kirchhoff law (F.1) and the boundary conditions for the twist, we find that

$$\gamma = 0 \quad , \quad Q = -EI\kappa_w' \quad , \quad P = EI\kappa_n' \quad (\text{F.2})$$

so that finally the curvilinear derivatives of the material frame simplify in

$$\boldsymbol{\tau}' = \kappa_w\mathbf{n} - \kappa_n\mathbf{w} \quad , \quad \mathbf{n}' = -\kappa_w\boldsymbol{\tau} \quad , \quad \mathbf{w}' = \kappa_n\boldsymbol{\tau} \quad (\text{F.3})$$

and the curvilinear derivative of the internal force vector that appears on the right hand side of the first Kirchhoff equation (F.1) reads

$$\mathbf{F}' = \left(T + \frac{1}{2}EI(\kappa_n^2 + \kappa_w^2) \right)' \boldsymbol{\tau} + \left(\kappa_w T - EI\kappa_w'' \right) \mathbf{n} - \left(\kappa_n T - EI\kappa_n'' \right) \mathbf{w}. \quad (\text{F.4})$$

The boundary conditions read $\mathbf{r} = \boldsymbol{\tau} = \mathbf{0}$ at $s = 0$ and $T = \kappa_n = \kappa_n' = \kappa_w = \kappa_w' = 0$ at $s = 1$.

F.1.2 Linearization of the structural model

As explained in Section 5.2, we expand $\mathbf{r}(s, t) = \mathbf{r}_0(s) + Y(s, t)\mathbf{e}_y$ where the transverse displacement Y is taken as a first order perturbation to the static shape \mathbf{r}_0 . At the leading order the deformation is contained exclusively in the xz -plane so κ_n is a first order perturbation as well and we also expand $\kappa_w = \kappa_0 + \delta\kappa$ and the frame vectors

$$\boldsymbol{\tau} = \boldsymbol{\tau}_0 + \delta\boldsymbol{\tau} \quad , \quad \mathbf{n} = \mathbf{n}_0 + \delta\mathbf{n} \quad , \quad \mathbf{w} = \mathbf{e}_y + \delta\mathbf{w}. \quad (\text{F.5})$$

Using (F.3), the inextensibility condition and all the expansions above mentioned, we obtain after some calculations the expansions of the material frame

$$\boldsymbol{\tau} = \boldsymbol{\tau}_0 + Y'\mathbf{e}_y \quad , \quad \mathbf{n} = \mathbf{n}_0 + \alpha\mathbf{e}_y \quad , \quad \mathbf{w} = \mathbf{e}_y - Y'\boldsymbol{\tau}_0 - \alpha\mathbf{n}_0 \quad (\text{F.6})$$

where the small angle α and the small curvature κ_n satisfy

$$\alpha' = -\kappa_0 Y' \quad , \quad \kappa_n = \kappa_0 \alpha - Y'' \quad (\text{F.7})$$

and $\delta\kappa_w = 0$. Besides, expanding all the terms in (F.4), we obtain up to the linear order

$$\mathbf{F}' = \left(T + \frac{1}{2}EI\kappa_0^2 \right)' \boldsymbol{\tau}_0 + \left(\kappa_0 T - EI\kappa_0'' \right) \mathbf{n}_0 + \left((T - EI\kappa_0^2) Y'' - \frac{3}{2}EI(\kappa_0^2)' Y' - EII Y^{(4)} \right) \mathbf{e}_y. \quad (\text{F.8})$$

F.1.3 Linearization of the fluid forces

The oscillating lift force \mathbf{p}_w defined in (5.3) is a linear order term by assumption. On the other hand, the resistive and reactive forces (5.1),(5.2) both include a leading order and a linear order term. First, the expansion of the relative velocity up to the linear order in Y gives $\mathbf{U}_{rel} = \dot{Y}\mathbf{e}_y - U\mathbf{e}_x = \dot{Y}\mathbf{e}_y - US_0\boldsymbol{\tau}_0 - UC_0\mathbf{n}_0$ so that projection on the tangent direction and its orthogonal plane using (F.6) yields

$$U_\tau \boldsymbol{\tau} = -US_0\boldsymbol{\tau}_0 - US_0 Y' \mathbf{e}_y \quad , \quad U_N \mathbf{N} = -UC_0\mathbf{n}_0 + \left(\dot{Y} + US_0 Y' \right) \mathbf{e}_y. \quad (\text{F.9})$$

Making use of that decomposition in (5.1) and (5.2), we obtain the linearized fluid loads

$$\mathbf{p}_{am} = -m_a U^2 \left(S_0^2 - \frac{1}{2}C_0^2 \right) \kappa_0 \mathbf{n}_0 - m_a \left(\ddot{Y} + 2US_0 \dot{Y}' + UC_0 \kappa_0 Y' + U^2 \left(\left[S_0^2 + \frac{1}{2}C_0^2 \right] Y' \right)' \right) \mathbf{e}_y \quad (\text{F.10})$$

$$\mathbf{p}_d = \frac{1}{2} \rho C_D D U^2 |C_0| C_0 \mathbf{n}_0 - \frac{1}{2} \rho C_D D U |C_0| \left(\dot{Y} + US_0 Y' \right) \mathbf{e}_y. \quad (\text{F.11})$$

F.1.4 Governing equations

Finally, the linearized structural acceleration reads $\ddot{\mathbf{r}} = \ddot{Y}\mathbf{e}_y$ so that substitution of (F.8),(F.10),(F.11) and (5.3) in the first Kirchhoff equation (F.1) provides, after projection along $\boldsymbol{\tau}_0$ and \mathbf{n}_0 , the leading order system of equation

$$\left(T + \frac{1}{2}EI\kappa_0^2\right)' = 0 \quad , \quad \left(\kappa_0 T - EI\kappa_0''\right) + \frac{1}{2}\rho C_D DU^2 |C_0| C_0 - m_a U^2 \left(S_0^2 - \frac{1}{2}C_0^2\right) \kappa_0 = 0 \quad (\text{F.12})$$

with leading order boundary conditions $\theta_0 = 0$ at $s = 0$ and $T = \kappa_0 = \kappa_0' = 0$ at $s = L$. The first equation provides the expression of the tension $T = -1/2EI\kappa_0^2$. Replacing T in the second equation yields the static equilibrium equation (5.6) after non-dimensionalization. Similarly, projection of (F.1) on \mathbf{e}_y yields

$$\begin{aligned} m\ddot{Y} = & \left((T - EI\kappa_0^2) Y'' - \frac{3}{2}EI (\kappa_0^2)' Y' - E I Y^{(4)} \right) \\ & - m_a \left(\ddot{Y} + 2US_0\dot{Y}' + UC_0\kappa_0 Y' + U^2 \left(\left[S_0^2 + \frac{1}{2}C_0^2 \right] Y' \right)' \right) \\ & - \frac{1}{2}\rho C_D DU |C_0| \left(\dot{Y} + US_0 Y' \right) + \frac{1}{4}\rho C_L^0 DU^2 C_0^2 q \quad (\text{F.13}) \end{aligned}$$

which gives the VIV equation (5.7) after replacement of the tension and non-dimensionalization.

F.2 Validity of the linearization

The model derived above and used throughout Chapter 5 is based on the assumption that the only relevant source of nonlinearity in the dynamics comes from the damping term in the Van der Pol wake oscillator. This term is indeed sufficient to ensure the saturation of the vibration amplitude in the limit-cycle to a magnitude consistent with physical observations. However, the linearization leading to the governing equation for the structure (5.7) relies on the assumption that the transverse displacement Y is a small perturbation to the leading order deformation $\mathbf{r}_0(s)$, while the amplitude of the limit-cycle oscillations due to VIVs is not infinitesimal. Thus, the adequacy of the linearization detailed in Appendix F.1 for modeling VIVs requires verification.

The linearization of the structural model performed in Appendix F.1.2 is purely geometrical and holds as long as $Y \ll L$. The numerical results displayed on Fig. 5.7(a) and 5.9(a) indicate that the amplitude of the transverse perturbation does not exceed $Y \lesssim 0.5D$ in the case of VIVs. The geometrical linearization thus still holds in the limit-cycle for the slender structures considered in this work $\Lambda = L/D \gg 1$.

On the other hand, the linearization of the fluid forces performed in Appendix F.1.3 relies on the additional assumption that the transverse velocity is small compared to the

free-stream $\dot{Y} \ll U$. The frequency of the VIVs is approximately equal to $f_w^0 = S_t U/D$ as shown on Fig. 5.3. Assuming an amplitude $Y \sim 0.5D$ and with $S_t = 0.2$, the order of magnitude of the transverse velocity scales as $\dot{Y} \sim 2\pi f_w^0 Y \sim 0.6U$, which is at the mathematical limit of validity of the linearization. Nonetheless, considering only the linear contribution of the fluid forces in the dynamic equation is consistent with the leading-order nature of the models generally used in VIV studies involving wake oscillator models (Skop and Luo, 2001; Facchinetti et al., 2004b; Mathelin and de Langre, 2005; Mukundan et al., 2009). A more detailed discussion about the appropriateness of such an approximation can be found in Skop and Balasubramanian (1997). If the nonlinearity in the Van der Pol wake oscillator is critical in the limitation of the amplitude of the vibrations in the limit-cycle, we expect that the influence of other nonlinearities should be less significant on a qualitative point of view. More details about the influence of nonlinearities arising from the structure, the fluid forces, or the coupling between them can be found in Srinil and Zanganeh (2012).

Finally, when the system becomes unstable to flutter, the amplitude of the oscillations becomes too large for the geometrical linearization of Appendix F.1.2 to remain valid. In this case, nonlinear coupling between the transverse and in-plane directions in the structural equation would eventually lead to a complex large-amplitude 3D motion.

Appendix G

Linear analysis for the transverse vibrations

G.1 Linear stability analysis for the coupled wake-structure system

To perform the linear stability analysis of the coupled system (5.7)-(5.8), we neglect the nonlinear term in Eq. (5.8) and assume a perturbation of the form $(Y, q)(s, t) = (\phi(s), \psi(s)) e^{i\omega t}$. The coupled system (5.7)-(5.8) then yields

$$\begin{aligned} & -v^2\omega^2\phi + i\omega\frac{\beta v^2}{S_t\Lambda} [2S_0\phi' + C_0(\kappa_0 + c_d\Lambda)\phi] \\ & + \left(\left[\frac{\beta v^2}{S_t^2\Lambda^2} \left(S_0^2 + \frac{1}{2}C_0^2 \right) + \frac{3}{2}\kappa_0^2 \right] \phi' \right)' + c_d\frac{\beta v^2}{S_t^2\Lambda} C_0 S_0 \phi' + \phi^{(4)} - c_l\frac{\beta v^2}{S_t^2} C_0^2 \psi = 0 \end{aligned} \quad (\text{G.1})$$

$$-\omega^2(\psi - A\phi) - i\omega\varepsilon(2\pi C_0)\psi + (2\pi C_0)^2\psi = 0 \quad (\text{G.2})$$

with boundary conditions $\phi = \phi' = 0$ at $s = 0$ and $\phi'' = \phi''' = 0$ at $s = 1$. We then solve the coupled quadratic eigenvalue problem (G.1)-(G.2) at the discretization points with the MatLab function `quadeig` of Hammarling et al. (2013). The linear frequency f_{lin} and growth rate σ of the linear modes are then related to the eigenvalues thus found by $\omega = 2\pi f_{lin} - i\sigma$.

G.2 Thresholds for the transverse flutter instability

The destabilization of the structural modes is due to the influence of the reactive force in the structural equation (5.7), and the effect of the oscillatory lift force due to the wake is most likely negligible in this regard. To compute the stability threshold for the structural modes only, we may thus neglect the coupling between equations (5.7)-(5.8) and consider exclusively the left-hand side of (5.7). Besides, the frequency of shedding f_w^0 is irrelevant in this case and we rescale the dimensional time with respect to the characteristic structural time $T_s = L^2\sqrt{(m + m_a)/EI}$ (as in Chapter 4) instead of f_w^0 . The governing equation then reduces to

$$\ddot{Y} + u\sqrt{\beta} \left[2S_0\dot{Y}' + C_0(\kappa_0 + c_d\Lambda)\dot{Y} \right] + \left(\left[u^2 \left(S_0^2 + \frac{1}{2}C_0^2 \right) + \frac{3}{2}\kappa_0^2 \right] Y' \right)' + c_d\Lambda u^2 C_0 S_0 Y' + Y^{(4)} = 0 \quad (\text{G.3})$$

where the flutter-specific reduced velocity $u = UL\sqrt{m_a/EI}$ (similar to that used in Chapter 4) is related to the VIV-specific reduced velocity used throughout Chapter 5 through $v = (S_t/\sqrt{\beta})\Lambda u$, and to the Cauchy number through $C_Y = c_d\Lambda u^2$. The stability thresholds found by linear stability analysis of Eq. (G.3) for $\beta = 0.5$ and three different aspect ratios are provided in Table G.1 in terms of the three parameters u , v and C_Y .

The threshold for $\Lambda = 10$ in terms of the VIV-specific reduced velocity $v_c = 35.8$ is very close to that found in Section 5.3.3 for the coupled system (5.7)-(5.8), $v_c = 34.9$. This confirms the very limited influence of the wake coupling on the structural stability. Besides, the thresholds expressed in term of the flutter-specific reduced velocity u seems almost insensitive to the aspect ratio Λ . Consequently, according to the scalings of the VIV-specific reduced velocity $v \propto \Lambda u$ and Cauchy number $C_Y \propto \Lambda u^2$ provided here, the stability thresholds in terms of both these parameters is close to proportional to the aspect ratio Λ .

	critical velocity u_c	critical velocity v_c	critical Cauchy number $C_{Y,c}$
$\Lambda = 10$	12.7	3.58×10^1	2.04×10^3
$\Lambda = 10^2$	16.1	4.55×10^2	3.30×10^4
$\Lambda = 10^3$	17.1	4.85×10^3	3.74×10^5

Table G.1: Structural stability thresholds in terms of the flutter-specific reduced velocity u , VIV-specific reduced velocity v , and Cauchy number C_Y .

Bibliography

- J. Aberle and J. Järvelä. Flow resistance of emergent rigid and flexible floodplain vegetation. *Journal of Hydraulic Research*, 51(1):33–45, 2013.
- J.D. Ackerman and A. Okubo. Reduced mixing in a marine macrophyte canopy. *Functional Ecology*, pages 305–309, 1993.
- S. Alben. The flapping-flag instability as a nonlinear eigenvalue problem. *Physics of Fluids*, 20(10):104106, 2008.
- S. Alben. Self-similar bending in a flow: The axisymmetric case. *Physics of Fluids*, 22(8):081901, 2010.
- S. Alben and M.J. Shelley. Flapping states of a flag in an inviscid fluid: bistability and the transition to chaos. *Physical review letters*, 100(7):074301, 2008.
- S. Alben, M. Shelley, and J. Zhang. Drag reduction through self-similar bending of a flexible body. *Nature*, 420(6915):479–481, 2002.
- S. Alben, M. Shelley, and J. Zhang. How flexibility induces streamlining in a two-dimensional flow. *Physics of Fluids*, 16(5):1694–1713, 2004.
- E.F. Albertoni, C. Palma-Silva, C.R.T. Trindade, and L.M. Furlanetto. Field evidence of the influence of aquatic macrophytes on water quality in a shallow eutrophic lake over a 13-year period. *Acta Limnologica Brasiliensia*, 26(2):176–185, 2014.
- M.E. Anderson, J. McKee Smith, and S.K. McKay. Wave dissipation by vegetation. *ERDC CHETN-I-82*, 2011.
- G.O. Antoine, E. de Langre, and S. Michelin. Optimal energy harvesting from vortex-induced vibrations of cables. *Proceedings of the Royal Society of London A: Mathematical, Physical and Engineering Sciences*, 468(2147), 2016.
- R.F. Arellano Castro, L. Guillaumot, A. Cros, and C. Eloy. Non-linear effects on the resonant frequencies of a cantilevered plate. *Journal of Fluids and Structures*, 46:165–173, 2014.
- G.R.S. Assi, N. Srinil, C.M. Freire, and I. Korkischko. Experimental investigation of the flow-induced vibration of a curved cylinder in convex and concave configurations. *Journal of Fluids and Structures*, 44:52–66, 2014.
- B. Audoly and Y. Pomeau. *Elasticity and geometry: from hair curls to the non-linear response of shells*. Oxford University Press, Oxford, UK, 2010.

- K.D. Bal, T.J. Bouma, K. Buis, E. Struyf, S. Jonas, H. Backx, and P. Meire. Trade-off between drag reduction and light interception of macrophytes: comparing five aquatic plants with contrasting morphology. *Functional Ecology*, 25(6):1197–1205, 2011.
- S. Balasubramanian, R.A. Skop, F.L. Haan, and A.A. Szewczyk. Vortex-excited vibrations of uniform pivoted cylinders in uniform and shear flow. *Journal of Fluids and Structures*, 14(1):65–85, 2000.
- T. Barois and E. de Langre. Flexible body with drag independent of the flow velocity. *Journal of Fluid Mechanics*, 735:R2, 2013.
- D.S. Barrett, M.S. Triantafyllou, D.K.P. Yue, M.A. Grosenbaugh, and M.J. Wolfgang. Drag reduction in fish-like locomotion. *Journal of Fluid Mechanics*, 392:183–212, 1999.
- S. Barsu, D. Doppler, J. John Soundar Jerome, N. Rivière, and M. Lance. Drag measurements in laterally confined 2d canopies: Reconfiguration and sheltering effect. *Physics of Fluids*, 28(10):107101, 2016.
- P.W. Bearman. Circular cylinder wakes and vortex-induced vibrations. *Journal of Fluids and Structures*, 27(5):648–658, 2011.
- M.M. Bernitsas, K. Raghavan, Y. Ben-Simon, and E.M. Garcia. Vivace (vortex induced vibration aquatic clean energy): A new concept in generation of clean and renewable energy from fluid flow. *Journal of Offshore Mechanics and Arctic Engineering*, 130(4):041101, 2008.
- P.M. Berry, M. Sterling, J.H. Spink, C.J. Baker, R. Sylvester-Bradley, S.J. Mooney, A.R. Tams, and A.R. Ennos. Understanding and reducing lodging in cereals. *Advances in Agronomy*, 84:217–271, 2004.
- G. Birkhoff and E.H. Zarantonello. *Jets, wakes and cavities*. New York: Academic Press, 1957.
- Y. Birot, D. Terrasson, T. Formery, and B. Roman-Amat. *Expertise Collective sur les tempêtes, la sensibilité des forêts, et sur leur reconstitution*. ECOFOR, 2000.
- R.E.D. Bishop and A.Y. Hassan. The lift and drag forces on a circular cylinder in a flowing fluid. *Proceedings of the Royal Society of London A: Mathematical, Physical and Engineering Sciences*, 277(1368):32–50, 1964.
- R.D. Blevins. *Flow-induced vibration*. Van Nostrand Reinhold Company, New York, NY, USA, 1990.
- M.L. Boller and E. Carrington. The hydrodynamic effects of shape and size change during reconfiguration of a flexible macroalga. *Journal of Experimental Biology*, 209(10):1894–1903, 2006.

-
- R. Bourguet, D. Lucor, and M.S. Triantafyllou. Mono- and multi-frequency vortex-induced vibrations of a long tensioned beam in shear flow. *Journal of Fluids and Structures*, 32:52–64, 2012.
- R. Bourguet, G.E. Karniadakis, and M.S. Triantafyllou. Multi-frequency vortex-induced vibrations of a long tensioned beam in linear and exponential shear flows. *Journal of Fluids and Structures*, 41:33–42, 2013.
- R. Bourguet, G.E. Karniadakis, and M.S. Triantafyllou. On the validity of the independence principle applied to the vortex-induced vibrations of a flexible cylinder inclined at 60° . *Journal of Fluids and Structures*, 53:58–69, 2015.
- C.G. Broyden. A class of methods for solving nonlinear simultaneous equations. *Mathematics of computation*, 19(92):577–593, 1965.
- F. Candelier, F. Boyer, and A. Leroyer. Three-dimensional extension of Lighthill’s large-amplitude elongated-body theory of fish locomotion. *Journal of Fluid Mechanics*, 674:196–226, 2011.
- S.R. Carpenter and D.M. Lodge. Effects of submersed macrophytes on ecosystem processes. *Aquatic Botany*, 26:341–370, 1986.
- A.C. Carruthers and A. Filippone. Aerodynamic drag of streamers and flags. *Journal of aircraft*, 42(4):976–982, 2005.
- S.K. Chakrabarti. *The theory and practice of hydrodynamics and vibration*. World scientific, NJ, USA, 2002.
- Y.B. Chang and P.M. Moretti. Flow-induced vibration of free edges of thin films. *Journal of fluids and structures*, 16(7):989–1008, 2002.
- J.R. Chaplin, P.W. Bearman, F.J. Huera Huarte, and R.J. Pattenden. Laboratory measurements of vortex-induced vibrations of a vertical tension riser in a stepped current. *Journal of Fluids and Structures*, 21(1):3–24, 2005.
- A.J. Clark, W. Landolt, J.B. Bucher, and R.J. Strasser. How wind affects the photosynthetic performance of trees: quantified with chlorophyll a fluorescence and open-top chambers. *Photosynthetica*, 38(3):349–360, 2000.
- B.S.H. Connell and D.K.P. Yue. Flapping dynamics of a flag in a uniform stream. *Journal of Fluid Mechanics*, 581:33–67, 2007.
- H.L. Dai, L. Wang, Q. Qian, and Q. Ni. Vortex-induced vibrations of pipes conveying fluid in the subcritical and supercritical regimes. *Journal of Fluids and Structures*, 39:322–334, 2013.
- H.L. Dai, L. Wang, Q. Qian, and Q. Ni. Vortex-induced vibrations of pipes conveying pulsating fluid. *Ocean Engineering*, 77:12–22, 2014.

- C.R. Darwin. *On the Origin of Species by Means of Natural Selection, or the Preservation of Favoured Races in the Struggle for Life*. John Murray, 1859.
- S.K. Datta and W.G. Gottenberg. Instability of an elastic strip hanging in an airstream. *Journal of Applied Mechanics*, 42(1):195–198, 1975.
- E. de Langre. Frequency lock-in is caused by coupled-mode flutter. *Journal of Fluids and Structures*, 22(6):783–791, 2006.
- E. de Langre. Effects of wind on plants. *Annual Review of Fluid Mechanics*, 40:141–168, 2008.
- E. de Langre, M.P. Païdoussis, O. Doaré, and Y. Modarres-Sadeghi. Flutter of long flexible cylinders in axial flow. *Journal of Fluid Mechanics*, 571:371–389, 2007.
- E. de Langre, A. Gutierrez, and J. Cossé. On the scaling of drag reduction by reconfiguration in plants. *Comptes Rendus Mecanique*, 340(1):35–40, 2012.
- A. de Vecchi, S.J. Sherwin, and J.M.R. Graham. Wake dynamics of external flow past a curved circular cylinder with the free-stream aligned to the plane of curvature. *Journal of Fluids and Structures*, 24(8):1262–1270, 2008.
- K.W. Demes, J.N. Pruitt, C.D.G. Harley, and E. Carrington. Survival of the weakest: increased frond mechanical strength in a wave-swept kelp inhibits self-pruning and increases whole-plant mortality. *Functional Ecology*, 27(2):439–445, 2013.
- M.W. Denny. Extreme drag forces and the survival of wind-and water-swept organisms. *Journal of Experimental Biology*, 194(1):97–115, 1994.
- M.W. Denny. Are there mechanical limits to size in wave-swept organisms? *Journal of Experimental Biology*, 202(23):3463–3467, 1999.
- M.W. Denny and B. Cowen. Flow and flexibility. II. The roles of size and shape in determining wave forces on the bull kelp *Nereocystis luetkeana*. *Journal of experimental biology*, 200(24):3165–3183, 1997.
- M.W. Denny, T.L. Daniel, and M.A.R. Koehl. Mechanical limits to size in wave-swept organisms. *Ecological Monographs*, 55(1):69–102, 1985.
- M.W. Denny, B. Gaylord, B. Helmuth, and T. Daniel. The menace of momentum: dynamic forces on flexible organisms. *Limnology and Oceanography*, 43(5):955–968, 1998.
- G.-J. Dong and X.-Y. Lu. Numerical analysis on the propulsive performance and vortex shedding of fish-like travelling wavy plate. *International Journal for Numerical Methods in Fluids*, 48(12):1351–1373, 2005.

-
- C. Dupuis and J. Rousselet. The equations of motion of curved pipes conveying fluid. *Journal of Sound and Vibration*, 153(3):473–489, 1992.
- C. Eloy, C. Souilliez, and L. Schouveiler. Flutter of a rectangular plate. *Journal of Fluids and Structures*, 23(6):904–919, 2007.
- C. Eloy, N. Kofman, and L. Schouveiler. The origin of hysteresis in the flag instability. *Journal of Fluid Mechanics*, 691:583–593, 2012.
- A.R. Ennos. The aerodynamics and hydrodynamics of plants. *Journal of Experimental Biology*, 202(23):3281–3284, 1999.
- M.L. Facchinetti, E. de Langre, and F. Biolley. Coupling of structure and wake oscillators in vortex-induced vibrations. *Journal of Fluids and Structures*, 19(2):123–140, 2004a.
- M.L. Facchinetti, E. de Langre, and F. Biolley. Vortex-induced travelling waves along a cable. *European Journal of Mechanics-B/Fluids*, 23(1):199–208, 2004b.
- R.A. Fairthorne. Drag of flags. In *Aeronautical Research Committee Reports and Memoranda*, number 1345, pages 887–891. Her Majesty Stationery Office, London, UK, 1930.
- G.R. Franzini, A.L.C. Fugarra, J.R. Meneghini, I. Korkischko, and R. Franciss. Experimental investigation of vortex-induced vibration on rigid, smooth and inclined cylinders. *Journal of Fluids and Structures*, 25(4):742–750, 2009.
- M.T. Friedland and M.W. Denny. Surviving hydrodynamic forces in a wave-swept environment: consequences of morphology in the feather boa kelp, *Egregia menziesii* (Turner). *Journal of Experimental Marine Biology and Ecology*, 190(1):109–133, 1995.
- B. Gaylord and M.W. Denny. Flow and flexibility. I. Effects of size, shape and stiffness in determining wave forces on the stipitate kelps *Eisenia arborea* and *Pterygophora californica*. *Journal of Experimental Biology*, 200(24):3141–3164, 1997.
- B. Gaylord, C.A. Blanchette, and M.W. Denny. Mechanical consequences of size in wave-swept algae. *Ecological monographs*, 64(3):287–313, 1994.
- B. Gaylord, B.B. Hale, and M.W. Denny. Consequences of transient fluid forces for compliant benthic organisms. *Journal of Experimental Biology*, 204(7):1347–1360, 2001.
- B. Gaylord, M.W. Denny, and M.A.R. Koehl. Modulation of wave forces on kelp canopies by alongshore currents. *Limnology and Oceanography*, 48(2):860–871, 2003.

- B. Gaylord, M.W. Denny, and M.A.R. Koehl. Flow forces on seaweeds: field evidence for roles of wave impingement and organism inertia. *The Biological Bulletin*, 215(3): 295–308, 2008.
- F. Ge, W. Lu, L. Wang, and Y.-S. Hong. Shear flow induced vibrations of long slender cylinders with a wake oscillator model. *Acta Mechanica Sinica*, 27(3):330, 2011.
- M. Ghisalberti and H.M. Nepf. Mixing layers and coherent structures in vegetated aquatic flows. *Journal of Geophysical Research: Oceans*, 107(C2), 2002.
- F. Gosselin and E. de Langre. Drag reduction by reconfiguration of a poroelastic system. *Journal of Fluids and Structures*, 27(7):1111–1123, 2011.
- F. Gosselin, E. de Langre, and B.A. Machado-Almeida. Drag reduction of flexible plates by reconfiguration. *Journal of Fluid Mechanics*, 650:319–341, 2010.
- P.S. Gurugubelli and R.K. Jaiman. Self-induced flapping dynamics of a flexible inverted foil in a uniform flow. *Journal of Fluid Mechanics*, 781:657–694, 2015.
- S. Hammarling, C.J. Munro, and F. Tisseur. An algorithm for the complete solution of quadratic eigenvalue problems. *ACM Transactions on Mathematical Software (TOMS)*, 39(3):18, 2013.
- D.L. Harder, O. Speck, C.L. Hurd, and T. Speck. Reconfiguration as a prerequisite for survival in highly unstable flow-dominated habitats. *Journal of Plant Growth Regulation*, 23(2):98–107, 2004.
- R.T. Hartlen and I.G. Currie. Lift-oscillator model of vortex-induced vibration. *Journal of the Engineering Mechanics Division*, 96(5):577–591, 1970.
- M. Hassani, N.W. Mureithi, and F. Gosselin. Large coupled bending and torsional deformation of an elastic rod subjected to fluid flow. *Journal of Fluids and Structures*, 62:367–383, 2016.
- S. Henriquez and A. Barrero-Gil. Reconfiguration of flexible plates in sheared flow. *Mechanics Research Communications*, 62:1–4, 2014.
- P.-Y. Henry, D. Myrhaug, and J. Aberle. Drag forces on aquatic plants in nonlinear random waves plus current. *Estuarine, Coastal and Shelf Science*, 165:10–24, 2015.
- R.C. Highsmith. Reproduction by fragmentation in corals. *Marine Ecology Progress Series*, pages 207–226, 1982.
- S.F. Hoerner. Fluid dynamic drag. 1965. *Bricktown, NJ: Published by the author*, 1965.
- L. Huang. Flutter of cantilevered plates in axial flow. *Journal of Fluids and Structures*, 9(2):127–147, 1995.

-
- E. Inoue. Studies of the phenomena of waving plants (“honami”) caused by wind. *Journal of Agricultural Meteorology*, 11(3):87–90, 1955.
- M.J. Jaffe. Thigmomorphogenesis: the response of plant growth and development to mechanical stimulation. *Planta*, 114(2):143–157, 1973.
- A. Jain and Y. Modarres-Sadeghi. Vortex-induced vibrations of a flexibly-mounted inclined cylinder. *Journal of Fluids and Structures*, 43:28–40, 2013.
- N. Jauvtis and C.H.K. Williamson. Vortex-induced vibration of a cylinder with two degrees of freedom. *Journal of Fluids and Structures*, 17(7):1035–1042, 2003.
- N. Jauvtis and C.H.K. Williamson. The effect of two degrees of freedom on vortex-induced vibration at low mass and damping. *Journal of Fluid Mechanics*, 509:23–62, 2004.
- M.M. Jensen and M.W. Denny. Life in an extreme environment: Characterizing wave-imposed forces in the rocky intertidal zone using high temporal resolution hydrodynamic measurements. *Limnology and Oceanography*, 61(5):1750–1761, 2016.
- G.H. Keulegan and L.H. Carpenter. Forces on cylinders and plates in an oscillating fluid. *Journal of Research of the National Bureau of Standards*, 60(5):423–440, 1958.
- A. Khalak and C.H.K. Williamson. Fluid forces and dynamics of a hydroelastic structure with very low mass and damping. *Journal of Fluids and Structures*, 11(8):973–982, 1997.
- A. Khalak and C.H.K. Williamson. Motions, forces and mode transitions in vortex-induced vibrations at low mass-damping. *Journal of Fluids and Structures*, 13(7-8):813–851, 1999.
- D. Kim and M. Gharib. Flexibility effects on vortex formation of translating plates. *Journal of Fluid Mechanics*, 677:255–271, 2011.
- R. King. An investigation of vortex-induced vibrations of sub-sea communications cables. In *Proceedings of the 6th International Conference on Flow-Induced Vibration, London, UK*, pages 443–454, 1995.
- M.A. Koehl. Ecological biomechanics of benthic organisms: life history, mechanical design and temporal patterns of mechanical stress. *Journal of Experimental Biology*, 202(23):3469–3476, 1999.
- M.A.R. Koehl. How do benthic organisms withstand moving water? *American Zoologist*, 24(1):57–70, 1984.
- M.A.R. Koehl and R.S. Alberte. Flow, flapping, and photosynthesis of *Nereocystis leutkeana*: a functional comparison of undulate and flat blade morphologies. *Marine Biology*, 99(3):435–444, 1988.

- M.A.R. Koehl, W.K. Silk, H. Liang, and L. Mahadevan. How kelp produce blade shapes suited to different flow regimes: a new wrinkle. *Integrative and Comparative Biology*, 48(6):834–851, 2008.
- A. Kornecki, E.H. Dowell, and J. O’Brien. On the aeroelastic instability of two-dimensional panels in uniform incompressible flow. *Journal of Sound and Vibration*, 47(2):163–178, 1976.
- K.A. Krumhansl, K.W. Demes, E. Carrington, and C.D.G. Harley. Divergent growth strategies between red algae and kelps influence biomechanical properties. *American Journal of Botany*, 102(11):1938–1944, 2015.
- C. Lemaitre, P. Hémon, and E. de Langre. Instability of a long ribbon hanging in axial air flow. *Journal of Fluids and Structures*, 20(7):913–925, 2005.
- M.J. Lighthill. Note on the swimming of slender fish. *Journal of fluid Mechanics*, 9(2):305–317, 1960.
- M.J. Lighthill. Large-amplitude elongated-body theory of fish locomotion. *Proceedings of the Royal Society of London. Series B. Biological Sciences*, 179(1055):125–138, 1971.
- D. Lopez. *Modeling reconfiguration strategies in plants submitted to flow*. PhD thesis, Ecole Polytechnique, Paris, 2012.
- D. Lopez, S. Michelin, and E. de Langre. Flow-induced pruning of branched systems and brittle reconfiguration. *Journal of Theoretical Biology*, 284(1):117–124, 2011.
- D. Lopez, C. Eloy, S. Michelin, and E. de Langre. Drag reduction, from bending to pruning. *Europhysics Letters*, 108(4):48002, 2014.
- D. Lucor and G.E. Karniadakis. Effects of oblique inflow in vortex-induced vibrations. *Flow, Turbulence and Combustion*, 71(1-4):375–389, 2003.
- D. Lucor, H. Mukundan, and M.S. Triantafyllou. Riser modal identification in CFD and full-scale experiments. *Journal of Fluids and Structures*, 22(6):905–917, 2006.
- M. Luhar and H.M. Nepf. Flow-induced reconfiguration of buoyant and flexible aquatic vegetation. *Limnology and Oceanography*, 56(6):2003–2017, 2011.
- M. Luhar and H.M. Nepf. From the blade scale to the reach scale: a characterization of aquatic vegetative drag. *Advances in Water Resources*, 51:305–316, 2013.
- M. Luhar and H.M. Nepf. Wave-induced dynamics of flexible blades. *Journal of Fluids and Structures*, 61:20–41, 2016.

-
- M. Luhar, E. Infantes, and H.M. Nepf. Seagrass blade motion under waves and its impact on wave decay. *Journal of Geophysical Research: Oceans*, 122:3736–3752, 2017.
- T.S. Lundgren, P.R. Sethna, and A.K. Bajaj. Stability boundaries for flow induced motions of tubes with an inclined terminal nozzle. *Journal of Sound and Vibration*, 64(4):553–571, 1979.
- H. Marcollo and J.B. Hinwood. On shear flow single mode lock-in with both cross-flow and in-line lock-in mechanisms. *Journal of Fluids and structures*, 22(2):197–211, 2006.
- L. Mathelin and E. de Langre. Vortex-induced vibrations and waves under shear flow with a wake oscillator model. *European Journal of Mechanics-B/Fluids*, 24(4):478–490, 2005.
- D. Meng and L. Chen. Nonlinear free vibrations and vortex-induced vibrations of fluid-conveying steel catenary riser. *Applied Ocean Research*, 34:52–67, 2012.
- R.A. Merriam. Fog drip from artificial leaves in a fog wind tunnel. *Water Resources Research*, 9(6):1591–1598, 1973.
- S. Michelin and O. Doaré. Energy harvesting efficiency of piezoelectric flags in axial flows. *Journal of Fluid Mechanics*, 714:489–504, 2013.
- S. Michelin, S.G. Llewellyn Smith, and B.J. Glover. Vortex shedding model of a flapping flag. *Journal of Fluid Mechanics*, 617:1–10, 2008.
- O. Miler, I. Albayrak, V.I. Nikora, and M. O’Hare. Biomechanical properties of aquatic plants and their effects on plant–flow interactions in streams and rivers. *Aquatic Sciences*, 74(1):31–44, 2012.
- A. Miliou, A. de Vecchi, S.J. Sherwin, and J.M.R. Graham. Wake dynamics of external flow past a curved circular cylinder with the free stream aligned with the plane of curvature. *Journal of Fluid Mechanics*, 592:89–115, 2007.
- L.A. Miller, A. Santhanakrishnan, S. Jones, C. Hamlet, K. Mertens, and L. Zhu. Re-configuration and the reduction of vortex-induced vibrations in broad leaves. *Journal of Experimental Biology*, 215(15):2716–2727, 2012.
- P.M. Moretti. Tension in fluttering flags. *International Journal of Acoustics and Vibration*, 8(4):227–230, 2003.
- J.R. Morison, J.W. Johnson, and S.A. Schaaf. The force exerted by surface waves on piles. *Journal of Petroleum Technology*, 2(05):149–154, 1950.
- C.K. Morooka and R.I. Tsukada. Experiments with a steel catenary riser model in a towing tank. *Applied Ocean Research*, 43:244–255, 2013.

- M.T. Morris-Thomas and S. Steen. Experiments on the stability and drag of a flexible sheet under in-plane tension in uniform flow. *Journal of Fluids and Structures*, 25(5):815–830, 2009.
- B. Moulia, C. Der Loughian, R. Bastien, O. Martin, M. Rodríguez, D. Gourcilleau, A. Barbacci, E. Badel, G. Franchel, C. Lenne, et al. Integrative mechanobiology of growth and architectural development in changing mechanical environments. In *Mechanical integration of plant cells and plants*, pages 269–302. Springer, 2011.
- H. Mukundan, Y. Modarres-Sadeghi, J.M. Dahl, F.S. Hover, and M.S. Triantafyllou. Monitoring VIV fatigue damage on marine risers. *Journal of Fluids and Structures*, 25(4):617–628, 2009.
- J.C. Mullarney and S.M. Henderson. Wave-forced motion of submerged single-stem vegetation. *Journal of Geophysical Research: Oceans*, 115:C12061, 2010.
- Q. Ni, M. Li, M. Tang, Y. Wang, Y. Luo, and L. Wang. In-plane and out-of-plane free vibration and stability of a curved rod in flow. *Journal of Fluids and Structures*, 49:667–686, 2014.
- B.R. Noack, F. Ohle, and H. Eckelmann. On cell formation in vortex streets. *Journal of Fluid Mechanics*, 227:293–308, 1991.
- T.-A. Okamoto and I. Nezu. Turbulence structure and “monami” phenomena in flexible vegetated open-channel flows. *Journal of Hydraulic Research*, 47(6):798–810, 2009.
- M.P. Païdoussis. *Fluid-structure interactions: slender structures and axial flow*, volume 2. Academic Press, London, 1998.
- M.P. Païdoussis, E. Grinevich, D. Adamovic, and C. Semler. Linear and nonlinear dynamics of cantilevered cylinders in axial flow. part 1: physical dynamics. *Journal of Fluids and Structures*, 16(6):691–713, 2002.
- M.P. Païdoussis, S.J. Price, and E. de Langre. *Fluid-structure interactions: cross-flow-induced instabilities*. Cambridge University Press, 2010.
- R.W. Pearcy. Sunflecks and photosynthesis in plant canopies. *Annual Review of Plant Biology*, 41(1):421–453, 1990.
- M. Piñeirua, B. Thiria, and R. Godoy-Diana. Modelling of an actuated elastic swimmer. *Journal of Fluid Mechanics*, 829:731–750, 2017.
- S. Puijalon, G. Bornette, and P. Sagnes. Adaptations to increasing hydraulic stress: morphology, hydrodynamics and fitness of two higher aquatic plant species. *Journal of Experimental Botany*, 56(412):777–786, 2005.
- C. Py, E. de Langre, and B. Moulia. A frequency lock-in mechanism in the interaction between wind and crop canopies. *Journal of Fluid Mechanics*, 568:425–449, 2006.

-
- J.S. Roden. Modeling the light interception and carbon gain of individual fluttering aspen (*Populus tremuloides* Michx) leaves. *Trees-Structure and Function*, 17(2):117–126, 2003.
- J.S. Roden and R.W. Pearcy. Effect of leaf flutter on the light environment of poplars. *Oecologia*, 93(2):201–207, 1993.
- M. Rudnicki, S.J. Mitchell, and M.D. Novak. Wind tunnel measurements of crown streamlining and drag relationships for three conifer species. *Canadian Journal of Forest Research*, 34(3):666–676, 2004.
- J. E Sader, J. Cossé, D. Kim, B. Fan, and M. Gharib. Large-amplitude flapping of an inverted flag in a uniform steady flow—a vortex-induced vibration. *Journal of Fluid Mechanics*, 793:524–555, 2016.
- K. Sand-Jensen. Drag and reconfiguration of freshwater macrophytes. *Freshwater Biology*, 48(2):271–283, 2003.
- T. Sarpkaya. A critical review of the intrinsic nature of vortex-induced vibrations. *Journal of Fluids and Structures*, 19(4):389–447, 2004.
- L. Schouveiler and A. Boudaoud. The rolling up of sheets in a steady flow. *Journal of Fluid Mechanics*, 563:71–80, 2006.
- L. Schouveiler, C. Eloy, and P. Le Gal. Flow-induced vibrations of high mass ratio flexible filaments freely hanging in a flow. *Physics of Fluids*, 17(4):047104, 2005.
- C. Semler, J.L. Lopes, N. Augu, and M.P. Païdoussis. Linear and nonlinear dynamics of cantilevered cylinders in axial flow. part 3: Nonlinear dynamics. *Journal of Fluids and Structures*, 16(6):739–759, 2002.
- B. Seyed-Aghazadeh, C. Budz, and Y. Modarres-Sadeghi. The influence of higher harmonic flow forces on the response of a curved circular cylinder undergoing vortex-induced vibration. *Journal of Sound and Vibration*, 353:395–406, 2015.
- M.J. Shelley and J. Zhang. Flapping and bending bodies interacting with fluid flows. *Annual Review of Fluid Mechanics*, 43:449–465, 2011.
- K. Singh, S. Michelin, and E. de Langre. Energy harvesting from axial fluid-elastic instabilities of a cylinder. *Journal of Fluids and Structures*, 30:159–172, 2012a.
- K. Singh, S. Michelin, and E. de Langre. The effect of non-uniform damping on flutter in axial flow and energy-harvesting strategies. *Proceedings of the Royal Society of London A: Mathematical, Physical and Engineering Sciences*, 468(2147):3620–3635, 2012b.

- F. Siniscalchi and V.I. Nikora. Flow-plant interactions in open-channel flows: A comparative analysis of five freshwater plant species. *Water Resources Research*, 48(5), 2012.
- F. Siniscalchi and V.I. Nikora. Dynamic reconfiguration of aquatic plants and its interrelations with upstream turbulence and drag forces. *Journal of Hydraulic Research*, 51(1):46–55, 2013.
- R.A. Skop and S. Balasubramanian. A new twist on an old model for vortex-excited vibrations. *Journal of Fluids and Structures*, 11(4):395–412, 1997.
- R.A. Skop and G. Luo. An inverse-direct method for predicting the vortex-induced vibrations of cylinders in uniform and nonuniform flows. *Journal of Fluids and Structures*, 15(6):867–884, 2001.
- N. Srinil. Multi-mode interactions in vortex-induced vibrations of flexible curved/straight structures with geometric nonlinearities. *Journal of Fluids and Structures*, 26(7):1098–1122, 2010.
- N. Srinil. Analysis and prediction of vortex-induced vibrations of variable-tension vertical risers in linearly sheared currents. *Applied Ocean Research*, 33(1):41–53, 2011.
- N. Srinil and H. Zanganeh. Modelling of coupled cross-flow/in-line vortex-induced vibrations using double duffing and van der pol oscillators. *Ocean Engineering*, 53: 83–97, 2012.
- N. Srinil, M. Wiercigroch, and P. O’Brien. Reduced-order modelling of vortex-induced vibration of catenary riser. *Ocean Engineering*, 36(17):1404–1414, 2009.
- N. Srinil, H. Zanganeh, and A. Day. Two-degree-of-freedom VIV of circular cylinder with variable natural frequency ratio: Experimental and numerical investigations. *Ocean Engineering*, 73:179–194, 2013.
- S. Starko and P.T. Martone. Evidence of an evolutionary-developmental trade-off between drag avoidance and tolerance strategies in wave-swept intertidal kelps (laminariales, phaeophyceae). *Journal of Phycology*, 52(1):54–63, 2016.
- S. Taneda. Waving motions of flags. *Journal of the Physical Society of Japan*, 24(2): 392–401, 1968.
- C. Tang, N.-S. Liu, and X.-Y. Lu. Dynamics of an inverted flexible plate in a uniform flow. *Physics of Fluids*, 27(7):073601, 2015.
- G.I. Taylor. Analysis of the swimming of long and narrow animals. *Proceedings of the Royal Society of London. Series A. Mathematical and Physical Sciences*, 214(1117): 158–183, 1952.

-
- J.W. Thomas. *Numerical partial differential equations: finite difference methods*, volume 22. Springer Science & Business Media, 1995.
- E.G. Tickner and A.H. Sacks. Engineering simulation of the viscous behavior of whole blood using suspensions of flexible particles. *Circulation research*, 25(4):389–400, 1969.
- A.D. Trim, H. Braaten, H. Lie, and M.A. Tognarelli. Experimental investigation of vortex-induced vibration of long marine risers. *Journal of Fluids and Structures*, 21(3):335–361, 2005.
- J.R. Usherwood, A.R. Ennos, and D.J. Ball. Mechanical and anatomical adaptations in terrestrial and aquatic buttercups to their respective environments. *Journal of Experimental Botany*, 48(7):1469–1475, 1997.
- B. Utter and M.W. Denny. Wave-induced forces on the giant kelp *Macrocystis pyrifera* (Agardh): field test of a computational model. *Journal of Experimental Biology*, 199(12):2645–2654, 1996.
- M.S. Van den Berg, H. Coops, M.-L. Meijer, M. Scheffer, and J. Simons. Clear water associated with a dense chara vegetation in the shallow and turbid lake veluwemeer, the netherlands. In *The structuring role of submerged macrophytes in lakes*, pages 339–352. Springer, 1998.
- J.K. Vandiver. Drag coefficients of long flexible cylinders. In *Offshore Technology Conference*. Offshore Technology Conference, 1983.
- J.K. Vandiver. Dimensionless parameters important to the prediction of vortex-induced vibration of long, flexible cylinders in ocean currents. *Journal of Fluids and Structures*, 7(5):423–455, 1993.
- R. Violette, E. de Langre, and J. Szydlowski. Computation of vortex-induced vibrations of long structures using a wake oscillator model: comparison with DNS and experiments. *Computers & Structures*, 85(11):1134–1141, 2007.
- R. Violette, E. de Langre, and J. Szydlowski. A linear stability approach to vortex-induced vibrations and waves. *Journal of Fluids and Structures*, 26(3):442–466, 2010.
- E. Viot, X. Amandolese, and P. Hémon. Fluttering flags: an experimental study of fluid forces. *Journal of Fluids and Structures*, 43:385–401, 2013.
- S. Vogel. Drag and flexibility in sessile organisms. *American Zoologist*, 24(1):37–44, 1984.
- S. Vogel. Drag and reconfiguration of broad leaves in high winds. *Journal of Experimental Botany*, 40(8):941–948, 1989.

- S. Vollsinger, S.J. Mitchell, K.E. Byrne, M.D. Novak, and M. Rudnicki. Wind tunnel measurements of crown streamlining and drag relationships for several hardwood species. *Canadian Journal of Forest Research*, 35(5):1238–1249, 2005.
- V. Vuik, S.N. Jonkman, B.W. Borsje, and T. Suzuki. Nature-based flood protection: the efficiency of vegetated foreshores for reducing wave loads on coastal dikes. *Coastal Engineering*, 116:42–56, 2016.
- V. Vuik, H.Y.S. Heo, Z. Zhu, B.W. Borsje, and S.N. Jonkman. Stem breakage of salt marsh vegetation under wave forcing: A field and model study. *Estuarine, Coastal and Shelf Science*, 2017.
- Y. Watanabe, S. Suzuki, M. Sugihara, and Y. Sueoka. An experimental study of paper flutter. *Journal of Fluids and Structures*, 16(4):529–542, 2002.
- W.J. Weaver, S.P. Timoshenko, and D.H. Young. *Vibration problems in engineering*. John Wiley & Sons, Hoboken, NJ, USA, 1990.
- WEB01. Flag tree. URL <http://www.crosthwaiteandlyth.co.uk/images/gallery/winter09-10b/David's%20Flag%20Tree%203.JPG>. Accessed on November 22, 2017.
- P. Whittaker, C.A.M.E. Wilson, J. Aberle, H.P. Rauch, and P. Xavier. A drag force model to incorporate the reconfiguration of full-scale riparian trees under hydrodynamic loading. *Journal of Hydraulic Research*, 51(5):569–580, 2013.
- P. Whittaker, C.A.M.E. Wilson, and J. Aberle. An improved cauchy number approach for predicting the drag and reconfiguration of flexible vegetation. *Advances in Water Resources*, 83:28–35, 2015.
- A. Wilk and M. Skuta. Laboratory tests of the aerodynamic drag coefficient of the flag as a body with low stiffness. *Task Quarterly*, 13(1-2):5–14, 2009.
- C.H.K. Williamson. Vortex dynamics in the cylinder wake. *Annual Review of Fluid Mechanics*, 28(1):477–539, 1996.
- C.H.K. Williamson and R. Govardhan. Vortex-induced vibrations. *Annual Review of Fluid Mechanics*, 36:413–455, 2004.
- C.H.K. Williamson and R. Govardhan. A brief review of recent results in vortex-induced vibrations. *Journal of Wind Engineering and Industrial Aerodynamics*, 96(6-7):713–735, 2008.
- C.A.M.E. Wilson, P. Xavier, T. Schoneboom, J. Aberle, H.P. Rauch, W. Lammeranner, C. Weissteiner, and H. Thomas. The hydrodynamic drag of full scale trees. *Fluvial Hydraulics River Flow*, pages 453–459, 2010.
- X. Wu, F. Ge, and Y. Hong. A review of recent studies on vortex-induced vibrations of long slender cylinders. *Journal of Fluids and Structures*, 28:292–308, 2012.

- Y. Yadykin, V. Tenetov, and D. Levin. The flow-induced vibration of a flexible strip hanging vertically in a parallel flow part 1: Temporal aeroelastic instability. *Journal of Fluids and Structures*, 15(8):1167–1185, 2001.
- K. Yamazaki. Gone with the wind: trembling leaves may deter herbivory. *Biological Journal of the Linnean Society*, 104(4):738–747, 2011.
- X. Yang and M. Liu. Bending modes and transition criteria for a flexible fiber in viscous flows. *Journal of Hydrodynamics*, 28(6):1043–1048, 2016.
- X. Yang, M. Liu, and S. Peng. Smoothed particle hydrodynamics and element bending group modeling of flexible fibers interacting with viscous fluids. *Physical Review E*, 90(6):063011, 2014.
- H. Zhu, P. Lin, and J. Yao. An experimental investigation of vortex-induced vibration of a curved flexible pipe in shear flows. *Ocean Engineering*, 121:62–75, 2016.
- L. Zhu. Viscous flow past a flexible fibre tethered at its centre point: vortex shedding. *Journal of Fluid Mechanics*, 587:217–234, 2007.
- L. Zhu. Scaling laws for drag of a compliant body in an incompressible viscous flow. *Journal of Fluid Mechanics*, 607:387–400, 2008.
- L. Zhu and C.S. Peskin. Drag of a flexible fiber in a 2D moving viscous fluid. *Computers & fluids*, 36(2):398–406, 2007.

Publications

- T. Leclercq and E. de Langre. Drag reduction by elastic reconfiguration of non-uniform beams in non-uniform flows. *Journal of Fluids and Structures*, 60:114–129, 2016. doi: 10.1016/j.jfluidstructs.2015.10.007.
- T. Leclercq and E. de Langre. Reconfiguration of elastic blades in oscillatory flow. *Journal of Fluid Mechanics*, 838:606–630, 2018a. doi: 10.1017/jfm.2017.910.
- T. Leclercq, N. Peake, and E. de Langre. Does flutter prevent drag reduction by reconfiguration? *Proceedings of the Royal Society of London A: Mathematical, Physical and Engineering Sciences*, 474:20170678, 2018. doi: 10.1098/rspa.2017.0678.
- T. Leclercq and E. de Langre. Vortex-induced vibrations of cylinders bent by the flow. *submitted to the Journal of Fluids and Structures*, 2018b. (under revision).



Drag reduction by elastic reconfiguration of non-uniform beams in non-uniform flows



Tristan Leclercq*, Emmanuel de Langre

Department of Mechanics, LadHyX, CNRS, École Polytechnique, 91128 Palaiseau, France

ARTICLE INFO

Article history:

Received 11 June 2015

Accepted 18 October 2015

Keywords:

Drag reduction

Elastic reconfiguration

Vogel exponent

Non-uniform flow

Self-similarity

ABSTRACT

Flexible systems bending in steady flows are known to experience a lesser drag compared to their rigid counterpart. Through a careful dimensional analysis, an analytical expression of the Vogel exponent quantifying this reduction of drag is derived for cantilever beams, within a framework based on spatial self-similar modelling of the flow and structural properties at the clamped edge of the structure. Numerical computations are performed on various situations, including systems involving more complex distributions of the flow or structural parameters. The scaling of drag versus flow velocity for large loadings is shown to be well predicted by fitting the system properties by simple power laws at the scale of the length on which significant bending occurs. Ultimately, the weak sensitivity of the Vogel exponent to the parameters of the system provides an explanation to the rather reduced scattering of the Vogel exponents around -1 observed on most natural systems in aquatic or aerial vegetation.

© 2015 Elsevier Ltd. All rights reserved.

1. Introduction

It has been well known, since the seminal work of Vogel (1984), that flexible structures subjected to fast flows experience a drag F that grows slower with the velocity than if they were rigid. When the velocity U of the flow exceeds a given threshold, the classical quadratic velocity–drag law that holds for rigid bodies at large Reynolds number changes to a smaller power law $F \propto U^{2+\nu}$ characterized by the so-called Vogel exponent ν , which is negative. This phenomenon is for instance broadly observed in nature. Indeed, plants growing in fast flow environments are very often made of flexible tissues that bend to comply with the flow, hence lowering the risk of failure by fracture or uprooting.

To get a better understanding of the underlying mechanisms, Alben et al. (2002, 2004) first studied the model problem of an elastic one dimensional fibre in an inviscid two dimensional flow, both experimentally and numerically. Their study revealed the importance of a single control parameter, which they call the elasto-hydrodynamical number, related to the more commonly used Cauchy number C_γ (Tickner and Sacks, 1969; Chakrabarti, 2002; de Langre, 2008), that scales the competing effects of fluid loading to the elastic restoring force. The model of Alben et al. (2002, 2004) exhibits the expected transition from the classical rigid-body U^2 drag scaling law to a new $U^{4/3}$ drag law concomitant with the convergence towards a self-similar shape at large Cauchy numbers. Gosselin et al. (2010) obtained similar results for a finite width plate with a simplified model of fluid loading. They also managed to predict the same asymptotic drag scaling law from a very simple dimensional analysis. In order to explain the drag reduction due to the rolling up of daffodil leaves originally

* Corresponding author.

E-mail addresses: leclercq@ladhyx.polytechnique.fr (T. Leclercq), delangre@ladhyx.polytechnique.fr (E. de Langre).

observed by Vogel (1984), Schouveiler and Boudaoud (2006) obtained theoretical and experimental estimates of the Vogel exponent for circular plastic sheets cut along a radius. They found a drag scaling as $U^{2/3}$, while a theoretical and numerical study by Alben (2010) on the same system concludes that the drag increases as U^1 . Recent studies have proposed models that account for additional effects such as gravity (Luhar and Nepf, 2011), viscosity (Zhu and Peskin, 2007; Zhu, 2008), shear background flow (Henriquez and Barrero-Gil, 2014) or unsteady wake effects due to vortex shedding at the edges (Yang et al., 2014).

Many experimental measurements made either in the field or in the laboratory have also been able to provide estimates of the Vogel exponents for systems as diverse as full trees, grasses, flowers, leaves, near-shore marine macrophytes or freshwater algae. Some quite comprehensive reviews such as Harder et al. (2004) or de Langre et al. (2012) list Vogel exponents varying in a range around -0.7 , between 0 and -1.3 at most for such systems. What is especially striking is not the scattering of Vogel exponents found for different systems, but much more the robustness of the drag reduction phenomenon with respect to the great variability of structural and flow configurations, and the rather narrow range in which the Vogel exponents usually lie. From the assumption that the scaling of drag reduction results from the loss of one typical length scale, de Langre et al. (2012) showed that the Vogel exponent of any structure made of beams and plates (such as most plants) should exhibit approximately the same behaviour. By a simple dimensional analysis, they recovered the classical $-2/3$ Vogel exponent found by Alben et al. (2002, 2004) and Gosselin et al. (2010). They further claimed that non-linearity in the material constitutive law should have little impact on the scaling of drag. Any possible effect of flow or structural non-uniformities was however not addressed in this study, and nor was it, to the authors' knowledge, in any other one, with the only exception of Henriquez and Barrero-Gil (2014) in the specific case of shear flow. A range of models is clearly missing to fill the gap between the idealized cases above and the more complex natural configurations.

The goal of the present work is to provide a general framework for the derivation of the Vogel exponent of a flexible beam in the limit of large velocity flows. It includes most possible non-uniformities in the flow or structural parameters, but it excludes the additional effects of viscosity, unsteadiness in the wake or in the background flow, or other external forces such as gravity. In some aspects, it is a generalization of the works of Gosselin et al. (2010), de Langre et al. (2012) and Luhar and Nepf (2011).

In Section 2, the general framework of this study is described. In Section 3, a theoretical analysis of drag reduction of a system described by self-similar fluid and structural parameters is presented. In Section 4, the results of numerical simulations performed on several practical cases are given. Finally, Section 5 discusses the implications of the present results regarding the understanding and the predictability of the typical values of the Vogel exponents of actual systems. A nomenclature of the main variables used throughout this paper is given in Table 1.

2. Model

The model used in this paper is represented in Fig. 1. The elastic body is a cantilever beam of length L bending in the xz -plane. The width W , thickness D and material stiffness may all vary with the curvilinear coordinate s . The height $z(s)$ and

Table 1
Nomenclature.

$L, W(s), D(s)$	Length, width and thickness of the beam
$EI(s)$	Bending stiffness in the case of linear elasticity
$C_D(s)$	Cross-section drag coefficient
$\rho(z)$	Fluid density distribution
$U(z), U_0$	Flow profile and reference velocity
$\theta(s), \kappa(s)$	Inclination angle of the beam from the vertical axis and curvature
$m(s), m_0$	Internal bending moment and reference value
$f_n(s)$	Internal shear force
$q(s), q_0$	Local normal fluid load and reference value
$c(\theta)$	Angular dependence of the normal fluid load
$g(\kappa), \alpha$	Function and exponent associated with the material constitutive law
$b(s), b_0, \beta$	Distribution, reference and exponent associated with the stiffness factor
$w(s), w_0, \gamma$	Distribution, reference and exponent associated with the cross-section shape factor
$p(z), p_0, \mu$	Distribution, reference and exponent associated with the pressure
ϕ, ψ	Geometrical and material parameter
F, F_{rigid}	Drag force on the flexible/rigid beam
\mathcal{R}	Reconfiguration number
C_Y	Cauchy number
ν, ν_∞	Local and asymptotic Vogel exponents
ℓ	Characteristic non-dimensional bending length
L_B	Characteristic non-dimensional boundary layer thickness
δ	Characteristic non-dimensional tapering length

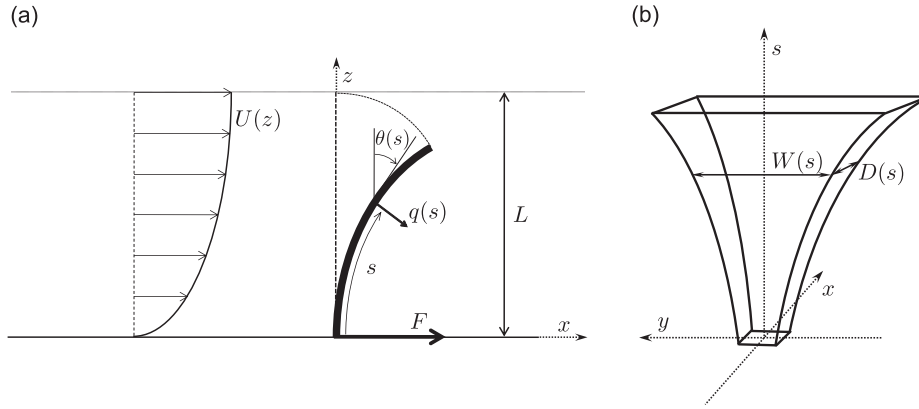


Fig. 1. Description of the system. (a) Side view of the beam bending in the flow. (b) Front view of the unbent structure.

curvature $\kappa(s)$ are related to the local angle of the beam with the vertical axis $\theta(s)$ by the kinematic relationships:

$$z = \int_0^s \cos \theta(s') ds', \quad \kappa = \frac{\partial \theta}{\partial s}. \quad (1)$$

We assume a rather general form of the constitutive law relating the internal bending moment m to the curvature κ :

$$m(s, \kappa) = b(s)g(\kappa), \quad (2)$$

where $b(s)$ is a local coefficient that accounts for the local stiffness and geometry, while $g(\kappa)$ is characteristic of the material constitutive law, which we take to be uniform on the beam. For instance, in the case of linear elasticity, $g(\kappa) = \kappa$ and $b(s) = EI(s)$ is the local bending stiffness of the beam. Under the assumption that the local radius of curvature $1/\kappa$ remains large compared to the thickness D ($\kappa D \ll 1$), Kirchoff's equations for rods (see for instance [Audoly and Pomeau, 2010](#)) relates the internal shear force f_n to the internal bending moment m by

$$f_n = -\frac{\partial m}{\partial s}. \quad (3)$$

We further assume that the structure is placed in a horizontal flow $U(z)$ of a fluid of density ρ . Both U and ρ may vary with the vertical coordinate z , [Fig. 1a](#) only displaying a velocity profile $U(z)$ for clarity. We restrict our study to large Reynolds numbers, so that viscosity effects are neglected. The local fluid load q is then purely normal. In the case of uniform flow, it is usually considered that the normal fluid load includes one term due to the so-called “reactive force” ($\sim \rho U^2 W D \kappa$ in the steady limit of the model of [Lighthill, 1971](#), see also [Candelier et al., 2011](#)) and one other term due to flow separation (“resistive force” $\sim \rho U^2 W$ in the model of [Taylor, 1952](#)). Thus, in the slender body assumption $\kappa D \ll 1$, the resistive force is dominant. We assume that this is still the case for our vertically varying flow, and so we take q as purely resistive and independent of the body curvature. We assume a somewhat general form

$$q(s, z, \theta) = p(z)w(s)c(\theta), \quad (4)$$

where $p(z)$ accounts for the local dynamic pressure due to the undisturbed background flow at height z on the beam, $w(s)$ is a shape coefficient that accounts for the interactions of the normal flow with the local cross-section, and $c(\theta)$ is a projection term due to the local angle of the cross-section with respect to the background flow. It is not always obvious that the s - and θ -dependency can be decoupled, as the structure of the boundary layer and of the recirculating flow downstream will be modified by the angle of incidence. However, it is usually considered that to the first order, the resistive normal force only depends on the interaction between the cross-section and the flow in a plane normal to it, hence the expression chosen. The most classical example of such model is the resistive pressure drag derived by [Taylor \(1952\)](#): $q = 1/2 \rho C_D W U_n^2$ where ρ is the fluid density, W the local width of the structure, $U_n = U \cos \theta$ the normal projection of the local flow velocity, and C_D a drag coefficient that accounts for the shape of the local cross-section. Specifically, Taylor's model is equivalent to considering

$$p(z) = \frac{1}{2} \rho(z) U^2(z), \quad w(s) = C_D(s) W(s), \quad c(\theta) = \cos^2 \theta. \quad (5)$$

Note that the model chosen here only gives an approximation of the exact loading. In particular, the modifications of the flow caused by the structure itself are neglected. However, the close similarity of the results obtained, on the one hand by [Gosselin et al. \(2010\)](#) with the present model, and on the other hand by [Alben et al. \(2002, 2004\)](#) who computed the pressure force distribution on the actual structure using a much more complex algorithm, indicates that the exact form of the force has little impact on the asymptotic scaling of the drag. Unless otherwise stated, $c(\theta) = \cos^2 \theta$ is used everywhere in the rest of this paper. The framework of the present paper includes the study of the influence of the still unspecified form of $g(\kappa)$, $b(s)$, $w(s)$, and $p(z) \propto U^2(z)$. Note that the dynamic pressure due to the background flow at a given point in space does not depend on the position of the structure, so $p(z)$ only depends on the Cartesian coordinate z (assuming the flow is invariant in the x -direction). On the other hand, the elasticity factor $b(s)$ and the cross-section shape coefficient $w(s)$ are structural properties that are specific to a given location along the beam span s , even though the Cartesian coordinates (x, z)

of that physical point change as the beam bends. The internal bending moment $m(s)$ depends on the curvilinear coordinate s explicitly via the local stiffness factor $b(s)$, but also implicitly via the local value of the curvature $\kappa(s)$ in the material constitutive law $g(\kappa)$.

Following [Luhar and Nempf \(2011\)](#), the local equilibrium at a given point s^* between the local internal shear force and the normal fluid load yields the governing equation

$$\frac{\partial m}{\partial s} \Big|_{s^*} = - \int_{s^*}^L q(s) \cos(\theta(s) - \theta(s^*)) ds, \tag{6}$$

where the force-free boundary condition $f_n=0$ at the free end $s=L$ has been used. Non-dimensionalizing this equation yields one governing parameter called the Cauchy number

$$C_Y = \frac{q_0 L}{m_0/L} \sim \frac{\text{typical external fluid load}}{\text{typical elastic restoring force}}, \tag{7}$$

considering that q_0 and m_0 are the orders of magnitude of the fluid load q and internal moment m in Eq. (6). Besides, the total drag of the beam reads

$$F = \int_0^L q(s) \cos(\theta(s)) ds. \tag{8}$$

The focus of this paper is the scaling of the drag force, F , with the velocity of the flow. In the case of a flow that may not be uniform, we have to choose a reference velocity U_0 that scales the velocity at any point in the flow field. We are then interested in the variations of the Vogel exponent ν such that F scales as $U_0^{2+\nu}$, noted $F \propto U_0^{2+\nu}$. At large Reynolds number and in the limit of a rigid structure, the drag force is expected to grow as U_0^2 . Following [Gosselin et al. \(2010\)](#), to isolate the contribution of flexibility to the velocity–drag law, we define the reconfiguration number

$$\mathcal{R} = \frac{F}{F_{\text{rigid}}}, \tag{9}$$

so that $\mathcal{R} \propto U_0^\nu$. The actual governing parameter being the Cauchy number, we will prefer to work in the C_Y – \mathcal{R} space rather than the U_0 – F space. The Cauchy number being proportional to the typical fluid load $q_0 \propto U_0^2$, the local Vogel exponent can be computed directly in the C_Y – \mathcal{R} space as

$$\nu = 2 \frac{\partial \log \mathcal{R}}{\partial \log C_Y}. \tag{10}$$

A schematic view of the correspondence between the three different representations of a velocity–drag relationship is displayed in [Fig. 2](#) in arbitrary units. The Vogel exponent displayed in [Fig. 2c](#) corresponds to twice the slope of the loglog plot $\mathcal{R}(C_Y)$ shown in [Fig. 2b](#). In this particular case, the Vogel exponent asymptotically goes to -1 for large Cauchy numbers, so that the velocity–drag law goes from quadratic to linear.

In the remaining of this paper, unless otherwise stated, the Cauchy number is always defined based on the flow and structural properties at the tip of the upright beam.

3. Drag reduction in a self-similar framework

First, we further assume that the pressure, cross-section shape and stiffness parameters $p(z)$, $w(s)$ and $b(s)$ can be expressed as power functions of their respective arguments, namely

$$p(z) = p_0 \left(\frac{z}{L}\right)^\mu, \quad w(s) = w_0 \left(\frac{s}{L}\right)^\gamma, \quad b(s) = b_0 \left(\frac{s}{L}\right)^\beta. \tag{11}$$

Note that, although these power-law formulations of the structural parameters w and b may recall those of [Lopez et al.](#)

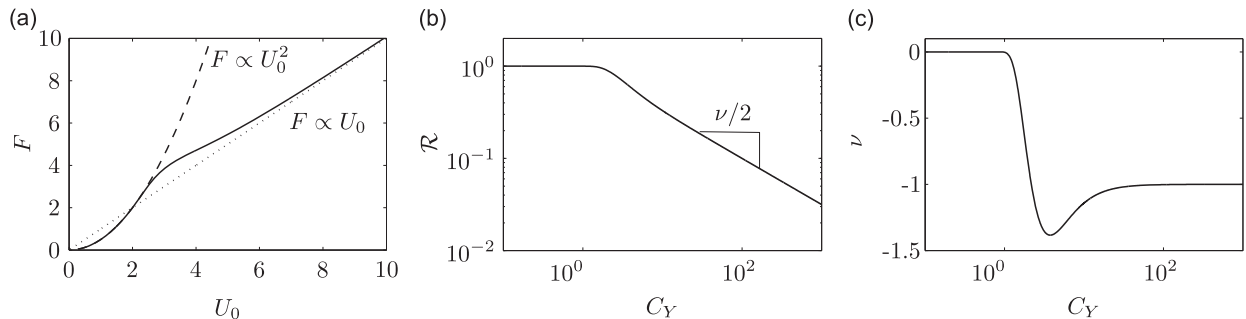


Fig. 2. Schematic view of the loading–drag relationship in the different parameter spaces (arbitrary units). U_0 : reference flow velocity, F : drag force, C_Y : Cauchy number, \mathcal{R} : Reconfiguration number, and ν : Vogel exponent.

(2011) for a slender cone, or those of Lopez et al. (2014) for a tree-like structure, they actually describe quite different distributions because the curvilinear coordinate s used in these papers was defined from the free tip towards the floor instead of the other way around here. We also assume that the material constitutive law may differ from linear elasticity by considering a more general dependency on curvature, still in the form of a power law

$$g(\kappa) = \kappa^\alpha. \quad (12)$$

Substituting (11) and (12) and the particular form $c(\theta) = \cos^2\theta$ into (6), the equilibrium equation reads

$$\frac{\partial}{\partial s}(s^\beta \kappa^\alpha) \Big|_{s^*} = -C_Y \int_{s^*}^1 \left(\int_0^s \cos \theta(s') ds' \right)^\mu s^\gamma \cos^2(\theta) \cos(\theta - \theta^*) ds, \quad (13)$$

where all the space variables have been made non-dimensional using the beam length L , and the Cauchy number C_Y has been defined as

$$C_Y = \frac{p_0 w_0 L}{b_0 L^{-1-\alpha}}. \quad (14)$$

From (8), the total drag force on the beam in this framework reads

$$F = p_0 w_0 L \int_0^1 \left(\int_0^s \cos \theta(s') ds' \right)^\mu s^\gamma \cos^3(\theta) ds. \quad (15)$$

We further assume that the drag is bounded by that on a rigid structure, namely

$$F_{\text{rigid}} = p_0 w_0 L \int_0^1 s^{\mu+\gamma} ds = \frac{p_0 w_0 L}{1+\mu+\gamma}. \quad (16)$$

For this quantity to be finite, it is required that $\mu+\gamma > -1$. Using (9), (15) and (16), the reconfiguration number now reads

$$\mathcal{R} = (1+\mu+\gamma) \int_0^1 \left(\int_0^s \cos \theta(s') ds' \right)^\mu s^\gamma \cos^3(\theta) ds. \quad (17)$$

Within this framework, the asymptotic Vogel exponent for large Cauchy numbers, noted ν_∞ , can now be inferred from a dimensional analysis that accounts for the particular power-like form of the flow and structural parameters. The flow pressure p , the cross-section shape coefficient w and the bending stiffness b are characterized by their respective invariants:

$$\begin{aligned} I_p &= \frac{p(z)}{z^\mu} = \frac{p_0}{L^\mu} [\text{kg m}^{-1-\mu} \text{s}^{-2}], \\ I_w &= \frac{w(s)}{s^\gamma} = \frac{w_0}{L^\gamma} [\text{m}^{1-\gamma}], \\ I_b &= \frac{b(s)}{s^\beta} = \frac{b_0}{L^\beta} [\text{kg m}^{2+\alpha-\beta} \text{s}^{-2}]. \end{aligned} \quad (18)$$

The Vaschy–Buckingham theorem predicts three non-dimensional figures which we choose to be the non-dimensional drag force, the Cauchy number and the aspect ratio:

$$\tilde{F} = \frac{F}{I_p I_w L^{1+\mu+\gamma}}, \quad C_Y = \frac{I_p I_w L^{1+\mu+\gamma}}{I_b L^{-1-\alpha+\beta}}, \quad \Lambda = \frac{w_0}{L}. \quad (19)$$

Following Gosselin et al. (2010), we disregard the effect of the aspect ratio Λ so that the problem reduces to finding the relationship between \tilde{F} and C_Y , or equivalently to determining the function \mathcal{G} such that

$$F = I_p I_w L^{1+\mu+\gamma} \mathcal{G} \left(\frac{I_p I_w L^{2+\mu+\gamma+\alpha-\beta}}{I_b} \right). \quad (20)$$

For highly bent structures, Gosselin et al. (2010) demonstrated that the drag no longer depends on the beam length L . Hence, function \mathcal{G} must be taken as a power function $\mathcal{G}(C_Y) \propto C_Y^\varphi$ that cancels the overall exponent of L in (20), meaning

$$(1+\mu+\gamma) + \varphi(2+\mu+\gamma+\alpha-\beta) = 0. \quad (21)$$

Consequently, the asymptotic drag force scales as

$$F \propto \frac{(I_p I_w)^{1+\varphi}}{I_b^\varphi} \quad \text{with} \quad \varphi = -\frac{1+\mu+\gamma}{2+\mu+\gamma+\alpha-\beta}. \quad (22)$$

We are interested in the scaling of the drag force with the velocity U_0 , which only appears in the flow pressure invariant through $I_p \propto p_0 \propto U_0^2$. Therefore, F scales as $U_0^{2+2\varphi}$ and the asymptotic Vogel exponent naturally appears as $\nu_\infty = 2\varphi$. Ultimately,

$$\nu_\infty = -2 \frac{1+\mu+\gamma}{2+\mu+\gamma+\alpha-\beta}. \quad (23)$$

For a uniform, linearly elastic, rectangular plate bending in a uniform flow, $(\alpha, \beta, \gamma, \mu) = (1, 0, 0, 0)$, so that $\nu_\infty = -2/3$, which is

consistent with Alben et al. (2002, 2004) and Gosselin et al. (2010). In the case of a non-linear stress–strain relationship $\sigma \propto \varepsilon^{1/N}$ considered in de Langre et al. (2012), we get $\alpha = 1/N$ in our model, and so we recover the asymptotic result $\nu_\infty = -(2N)/(2N+1)$.

If it is well known that the effects of flexibility are negligible below $C_Y \sim 1$, no study has ever predicted, to the authors' knowledge, the threshold above which the Vogel exponent should finally reach its asymptotic value. This threshold can however be estimated by looking at the global balance of forces on the beam. Assuming that the beam length L loses its relevance when the beam is highly bent implies that there must exist a smaller region of length ℓ , function of the level of loading only, on which all the significant interactions between the beam and the flow concentrate. This inner region is thus responsible for the dominant contribution to the drag, and show a large curvature responsible for the balancing force. Assuming that the contribution of the region $s > \ell$ to the drag is negligible, (15) gives the dominant contribution to the drag as

$$F \sim p_0 w_0 L \ell^{1+\mu+\gamma}. \quad (24)$$

On the other hand, using (3), (2), (11) and (12), the internal shear force at the base can be roughly estimated as

$$f_n(0) \sim b_0 \ell^\beta (L \ell)^{-1-\alpha} = b_0 L^{-1-\alpha} \ell^{-1-\alpha+\beta}. \quad (25)$$

Balancing these two quantities yields

$$\ell^{-(2+\mu+\gamma+\alpha-\beta)} \sim \frac{p_0 w_0 L}{b_0 L^{-1-\alpha}}, \quad (26)$$

which is the Cauchy number defined in Eq. (14). We now choose the specific value of ℓ as follows:

$$\ell = C_Y^{-(1/(2+\mu+\gamma+\alpha-\beta))}. \quad (27)$$

This analysis highlights the emergence of an intrinsic characteristic length ℓ that characterizes the region of the beam on which the interactions governing its behaviour concentrate. Note that this length differs from the effective length used in Luhar (2012). If ℓ is larger than 1 (or equivalently $C_Y < 1$), the flow interacts with the beam on its whole length and the structural behaviour is close to that of a rigid beam. On the other hand, if $\ell \ll 1$, then the interactions in the region of length ℓ dominate the behaviour of the beam, and so the asymptotic regime is reached. This regime, where the Vogel exponent given by (10) has become constant, should thus be expected to be obtained above a threshold that is expressed in terms of some critical value of ℓ instead of C_Y . Depending on the exponent of the power law relating ℓ to C_Y , the gap between the onset of significant bending ($C_Y=1$) and the convergence of the asymptotic regime ($\ell \ll 1$) might cover a wider or smaller range of loadings. This analysis is consistent with the dimensional analysis above. Indeed, injecting (27) into (24) and using the fact that the pressure of reference p_0 and the Cauchy number C_Y both scale as U_0^2 easily yields

$$F \sim U_0^{2-2(1+\mu+\gamma)/(2+\mu+\gamma+\alpha-\beta)}, \quad (28)$$

and so the asymptotic Vogel exponent given by Eq. (23) is obviously recovered.

Note that the choice of expression (27) to define ℓ is somewhat arbitrary, as no actual ‘‘bending length’’ can be uniquely defined on the physical system. Eq. (27) essentially represents a scaling of the Cauchy number that transforms a ratio of forces into the ratio of some characteristic bending length over the length of the beam. As such, it gives a different interpretation of the Cauchy number, but it does not correspond to a physical quantity that can be easily measured or obtained as the output of a numerical simulation.

4. Applications

4.1. Numerical method

To check the validity of our Eq. (23) for the asymptotic Vogel exponent as well as the predicted threshold discussed above, we numerically compute the Vogel exponent in different cases by solving (13). To solve the integrodifferential equation, we use a first order centred finite difference scheme with the discrete boundary conditions $\theta_1 = 0$, $\theta_{N+1} - \theta_N = 0$ (Thomas, 1995). The integrals are computed by the trapezoidal rule. The resulting non-linear system of equations is solved using a pseudo-Newton solver (so-called method of Broyden, see Broyden, 1965). The beam is discretized with $N=30$ panels. For $C_Y \leq 1$, the beam bends very little, so we use a uniform mesh. When the beam reconfigures significantly, we have seen that its curvature tends to concentrate in a small region of characteristic non-dimensional length ℓ near the clamped edge. In order to model the curved region with accuracy when $C_Y \geq 1$, we use a non-uniform mesh $s_k = (k/(N+1))^\chi$ with $\chi = \log \ell / \log 2$ so that $s_{(N+1)/2} = \ell$, meaning that half of the points are in the curved region $s \leq \ell$. This mesh scales with the characteristic bending length in the curved region, and so it is not necessary to increase the number of points to maintain a good accuracy when the beam is highly bent. Convergence was checked on a few cases by measuring the relative error on the asymptotic Vogel exponent. On all the cases tested, doubling the number of points changed the value of the asymptotic Vogel exponent by less than 0.1%.

4.2. A uniform beam in a shear flow

One first situation that is of particular interest is the case of reconfiguration in a sheared flow. This situation is observed for instance for aquatic organisms in underwater boundary layers or within canopies (see [Luhar, 2012](#)). We consider a plate of constant width W and cross-section drag coefficient C_D , made of a linearly elastic material of uniform bending stiffness EI , deforming in a flow of uniform density ρ with a sheared velocity profile:

$$U = U_0 \left(\frac{z}{L} \right)^{\mu/2}. \quad (29)$$

Assuming Taylor's model for the local fluid load, the parameters of the model specifically read

$$p(z) = \frac{1}{2} \rho U_0^2 \left(\frac{z}{L} \right)^\mu, \quad w(s) = C_D W, \quad c(\theta) = \cos^2 \theta, \quad b(s) = EI, \quad g(\kappa) = \kappa, \quad (30)$$

which corresponds to a constitutive law, stiffness and cross-section shape exponents respectively $(\alpha, \beta, \gamma) = (1, 0, 0)$ with the shear exponent μ being the only varying parameter. Hence, from (23), the theoretical asymptotic Vogel exponent is predicted as

$$\nu_\infty = -2 \frac{1+\mu}{3+\mu}. \quad (31)$$

In the case of a uniform flow $\mu=0$, we recover the classical $\nu_\infty = -2/3$ of [Gosselin et al. \(2010\)](#). From (27), the characteristic bending length reads here

$$\ell = C_Y^{-1/(3+\mu)}. \quad (32)$$

To numerically confirm these predictions, we solve the non-dimensional governing equation Eq. (13) that reads in this specific case:

$$\frac{\partial^2 \theta}{\partial s^2} \Big|_{s^*} = -C_Y \int_{s^*}^1 \left(\int_0^s \cos \theta(s') ds' \right)^\mu \cos^2 \theta(s) \cos(\theta(s) - \theta(s^*)) ds, \quad (33)$$

with the Cauchy number

$$C_Y = \frac{\rho U_0^2 C_D W L^3}{2EI}. \quad (34)$$

[Fig. 3](#) shows the results of the computational approach. In [Fig. 3a](#), the deflection of the beam for increasing loads is shown in the case of a linear flow $\mu/2 = 1$. As expected, significant bending is observed when $C_Y > 1$. The evolution of the reconfiguration number and of the Vogel exponent in [Fig. 3b](#) and [c](#) stresses the existence of two asymptotic regimes. At low Cauchy numbers, the structure behaves as a rigid beam so the Vogel exponent is null no matter the flow profile. At very large Cauchy numbers however, the Vogel exponent converges towards a constant that depends on the shear exponent μ . The asymptotic Vogel exponent numerically obtained for varying flow profiles is plotted in [Fig. 10](#) in the Appendix, for $C_Y = 10^5$ (which implies $\ell = 0.02$ for $\mu/2 = 0$ and $\ell = 0.2$ for $\mu/2 = 2$). It shows excellent agreement with the theoretical value given by (23). We re-plot in [Fig. 4](#) the evolution of the Vogel exponent as a function of the characteristic bending length ℓ given by (32) instead of the Cauchy number C_Y . In the three cases displayed, the Vogel exponent was within 2% of the asymptotic value for $\ell < 0.2$. This confirms that the threshold for the asymptotic regime is well expressed, for any value of the parameter μ , in terms of the same critical value of ℓ .

The asymptotic results shown in [Fig. 10](#) contradict the preliminary results of [Henriquez and Barrero-Gil \(2014\)](#). The origins of these discrepancies are discussed in the Appendix.

4.3. A uniform beam in a Blasius boundary layer

The particular power-like form of the pressure, cross-section shape and stiffness distributions $p(z)$, $w(s)$, $b(s)$, as well as the constitutive law $g(\kappa)$, is a necessary assumption for the theoretical derivation of the asymptotic expression (23) that may appear like a strong limitation of the model above. It seems however that the actual scope of applicability of (23) encompasses a much wider range of practical situations. For highly bent structures, the curvature tends to concentrate in a small "inner" region $s < \ell$ near the clamped edge. As explained in [Alben et al. \(2002, 2004\)](#), the "outer" portion of the system located above ℓ "sits" in the wake created by the deflection of the incident flow heading to the inner region upstream, and so it only endures very little fluid loading. Consequently, the outer domain only has negligible influence on the overall shape and drag of the structure, and only the spatial dependency of the flow and structural parameters inside the inner domain is actually relevant to the modelling of the system. The whole theory above should thus remain valid as long as power function approximations can accurately model these parameters at the scale of ℓ only, and not necessarily at the scale of the whole beam length.

To better understand the implications above, we consider the reconfiguration of a non-tapered, elastic, homogeneous beam, in a Blasius boundary layer. In this case, all the structural parameters are spatially invariant, but the flow exhibits a more intricate shear profile than a simple power-law fit in z . For the sake of clarity, all the space variables have been

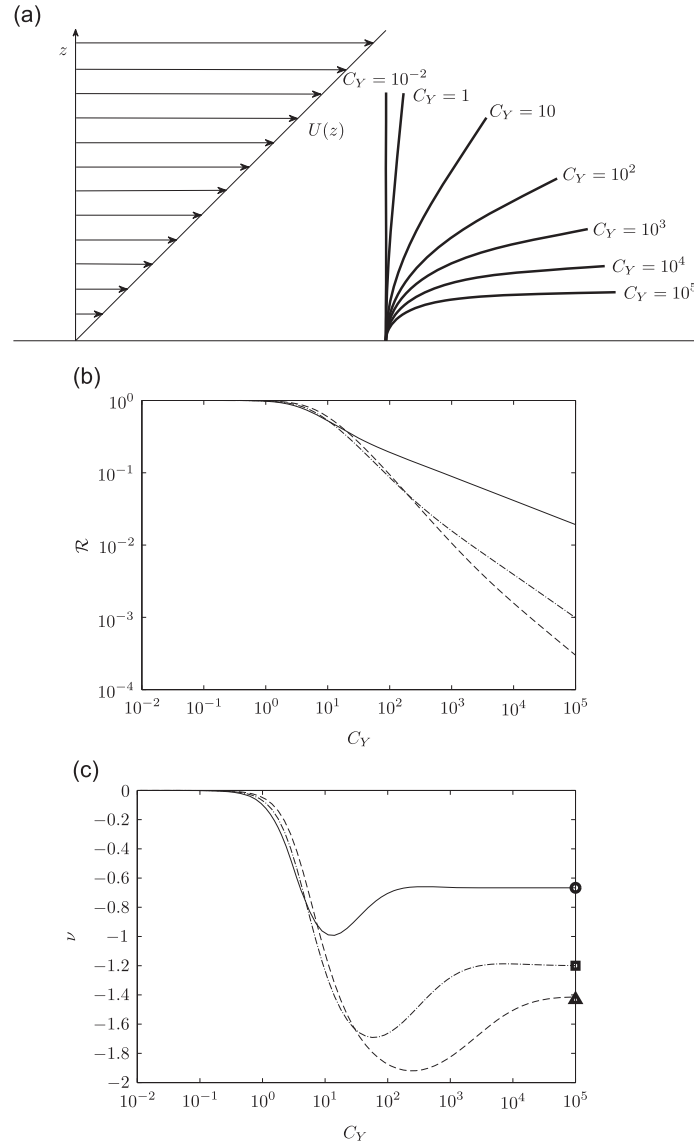


Fig. 3. A uniform beam in a shear flow. (a) Deformation of the beam in a linear flow profile $\mu/2 = 1$. (b) and (c) Reconfiguration number \mathcal{R} and Vogel exponent ν as functions of the Cauchy number C_Y : uniform flow profile $\mu/2 = 0$ (—), linear flow profile $\mu/2 = 1$ (- · -), and quadratic flow profile $\mu/2 = 2$ (---). Asymptotic Vogel exponent predicted by Eq. (23), uniform flow profile $\mu/2 = 0$ (○), linear flow profile $\mu/2 = 1$ (□), and quadratic flow profile $\mu/2 = 2$ (△).

normalized by the length of the beam, or equivalently $L = 1$. In the model of Blasius, the vertical velocity is negligible and the horizontal velocity is expressed as

$$U(x, z) = U_\infty f'(\eta), \tag{35}$$

with the similarity variable $\eta = z\sqrt{R_e^L/x}$, the Reynolds number based on the length of the beam and outer flow velocity R_e^L , and f the solution of the Blasius boundary layer equations:

$$2f''' + ff'' = 0, \quad f(0) = f'(0) = 0, \quad f(\eta) \xrightarrow{\eta \rightarrow \infty} 1. \tag{36}$$

The resulting flow profile, shown in Fig. 5a for a fixed value of x , is characterized by a smooth transition from a linear increase with slope $U_\infty/L_B(x)$ near the wall saturating to a uniform magnitude U_∞ far from it. The two domains are roughly delimited, at each location x , by the dimensionless characteristic length scale

$$L_B(x) = \frac{1}{f''(0)} \sqrt{\frac{x}{R_e^L}}, \tag{37}$$

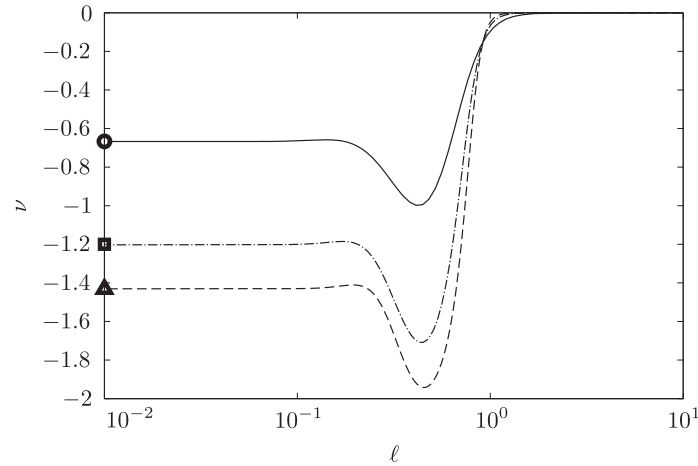


Fig. 4. A uniform beam in a shear flow. Variation of the Vogel exponent in the ℓ - ν space, uniform flow profile $\mu/2 = 0$ (—), linear flow profile $\mu/2 = 1$ (- - -), and quadratic flow profile $\mu/2 = 2$ (- · - ·). Asymptotic Vogel exponent predicted by Eq. (23), uniform flow profile $\mu/2 = 0$ (○), linear flow profile $\mu/2 = 1$ (□), and quadratic flow profile $\mu/2 = 2$ (△).

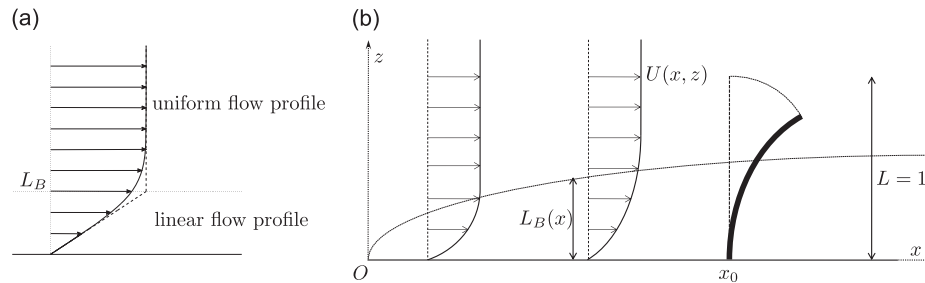


Fig. 5. Description of the reconfiguration in a Blasius boundary layer. (a) Blasius profile $U(x, z)$ at a fixed x . (b) Beam deforming in a Blasius boundary layer.

such that

$$U(x, z) \sim U_\infty \text{ for } z \gg L_B(x) \quad \text{and} \quad U(x, z) \sim \frac{U_\infty}{L_B(x)} z \text{ for } z \ll L_B(x). \quad (38)$$

The approach presented in this paper is based on the assumption that the flow is invariant in the x -direction, and so the x -dependency of the Blasius flow inside the boundary layer would a priori prevent (23) to be valid. However, the region of space swept by the deforming beam extends at most one beam length downstream of its anchorage point x_0 (see Fig. 5b). If the structure is placed far enough from the origin of the boundary layer ($x_0 \gg 1$), then $L_B(x) \sim L_B(x_0)$ anywhere in the vicinity of the beam, and so the flow can be considered locally horizontally invariant. The coexistence of the two flow regimes along the vertical axis makes room for two different characteristic velocities according to (38): $U_0 = U_\infty$ in the uniform domain, and $U_0 = U_\infty/L_B$ in the linear domain. Two Cauchy numbers can subsequently be defined according to (14): $C_{Y,uni}$ is based on the uniform outer flow velocity $U_0 = U_\infty$, while $C_{Y,lin} = C_{Y,uni}/L_B^2$ is based on the inner characteristic velocity $U_0 = U_\infty/L_B$. Fig. 6a displays the evolution of the Vogel exponent as the loading increases, for several fixed values of $L_B \leq 1$. The parameter chosen to describe the fluid loading is the Cauchy number based on the uniform outer flow, $C_{Y,uni}$.

Evidently, if $L_B \geq 1$, then the beam lies entirely in a linearly sheared flow even when it stands upright. This situation is strictly equivalent to the shear flow case studied in Section 4.2 with pressure shear exponent $\mu = 2$, if the Cauchy number C_Y is identified with the linear flow Cauchy number $C_{Y,lin}$. For $L_B = 1$, $C_{Y,lin} = C_{Y,uni}$ and the evolution of the Vogel exponent shown in Fig. 6a, is very similar to the curve obtained for a linear velocity profile in Fig. 3c.

On the other hand, structures reconfiguring in boundary layers smaller than their length ($L_B < 1$) experience much more intricate behaviours. Fig. 6b shows a zoom on the near-wall region of a beam reconfiguring in a Blasius boundary layer a hundred times smaller than its size ($L_B = 10^{-2}$). This plot should be analysed jointly with the corresponding curve in 6a. When the Cauchy number is small, the linear flow region is much smaller than the portion of the beam that experiences significant bending. The inner domain $s < \ell$ is mostly subjected to the uniform flow $U = U_\infty$, and the influence of the linear flow on the very bottom of the beam is negligible. Consequently, the evolution of the Vogel exponent for $C_{Y,uni} < 10^2$ is very similar to that obtained for a uniform flow in Fig. 3c. As the loading increases, the beam bends more and more and as a result the linear flow covers an increasing portion of the inner region. It follows that the Vogel exponent decreases for $C_{Y,uni} > 10^2$. Asymptotically, when the bending region is fully confined inside the boundary layer, the Vogel exponent catches up with the asymptotic value characteristic of linear shear, $\nu_\infty = -6/5$. The same analysis remains valid for other boundary layers smaller than the beam $L_B < 1$. If the loading increases enough, the beam will always eventually dive entirely

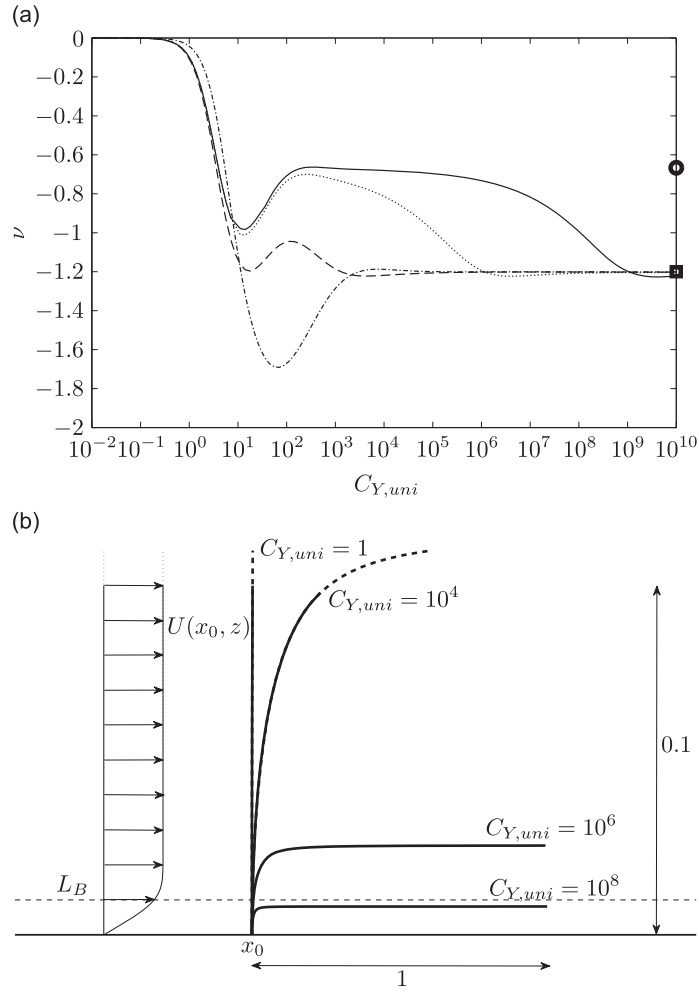


Fig. 6. Reconfiguration in a Blasius boundary layer, anchorage point $x_0 = 10^7$. (a) Vogel exponent ν as a function of the Cauchy number $C_{Y,uni}$, $L_B = 10^{-3}$ (—), $L_B = 10^{-2}$ (···), $L_B = 10^{-1}$ (---), and $L_B = 1$ (- · - ·). Asymptotic Vogel exponent predicted by Eq. (23), uniform flow profile (\circ), and linear flow profile (\square). (b) Zoom near the clamped edge of a beam bending in a Blasius boundary layer, $L_B = 10^{-2}$.

inside the boundary layer and the Vogel exponent will asymptotically reach the theoretical value predicted for a linear flow profile. But the threshold above which this asymptotic regime is reached depends on the thickness of the boundary layer L_B . The larger L_B , the sooner the shear flow will dominate. Precisely, the relative impacts of the uniform and linear flow regions can be estimated by comparing the thickness of the boundary layer L_B to the size of the bending region ℓ . However, the expression of ℓ depends on which of the uniform or linear flow dominates. In the uniform outer flow, (27) yields $\ell_{uni} = C_{Y,uni}^{-1/3}$, while in the linear region it would predict $\ell_{lin} = C_{Y,lin}^{-1/5} = L_B^{2/5} C_{Y,uni}^{-1/5} = L_B^{2/5} \ell_{uni}^{3/5}$. At the threshold between the two regimes, $\ell_{uni} = \ell_{lin} = L_B$, which also yields $C_{Y,uni} = L_B^{-3}$. Note that this threshold specifically sets the lower bound (in terms of the Cauchy number) to the purely linear flow approximation, but the purely uniform flow approximation loses its validity for much smaller loads. Indeed, for ℓ smaller but close to L_B , the region of the beam that concentrates the interaction with the flow is already confined inside the boundary layer so that the influence of the uniform domain above totally vanishes. Conversely, for $\ell > L_B$, the influence of the linear domain never strictly vanishes, and its influence becomes negligible only for $\ell \gg L_B$. This result is consistent with the thresholds for convergence towards the linear regime observed for the different cases in Fig. 6a. For L_B equal to 10^{-1} , 10^{-2} and 10^{-3} , the Vogel exponent was within 2.5% of its expected asymptotic value $\nu_\infty = -6/5$ for $C_{Y,uni}$ respectively superior to $10^{2.9}$, $10^{5.85}$ and $10^{8.8}$. If the thickness of the boundary layer L_B is small enough, the influence of the linear region may remain negligible for loadings large enough to permit convergence of the Vogel exponent in the uniform domain, before it reaches the linear domain. This is observed for instance in Fig. 6a, where the Vogel exponent for $L_B = 10^{-3}$ displays a plateau around the asymptotic uniform flow Vogel exponent $\nu = -2/3$ for $C_{Y,uni} \sim 10^2 - 10^5$, before switching to the asymptotic linear flow Vogel exponent $\nu_\infty = -6/5$ above $C_{Y,uni} \sim L_B^{-3} = 10^9$. On the other hand, for thicker boundary layers ($L_B \geq 10^{-2}$), the influence of the linear domain may not be neglected for loadings large enough to reach convergence in the uniform domain. For $L_B = 10^{-1}$, convergence to the asymptotic regime is approximately concomitant with the switch from uniform to linear flow regime. The small hump around $C_{Y,uni} = 10^2$ illustrates the successive dominance of the uniform flow that tends to bring the Vogel exponent closer to $\nu = -2/3$ as the asymptotic regime approaches, soon overcome by the linear flow whose influence is to decrease it to $\nu = -6/5$. When

$L_B = 1$, the linear flow region dominates as soon as reconfiguration occurs, so the early effects of the uniform domain are not even noticeable in Fig. 6a.

This example shows that our approach based on self-similarity actually provides understanding of the behaviour of much more complex configurations. Strictly speaking, there will always be an asymptotic regime, should it be reached for extremely large Cauchy numbers. Indeed, as the structure bends, curvature always concentrate in a region of characteristic length ℓ that gets smaller and smaller, so that it eventually gets small enough for all the parameters to be well approximated by power laws at its scale. Thus, the actual asymptotic Vogel exponent is given by (23) using the exponents of the first order in the power law expansions of the structural and flow parameters at the foot of the beam. Yet, the threshold above which these power law approximations all hold may be too large to be ever reached in practice. In this case, intermediate asymptotic regimes may arise on whole ranges of Cauchy numbers. We may conclude that convergence of the Vogel exponent towards a constant independent of the loading may occur if the bending length ℓ is either much larger or much smaller than any of the other characteristic length scales involved.

4.4. A non-uniform beam in a uniform flow

To further check the validity of the asymptotic expression (23), we compared it to the numerically computed asymptotic Vogel exponent in some other cases involving variations of the material constitutive law, material stiffness or structural cross-section shape. To make sure that the asymptotic regime was reached in the numerical simulations, a large enough value of the Cauchy number ($C_Y = 10^5$) was chosen so that the characteristic bending length ℓ would be inferior to 0.1 in all cases. The results are shown in Table 2, along with the corresponding ℓ -value. Agreement is excellent in all the cases considered.

A more intricate example is that of a linearly tapered beam of increasing width W , namely

$$W(s) = W_1 + (W_0 - W_1)s, \quad (39)$$

as shown in Fig. 7. In most cases, we would then expect the bending stiffness to also vary, but to highlight the effect of the cross-flow area alone, we assume here that the variations of the cross-sectional shape and elastic modulus are chosen such that the bending stiffness remains uniform. Consistently with (14), we define the Cauchy number as in Eq. (34) using the width at the tip W_0 as characteristic width. Note that the case $W_0 - W_1 = 0$ corresponds to the constant width problem $\gamma = 0$, while the case $W_1 = 0$ corresponds to the linear width problem $\gamma = 1$. We define the characteristic length δ as shown in Fig. 7,

Table 2

Comparison of the theoretical and numerically computed Vogel exponents for varying systems.

System	α	β	γ	μ	Theoretical ν_∞ (23)	Numerical ν at $C_Y = 10^5$	ℓ -Value (27) at $C_Y = 10^5$
Benchmark case	1	0	0	0	$-2/3$	-0.6681	0.02
Elastoplastic behaviour	0.5	0	0	0	-0.8	-0.8013	0.01
Rigid base	1	-1	0	0	-0.5	-0.5006	0.06
Linear width	1	0	1	0	-1	-1.0024	0.06

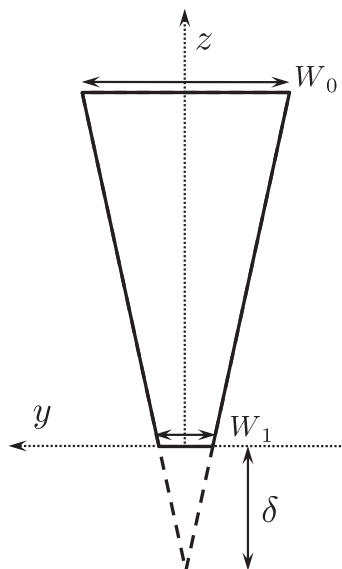


Fig. 7. Tapered beam.

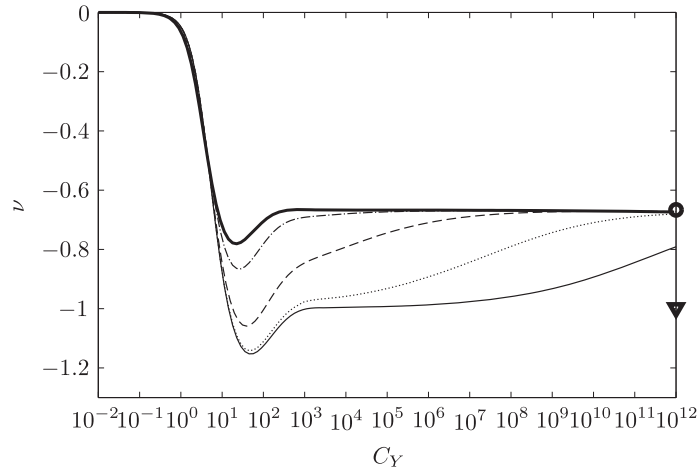


Fig. 8. Vogel exponent ν of a tapered beam for increasing Cauchy numbers C_Y , $\delta = 10^{-3}$ (—), $\delta = 10^{-2}$ (···), $\delta = 10^{-1}$ (---), $\delta = 1$ (- · -), and $\delta = +\infty$ (thick —). Asymptotic Vogel exponent predicted by Eq. (23), constant width (o) and linear width (v).

such that $W(-\delta) = 0$:

$$\delta = \frac{W_1}{W_0 - W_1}. \quad (40)$$

This quantity can be seen as the length on which the width must vary to significantly deviate from W_1 due to the given slope. Notably, the relative gap between $W(s)$ and W_1 can be expressed as

$$\frac{W(s) - W_1}{W_1} = \frac{s}{\delta}. \quad (41)$$

In other words, the quantity δ is a measure of the length of validity of the uniform width approximation, as L_B was characteristic of the length of validity of the linear flow approximation in the Blasius boundary layer. Hence, the evolution of the computed Vogel exponents shown in Fig. 8 for several values of δ and for increasing Cauchy numbers may be explained in a similar fashion. The Vogel exponent converges at large Cauchy numbers towards the theoretical value $\nu_\infty = -2/3$, consistently with the first order W_1 in the power function expansion (39). For $\delta > 1$, the Vogel exponent deviates very little from that of a beam of uniform width ($\delta = \infty$). Conversely, for very small δ such as 10^{-3} , the structure behaves as a beam of linear width, long enough to exhibit an intermediate asymptotic regime $\nu = -1$ on a broad range of loadings. Structures with intermediate δ -values show an earlier shift from linear-like to uniform-like behaviour that do not allow intermediate convergence of the Vogel exponent. Finally, it should be noted that the characteristic bending lengths reads here $\ell = C_Y^{-1/4}$ in the linear width regime. Hence, the threshold between the two regimes, $\ell/\delta = 1$, reads in this case $C_Y \sim \delta^{-4}$. Contrary to the case of reconfiguration in a boundary layer, this threshold here must be thought of as a reference load around which both the uniform and linear terms of the width (39) influence the behaviour of the beam equally. It is not a critical load above or under which one of the two regimes loses all influence. This is so because, while the two flow domains of the boundary layer were spatially separated (above and below L_B), the two terms of $W(s)$ coexist everywhere, including at the clamped edge. If each term can be neglected, respectively far above or far below the threshold $C_Y = \delta^{-4}$, none of them can be ignored in the transition range around this value. This is consistent with the evolutions displayed in Fig. 8. At $C_Y = \delta^{-4}$, the Vogel exponent is equal to -0.79 for all three values $\delta = 10^{-1}$, 10^{-2} and 10^{-3} .

One may wonder what would happen if the width was decreasing from base to tip instead of increasing. In this case, $\delta < -1$ means that the effects of the slope are only noticeable near the tip, but never near the base where the finite value dominates in any case. In other words, the effects of taper may slightly affect the Vogel exponent for low Cauchy numbers, but the drag rapidly resembles that of a beam of constant width W_1 as soon as bending is significant. These expectations are confirmed by numerical simulations, not shown.

These results shed light on the apparent contradiction between the two asymptotic Vogel exponents for a disk cut along many radii derived respectively by numerical computations ($\nu_\infty = -2/3$) and by dimensional analysis ($\nu_\infty = -1$) in Gosselin et al. (2010). In the latter, it was assumed that because the inner radius R_i was 4–6 times smaller than the exterior radius the small width at the base $W_1 \propto R_i$ could be neglected. However, because the bending stiffness EI , proportional to the width W , cannot vanish at the base, it was assumed that the inner radius still influenced the drag through its finite contribution to the characteristic bending stiffness at the base. Consequently, their analysis corresponds to the case of a purely linear increase of the width from 0 at the base ($\gamma = 1$), on a beam with a non-vanishing bending stiffness ($\beta = 0$), hence the predicted Vogel exponent $\nu_\infty = -1$. However Fig. 8 clearly shows that for δ as small as 10^{-1} , we do not see a plateau at $\nu = -1$ before the effects of the actually non-vanishing width are observed. The two taper ratios considered in Gosselin et al. (2010), $\delta = 0.22$ and 0.32 are even larger, and so the assumption of negligible base width does not hold there. A Vogel exponent of $-2/3$ is in fact to be expected, and that was indeed the result of their numerical computations. Note that the experimental results in

Gosselin et al. (2010) do not match either $\nu = -2/3$ nor $\nu = -1$, neither for the cut-disk nor for the single rectangular plate. The largest Cauchy number considered in the experiments barely exceeded 10^2 , so it is very likely that the asymptotic regime was simply not reached. However, the close values of the Vogel exponents computed in both cases ($\nu = -1.3$ for the cut-disk and $\nu = -1.4$ for the rectangular plate) may indicate that the cut-disk behaves similarly to the rectangular plate, consistently with our expectations.

It should also be noted that the influence of other types of tapering was also addressed by Lopez (2012), for slender cones and tree-like structures with rectangular cross-sections (see also Lopez et al., 2014). It was found in both cases that taper had no influence on the scaling of drag, as numerical computations all yielded the same asymptotic Vogel exponent $\nu_\infty = -2/3$. As a matter of fact, as the vertical axis used in these studies was reversed with respect to ours, both the cross-flow width and the thickness of the beam would reach finite values at the clamped edge for any of the geometries considered. Consequently, according to the present study, the drag experienced by such structures in the limit of large loadings scales as that on a beam of uniform properties $(\alpha, \beta, \gamma, \mu) = (1, 0, 0, 0)$. According to Eq. (23), this indeed yields $\nu_\infty = -2/3$.

5. Discussion

5.1. On the use of Eq. (23) for actual systems

Eq. (23) gives the Vogel exponent for large Cauchy numbers in the general case as a function of the exponents α (constitutive law $g(\kappa)$), β (stiffness distribution $b(s)$), γ (cross-section shape distribution $w(s)$), and μ (pressure distribution $p(z)$). Interestingly, (23) can also be written in a simpler form

$$\nu_\infty = -\frac{2}{1 + \psi/\phi} \quad (42)$$

that highlights the influence of only two parameters: on the one hand, a *geometrical* parameter $\phi = 1 + \mu + \gamma$ that accounts for the distribution of fluid loading on the structure, and on the other hand, a *material* parameter $\psi = 1 + \alpha - \beta$ that characterizes the restoring stresses.

In practice, the ranges accessible to the exponents α , β , γ and μ are bounded by limitations of multiple kinds. First, considering the rigid-body force a limiting value, the finiteness of the drag force mathematically requires that $\gamma + \mu > -1$ (see Section 3). But in fact, neither the structural cross-section nor the flow profile of actual systems can possibly diverge at $s=0$, so γ and μ must actually be both positive or null in practice. Moreover, to ensure that the structural stress vanishes for zero curvature, the exponent α of the material constitutive law $g(\kappa)$ has to be strictly positive. Finally, the bending moment at the base cannot vanish when a loading exists. If the stiffness at the base $b(0)$ was null, the curvature there would need to be infinite and the resulting discontinuity in the angle θ across the boundary $s=0$ would make the problem ill-posed. The minimum energy solution would obviously be the straight horizontal beam, which experiences neither drag nor internal stress. To eliminate this case, $b(0)$ must be different from 0, so the exponent β of the self-similar stiffness function $b(s)$ must be negative or null. Note that a system with zero-stiffness at the base would essentially revert to a pin joint free to rotate, with a Neumann boundary condition at $s=0$. This would define a different system that falls out of the scope of this study, and that would experience zero drag no matter the magnitude of the fluid loading. Consequently, the lower physically admissible boundaries for the geometrical and material parameters of our system are $\psi > 1$ and $\phi \geq 1$.

Moreover, practical considerations further set upper boundaries to the typical values expected for these parameters. First, the vast majority of actual structures have finite width, and only quite exotic systems would exhibit cross-sections increasing more than linearly. It also seems unlikely that an actual flow would show more than linear shear, so we may reasonably expect the geometrical parameter ϕ to remain approximately below 3 in most cases. Besides, the constitutive law of most elastic materials should not deviate much from linearity ($\alpha=1$). Even the extreme case of perfect plasticity may be represented by taking $\alpha=0$, as noted by de Langre et al. (2012), and a larger value $\alpha=2$ would already be a very strong exponent. Besides, continuous structures generally show rather smooth variations of their stiffness, so that the magnitude of the exponent of the stiffness distribution, $|\beta|$, should really not deviate much at all from 0. Nonetheless, the use of the present model with $\beta \neq 0$ might constitute a valid approach to handle the overall behaviour of compound or branched structures such as trees. Indeed, the drag of such structure is the sum of the individual drag forces on each of its constitutive elements: trunk, branches, and leaves. The relative contribution of each term is proportional to the projected area of each element. If we model the structure as an equivalent beam with local stiffness based on the weighted mean of the individual elements at a given height, we would expect the equivalent stiffness to decrease by several orders of magnitude from bottom (trunk) to top (leaves). At this point, the validity of this modelling is purely speculative and further investigations should be carried on to analyse its relevance. But in any case, β as low as -1 leads to variations of the stiffness factor that seem already quite sharp for an actual structure, and so we do not expect the material parameter ψ to exceed 3 by much in general.

Considering all these limitations, we may now estimate the expected range of variation of the Vogel exponent. The isovalues of the asymptotic Vogel exponent ν_∞ predicted by (42) are displayed in Fig. 9. They clearly indicate that, in these typical ranges of the geometrical and material parameters $\phi \in [1, 3]$ and $\psi \in [1, 3]$, ν_∞ may approximately vary between $-1/2$ and $-4/3$ at most. To illustrate the diversity of situations included in this rather narrow parameter space domain, a few practical configurations are marked with crosses on (42). Case A is the benchmark case of Alben et al. (2002, 2004) and Gosselin et al. (2010), where all is

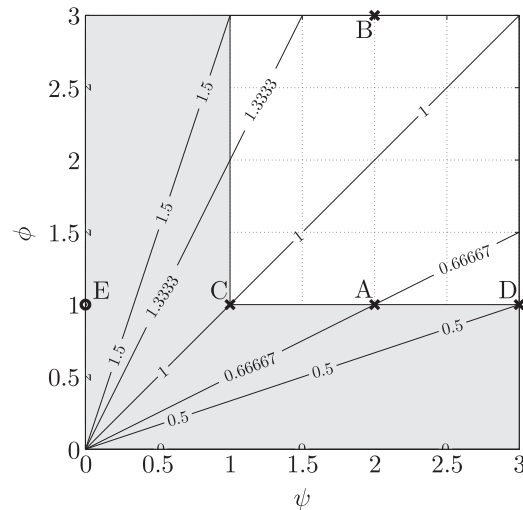


Fig. 9. Absolute value of the Vogel exponent in the reduced parameter space ψ – ϕ . The domain shaded in grey corresponds to non-physical ranges. Practical cases: A–E (see text for the details).

homogeneous and the constitutive law is linear: $(\alpha, \beta, \gamma, \mu) = (1, 0, 0, 0)$. Case B is the linear flow case shown in Fig. 3a: $(\alpha, \beta, \gamma, \mu) = (1, 0, 0, 2)$. Case C would correspond to a uniform, perfectly plastic beam, in a uniform flow: $(\alpha, \beta, \gamma, \mu) = (0, 0, 0, 0)$. Finally, case D would characterize a system with either $(\alpha, \beta, \gamma, \mu) = (2, 0, 0, 0)$ (non-linear constitutive law $g(\kappa) = \kappa^2$) or $(\alpha, \beta, \gamma, \mu) = (1, -1, 0, 0)$ (global model of a tree with infinite stiffness at the base and flexible branches). Overall, we expect that in most situations of practical interest, the Vogel exponent at large Cauchy numbers will not deviate much from -1 . This is consistent with observations on plants, as discussed in the Introduction. Case E will be discussed in Section 5.3.

5.2. On the robustness of the results

The use of Eq. (23) to predict the asymptotic Vogel exponent of a given system relies on the ability to fit a power-law on the spatial distributions of the structural and flow parameters, at least at the scale of the typical length on which significant bending is observed. This requirement may appear as a very limiting factor, because some parameters may exhibit complex variations, and because accurate assessment of the exponents might be challenging. However these two apparent issues might not be as problematic as one might expect.

First, it follows from Sections 4.3 and 4.4 that discrepancies between the actual distributions of the parameters and their best power-law approximations affect very little the validity of the analytical estimation of the Vogel exponent by (23). For instance, it is striking that a beam with taper ratio as large as 10, or even close to 100, still does not exhibit any intermediate plateau similar to the asymptotic regime of a linearly tapered one. In fact, drag reduction on a beam with taper ratio of order 10 is very similar to that of a beam of constant width equal to the base width. Similarly, a structure in a Blasius boundary layer of thickness one order of magnitude smaller than its size is well described, as far as the asymptotic scaling of drag is concerned, by a beam entirely inside the boundary layer. In other words, the ability of (23) to provide accurate estimation of the Vogel exponent of actual systems seems very robust with respect to the accuracy of the self-similar fit of the system parameters. Crude power-law fits at the scale of the bending length are likely to yield rather good results.

Second, the consequences of poor estimations of the exponents of the flow and structural parameter distributions $\alpha, \beta, \gamma, \mu$ also appear limited. It is noticeable in Fig. 9 that the asymptotic Vogel exponent ν_∞ does not vary much in the domain under consideration. The larger the geometrical and material parameters ϕ and/or ψ , the less sensitive the Vogel exponent becomes to small variations of the parameters. As already noted in de Langre et al. (2012), in the case of a uniform beam in a uniform flow, a quadratic material constitutive law (case D in Fig. 9) is expected to lead to a Vogel exponent of -0.5 , which differs very little from the $-2/3$ exponent characteristic of linear elasticity (case A). Similarly, changing a linearly elastic, uniform beam from a linearly sheared flow (case B, $\mu=2$ so $\phi=3$) to an environment with half less shear ($\mu=1$ so $\phi=2$) would only reduce the Vogel exponent from $-6/5$ to -1 . Hence, the estimation of the asymptotic Vogel exponent given by (23) is expected to be also robust with respect to the possible errors made in estimating the fitting exponents.

To conclude, it may be said that the prediction of the Vogel exponent using Eq. (23) is quite robust with regard to the parameters of the model.

5.3. On the limits of the model

The whole theory derived in this paper is based on assumptions of three different natures.

First, assumptions have been made regarding the way the action of the flow on the deforming structure is handled. The choice of the simplified form for the local fluid loading (4) has already been discussed in Section 2. As to the specific form of the

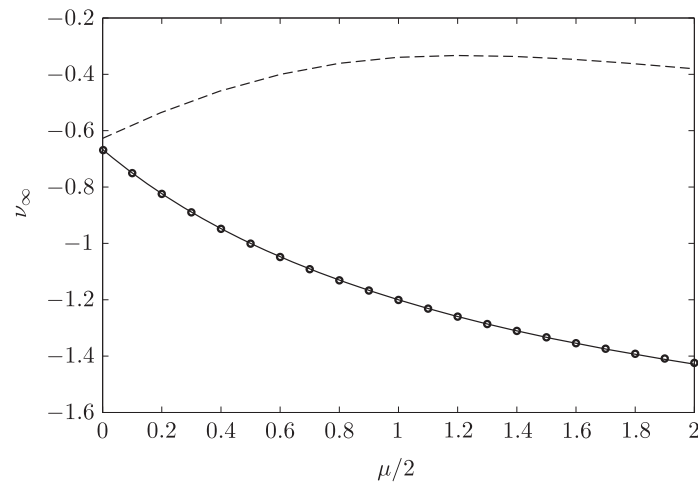


Fig. 10. Asymptotic Vogel exponent ν_∞ for large Cauchy numbers as a function of the flow profile exponent $\mu/2$. Henriquez and Barrero-Gil, 2014 (---), present results given by Eq. (23) (—), and numerical simulations at $C_Y = 10^5$ (o).

projection term in the fluid loading distribution $c(\theta) = \cos^2 \theta$ used all along the present study following Taylor (1952), alternative admissible forms $c(\theta) = \cos^n \theta$ with $n \geq 1$ were numerically tested, and did not lead to any significant alteration of the results.

Second, the study is limited to the influence of the steady background flow at large Reynolds number, in an otherwise force-free environment. Namely, other effects such as gravity, viscosity, vortex shedding or dynamic effects have been neglected here. Depending on the situation, these additional forces may impact the Vogel exponent of natural systems and explain some of the scattering noted in the measurements performed on actual biological or man-made systems. Yet, consistently with the results of Luhar and Nepf (2011) and Zhu (2008), we do not expect that the present results will be largely affected by the effects of gravity or viscosity. The field of dynamics however still requires further investigations (see Kim and Gharib, 2011 or Luhar, 2012).

Third, as to the type of system chosen, we have considered exclusively the reconfiguration of flexible cantilever beams in cross-flow. Eq. (23) might actually remain valid for a broader range of systems, if the mechanism of reconfiguration is resemblant enough to the axial bending considered here. Formula (42) directly embodies the competition between the fluid loading, characterized by the geometrical parameter ϕ , and the structural restoring force, characterized by the material parameter ψ . All along this paper, we have considered the restoring force to be the internal elastic bending force, but it might very well be of a different nature. For instance, Barois and de Langre (2013) showed that a ribbon with a weight at one end exhibits a constant drag. In that case, the fluid loading is of the same nature as in the present study, but the restoring force is the constant axial tension due to the weight. For such system, the material parameter is $\psi=0$ because there is no length scale associated with the restoring force. It lies out of the admissible range defined earlier, and Eq. (42) yields an asymptotic Vogel exponent $\nu_\infty = -2$ (case E in Fig. 9). This does indeed correspond to a constant drag. Conversely, there does not seem to be any obvious analogy between the present study and the rolling up of sheets cut along one radius treated by Schouveiler and Boudaoud (2006) and Alben (2010). In their case, drag reduction is the result of a more complex three dimensional bending process that does not resemble the mechanism considered here.

Finally, it should be noted that the approach used here may easily be adapted to assess the asymptotic effect of elastic reconfiguration on other physical quantities such as the torque at the base of the structure. After some straightforward calculations, the analytical expression found for the Vogel exponent is similar to (42) except that the geometrical and material parameters ϕ and ψ must be respectively replaced by $1+\phi$ and $1+\psi$.

6. Conclusions

To conclude, we may say that this work provides a framework for the understanding of the typical values of Vogel exponents observed in nature. It was shown that the scaling of drag with respect to the flow velocity, in the limits of large loadings, mostly depends on the best power-law approximation of the flow and structural parameter distributions at the scale of the length on which significant bending occurs. An analytical formula relating the asymptotic Vogel exponent to the fitting exponents was derived in Eq. (23), and the sensitivity of this expression with respect to the accuracy of the modelling was shown to be weak.

More importantly, the application of Eq. (23) to a variety of actual systems highlighted the fact that scattering of the Vogel exponents due to non-uniformities in the structural or flow distributions is expected to remain small. Consistently with experimental observations, the predicted Vogel exponents for large loadings always lie around -1 . Consequently, the scaling of the drag on bending beams appears as a characteristic of the mechanism of elastic reconfiguration that depends only on a very limited extent on the actual features of the system. The present study is however limited to quasi-static

configurations. The effects of possible coupling between the structural inertia and the flow dynamics, should it be originated by a time-varying background flow or the consequence of unsteady vorticity shedding in the wake of the structure, still remains to be further investigated.

Acknowledgement

The authors would like to acknowledge financial support from the DGA/DSTL Grant 2014.60.0005 and fruitful discussions with Nigel Peake from the DAMTP, Cambridge, UK.

Appendix A. Comparison with the results of Henriquez and Barrero-Gil (2014)

The problem of reconfiguration in a sheared flow addressed in Section 4.2 is identical to that treated by Henriquez and Barrero-Gil (2014). However, our results strongly differ from theirs, as illustrated in Fig. 10 and discussed below.

There seem to be several possible causes for these discrepancies. First, the choice of the reconfiguration factor \mathcal{R} in Eq. (9) of Henriquez and Barrero-Gil (2014) is non-classical. The numerator does indeed correspond to the total drag on the elastic structure as in the present paper. Yet, the denominator used in Henriquez and Barrero-Gil (2014) does not represent exactly the force on the rigid body. Second, the Vogel exponent is defined as $\nu = 1/2 \times \partial \log \mathcal{R} / \partial \log C_Y$ instead of $\nu = 2 \times \partial \log \mathcal{R} / \partial \log C_Y$ given in Eq. (10) of the present paper to be consistent with $F \propto U^{2+\nu}$. Besides, we believe their numerical solution technique might not be as accurate as ours. As explained in Section 4.1, the inhomogeneous bending along the beam axis makes their choice of uniform mesh with 20 discretization points ill-suited to the large deformation cases investigated here. Finally, the largest Cauchy numbers investigated in Henriquez and Barrero-Gil (2014) do not exceed 10^4 , and their definition of the Cauchy number does not include the contribution of the drag coefficient C_D which they choose as 0.4. Hence, the asymptotic results they show correspond to a value of $C_Y \simeq 10^{3.6}$ in our simulations. This does not reach the asymptotic regime for the largest shear exponents.

The very good fit shown in Fig. 10 between our numerical simulations and our Eq. (23) strengthens our confidence in the results of the present study.

References

- Alben, S., 2010. Self-similar bending in a flow: the axisymmetric case. *Physics of Fluids* 22 (8), 081901.
- Alben, S., Shelley, M., Zhang, J., 2002. Drag reduction through self-similar bending of a flexible body. *Nature* 420 (6915), 479–481.
- Alben, S., Shelley, M., Zhang, J., 2004. How flexibility induces streamlining in a two-dimensional flow. *Physics of Fluids* 16 (5), 1694–1713.
- Audoly, B., Pomeau, Y., 2010. *Elasticity and Geometry: From Hair Curls to the Non-Linear Response of Shells*. Oxford University Press, Oxford, UK.
- Barois, T., de Langre, E., 2013. Flexible body with drag independent of the flow velocity. *Journal of Fluid Mechanics* 735, R2.
- Broyden, C.G., 1965. A class of methods for solving nonlinear simultaneous equations. *Mathematics of Computation*, 577–593.
- Candelier, F., Boyer, F., Leroyer, A., 2011. Three-dimensional extension of Lighthill's large-amplitude elongated-body theory of fish locomotion. *Journal of Fluid Mechanics* 674, 196–226.
- Chakrabarti, S.K., 2002. *The Theory and Practice of Hydrodynamics and Vibration*, 20. World Scientific, New Jersey.
- de Langre, E., 2008. Effects of wind on plants. *Annual Review of Fluid Mechanics* 40, 141–168.
- de Langre, E., Gutierrez, A., Cossé, J., 2012. On the scaling of drag reduction by reconfiguration in plants. *Comptes Rendus Mecanique* 340 (1), 35–40.
- Gosselin, F., de Langre, E., Machado-Almeida, B., 2010. Drag reduction of flexible plates by reconfiguration. *Journal of Fluid Mechanics* 650, 319–341.
- Harder, D.L., Speck, O., Hurd, C.L., Speck, T., 2004. Reconfiguration as a prerequisite for survival in highly unstable flow-dominated habitats. *Journal of Plant Growth Regulation* 23 (2), 98–107.
- Henriquez, S., Barrero-Gil, A., 2014. Reconfiguration of flexible plates in sheared flow. *Mechanics Research Communications* 62, 1–4.
- Kim, D., Gharib, M., 2011. Flexibility effects on vortex formation of translating plates. *Journal of Fluid Mechanics* 677, 255–271.
- Lighthill, M.J., 1971. Large-amplitude elongated-body theory of fish locomotion. *Proceedings of the Royal Society of London. Series B. Biological Sciences* 179 (1055), 125–138.
- Lopez, D., 2012. *Modeling Reconfiguration Strategies in Plants Submitted to Flow* (Ph.D. thesis). Ecole Polytechnique.
- Lopez, D., Michelin, S., de Langre, E., 2011. Flow-induced pruning of branched systems and brittle reconfiguration. *Journal of Theoretical Biology* 284 (1), 117–124.
- Lopez, D., Eloy, C., Michelin, S., de Langre, E., 2014. Drag reduction, from bending to pruning. *EPL (Europhysics Letters)* 108 (4), 48002.
- Luhar, M., 2012. *Analytical and Experimental Studies of Plant-Flow Interaction at Multiple Scales* (Ph.D. thesis). Massachusetts Institute of Technology.
- Luhar, M., Nepf, H.M., 2011. Flow-induced reconfiguration of buoyant and flexible aquatic vegetation. *Limnology and Oceanography* 56 (6), 2003–2017.
- Schouveiler, L., Boudaoud, A., 2006. The rolling up of sheets in a steady flow. *Journal of Fluid Mechanics* 563, 71–80.
- Taylor, G.I., 1952. Analysis of the swimming of long and narrow animals. *Proceedings of the Royal Society of London. Series A. Mathematical and Physical Sciences* 214(1117), 158–183.
- Thomas, J.W., 1995. *Numerical Partial Differential Equations: Finite Difference Methods*, vol. 22. Springer Science & Business Media, Berlin, Germany.
- Tickner, E.G., Sacks, A.H., 1969. Engineering simulation of the viscous behavior of whole blood using suspensions of flexible particles. *Circulation Research* 25 (4), 389–400.
- Vogel, S., 1984. Drag and flexibility in sessile organisms. *American Zoologist* 24 (1), 37–44.
- Yang, X., Liu, M., Peng, S., 2014. Smoothed particle hydrodynamics and element bending group modeling of flexible fibers interacting with viscous fluids. *Physical Review E* 90 (6), 063011.
- Zhu, L., 2008. Scaling laws for drag of a compliant body in an incompressible viscous flow. *Journal of Fluid Mechanics* 607, 387–400.
- Zhu, L., Peskin, C.S., 2007. Drag of a flexible fiber in a 2D moving viscous fluid. *Computers & fluids* 36 (2), 398–406.

Reconfiguration of elastic blades in oscillatory flow

Tristan Leclercq^{1,†} and Emmanuel de Langre¹

¹Department of Mechanics, LadHyX, CNRS, École Polytechnique, 91128 Palaiseau, France

(Received 23 July 2017; revised 8 November 2017; accepted 13 December 2017)

When subjected to a steady cross-flow, the deformation of flexible blades is known to result in the alleviation of the internal stresses in comparison to rigid structures. In the field of biomechanics, the flow-induced deformations of flexible structures leading to stress reduction have been often referred to as ‘reconfiguration’ in order to highlight the alleged benefits of such an adaptive process. In this paper, we investigate the reconfiguration of thin elastic blades and the resulting internal stresses when the flow about the blade is oscillatory. Our approach, based on numerical simulations using reduced order fluid force models, is validated by experimental observations. Through a systematic investigation of the response of the structure, we identify four kinematic regimes depending on the excursion of the fluid particles relative to the dimensions of the blade and on the frequency of the flow oscillations relative to the characteristic frequency of the blade. When the flow amplitude is smaller than the structural width, fluid inertia dominates over drag and the fluid–structure coupling triggers resonances that may cause a magnification of the internal stresses. But the small magnitude of the fluid load in this regime is unlikely to cause any severe damage in practice. Otherwise, when drag is the dominant load, flexibility always permits a reduction of the internal stresses. As in the static case, dynamic reconfiguration results in the concentration of the stresses within a small bending length whose scaling depends on the kinematic regime. The magnitude of the stresses does not depend on the actual length of the structure anymore, which suggests the absence of mechanical limitations to the axial growth of wave-swept plants. However, the risk of resonances originating from the inertial load when the blade width compares with the flow excursion favours elongated shapes that best accommodate the oscillatory fluid loadings.

Key words: aerodynamics, flow–structure interactions

1. Introduction

The deformation of flexible bodies subject to a transverse oscillatory flow has raised the attention of the scientific community for some time and with different motivations. The propulsive performances of deformable bodies depend on the flexibility of the structure (Lighthill 1960, 1971; Katz & Weihs 1978, 1979). More specifically, the dynamic coupling with the deformation resulting from the oscillatory

[†] Email address for correspondence: tristan.leclercq@polytechnique.edu

forcing may trigger resonances or involve nonlinear effects of paramount importance (Alben 2008; Michelin & Llewellyn Smith 2009; Ramanarivo, Godoy-Diana & Thiria 2011; Paraz, Eloy & Schouveiler 2014; Paraz, Schouveiler & Eloy 2016; Piñeirua, Thiria & Godoy-Diana 2017). Similarly, flexible structures forced into a transverse motion within an axial flow may harvest energy from the fluid, and the nature of the deformation depending on the features of the forcing influences the efficiency of the process (Liu, Xiao & Cheng 2013).

The transverse fluid loads are also responsible for internal stresses that may endanger the structural integrity. As a strategy for survival, large plants living in flow-dominated habitats are usually very flexible (Harder *et al.* 2004). Thanks to their ability to deform under the influence of the current, flexible structures are able to reduce their frontal area, reshape themselves in a more streamlined fashion, or even shelter in regions where the flow is slower. The work of Vogel (1984) and Vogel (1989) has highlighted that this instantaneous, passive and reversible change of shape leads to a significant reduction of the internal stresses in the flexible plants subjected to high velocity flows. Because of the alleged adaptive nature of these flow-induced deformations, Vogel (1984) has suggested the use of the word ‘reconfiguration’ owing to the more positive overtone associated with this term. Thereafter, several authors have contributed to quantitatively evaluate the drag reduction due to elastic reconfiguration in steady currents on model systems (Alben, Shelley & Zhang 2002, 2004; Gosselin, de Langre & Machado-Almeida 2010; Luhar & Nepf 2011; Hassani, Mureithi & Gosselin 2016; Leclercq & de Langre 2016).

But the question arises of whether the benefits of flexibility would still prevail in an oscillatory flow such as that encountered by salt marsh vegetation, seagrasses, or macroalgae in the near-shore waves. Koehl (1984) pointed out that the fluid acceleration forces in an oscillatory flow, proportional to the volume of the plant when the drag is only proportional to its frontal area, may be the dominant load that bulk organisms have to withstand (see also Denny, Daniel & Koehl 1985). On the other hand, flexible organisms long enough to move significantly with the flow may endure less severe relative flow and possibly benefit from a reduction of the associated loads. But the displacement of the structure is also responsible for additional inertial loads, so the actual consequences of flexibility in an oscillatory flow may be strongly dependent on the nature of the dynamic response of the deformable structure. Different mechanical models have been proposed to replicate the motion of macroalgae under the action of waves. For instance, see Friedland & Denny (1995) for fully submerged flexible plants, Utter & Denny (1996), Denny & Cowen (1997) for algae larger than the water depth and Gaylord & Denny (1997) for stipitate kelps. But the question of how the dynamical response and the associated loads may change when the rigidity of the structure is varied was first addressed by Luhar & Nepf (2016). Their study suggests, based on experimental results, that the drag on deformable structures may be expressed as that on a rigid structure with an effective length corresponding to the part of the actual structure over which significant relative fluid motion occurs. A scaling of this effective length with the flexibility was provided, with the aim to provide a tool to account for the deformability of near-bed organisms in the models of wave-energy dissipation (see also Luhar, Infantes & Nepf 2017). But the work of Luhar & Nepf (2016) focuses on the specific case where the amplitude of the flow is at most of the order of the length of the structure. They do not investigate either the dynamic interactions (such as possible resonance effects) due to high frequency loading. Besides, for particular values of the parameters, Luhar & Nepf (2016) notice an increase of the drag compared to the rigid case that is still not fully understood.

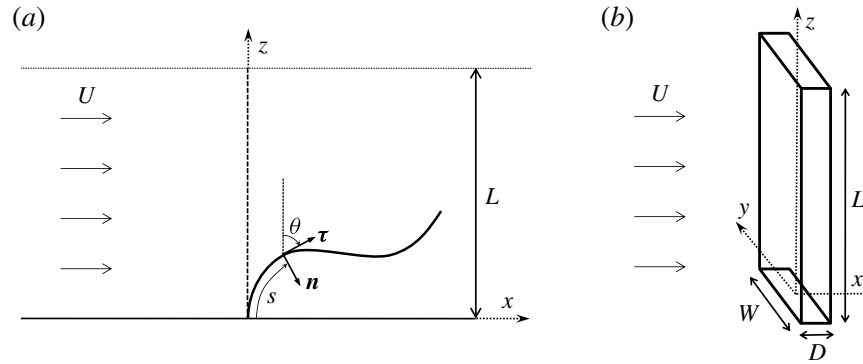


FIGURE 1. (a) Side view of the bending structure. (b) Dimensions of the undeformed blade.

In order to identify and understand the different mechanisms involved, a systematic analysis exploring the space of forcing parameters is therefore still required. In this paper, we intend to elucidate the nature of the dynamical response of such a cantilever structure depending on the amplitude and frequency of the oscillating cross-flow, in the ideal case of a uniform flow. Our approach is mostly based on numerical simulations using reduced-order force models, with experimental validation. Our goal is then to assess how the structural stresses vary compared to the rigid case, depending on the different dynamical regimes.

In § 2 we introduce the theoretical model and the numerical method we chose to reproduce the dynamics of the system. In § 3 we present an experimental set-up used for visualizing the actual deformation of blades in oscillatory forced motion and to validate the model. We then identify four different kinematic regimes for varying ranges of the forcing amplitude and frequency in § 4, before discussing the resulting flexibility-induced variations of the structural stress in § 5. Finally, § 6 extends the discussion to provide general findings and to comment on previous work.

2. Model

2.1. Theory

We consider a neutrally buoyant, cantilever beam of length L , width W and thickness D , placed perpendicular to a uniform oscillatory flow of velocity $\mathbf{U}(t) = A\Omega \sin(\Omega t)\mathbf{e}_x$ in a fluid of density ρ (see figure 1). The amplitude A corresponds to the maximal horizontal excursion of the fluid particles over one cycle, while Ω is the angular frequency of the oscillations.

We assume the thickness of the plate is small compared to its width ($D \ll W$) so that deflection under the effect of the flow is confined in the xz -plane. We also assume the structure is slender ($L \gg W$) so we can model it as a two-dimensional inextensible Euler–Bernoulli beam of bending stiffness EI and mass per unit length m (see Audoly & Pomeau 2010). The curvilinear coordinate s represents the distance from the clamped edge along the span, and we use the prime symbol $(\cdot)'$ to denote differentiation with respect to s . Hereafter, θ is the local angle of the tangent $\boldsymbol{\tau} = \mathbf{r}'$ with the vertical axis \mathbf{e}_z , where $\mathbf{r} = x(s, t)\mathbf{e}_x + z(s, t)\mathbf{e}_z$ is the position vector. Following Audoly & Pomeau (2010), the dynamic equilibrium reads

$$m\ddot{\mathbf{r}} = \mathbf{F}' + \mathbf{q}, \quad (2.1)$$

where \mathbf{q} is the external load per unit length on the structure, $\mathbf{F} = T\boldsymbol{\tau} + Q\mathbf{n}$ is the internal force vector, with T the tension and Q the shear force and the overdot stands for time derivation. The internal bending moment M is related to the local curvature $\kappa = \theta'$ by $M = EI\kappa$, and the shear force Q is given by $Q = -M' = -EI\kappa'$. Clamping implies $x = z = \theta = 0$ at $s = 0$, while the free tip condition reads $T = M = Q = 0$ at $s = L$.

Because the structure is neutrally buoyant, its density is also ρ and gravity and buoyancy forces cancel each other. We assume large Reynolds number so that friction forces are negligible. Following Eloy, Kofman & Schouveiler (2012), Singh, Michelin & de Langre (2012), Michelin & Doaré (2013), Piñeirua *et al.* (2017) we model the effect of the relative flow as a combination of two external loads distributed along the span. First, the resistive drag (Taylor 1952)

$$\mathbf{q}_d = -1/2\rho C_D W |U_n| U_n \mathbf{n} \quad (2.2)$$

due to the pressure in the wake is purely normal. It is proportional to the square of the normal component U_n of the relative velocity $\mathbf{U}_r = U_\tau \boldsymbol{\tau} + U_n \mathbf{n} = \dot{\mathbf{r}} - \mathbf{U}$. The drag coefficient C_D depends on the geometry of the cross-section and is typically of order $O(1)$. In pure sinusoidal flow, it slightly varies with the frequency through the Keulegan–Carpenter number $K_C = U/Wf = 2\pi A/W$ (Keulegan & Carpenter 1958). But in the case of a deformable body, the relative flow varies along the span and is not purely sinusoidal because of the motion of the structure itself. The exact value of C_D is however not critical here so we will simply use the value for steady flows. We will also assume a rectangular cross-section so we will use $C_D = 2$. The second force component is the reactive (or added mass) force (Lighthill 1971; Candelier, Boyer & Leroyer 2011)

$$\mathbf{q}_{am} = -m_a \left[\partial_t (U_n \mathbf{n}) - \partial_s (U_n U_\tau \mathbf{n}) + \frac{1}{2} \partial_s (U_n^2 \boldsymbol{\tau}) \right], \quad (2.3)$$

where the added mass is given by $m_a = \rho \pi W^2 / 4$. This expression involves the normal component but also the tangential component U_τ of the relative velocity. In the case of an inextensible beam, this force becomes purely normal and its expression may be simplified in

$$\mathbf{q}_{am} = -m_a \left[(\ddot{\mathbf{r}} - \dot{\mathbf{U}}) \cdot \mathbf{n} - 2\dot{\theta} U_\tau + \kappa \left(U_\tau^2 - \frac{1}{2} U_n^2 \right) \right] \mathbf{n}. \quad (2.4)$$

Finally, because the fluid itself is accelerated, a third force component has to be considered, called the virtual buoyancy force (Blevins 1990)

$$\mathbf{q}_{vb} = m_d \dot{\mathbf{U}}. \quad (2.5)$$

This term is due to the pressure gradient induced by the acceleration of the fluid. It is equivalent to the Archimedes force, only the acceleration of gravity is replaced by the acceleration of the fluid. It is proportional to the displaced mass per unit length $m_d = \rho W D$. We have assumed so far that the structure is fixed in an oscillating fluid. If the clamped edge of the structure was set into a forced horizontal motion of velocity $\mathbf{U}_f = U_f \mathbf{e}_x$, then the equilibrium equation in the frame of the structure (2.1) would include an additional load due to the inertial pseudo-force $\mathbf{q}_i = -m\dot{\mathbf{U}}_f$. For a neutrally buoyant structure the displaced mass is equal to the structural mass ($m_d = m$), so this inertial force has the same expression as the virtual buoyancy term (2.5) if $\mathbf{U}_f = -\mathbf{U}$. Thus, oscillating a plate in a still fluid is actually equivalent to having a fixed structure

in an oscillating flow, providing that the structure has the same density as the fluid. For practical reasons, in the experiments of § 3, we set the structure into motion rather than the fluid.

In the following, we will only consider very thin blades $D \ll W$ (equivalently $m = m_d \ll m_a$) so that we may neglect the structural inertia and the virtual buoyancy. The dynamic equilibrium (2.1) then reads

$$\left[T + \frac{1}{2}EI\kappa^2\right]' \boldsymbol{\tau} + [\kappa T - EI\kappa'']\mathbf{n} + \mathbf{q}_d + \mathbf{q}_{am} = 0. \quad (2.6)$$

After projection on the tangential and normal directions and elimination of the unknown tension T , we finally obtain a single differential equation for the kinematic variables κ , θ , \mathbf{r}

$$EI \left[\kappa'' + \frac{1}{2}\kappa^3\right] + \frac{1}{2}\rho C_D W |U_n| U_n + m_a \left[\ddot{\mathbf{r}} \cdot \mathbf{n} + \kappa \left(U_\tau^2 - \frac{1}{2}U_n^2\right) - 2\dot{\theta}U_\tau - \Omega^2 A \cos \theta \cos(\Omega t)\right] = 0. \quad (2.7)$$

We non-dimensionalize all the variables using the length of the structure L and the scale of the natural period of the structure in small-amplitude oscillations in the fluid $T_s = L^2 \sqrt{m_a/EI}$. We finally obtain, in non-dimensional form

$$\kappa'' + \frac{1}{2}\kappa^3 + \lambda |U_n| U_n + \ddot{\mathbf{r}} \cdot \mathbf{n} + \kappa \left(U_\tau^2 - \frac{1}{2}U_n^2\right) - 2\dot{\theta}U_\tau - \omega^2 \alpha \cos \theta \cos(\omega t) = 0, \quad (2.8)$$

with boundary conditions $\mathbf{r} = 0$ and $\theta = 0$ at the clamped edge $s = 0$ and $\kappa = \kappa' = 0$ at the free tip $s = 1$, and the tangential and normal relative velocities $U_\tau = \dot{\mathbf{r}} \cdot \boldsymbol{\tau} - \alpha \omega \sin(\omega t) \sin \theta$ and $U_n = \dot{\mathbf{r}} \cdot \mathbf{n} - \alpha \omega \sin(\omega t) \cos \theta$. This system is ruled by three non-dimensional parameters that are

$$\alpha = \frac{A}{L}, \quad \omega = \Omega T_s, \quad \lambda = \frac{\rho C_D W L}{2m_a} = \left(\frac{2}{\pi} C_D\right) \frac{L}{W}. \quad (2.9a-c)$$

The first two parameters α and ω respectively scale the amplitude and frequency of the background flow to the length and natural frequency of the structure, while $\lambda = O(L/W)$ is mostly a slenderness parameter specific to the structure alone. Because our model is only valid for slender structures, we are restricted to $\lambda \gg 1$. Note that, when studying the influence of flexibility on the loads endured by a structure, the classical non-dimensional parameter that describes the competition between the fluid loading stemming from the resistive drag and the elastic restoring force is the Cauchy number C_Y (Tickner & Sacks 1969; Chakrabarti 2002; de Langre 2008). Following the definition of Gosselin *et al.* (2010) in the case of the static reconfiguration of cantilever beams, we may here define a Cauchy number based on the maximum velocity of the flow ($A\Omega$) as $C_Y = \rho C_D W L^3 (A\Omega)^2 / EI = \lambda \alpha^2 \omega^2$. In the governing equation (2.8), given the scaling of the normal relative velocity component $U_n = O(\alpha \omega)$, the resistive drag term $\lambda |U_n| U_n$ directly scales as $\lambda \alpha^2 \omega^2 = C_Y$ owing to the choice of characteristic length and time chosen for normalization.

2.2. Numerical resolution

We numerically solve (2.8) along with the boundary conditions using a time stepping scheme. The one-dimensional structure is discretized using the Gauss–Lobatto distribution $s_k = 1/2(1 - \cos((k-1)/(N-1)\pi))$ with $N = 100$ points. The curvilinear derivatives and integrals are computed respectively by Chebyshev collocation and the

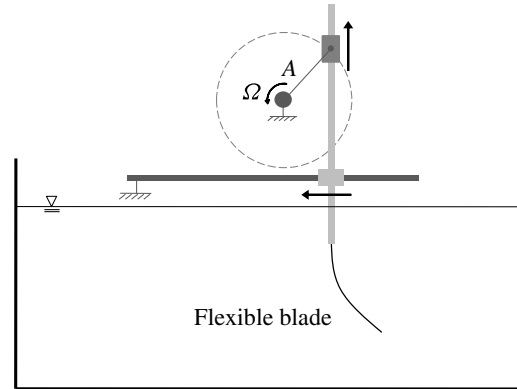


FIGURE 2. Schematic view of the experimental set-up.

Clenshaw–Curtis quadrature formulae. We evaluate the time derivatives at time t_n with implicit second-order accurate finite differences with 10^3 time steps per forcing cycle in most cases. The time step is reduced further to maintain good accuracy when a smaller time scale is involved in §§ 4.2 and 5.4. At each time step, we solve the boundary value problem in $\kappa_n(s)$ with a pseudo-Newton solver (method of Broyden 1965). The computations are carried on until a limit cycle is found.

3. Experiments and validation of the model

We conducted experiments to visualize the actual kinematics of slender blades in an oscillatory flow and validate our model. The set-up of the experiment is depicted in figure 2.

The flexible object is a rectangular piece of 20×2 cm (so that $\lambda = 12.7$) and bending stiffness $EI = 1.68 \times 10^{-4}$ N m² that was cut out of a plastic document cover of thickness 0.49 mm and density 895 kg m⁻³. This plate has a mass per unit length $m = 8.72 \times 10^{-3}$ kg m⁻¹, displaced mass per unit length $m_d = 9.74 \times 10^{-3}$ kg m⁻¹ and added mass per unit length $m_a = 3.14 \times 10^{-1}$ kg m⁻¹. Thus, $m/m_a = 2.8 \times 10^{-2}$ and $m_d/m_a = 3.1 \times 10^{-2}$ so that the structural inertia and the virtual buoyancy are indeed negligible. In order to get the desired relative flow, we forced the clamped edge of the blade into an oscillatory translation of opposite velocity $-U(t)$ and analysed the dynamic deformation of the structure in the oscillating frame. The flexible structure is clamped at the bottom of a vertical rigid rod and fully immersed in a rectangular water tank of horizontal dimensions 58×35 cm and 48 cm of water depth. The rod crossing the free surface is streamlined in the direction of the motion in order to induce as little perturbation as possible in the fluid. The forcing motion is obtained through a DC motor driving an arm of length A in rotation. The speed of rotation Ω is tuned by changing the voltage at the terminals of the motor. The arm is attached to a carriage freely translating on a vertical rail, which in turn is fixed on an another carriage sliding on an horizontal rail. The mounting rod is linked to the latter carriage so that it is driven into the desired sinusoidal translation of amplitude A and angular frequency Ω as the arm rotates. The amplitude A could be varied continuously between 5.4 ($\alpha = 0.27$) and 13 cm ($\alpha = 0.65$), and the frequency between 0.21 ($\omega = 2.3$) and 1.08 Hz ($\omega = 12.0$). The motion of the whole structure is filmed with a fixed camera in front of the tank at 100 fps and the position and deformation of the blade through time is extracted from each frame. The deformation

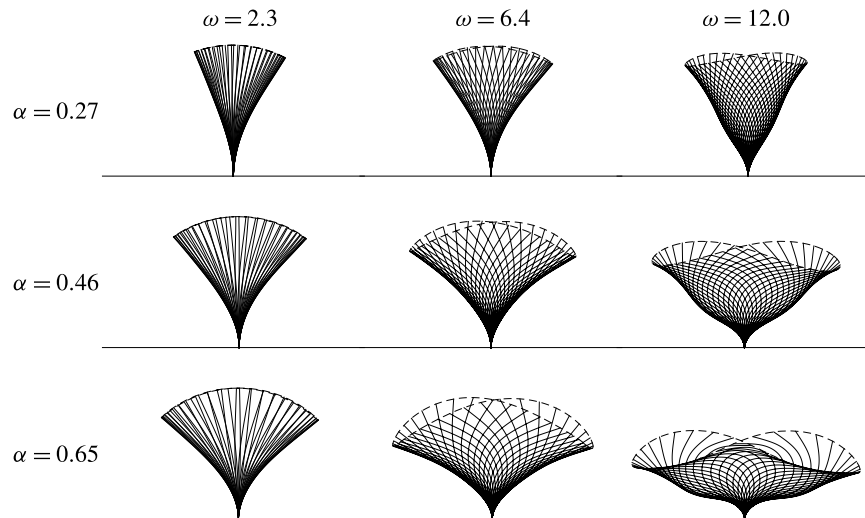


FIGURE 3. Phase-averaged experimental oscillation cycle for varying amplitudes α and frequencies ω . Snapshots of the structural shape (—) and tip trajectory (---).

in the oscillating frame is then phase averaged over a minimum of 10 cycles to get a unique cycle representative of the whole run.

The results for three different amplitudes and frequencies spanning the experimental domain are shown in figure 3. In this range of forcing parameters, we notice a diversity of behaviours. For a given frequency ratio ω , the maximum deflection of the blade increases with the amplitude of the forcing α . However, the horizontal excursion of the structure is obviously limited by its own length, so the amplitude of the motion has to saturate when α is increased even more. Besides, the maximum deflection is clearly increasing with the forcing frequency for the largest forcing amplitude $\alpha = 0.65$, but this is much less obvious for the smallest amplitude $\alpha = 0.27$. On the other hand, for any given forcing amplitude α , the dynamics of the deformation is greatly affected when the forcing frequency is increased. For the smallest frequency ratio $\omega = 2.3$, the tip follows the same trajectory during both half-cycles and remains close to the unit circle. The motion of the whole blade is therefore approximately in phase, and curvature is concentrated near the clamped edge while the rest of the beam remains straight. This deforming shape is similar to the static reconfiguration that occurs in steady flow (Gosselin *et al.* 2010). Conversely, when the frequency is increased, the tip follows a figure-of-eight trajectory and we notice curvature waves propagating along the span in the course of the cycle indicating an increasing spanwise phase shift. This indicates a highly dynamic response that cannot be considered quasi-steady *a priori*. Besides, the propagation of curvature waves may induce large loads anywhere along the span and not restricted to the clamping point.

In order to validate the numerical model of §2, we also compared these experimental observations to the output of the numerical simulations. As shown in figure 4(a), the numerical results for the amplitude of deflection at the tip X_{tip} match very closely the experimental measurements. The snapshots displayed in figure 4(b) for two cases at the boundaries of our experimental domain (indicated in figure 4a) also show very good agreement between the observations and the simulations. Additional experimental validation of the model for smaller forcing amplitudes can be found in Piñeira *et al.* (2017).

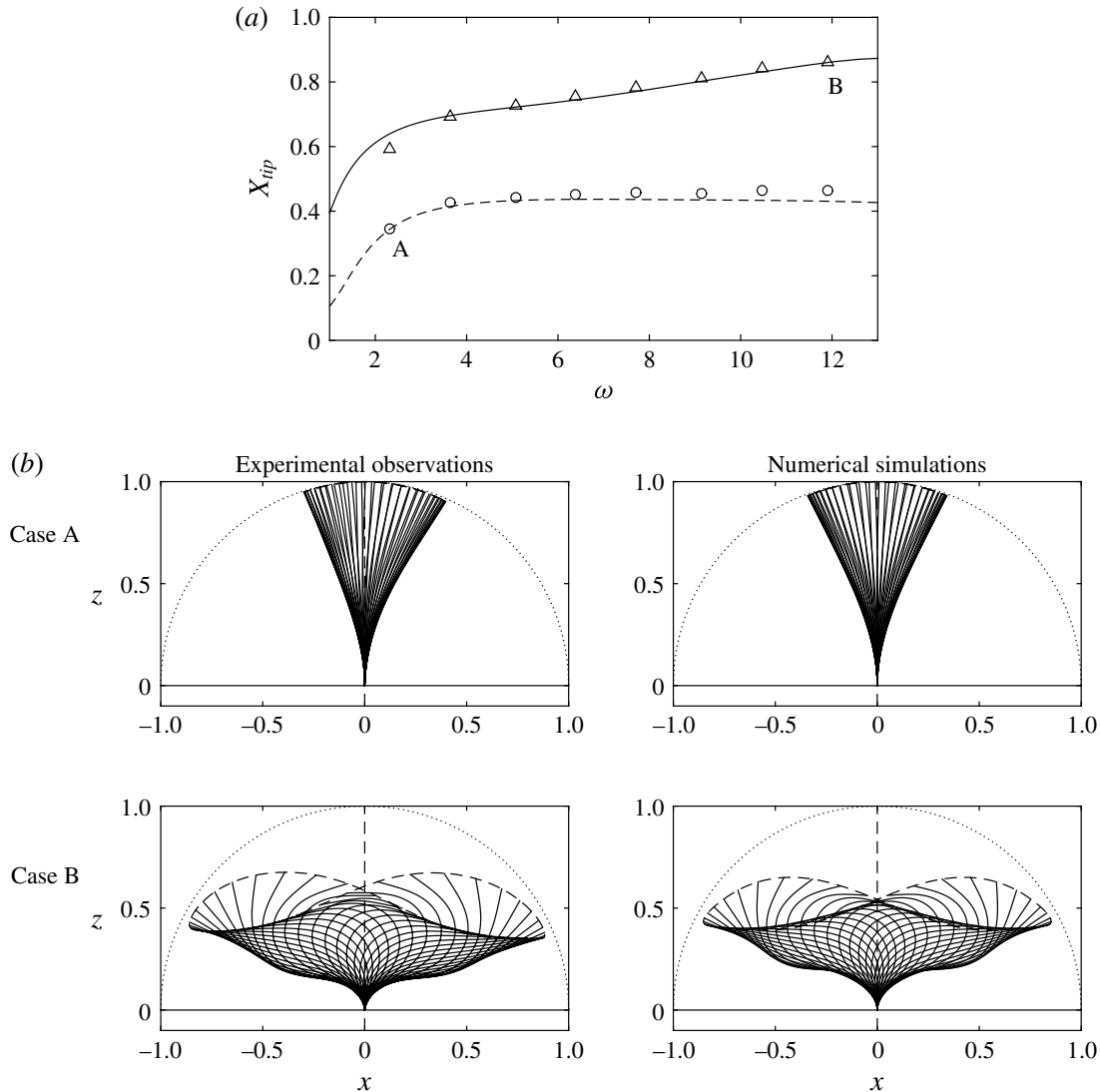


FIGURE 4. Comparison between experimental observations and numerical simulations. (a) Amplitude of the deflection at the tip against the frequency ratio, for $\alpha = 0.27$ (numerical ---, experimental \circ), $\alpha = 0.65$ (numerical —, experimental \triangle). (b) Deformed shape found experimentally (left) and numerically (right), in case A (top, $\alpha = 0.27$, $\omega = 2.3$) and case B (bottom, $\alpha = 0.65$, $\omega = 12.0$).

These results confirm the validity of our model, and we will therefore use it in the following to systematically explore the parameter space within and beyond the experimentally accessible range.

4. Kinematics

4.1. Small amplitude of flow oscillation $\alpha = A/L \ll 1$

Let us first consider the situation where the amplitude of forcing is small ($\alpha \ll 1$). The excursion of the fluid particles being small compared to the length of the blade, we may also assume that the deflection remains small as well $|x(s, t)| \ll 1$. Neglecting all the geometrical nonlinearities in (2.8) thus yields the small-amplitude equation

$$x^{(4)} + \ddot{x} = \alpha\omega^2 \cos(\omega t) - \lambda|\dot{x} - \alpha\omega \sin(\omega t)|(\dot{x} - \alpha\omega \sin(\omega t)), \quad (4.1)$$

with boundary conditions $x = x' = 0$ at $s = 0$ and $x'' = x''' = 0$ at $s = 1$. Equation (4.1) is the standard cantilever beam linear oscillator, forced on the right-hand side by the fluid inertia and the resistive drag. Note that only the nonlinearities of geometrical nature have been removed but the quadratic relative velocity term of the resistive drag has been retained at this point. Indeed, the slenderness parameter λ that scales this term is large and the order of magnitude of the whole resistive drag term depends as much on the scaling of λ as it depends on that of α . Besides, no assumption has been made regarding the characteristic time scale for the variations of x , and there is no reason to presume that \dot{x} should be small compared to the free-stream velocity based on the sole assumption that x is small.

If the period of the forcing is large compared to the characteristic response time of the structure ($\omega < 1$), we may assume that the structure is in static equilibrium with the fluid forcing at all times. Consequently, we may neglect the velocity and acceleration of the structure and (4.1) reduces to the small-amplitude static equation

$$x^{(4)} = \alpha \omega^2 [\cos(\omega t) + (\lambda \alpha) |\sin(\omega t)| \sin(\omega t)]. \quad (4.2)$$

The left-hand side of this equation now involves only the linearized stiffness force, while the fluid forcing on the right-hand side is the same as that a perfectly rigid blade would endure.

On the other hand, if the forcing varies with a period comparable to the characteristic structural response time or faster ($\omega > 1$), we may then assume that the amplitude and the frequency of the response will scale as those of the forcing, as is usually the case for linear oscillators (see for instance Blevins 1990). We thus define the rescaled deflection and time $\tilde{x} = x/\alpha$, $\tilde{t} = \omega t$, so that the small-amplitude equation (4.1) can be written

$$\frac{1}{\omega^2} \tilde{x}^{(4)} + \ddot{\tilde{x}} = \cos(\tilde{t}) - K_C |\dot{\tilde{x}} - \sin(\tilde{t})| (\dot{\tilde{x}} - \sin(\tilde{t})), \quad (4.3)$$

which now only depends on two parameters: the frequency parameter ω and a new amplitude parameter $K_C = \lambda \alpha = (2C_D/\pi)A/W$ that compares the fluid particles excursion to the width instead of the length of the blade. This parameter is a problem-specific formulation of the classical Keulegan–Carpenter number that compares the respective magnitudes of the drag and the fluid inertial forces. When K_C is small, the fluid inertia dominates over drag and *vice versa*.

Let us first look at the asymptotic limit of infinitely small amplitude of the forcing $K_C \rightarrow 0$. The nonlinear drag term can be neglected and (4.3) then simply describes a linear oscillator with sinusoidal forcing due to the fluid inertial term. It can be solved analytically and the solution is

$$\tilde{x}(s, \tilde{t}) = 2 \sum_{m=0}^{+\infty} \frac{\sigma_m}{k_m} \frac{\omega^2}{k_m^4 - \omega^2} X_m(s) \cos \tilde{t}, \quad (4.4)$$

with the wavenumbers k_m satisfying $\cos k_m \cosh k_m + 1 = 0$, the classical cantilever beam modes $X_m(s) = [\cosh(k_m s) - \cos(k_m s)] - \sigma_m [\sinh(k_m s) - \sin(k_m s)]$ and $\sigma_m = (\sinh k_m - \sin k_m) / (\cosh k_m + \cos k_m)$ (see Weaver, Timoshenko & Young 1990).

Figure 5(a) compares the amplitude of the maximum deflection for different values of K_C , and for the asymptotic solution (4.4), as a function of ω . This analytical solution is in good agreement with the model predictions for any $K_C \leq 1$, and it

shows that the system behaves as a high-pass filter in this range of the parameter space. As the frequency increases, successive beam modes are excited and resonances occur when the frequency of the forcing matches one of the natural modes of the structure $\omega = k_m^2$. For finite but small K_C , drag acts as a damping term that saturates the amplitude of the resonances but does not seem to affect significantly the modal shape of the deforming structure. The deformation of the beam close to the first three resonances ($\omega_1 = 3.5$, $\omega_2 = 22.0$, $\omega_3 = 61.7$) for $K_C = 10^{-2}$ in figure 5(b) is indeed similar to the corresponding beam modes X_1 , X_2 , X_3 involved in the asymptotic solution (4.4). Note that when K_C is close to 1, the nonlinear drag term is also responsible for a drift of the resonance frequencies that has been studied in Arellano Castro *et al.* (2014). This effect is not obvious in figure 5(a) because of the very strong attenuation of the resonance peak for $K_C = 1$, but is more visible in the structural stress analysis of figure 9(a).

On the other hand, if we increase the fluid particles excursion beyond the width of the structure ($K_C \gg 1$), a change in physical behaviour occurs. Drag becomes the dominant term in (4.3). The leading-order solution now is $\tilde{x}(s, \tilde{t}) = \cos \tilde{t}$, which amounts to considering that the structure is convected exactly with the fluid particles. Therefore, we may call this regime the convective regime. This solution is however incompatible with the boundary condition at the clamped edge $\tilde{x}(0, \tilde{t}) = 0$, so an elastic boundary layer develops close to the clamping point. The relative magnitude of the terms in (4.3) suggests that the thickness of the boundary layer scales as $\delta = (K_C \omega^2)^{-1/4}$. Rescaling the curvilinear coordinate $\hat{s} = s/\delta$ in (4.3) provides the leading-order equation for the inner solution

$$\partial_{\hat{s}}^4 \tilde{x} = |\dot{\tilde{x}} - \sin(\tilde{t})|(\dot{\tilde{x}} - \sin(\tilde{t})), \quad (4.5)$$

with boundary conditions $\tilde{x} = \partial_{\hat{s}} \tilde{x} = 0$ at $\hat{s} = 0$ and $\partial_{\hat{s}}^2 \tilde{x} = \partial_{\hat{s}}^3 \tilde{x} = 0$ at $\hat{s} = 1/\delta$.

The dynamic deformation of the structure displayed in figure 5(c) for $K_C = 10^2$ for the same values of frequency ratios as in figure 5(b) clearly shows the concentration of the curvature close to the clamped edge and the passive convection of the main part of the structure. The resonances previously observed in the modal regime in figure 5(a) are now completely damped out when $K_C = 10^2$. Compared to the case $K_C = 1$, this curve is shifted one decade to the left as the proper scaling parameter is now $\sqrt{K_C} \omega$ instead of ω , and $\sqrt{K_C} = 10$ for $K_C = 10^2$. The scaling of the boundary layer thickness δ is similar to that of the effective length of Luhar & Nepf (2016), as it is based on the equilibrium between the same forces. A similar problem had also been considered in Mullarney & Henderson (2010). In the case of a wave-like flow, the authors neglected the quadratic nonlinearity in order to get an analytical solution.

4.2. Large amplitude of flow oscillation $\alpha = A/L \gg 1$

In the convective regime discussed above, the structure is purely convected with the fluid particles on most of its span over the whole cycle. But when the amplitude becomes larger than the length of the structure, geometric saturation of the deflection occurs because the structure cannot extend further than its own length. The deflection is now of order $x = O(1)$ and so we cannot neglect the geometrical nonlinearities of (2.8) anymore. The slenderness λ becomes the relevant parameter to compare drag to the fluid inertial forces in lieu of the Keulegan–Carpenter number K_C . Because we only consider elongated structures $\lambda \gg 1$ in this study, drag will always be the dominant term in the large-amplitude regime.

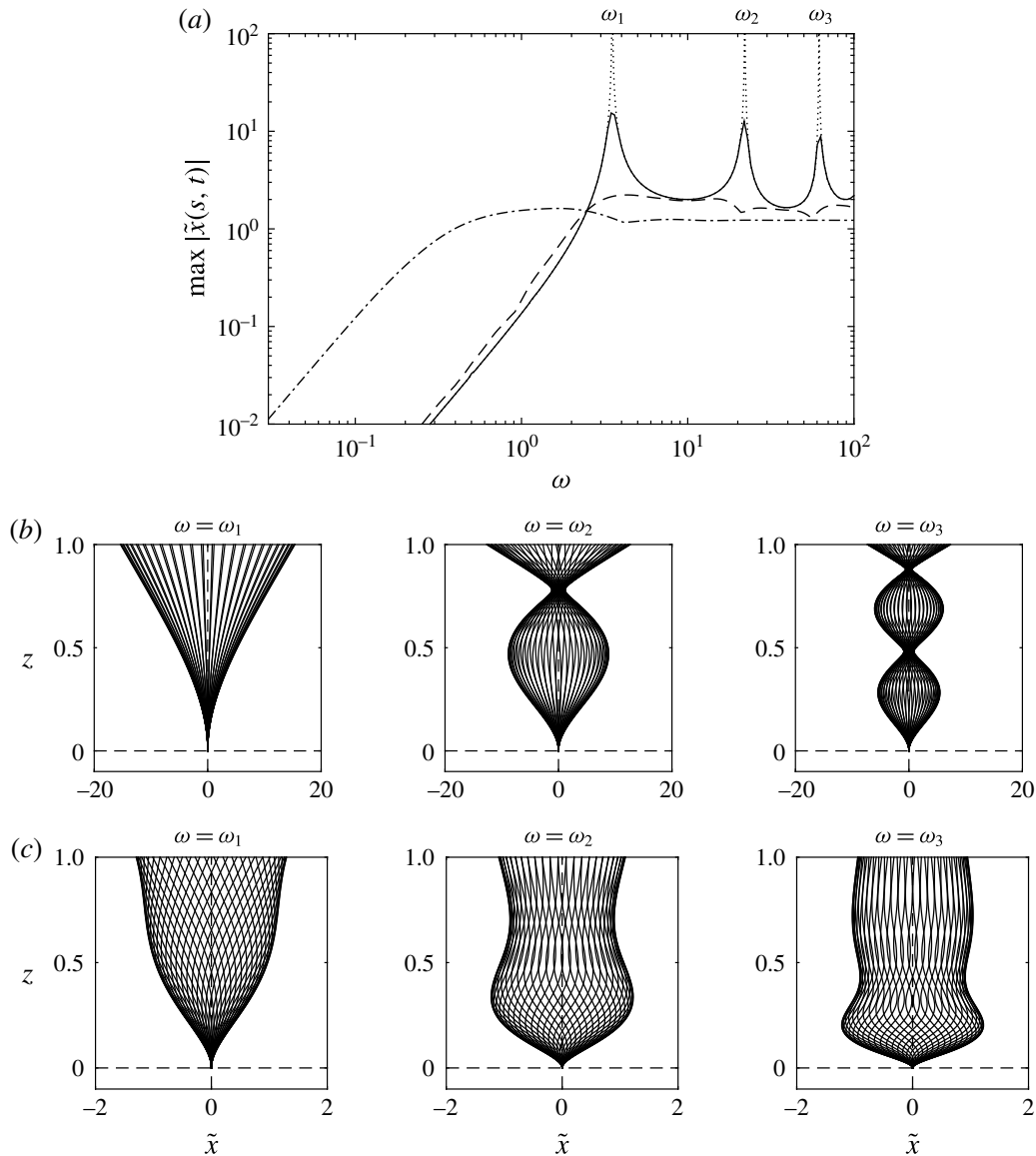


FIGURE 5. (a) Amplitude of the maximum scaled deflection obtained with (4.3) against the frequency ratio. $K_C = 10^{-2}$ (—), $K_C = 10^0$ (---), $K_C = 10^2$ (— · —). Analytical solution for $K_C \rightarrow 0$ (· · · · ·). (b) Snapshots of the beam over one cycle obtained with (4.3) for $K_C = 10^{-2}$ (modal regime) and for $\omega = \omega_1$ (resonance of mode 1), $\omega = \omega_2$ (resonance of mode 2), $\omega = \omega_3$ (resonance of mode 3). (c) Same as (b) but with $K_C = 10^2$ (convective regime).

The dynamic deformations obtained with (2.8) in two cases with similar amplitude $\alpha = 10^2$ and slenderness $\lambda = 12.7$ but different frequencies are compared in figure 6 with 100 snapshots per cycle with constant time interval. In the small frequency case (a), the deformation looks quasi-static. Transition from one side to the other is slow (many snapshots distributed from left to right) and the curvature is essentially concentrated near the clamped edge during the whole cycle. On the other hand, in the larger frequency case (b), the structure switches sides very fast (few snapshots visible in the centre while many are superimposed on the sides) and curvature waves propagate very quickly along the span during reversal. Therefore, the cycle may be

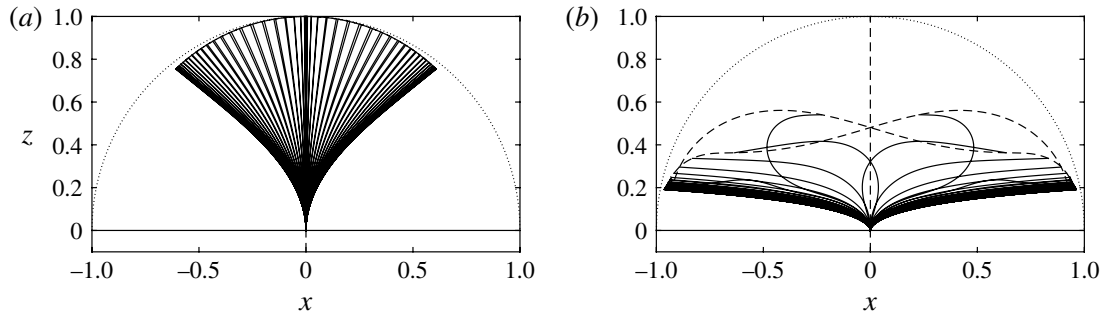


FIGURE 6. Snapshots of the deforming structure over one cycle (—) and tip trajectory (---) obtained with (2.8) for $\lambda = 12.7$, $\alpha = 10^2$. (a) $\omega = 10^{-2}$, (b) $\omega = 1$.

decomposed into two steps: first, a fast reversal period during which the structure switches from one side to the other immediately after flow reversal, followed by a longer period of quasi-static adaptation to the increasing magnitude of the drag. Because the dominant drag force $\lambda|U_n|U_n \propto \lambda\alpha^2\omega^2$ is proportional to ω^2 , the maximum drag is larger in the large frequency case in figure 6, which explains why the maximum deflection is enhanced.

To estimate the time scale of reversal T_r , let us assume that shortly before flow reversal, the structure is fully reconfigured on one side $x(s=1, t=0) = -1$. At flow reversal $t=0$, drag starts pushing the structure to the other side. Let us assume that the blade is purely convected until it is fully reconfigured on the other side at the end of the reversal time $x(s=1, t=T_r) = 1$. In that case, we may write

$$2 = x_{ip}(T_r) - x_{ip}(0) = \int_0^{T_r} \alpha\omega \sin(\omega t) dt \simeq \int_0^{T_r} \alpha\omega^2 t dt = \frac{1}{2}\alpha(\omega T_r)^2, \quad (4.6)$$

where the linearization holds owing to the fact that reversal occurs on a time scale much smaller than the period of the cycle ($\omega T_r \ll 2\pi$). We finally obtain $T_r = 2/(\omega\sqrt{\alpha})$. This expression of the reversal time is normalized by the scale of the natural period of the structure. It is more relevant than ω to assess the quasi-steady nature of the deformation in the large-amplitude regime because it compares only the time scale on which structural motion is significant (instead of the whole cycle period) to the characteristic structural response time. Indeed, in figure 6(a), the large reversal time $T_r = 20$ allows the structure to be in quasi-static equilibrium with the fluid loading at all times. Conversely, in figure 6(b) the small reversal time $T_r = 0.2$ is responsible for the propagation of curvature waves during reversal. Hence, when $T_r \gg 1$, the structure is in static equilibrium with the fluid forces during the whole cycle, while the quasi-static character of the deformation is lost during the fast reversal when $T_r \ll 1$.

A zoom on the trajectory of the tip around flow reversal in the case of figure 6(b) shown in figure 7 (solid line) confirms that reversal occurs approximately between $t/T_r = 0$ and $t/T_r = 1$. When the slenderness parameter is increased (broken lines, $\lambda = 127$), the time scale of the dynamics remains unchanged. The same graphs, for the same T_r but for a smaller or a larger amplitude ($\alpha = 10$ and $\alpha = 10^3$ respectively), not shown here, are practically indistinguishable from that in figure 7. This result confirms that the amplitude and frequency parameters influence the kinematics of the reversal exclusively through the combined parameter T_r . Besides, because the structural mass was neglected, no dynamic excitation possibly resulting from the violent reversal is allowed to persist after T_r .

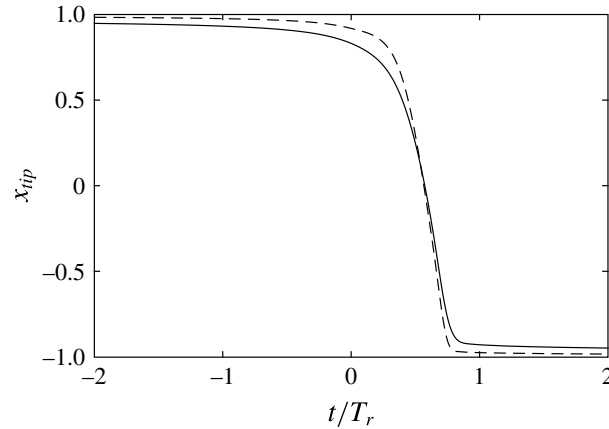


FIGURE 7. Horizontal displacement of the tip during flow reversal against the rescaled time t/T_r , for $\alpha = 10^2$, $T_r = 0.2$ ($\omega = 1$) and $\lambda = 12.7$ (—), $\lambda = 127$ (---).

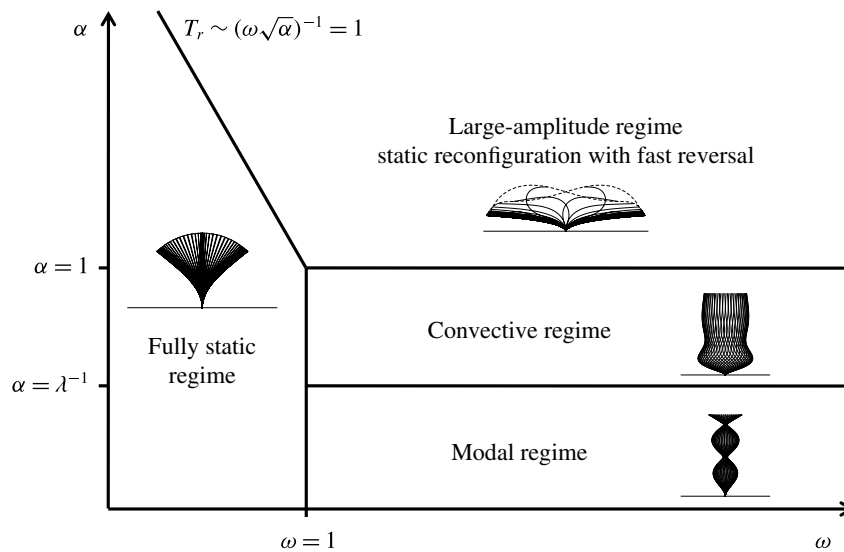


FIGURE 8. Schematic view of the kinematic regimes in the amplitude–frequency space.

4.3. Summary of the kinematic regimes

So far we have found that depending on the amplitude and frequency of the oscillating flow with respect to the dimensions and natural frequencies of the blade, four different kinematic regimes may exist. Their respective locations in the parameter space are summarized in figure 8.

First, if the amplitude is much smaller than the length of the blade ($\alpha \ll 1$ or equivalently $A \ll L$) and the frequency of the flow smaller than that of the structure ($\omega < 1$ or equivalently $\Omega < 1/T_s$), the structure is in static equilibrium with the fluid forces at all times. On the other hand, if the frequency is now comparable or larger than the characteristic structural frequency ($\omega > 1$ or equivalently $\Omega > 1/T_s$), the kinematics further depends on the ratio of the amplitude of the flow to the width of the structure. If the amplitude is much smaller than the width of the blade ($A \ll W$, or equivalently $K_C = \lambda\alpha \ll 1$), the structure behaves as a linear oscillator and we are in the modal regime. If the amplitude is large compared to the width, but small compared to the length ($W \ll A \ll L$, or equivalently $K_C = \lambda\alpha \gg 1$ and $\alpha \ll 1$),

an elastic boundary layer develops close to the clamped edge in which all the curvature is confined, while the rest of the structure is passively convected with the fluid particles. This convective regime occurs because of the saturation of the drag term in the small-amplitude equation (4.1).

Now, if the amplitude is increased further and becomes larger than the length of the blade ($A \gg L$ or equivalently $\alpha \gg 1$), the convection of the blade by the fluid is limited to its own length and the blade deformation is subject to geometric saturation. The convection process is therefore limited in time to a short reversal period, right after flow reversal, and during which the blade switches side at the speed of the fluid particles, followed by a longer period of quasi-static adaptation to the increasing magnitude of the drag force. If reversal occurs on a longer time scale than the characteristic structural response time ($T_r \sim 1/(\omega\sqrt{\alpha}) \gg 1$), the structure has time to reach the static equilibrium with the fluid forces at all time. Conversely, if reversal is faster than the characteristic time of the structure ($T_r \sim 1/(\omega\sqrt{\alpha}) \ll 1$), the quasi-static nature of the large-amplitude structural response is lost during the short time needed for reversal.

5. Structural stress analysis

5.1. Stress reduction due to flexibility

Depending on the kinematic regime, we expect that the consequences of flexibility in terms of magnitude and repartition of the internal stresses will vary. Our main interest is to assess whether flexibility makes a blade more or less likely to break in a given flow. Structural failure may occur when, at a given time t , the stress due to the loads exceeds a given threshold called the breaking strength, at some location within the structure. For an Euler–Bernoulli beam in two-dimensional bending, the stress tensor may essentially be reduced to two components, the tensile (or compressive) stress σ_τ and the shear stress σ_n . Both quantities vary along the span but also within the cross-section. The maximum tensile stress is reached at the edges of the cross-section and depends linearly on the internal bending moment $\sigma_\tau \propto MD/I \propto M/WD^2$. Conversely, the shear stress reaches its maximum on the neutral axis and it is proportional to the internal shear force $\sigma_n \propto Q/WD$. Thus, following the dedicated terminology of Gosselin *et al.* (2010), we may define two reconfiguration numbers

$$\mathcal{R}_\tau = \frac{\max |M(s, t)|}{\max |M_{rigid}(s, t)|}, \quad \mathcal{R}_n = \frac{\max |Q(s, t)|}{\max |Q_{rigid}(s, t)|} \quad (5.1a,b)$$

that compare the maximum stresses endured over a cycle at any point along the structure to the maximum value the same structure would have to endure if it were rigid. The reconfiguration numbers are smaller than one if the flexibility is beneficial in terms of internal stresses, and larger than unity if it is detrimental.

Our shear reconfiguration number \mathcal{R}_n is equivalent to the reconfiguration number defined in Gosselin *et al.* (2010) and Leclercq & de Langre (2016) in the static case. Their definition is based on the total drag $Q(s=0)$ instead of the maximum of the shear force $\max |Q|$, but the shear force is in fact maximum at the clamped edge in their case so it is equal to the total drag. Our \mathcal{R}_n is also quite similar to the effective length defined by Luhar & Nepf (2016), only the latter was based on the root-mean-square value of the total drag $Q(s=0)$ instead of the spatio-temporal maximum of Q . This is so because the goal of Luhar & Nepf (2016) was to provide insight about how flexibility affects energy dissipation in the background flow, while our focus is

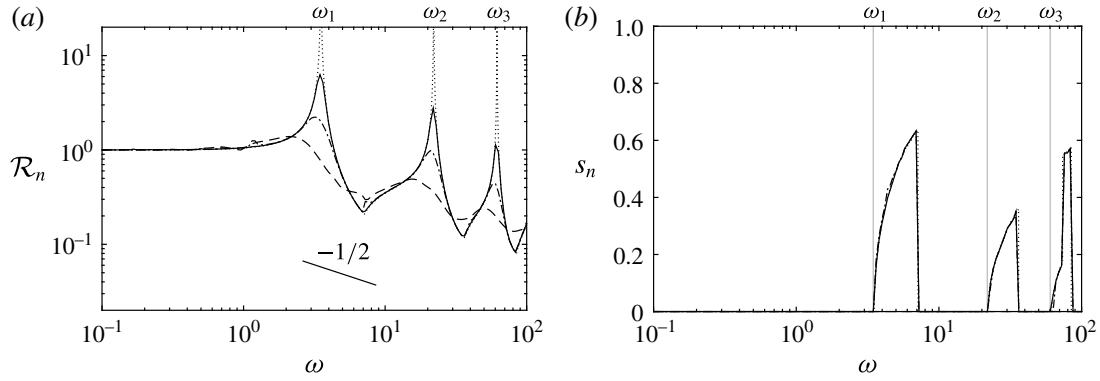


FIGURE 9. Shear reconfiguration number (a) and location of maximum shear stress along the span (b), in the modal regime, against the frequency ratio, for $K_C = 10^{-2}$ (—), $K_C = 10^{-1}$ (— · —), $K_C = 10^0$ (---) and analytical solution for $K_C \rightarrow 0$ (·····).

the ability of the structure to withstand the fluid loads. For the sake of simplicity, in the rest of this article we will only present results about the shear stress σ_n and shear reconfiguration number \mathcal{R}_n . The results about the tensile stress are actually quite similar and will be provided in appendix A.

5.2. Rigid case

In the case of a perfectly rigid structure, the combination of the external fluid forces (2.2) and (2.4) results in a span-invariant, purely horizontal load

$$q_{rigid}(t) = \alpha \omega^2 [\cos(\omega t) + (\lambda \alpha) |\sin(\omega t)| \sin(\omega t)] \quad (5.2)$$

that also reads, in terms of the Cauchy number ($C_Y = \lambda \alpha^2 \omega^2$) and Keulegan–Carpenter number ($K_C = \lambda \alpha$)

$$q_{rigid}(t) = \frac{C_Y}{K_C} [\cos(\omega t) + K_C |\sin(\omega t)| \sin(\omega t)]. \quad (5.3)$$

The first term is an inertia term, proportional to the flow acceleration, while the second term is the resistive drag force proportional to the velocity squared. Integration from the free tip provides the internal bending moment and shear force

$$M_{rigid}(s, t) = -\frac{1}{2} q_{rigid}(t) (1-s)^2, \quad Q_{rigid}(s, t) = -q_{rigid}(t) (1-s) \quad (5.4a, b)$$

that are maximum at the clamped edge and $\max |M_{rigid}(s, t)| = 1/2 \max |Q_{rigid}(s, t)| = 1/2 \max |q_{rigid}(t)|$ with

$$\max |q_{rigid}(t)| = \frac{C_Y}{K_C} \quad \text{if } K_C \leq \frac{1}{2}; \quad C_Y \left(1 + \frac{1}{4K_C^2}\right) \quad \text{if } K_C \geq \frac{1}{2}. \quad (5.5a, b)$$

5.3. Small amplitude of flow oscillation $\alpha = A/L \ll 1$

As for the kinematics, let us first consider the case where the amplitude of forcing is small compared to the length of the structure ($\alpha \ll 1$). Depending on the value of the Keulegan–Carpenter number K_C , the system will be in the modal or convective regime.

The variations of the shear reconfiguration number with the frequency ratio are shown in figure 9(a) for different values of K_C in the modal regime. Because the

system behaves as a high-pass filter, the blade remains rigid in the quasi-static limit $\omega < 1$ and so there is no drag reduction in this regime $\mathcal{R}_n \sim 1$. For larger frequencies, the reconfiguration number decreases overall but peaks at the successive resonances. The magnitude of the peaks is mitigated when the Keulegan–Carpenter number is increased due to damping by the drag term. The resonance frequencies are decreased as well owing to the nonlinearity of the drag term, as explained in Arellano Castro *et al.* (2014). But when K_C is small enough, the reconfiguration number may even exceed unity close to the first resonances. In these particular cases, flexibility may therefore be responsible for a magnification of the shear stress. Apart from the resonances, the slope of the overall decay may be estimated by a scaling argument. Far from the resonances, the amplitude of the deflection is of the order of the fluid particles excursion $x = O(\alpha)$. The non-dimensional shear force $Q = \kappa'$, is thus of order $O(\alpha \times k^3)$ with the wavenumber of the dominant mode $k \sim \sqrt{\omega}$, while the rigid shear force is of order $O(C_Y/K_C) = O(\alpha\omega^2)$ according to (5.5). Thus, the shear reconfiguration number is $\mathcal{R}_n \sim k^{-1} \sim \omega^{-1/2}$, which is consistent with the slope observed in figure 9(a).

As shown in figure 9(b), the location s_n along the span of the blade where the maximum shear stress $\max(\sigma_n)$ is reached varies with the frequency. In the rigid domain $\omega < 1$ the maximum stress remains at the clamped edge, until the first resonance is reached. After ω_1 , the maximum stress starts moving from the clamped edge towards the free tip as \mathcal{R}_n decreases, before suddenly going back to the clamping point as \mathcal{R}_n starts increasing again, until the second resonance is attained. Similarly, after ω_2 , the locus moves again as \mathcal{R}_n decreases and then comes back as \mathcal{R}_n starts increasing towards the next resonance, and so on. This trajectory of the most solicited spot is independent of K_C , except close to the transition towards the convective regime. Indeed, for $K_C = 1$, the maximum shear stress remains at the clamping point for any value of the frequency ratio.

In the convective regime $K_C > 1$, we have shown that all the curvature concentrates within an elastic boundary layer of typical size $\delta = (K_C \omega^2)^{-1/4}$ close to the attachment point. Consequently, the location of the maximum stress is always located at the clamping point in the convective regime. Besides, the variations of the shear reconfiguration number \mathcal{R}_n , displayed as a function of the frequency ratio in figure 10(a), all collapse on the same curve when replotted as a function of $K_C \omega^2$ in figure 10(b). Even the transition case $K_C = 1$ also follows the same trend on average, but still exhibits some variations and small resonances due to the persistent modal nature of the response. When $K_C \omega^2 < 1$, the scale of the boundary layer exceeds the length of the structure so the blade behaves rigidly and $\mathcal{R}_n \sim 1$. Conversely when $K_C \omega^2 > 1$, the motion allowed by the flexibility is responsible for an alleviation of the internal shear stress. We may estimate the slope of the asymptotic decay by a similar argument as in the modal regime. Assuming that the characteristic bending length scales as the boundary layer thickness δ , we now have $Q \sim O(\alpha \times \delta^{-3})$ and the rigid shear force of order $O(C_Y) = O(\alpha\delta^{-4})$. We thus obtain $\mathcal{R}_n \sim \delta \sim (K_C \omega^2)^{-1/4}$, in agreement with figure 10(b). Note that, as illustrated in figure 10(a), reconfiguration in the elastic boundary layer occurs even in the quasi-static regime $\omega < 1$ provided that $K_C \omega^2 > 1$. Indeed, in this particular case, the rigid force q_{rigid} that appears on the right-hand side of the small-amplitude static equation (4.2) would actually lead to static deformations exceeding the excursion of the fluid particles. This is not possible in this drag-dominated regime as only strong inertial forces can cause the structure to overshoot the fluid particles. The drag term of (4.3) thus ensures the limitation of the structural excursion to that of the fluid particles, while only the elastic boundary layer

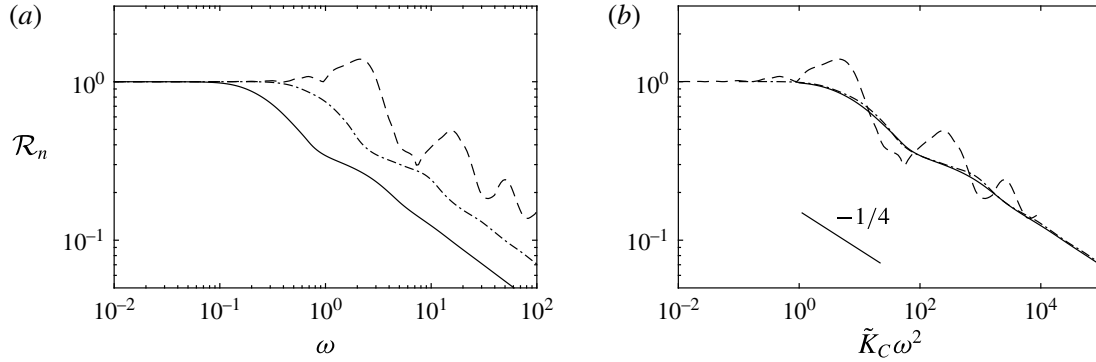


FIGURE 10. Shear reconfiguration number in the convective regime against (a) the frequency ratio ω , (b) the rescaled parameter $K_C \omega^2$, for $K_C = 10^0$ (---), $K_C = 10^1$ (— · —), $K_C = 10^2$ (—).

that develops close to the clamped edge actually satisfies the quasi-static equilibrium between the elasticity forces and the drag (which amounts to neglecting the $\dot{\tilde{x}}$ terms in the boundary layer equation (4.5)). Consequently, the scaling of the drag associated with reconfiguration in the elastic boundary layer remains valid in this domain as well.

5.4. Large amplitude of flow oscillation $\alpha = A/L \gg 1$

In the large-amplitude regime ($\alpha > 1$), we have proven that significant structural motion may only occur during a short period of time T_r following flow reversal ($\omega t = 0$). During that time, the flow magnitude is close to zero and the drag force is at its minimum. Drag being the dominant term of the equation, we expect the largest stress to be experienced when it is at its maximum around $\omega t = \pm\pi/2$, at a time where the structure is in quasi-static equilibrium with the flow forces. Besides, the flow acceleration cancels out when the flow magnitude is maximum so that, at the time where the stress peaks, equation (2.8) reduces to the static equation

$$\kappa'' + \frac{1}{2}\kappa^3 - C_Y \left[|\cos \theta| \cos \theta - \frac{1}{\lambda} \kappa \left(\sin^2 \theta - \frac{1}{2} \cos^2 \theta \right) \right] = 0. \quad (5.6)$$

In the quasi-static part of the cycle, the amplitude and frequency parameter influence the shape of the structure and the internal stress only through the Cauchy number $C_Y = \lambda \alpha^2 \omega^2$. Consequently, the evolution of the shear reconfiguration number shown in figure 11(a) as a function of the frequency ratio ω (for $\lambda = 12.7$) collapse very well on the static curve obtained with (5.6) when replotted as a function of the Cauchy number in figure 11(b). The curves are perfectly superimposed for $\alpha = 10$, but even for α as small as 1, agreement is already very good. When the Cauchy number is less than 1, deflection is negligible so (5.6) actually reduces to the small-amplitude static equation (4.2). In this limit, even though the amplitude of the forcing is large $\alpha > 1$, we actually recover the small-amplitude static regime in which the structure experiences the same amount of stress as if it were rigid $\mathcal{R}_n \sim 1$.

On the other hand, when the Cauchy number is large $C_Y > 1$, the stress is much reduced. In the limit where drag dominates over the added mass corrective term (limit of infinite slenderness $\lambda \rightarrow \infty$), the static equation (5.6) has a self-similar structure. The scaling of the terms of the equation provides the length of the self-similar

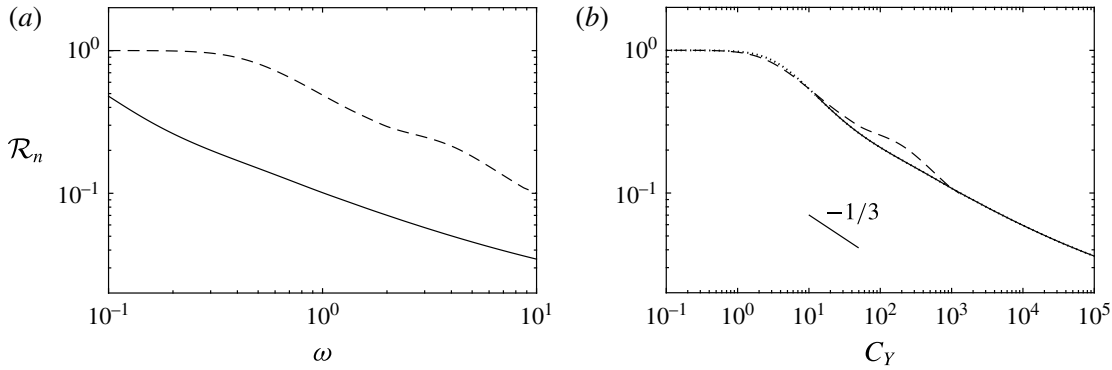


FIGURE 11. Shear reconfiguration number in the large-amplitude regime for $\lambda = 12.7$, against (a) the frequency ratio ω , (b) the Cauchy number C_Y , for $\alpha = 10^0$ (---), $\alpha = 10^1$ (—). Static solution obtained with (5.6) (⋯⋯⋯, on (b) only).

boundary layer $\ell_s = C_Y^{-1/3}$ within which all the curvature concentrates. Consequently we may here again estimate the asymptotic behaviour of the shear reconfiguration number by a scaling argument. In this case, the saturated angle θ is of order $O(1)$ so the shear force $Q = \kappa' \sim O(1 \times \ell_s^{-2})$. The rigid shear force is of order $O(C_Y) = O(\ell_s^{-3})$ so we get $\mathcal{R}_n \sim \ell_s \sim C_Y^{-1/3}$. The slope in figure 11(b) is close but differs slightly from that estimation. The analysis of appendix B shows that this discrepancy is due to the rather small value of $\lambda = 12.7$. For any larger slenderness, the asymptotic scaling provided here matches very well the numerical results. Note that this bending length is similar to that previously found by Gosselin *et al.* (2010) who neglected the cubic term in curvature in their governing equation, as well as that found by Alben *et al.* (2004) for the case of a two-dimensional plate (opposite limit of infinite width). The extended validity of this static bending length to the case of large-amplitude unsteady flows was moreover suggested in Luhar & Nepf (2016).

Note finally that this analysis is independent of the magnitude of the reversal time T_r . The key point of this analysis lies in the fact that even if significant dynamics may be involved during reversal when $T_r \gg 1$, the maximum stress is endured at a time when the structure is in static equilibrium with the fluid forces. This remains obviously true when $T_r \ll 1$ and static equilibrium is enforced at all times.

6. Discussion

6.1. Stress alleviation due to flexibility and bending length

Depending on the values of the amplitude and frequency of the oscillating flow, we have identified four distinct kinematic regimes summarized in figure 8. In each regime, the consequences of the flexibility on the magnitude of the internal stress are different. The varying scalings of the shear reconfiguration number \mathcal{R}_n depending on the amplitude and frequency of the flow are schematically displayed in figure 12.

As long as the forcing is dominated by the inertial forces (in the modal regime $A \ll W$), there exists a risk of resonance if the frequency of the flow matches one of the natural frequencies of the structure. This is a case where the dynamical motion allowed by the flexibility may be responsible for a magnification of the internal stress. However, this is also the region in the parameter space where the loading is the lowest and so this is unlikely to cause any severe damage. Far from the resonances and in all other cases, flexibility always alleviates the magnitude of the internal stress.

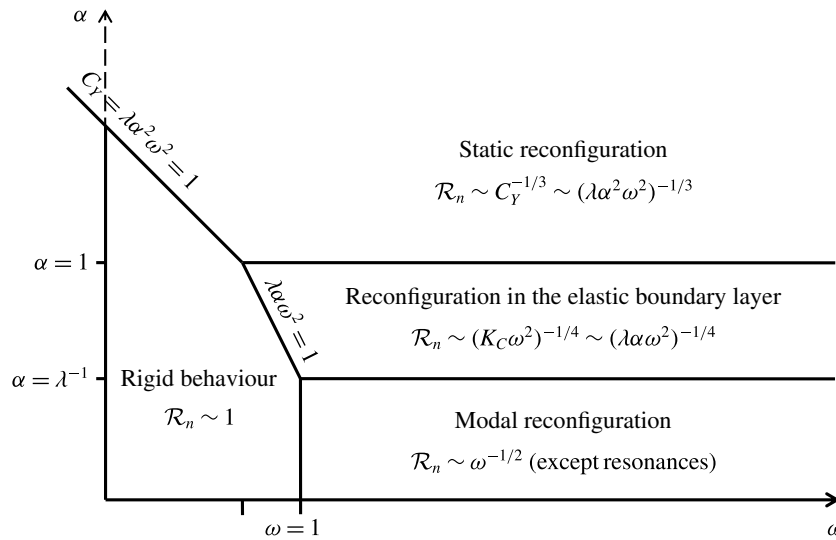


FIGURE 12. Schematic view of the reconfiguration regimes in the amplitude–frequency space.

The general scaling of the reconfiguration numbers is related to some characteristic bending length ℓ_b such that $\mathcal{R}_n \sim \ell_b$ and $\mathcal{R}_\tau \sim \ell_b^2$ (see appendix A), but the scaling of that very bending length depends on the reconfiguration regime. In the modal regime ($A \ll W$), the bending length is proportional to the wavelength of the dominant mode that varies as $\ell_b = k^{-1} = \omega^{-1/2}$. In the convective regime ($W \ll A \ll L$), curvature is confined in the elastic boundary layer so naturally $\ell_b = \delta = (\lambda\alpha)^{-1/4} \omega^{-1/2}$. The characteristic bending length varies continuously between the two small-amplitude regimes as their expressions are similar at the transition when $K_C = \lambda\alpha = 1$. On the other hand, in the large-amplitude regime ($A \gg L$) the bending length transitions to $\ell_b = \ell_s = C_Y^{-1/3} = (\lambda\alpha^2 \omega^2)^{-1/3}$. The boundary of the rigid domain with the three different reconfiguration regimes is nonetheless continuous as illustrated in figure 12.

6.2. Consequences in terms of growth pattern of aquatic flexible plants

In any of the three reconfiguration regimes, the reconfiguration numbers scale in dimensional form with the length of the blade as $\mathcal{R}_n \sim L^{-1}$ and $\mathcal{R}_\tau \sim L^{-2}$. Given the scalings of the rigid loads and of the internal stresses in § 5.1, we thus obtain the cancellation of the dependency of the dimensional forces and internal stresses on the actual length of the blade $\sigma_n \propto Q \sim L^0$ and $\sigma_\tau \propto M \sim L^0$. This loss of relevance of the true length of the structure in aid of a smaller characteristic bending length was already pointed out in the steady case (see de Langre, Gutierrez & Cossé 2012) and remains valid in the oscillatory case. Consequently, it does not seem as if there is any mechanical limit to size in wave-swept flexible kelps, as long as growth is concentrated in the axial direction.

But real plants grow according to more complex allometric patterns (Denny & Cowen 1997; Gaylord & Denny 1997). Following the growth of a plant in the variables of figure 12 amounts to decreasing α from the top. In the static reconfiguration regime, the internal stresses σ_n and σ_τ are both independent of any of the three dimensions D , W , L and so growth does not affect the magnitude of the stresses in a given environment, no matter the allometry of the plant. When the structure reaches the convective regime ($L \geq A$), the stresses become decreasing

functions of the thickness D but remain independent of W and L . One might think that a growth pattern favouring thickness would be advantageous, but this is only so for thin plates $D < W$ for which the elastic effects are confined in the plane of the flow. A thicker structure might experience three-dimensional deformations that would make the dynamics considerably more complex. Finally, in the modal regime ($W \geq A$), the stresses now start increasing with the width W , and the risk of resonances may enhance the stresses even more depending on the frequency of the flow. It thus appears detrimental for a flexible plant to grow in width in excess of the fluid particle excursion.

These remarks come as complementary answers to the work of Koehl (1984) and especially Denny *et al.* (1985), Gaylord, Blanchette & Denny (1994) and Denny (1999). Koehl (1984) first noted that ‘flexibility in combination with great length provides a mechanism of avoiding bearing large forces in habitats subjected to oscillating flow’, in comparison to rigid organisms that need to remain small. However the question of whether there might be size limits imposed on wave-swept flexible organisms due to the oscillatory fluid loading has never received a definitive answer. Our results indicate that for slender, neutrally buoyant blades, the hydrodynamic loads do limit the width, but put no constraints on the axial growth.

6.3. Remarks on previous work about the convective regime

Most aquatic plants are close to neutrally buoyant and the horizontal amplitude of the passing waves is typically much larger than the width if not the length of these plants (see Gaylord *et al.* 1994; Denny & Cowen 1997; Gaylord & Denny 1997). Thus it seems that plants growing larger than the fluid particles excursion are likely to remain in the convective regime in order to avoid large flow-induced stresses. The work of Mullarney & Henderson (2010) and Luhar & Nepf (2016) has focused mainly on this convective regime. The latter show on their figure 11 that their effective length (analogous to our normal reconfiguration number \mathcal{R}_n) seems to scale as $(C_Y/\alpha)^{-1/4} = (\lambda\alpha\omega^2)^{-1/4} = \delta$. This result is consistent with the scaling of the elastic boundary layer that develops in the convective regime, and indeed almost all the experimental cases of Luhar & Nepf (2016) were obtained within the appropriate range $\alpha \leq 1$ and $K_C \geq 1$ (more precisely $0.06 \leq \alpha \leq 1.32$ and $0.76 \leq K_C \leq 4.2$). However, because the slenderness parameter of their blades is rather low (between $\lambda = 3.2$ and $\lambda = 12.7$), α and K_C are quite close to each other and consequently most of their points are very close to either one of the boundaries of that regime. Some particular points in that study show an increase of the load compared to the rigid case. The authors suggested that this might result from an interaction between the blade and the vortex shed at the tip. But these points are characterized by a rather small amplitude $\alpha = O(10^{-1})$ and Keulegan–Carpenter number $K_C \sim 0.7 - 1.2$, and forcing frequencies close to the resonance frequency $\omega \sim 1 - 5$. For instance, the largest load was obtained for ($\alpha = 0.12$, $K_C = 0.76$ and $\omega = 2.30$). It is thus a possibility that the load enhancement is simply the consequence of a resonance of the impinging wave with the first natural mode of the structure, due to the persistent modal nature of the dynamic response for such values of the parameters. Conversely, other points obtained for $\alpha = O(1)$ seem to collapse quite well with the others. We have shown that for such high values of the amplitude parameter, at least when $\lambda = 12.7$, the reconfiguration number should be close to its static equivalent. But if very slender structures exhibit a clear asymptotic regime $\mathcal{R}_n \sim C_Y^{-1/3}$, decreasing the slenderness below $O(10)$ mitigates the efficiency of the reconfiguration and increases the slope so that it may be difficult to know the difference with the scaling of the convective regime.

6.4. Limits and extensions of the model

In all this study we have focused exclusively on the case of an infinitely thin, neutrally buoyant blade. These two assumptions have allowed us to neglect both the displaced mass and the structural mass. In practice however, aquatic plants are not strictly speaking of the same density as the water and their thicknesses might not be negligible.

First, if the thickness of the neutrally buoyant blade is not negligible anymore, we need to consider the inertial and virtual buoyancy forces. These forces might be responsible for additional inertial effects in the large-amplitude regime, such as persistent oscillations following the quick reversal with $T_r < 1$, or a flutter instability similar to that observed on axial flags. The dynamics induced would then be responsible for additional loads that may challenge the findings of that study. However, we expect the consequences to remain marginal, as damping by the drag term would still dominate. This is even more so as the slenderness is increased and for infinite slenderness, we do not expect any significant discrepancy with the present work. Besides, the small-amplitude regimes would not be affected in any way as (4.1) would remain the same, providing that the characteristic time of the structure used for non-dimensionalization is redefined to account for the structural mass $T_s = L^2 \sqrt{(m_a + m)/EI}$.

If the structure is now lighter than the fluid, then its inertia is even more negligible. Buoyancy may still modify our results, but this effect should become negligible as soon as the fluid loading is dominant as explained in Luhar & Nepf (2011) and Luhar & Nepf (2016).

On the other hand, if the structure is much denser than the fluid, some more complicated dynamical effects might come into play due to the large structural inertia possibly overcoming even drag. We do not expect the conclusions of the present work to hold in that case.

7. Conclusion

This work provides a dynamical extension of the theory of reconfiguration to the case of oscillatory flow. Focusing on neutrally buoyant cantilever slender blades, we proved that flexibility is always favourable to reducing the internal stresses as long as drag dominates the fluid inertial forces. In fact, drag appears as the motor of reconfiguration. In large-amplitude oscillations (or equivalently in steady flow), drag is responsible for the static deflection that reduces the stress. In small-amplitude oscillations, it is also the saturation of the drag term that forces the passive convection of the structure with the fluid particles if the Keulegan–Carpenter number is large. Even in the less favourable case of small Keulegan–Carpenter numbers, it is the small drag term that saturates the resonances that occur due to the fluid inertia, even when the structural inertia is negligible. We also expect that drag would saturate flutter-like oscillations that might occur if the structural mass were not negligible, thus limiting the enhancement of the internal stresses to a bearable extent.

As in the static case, we have shown that dynamic reconfiguration results in the concentration of the stresses on a short bending length near the clamped edge, only the scaling of that bending length varies depending on the dynamic regime. Consequently, the dependency of the internal stresses on the actual length of the structure disappears, and there does not seem to be any mechanical limitation to the axial growth of plants living in wave-swept environment due to the hydrodynamic loads. However, in order to avoid deleterious inertial effects, it seems better to keep a much smaller width than

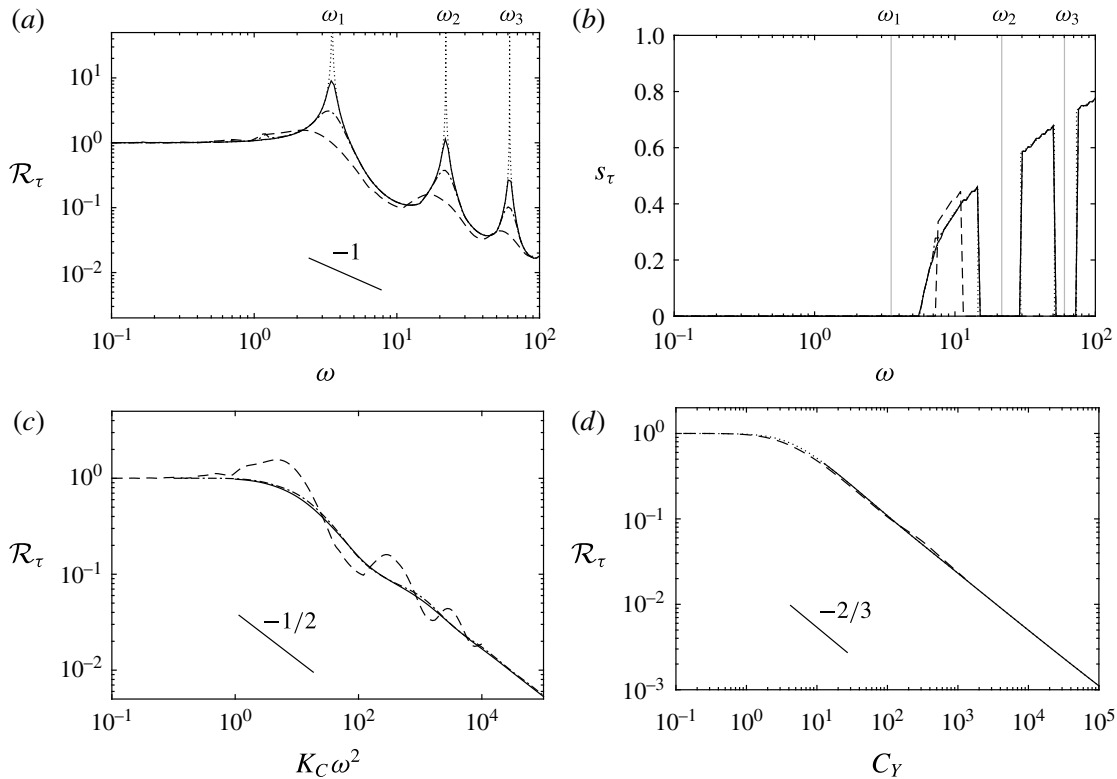


FIGURE 13. (a) Tensile reconfiguration number and (b) location of maximum tensile stress along the span in the modal regime, against the frequency ratio, for $K_C = 10^{-2}$ (—), $K_C = 10^{-1}$ (— · —), $K_C = 10^0$ (---) and analytical solution for $K_C \rightarrow 0$ (·····). (c) Tensile reconfiguration number against $K_C \omega^2$ in the convective regime $K_C = 10^0$ (---), $K_C = 10^1$ (— · —), $K_C = 10^2$ (—). (d) Tensile reconfiguration number in the large-amplitude regime for $\lambda = 12.7$, against the Cauchy number C_Y for $\alpha = 10^0$ (---), $\alpha = 10^1$ (—) and static solution obtained with (5.6) (·····).

the excursion of the fluid particles. In other words, if there is no limitations to growth in itself, there is an incentive to grow slender based on mechanical considerations. Of course, the actual growth pattern of aquatic plants also involves other aspects such as the optimization of its biological functions that we do not take into account here.

Up to here, only the inertia of the fluid has been accounted for. We expect the inclusion of significant structural inertia should considerably modify the results of the present work.

Acknowledgements

The authors would like to acknowledge financial support from the DGA/DSTL grant 2014.60.0005 and fruitful discussions with N. Peake from DAMTP, Cambridge, UK.

Appendix A. Tensile stress

Similarly to the shear reconfiguration number, the variations of the tensile reconfiguration number are displayed in figure 13(a) for the modal regime, along with the location of the maximum stress in figure 13(b). Figures 13(c) and 13(d) respectively show the results in the convective and large-amplitude regime. All the conclusions drawn about the shear reconfiguration number are still valid for the tensile

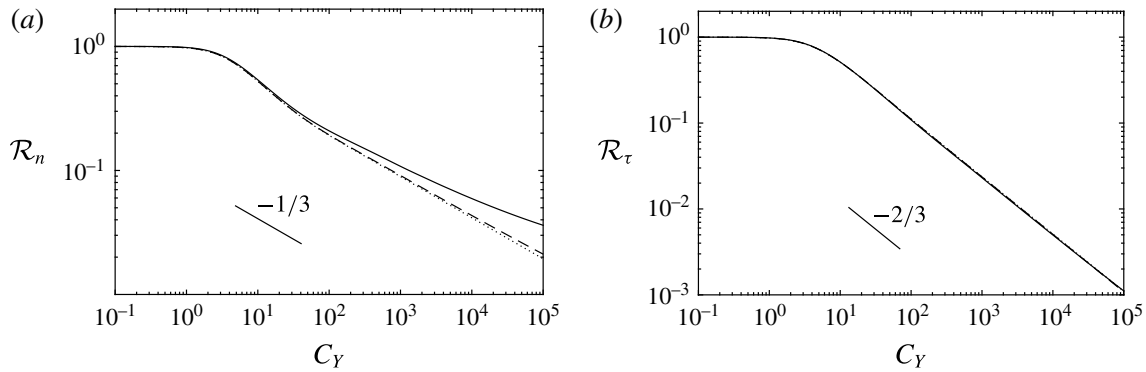


FIGURE 14. Variations of the static reconfiguration numbers obtained with (5.6) ((a) shear, (b) tensile) as a function of the Cauchy number C_Y , for $\lambda = 12.7$ (—), $\lambda = 127$ (---), $\lambda = 1270$ (.....).

number. The only noticeable difference is the asymptotic scaling for large loadings. Indeed, the non-dimensional bending moment $M = \kappa$ involves one less derivative in space than the shear force Q so that $M \sim Q \times \ell_b$, while the non-dimensional rigid load is unchanged. Therefore, $\mathcal{R}_\tau \sim \mathcal{R}_n \times \ell_b \sim \ell_b^2$. Finally, this provides $\mathcal{R}_\tau \sim \omega^{-1}$ in the modal regime, $\mathcal{R}_\tau \sim (K_C \omega^2)^{-1/2}$ in the convective regime and $\mathcal{R}_\tau \sim C_Y^{-2/3}$ in the large-amplitude regime, in agreement with the results shown.

Appendix B. Influence of the slenderness on the static reconfiguration

In the large-amplitude regime, most of the cycle is quasi-static and the system is well modelled by (5.6). The different static reconfiguration curves for varying slenderness parameters shown in figure 14 prove that the reconfiguration numbers converge on an asymptotic trend as the slenderness is increased. For any finite λ , the discrepancy with the asymptotic curve remains quite small for the shear stress, and almost completely imperceptible for the tensile stress. The asymptotic scaling provided in § 5 can therefore be used even for moderately large slenderness.

REFERENCES

- ALBEN, S. 2008 Optimal flexibility of a flapping appendage in an inviscid fluid. *J. Fluid Mech.* **614**, 355–380.
- ALBEN, S., SHELLEY, M. & ZHANG, J. 2002 Drag reduction through self-similar bending of a flexible body. *Nature* **420** (6915), 479–481.
- ALBEN, S., SHELLEY, M. & ZHANG, J. 2004 How flexibility induces streamlining in a two-dimensional flow. *Phys. Fluids* **16** (5), 1694–1713.
- ARELLANO CASTRO, R. F., GUILLAMOT, L., CROS, A. & ELOY, C. 2014 Non-linear effects on the resonant frequencies of a cantilevered plate. *J. Fluids Struct.* **46**, 165–173.
- AUDOLY, B. & POMEAU, Y. 2010 *Elasticity and Geometry: From Hair Curls to the Non-Linear Response of Shells*. Oxford University Press.
- BLEVINS, R. D. 1990 *Flow-Induced Vibration*. Van Nostrand Reinhold Company.
- BROYDEN, C. G. 1965 A class of methods for solving nonlinear simultaneous equations. *Math. Comput.* **19** (92), 577–593.
- CANDELIER, F., BOYER, F. & LEROYER, A. 2011 Three-dimensional extension of Lighthill's large-amplitude elongated-body theory of fish locomotion. *J. Fluid Mech.* **674**, 196–226.
- CHAKRABARTI, S. K. 2002 *The Theory and Practice of Hydrodynamics and Vibration*. World Scientific.

- DENNY, M. W. 1999 Are there mechanical limits to size in wave-swept organisms? *J. Expl Biol.* **202** (23), 3463–3467.
- DENNY, M. W. & COWEN, B. 1997 Flow and flexibility. II. The roles of size and shape in determining wave forces on the bull kelp *Nereocystis luetkeana*. *J. Expl Biol.* **200** (24), 3165–3183.
- DENNY, M. W., DANIEL, T. L. & KOEHL, M. A. R. 1985 Mechanical limits to size in wave-swept organisms. *Ecol. Monographs* **55** (1), 69–102.
- ELOY, C., KOFMAN, N. & SCHOUVEILER, L. 2012 The origin of hysteresis in the flag instability. *J. Fluid Mech.* **691**, 583–593.
- FRIEDLAND, M. T. & DENNY, M. W. 1995 Surviving hydrodynamic forces in a wave-swept environment: consequences of morphology in the feather boa kelp, *Egregia menziesii* (Turner). *J. Exp. Marine Biol. Ecology* **190** (1), 109–133.
- GAYLORD, B., BLANCHETTE, C. A. & DENNY, M. W. 1994 Mechanical consequences of size in wave-swept algae. *Ecol. Monographs* **64** (3), 287–313.
- GAYLORD, B. & DENNY, M. W. 1997 Flow and flexibility. I. Effects of size, shape and stiffness in determining wave forces on the stipitate kelps *Eisenia arborea* and *Pterygophora californica*. *J. Expl Biol.* **200** (24), 3141–3164.
- GOSSELIN, F., DE LANGRE, E. & MACHADO-ALMEIDA, B. A. 2010 Drag reduction of flexible plates by reconfiguration. *J. Fluid Mech.* **650**, 319–341.
- HARDER, D. L., SPECK, O., HURD, C. L. & SPECK, T. 2004 Reconfiguration as a prerequisite for survival in highly unstable flow-dominated habitats. *J. Plant Growth Regul.* **23** (2), 98–107.
- HASSANI, M., MUREITHI, N. W. & GOSSELIN, F. 2016 Large coupled bending and torsional deformation of an elastic rod subjected to fluid flow. *J. Fluids Struct.* **62**, 367–383.
- KATZ, J. & WEIHS, D. 1978 Hydrodynamic propulsion by large amplitude oscillation of an airfoil with chordwise flexibility. *J. Fluid Mech.* **88** (3), 485–497.
- KATZ, J. & WEIHS, D. 1979 Large amplitude unsteady motion of a flexible slender propulsor. *J. Fluid Mech.* **90** (4), 713–723.
- KEULEGAN, G. H. & CARPENTER, L. H. 1958 Forces on cylinders and plates in an oscillating fluid. *J. Res. Natl Bur. Stand.* **60** (5), 423–440.
- KOEHL, M. A. R. 1984 How do benthic organisms withstand moving water? *Am. Zool.* **24** (1), 57–70.
- DE LANGRE, E. 2008 Effects of wind on plants. *Annu. Rev. Fluid Mech.* **40**, 141–168.
- DE LANGRE, E., GUTIERREZ, A. & COSSÉ, J. 2012 On the scaling of drag reduction by reconfiguration in plants. *C. R. Méc* **340** (1), 35–40.
- LECLERCQ, T. & DE LANGRE, E. 2016 Drag reduction by elastic reconfiguration of non-uniform beams in non-uniform flows. *J. Fluids Struct.* **60**, 114–129.
- LIGHTHILL, M. J. 1960 Note on the swimming of slender fish. *J. Fluid Mech.* **9** (2), 305–317.
- LIGHTHILL, M. J. 1971 Large-amplitude elongated-body theory of fish locomotion. *Proc. R. Soc. Lond. B* **179** (1055), 125–138.
- LIU, W., XIAO, Q. & CHENG, F. 2013 A bio-inspired study on tidal energy extraction with flexible flapping wings. *Bioinspiration Biomimetics* **8** (3), 036011.
- LUHAR, M., INFANTES, E. & NEPF, H. M. 2017 Seagrass blade motion under waves and its impact on wave decay. *J. Geophys. Res.* **122**, 3736–3752.
- LUHAR, M. & NEPF, H. M. 2011 Flow-induced reconfiguration of buoyant and flexible aquatic vegetation. *Limnol. Oceanogr.* **56** (6), 2003–2017.
- LUHAR, M. & NEPF, H. M. 2016 Wave-induced dynamics of flexible blades. *J. Fluids Struct.* **61**, 20–41.
- MICHELIN, S. & DOARÉ, O. 2013 Energy harvesting efficiency of piezoelectric flags in axial flows. *J. Fluid Mech.* **714**, 489–504.
- MICHELIN, S. & LLEWELLYN SMITH, S. G. 2009 Resonance and propulsion performance of a heaving flexible wing. *Phys. Fluids* **21** (7), 071902.
- MULLARNEY, J. C. & HENDERSON, S. M. 2010 Wave-forced motion of submerged single-stem vegetation. *J. Geophys. Res.* **115**, C12061.
- PARAZ, F., ELOY, C. & SCHOUVEILER, L. 2014 Experimental study of the response of a flexible plate to a harmonic forcing in a flow. *C. R. Méc* **342** (9), 532–538.

- PARAZ, F., SCHOUVEILER, L. & ELOY, C. 2016 Thrust generation by a heaving flexible foil: resonance, nonlinearities, and optimality. *Phys. Fluids* **28** (1), 011903.
- PIÑEIRUA, M., THIRIA, B. & GODOY-DIANA, R. 2017 Modelling of an actuated elastic swimmer. *J. Fluid Mech.* **829**, 731–750.
- RAMANANARIVO, S., GODOY-DIANA, R. & THIRIA, B. 2011 Rather than resonance, flapping wing flyers may play on aerodynamics to improve performance. *Proc. Natl Acad. Sci. USA* **108** (15), 5964–5969.
- SINGH, K., MICHELIN, S. & DE LANGRE, E. 2012 The effect of non-uniform damping on flutter in axial flow and energy-harvesting strategies. *Proc. R. Soc. Lond. A* **468** (2147), 3620–3635.
- TAYLOR, G. I. 1952 Analysis of the swimming of long and narrow animals. *Proc. R. Soc. Lond. A* **214** (1117), 158–183.
- TICKNER, E. G. & SACKS, A. H. 1969 Engineering simulation of the viscous behavior of whole blood using suspensions of flexible particles. *Circulat. Res.* **25** (4), 389–400.
- UTTER, B. & DENNY, M. W. 1996 Wave-induced forces on the giant kelp *Macrocystis pyrifera* (Agardh): field test of a computational model. *J. Expl Biol.* **199** (12), 2645–2654.
- VOGEL, S. 1984 Drag and flexibility in sessile organisms. *Am. Zool.* **24** (1), 37–44.
- VOGEL, S. 1989 Drag and reconfiguration of broad leaves in high winds. *J. Expl Bot.* **40** (8), 941–948.
- WEAVER, W. J., TIMOSHENKO, S. P. & YOUNG, D. H. 1990 *Vibration Problems in Engineering*. Wiley.

Does flutter prevent drag reduction by reconfiguration?

T. Leclercq¹, N. Peake² and E. de Langre¹

Research



Cite this article: Leclercq T, Peake N, de Langre E. 2018 Does flutter prevent drag reduction by reconfiguration? *Proc. R. Soc. A* **474**: 20170678.

<http://dx.doi.org/10.1098/rspa.2017.0678>

Received: 22 September 2017

Accepted: 10 November 2017

Subject Areas:

fluid mechanics

Keywords:

drag reduction, reconfiguration, flutter, instability, fluid–structure interactions

Author for correspondence:

T. Leclercq

e-mail: tristan.leclercq@polytechnique.edu

¹Department of Mechanics, LadHyX, CNRS, École Polytechnique, 91128 Palaiseau, France

²Department of Applied Mathematics and Theoretical Physics, University of Cambridge, Wilberforce Road, Cambridge CB3 0WA, UK

TL, 0000-0002-5995-3354

The static reconfiguration of flexible beams exposed to transverse flows is classically known to reduce the drag these structures have to withstand. But the more a structure bends, the more parallel to the flow it becomes, and flexible beams in axial flows are prone to a flutter instability that is responsible for large inertial forces that drastically increase their drag. It is, therefore, unclear whether flexibility would still alleviate, or on the contrary enhance, the drag when flapping occurs on a reconfiguring structure. In this article, we perform numerical simulations based on reduced-order models to demonstrate that the additional drag induced by the flapping motion is almost never significant enough to offset the drag reduction due to reconfiguration. Isolated and brief snapping events may transiently raise the drag above that of a rigid structure in the particular case of heavy, moderately slender beams. But apart from these short peak events, the drag force remains otherwise always significantly reduced in comparison with a rigid structure.

1. Introduction

When flexible structures are placed in a fluid flow, the drag they experience is strongly modified by the deformation caused by that flow. In particular, the work of [1] has shown that plants in nature benefit from their flexibility and experience a lower drag force than if they were rigid. This ability to reduce flow-induced forces by passively adapting their shape is now thought to be a key factor in allowing aquatic organisms to survive in flow-dominated environments [2]. To better understand this phenomenon, the studies of [3,4] have analysed the mechanism of elastic reconfiguration and the resulting drag reduction of flat

plates in uniform, steady, large-Reynolds-number flow. More recent papers have additionally accounted for gravity and buoyancy [5], non-uniformities [6], non-planar deformations [7] or viscous effects [8–10].

All these studies assume static structural deflection in a steady background flow. However, the low-Reynolds-number study in [11] has shown that the vortices shed from the free tip may force a flexible fibre into a flapping motion. The efficiency of drag reduction when flapping occurs is then mitigated and depends on the mode of deformation [12]. Such self-induced dynamics has also been witnessed for large-Reynolds-number systems, for instance on tree leaves that flap in the wind [13–15]. The very occurrence of dynamics induces inertial loads that may enhance the drag, and one may wonder whether flexibility is associated with lower or larger drag in that case, compared with a rigid structure that does not reconfigure but does not flap either.

The cause and the nature of the flapping dynamics depend on the geometry of the structure and its orientation to the flow. When the structure is perpendicular to the flow, the vortices shed from the tip are obviously responsible for flow-induced vibrations [16]. Flexible structures exposed to a transverse flow become more and more aligned with it as they reconfigure, but the flapping of flags in the wind illustrates that structures parallel to the flow are also prone to self-induced dynamic oscillations [17–22]. This flag flutter instability results from the competition between the destabilizing aerodynamic pressure forces and the stabilizing rigidity of the structure, so slender structures in axial flow are also liable to it [23–28]. A few authors have tried to assess the drag of such structures theoretically [29], numerically [24] and experimentally [30–36]. All these works prove that the onset of flutter is associated with a large increase in the drag force, whose magnitude is strongly correlated to the periodicity and the envelope of the flutter mode.

As stated above, cantilever structures that bend in a transverse flow become more and more aligned with it, so that the flow about sufficiently deflected beams becomes mostly axial. If reconfiguration is known to have a drag-lowering effect that protects the structural integrity, the possible fluttering of highly reconfigured beams may, on the other hand, be responsible for a magnification of the drag, possibly leading to damage or breakage. In the literature, the small-amplitude vibrations of a naturally curved rod in a flow have been considered in [37], as well as the flapping dynamics of plates clamped in axial flow at their trailing edge instead of their leading edge (the so-called inverted flag problem [38–40]), and the flow-induced instability of filaments clamped at their trailing edge but deflected by gravity [41]. However, very little is known about the self-induced dynamics of structures passively bending under the effect of the flow, and even less about whether the resulting drag force is overall enhanced or reduced. The goal of this work is thus to determine if, and to what extent, the occurrence of flutter may impair the drag reduction abilities of flexible structures in transverse flow compared with rigid ones. We will focus on the case of cantilevered, elongated beams of arbitrary but uniform cross section.

The model used throughout the study is presented in §2. In §3, we discuss the domain of stability of the static reconfiguration. In §4, the post-critical flapping behaviour of the deflected structure is analysed. Finally, the consequences of flexibility in terms of total drag modulation when reconfiguration and flutter are both considered are discussed in §5.

2. Model

We consider the problem depicted in figure 1. A structure of length L , width W , thickness D and mass per unit length m is clamped perpendicular to a uniform and steady flow of velocity U of a fluid of density ρ .

We assume that the structure may only bend in the xz -plane and we neglect torsion or any out-of-plane deformation. The structure is elongated in the plane of bending ($L \gg D$), and we model it as a two-dimensional inextensible Euler–Bernoulli beam of bending stiffness EI [42]. The local angle θ of the tangent vector $\boldsymbol{\tau} = \boldsymbol{r}'$ is defined with respect to the vertical axis e_z , where $\boldsymbol{r} = x(s, t)\boldsymbol{e}_x$

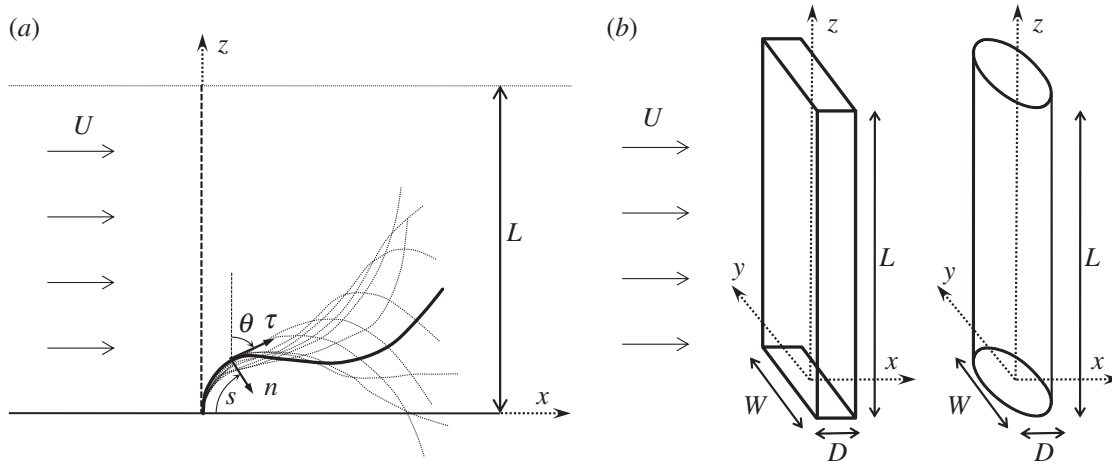


Figure 1. (a) Side view of the deforming structure. (b) Examples of geometries of two undeformed structures with different cross-section shapes.

$+z(s, t)\mathbf{e}_z$ is the position vector and the prime symbol (\cdot) denotes differentiation with respect to the curvilinear coordinate s . Following [42], the dynamic equilibrium reads

$$m\ddot{\mathbf{r}} = \mathbf{F}' + \mathbf{q}, \quad (2.1)$$

where \mathbf{q} is the external load per unit length on the structure, $\mathbf{F} = T\boldsymbol{\tau} + Q\mathbf{n}$ is the internal force vector and the overdot stands for time derivation. The internal bending moment M is related to the local curvature $\kappa = \theta'$ by $M = EI\kappa$, and the shear force Q is given by $Q = -M' = -EI\kappa'$. Clamping implies $x = z = \theta = 0$ at $s = 0$, while the free tip condition reads $T = M = Q = 0$ at $s = L$.

We disregard the influence of gravity and buoyancy forces, and we restrict our study to large Reynolds number so that friction drag is neglected. More details about the influence of friction can be found in [28]. We also assume that the structure is slender ($L \gg W$) so that the flow at a given location s along the span is dominated by its local two-dimensional component in the plane of the cross section. This assumption implies that we neglect the end-wall effects so that this problem physically amounts to considering that the structure is clamped in the middle region of the flow and there is no wall. Following Eloy *et al.* [43], Singh *et al.* [44,45] or Michelin & Doaré [46], we model the effect of the flow as a combination of two external loads distributed along the span. First, the reactive (or added mass) force is related to the potential component of the flow [47,48],

$$\mathbf{q}_{\text{am}} = -m_a[\partial_t(U_n\mathbf{n}) - \partial_s(U_n U_\tau \mathbf{n}) + \frac{1}{2}\partial_s(U_n^2 \boldsymbol{\tau})], \quad (2.2)$$

where the added mass is given by $m_a = \rho\pi W^2/4$. This expression involves the normal and tangential components of the relative velocity $\mathbf{U}_r = U_\tau \boldsymbol{\tau} + U_n \mathbf{n} = \dot{\mathbf{r}} - \mathbf{U}$. In the case of an inextensible beam, this force becomes purely normal and its expression may be simplified in

$$\mathbf{q}_{\text{am}} = -m_a[\ddot{\mathbf{r}} \cdot \mathbf{n} - 2\dot{\theta}U_\tau + \kappa(U_\tau^2 - \frac{1}{2}U_n^2)]\mathbf{n}, \quad (2.3)$$

as explained in appendix A. This reactive model has been extensively used in the literature for the linear stability analysis of straight beams in axial flow [27,28,49]. Indeed, as emphasized in [44,50], it is the potential component of the flow that is driving the instability. However, when studying the large-amplitude post-critical oscillations, an additional resistive contribution \mathbf{q}_d associated with flow separation in the plane of the cross sections has proved necessary to avoid unrealistically large flapping amplitude [44]. Besides, in our case, the beam is statically deflected by the effect of the cross-flow before it starts fluttering. The reactive term \mathbf{q}_{am} vanishes on a straight and motionless beam, so the resistive contribution \mathbf{q}_d is essential to bend the beam into a configuration prone to flutter. The semi-empirical formulation of [51] is unambiguously used in

the literature as a flapping amplitude-limiting term in flutter studies such as [43–45] or [46], as well as the driving force in the static reconfiguration studies of [4,6]. It reads

$$\mathbf{q}_d = -\frac{1}{2}\rho C_D W |U_n| U_n \mathbf{n}, \quad (2.4)$$

where C_D is a drag coefficient that depends on the geometry of the cross section and that is typically of order $O(1)$. For instance, we classically have $C_D = 1$ for a circular cross section, and $C_D = 1.8$ for a flat plate with rectangular cross section.

Combining (2.3) and (2.4) in the right-hand side of equation (2.1) yields the governing equation

$$m\ddot{\mathbf{r}} = [T + \frac{1}{2}EI\kappa^2]' \boldsymbol{\tau} + [\kappa T - EI\kappa''] \mathbf{n} + \mathbf{q}_{am} + \mathbf{q}_d. \quad (2.5)$$

After projection on the tangential and normal directions and elimination of the unknown tension T , we finally obtain a single integro-differential equation on the kinematic variables $\kappa, \theta, \mathbf{r}$:

$$\begin{aligned} (m + m_a)\ddot{\mathbf{r}} \cdot \mathbf{n} - m\kappa \int_L^s \ddot{\mathbf{r}} \cdot \boldsymbol{\tau} ds + EI \left[\kappa'' + \frac{1}{2}\kappa^3 \right] \\ + m_a \left[\kappa \left(U_\tau^2 - \frac{1}{2}U_n^2 \right) - 2\dot{\theta}U_\tau \right] + \frac{1}{2}\rho C_D W |U_n| U_n = 0. \end{aligned} \quad (2.6)$$

Following de Langre *et al.* [28] and Païdoussis [49], we non-dimensionalize all the variables using the length of the structure L and the scale of the natural period of the structure in small-amplitude oscillations in the fluid $T_s = L^2\sqrt{(m + m_a)}/EI$. We finally obtain, in non-dimensional form,

$$\ddot{\mathbf{r}} \cdot \mathbf{n} - (1 - \beta)\kappa \int_1^s \ddot{\mathbf{r}} \cdot \boldsymbol{\tau} ds + \kappa'' + \frac{1}{2}\kappa^3 + \beta \left[\kappa \left(U_\tau^2 - \frac{1}{2}U_n^2 \right) - 2\dot{\theta}U_\tau \right] + \beta\lambda |U_n| U_n = 0, \quad (2.7)$$

with the inextensibility condition $\mathbf{r}' = \boldsymbol{\tau}$, the boundary conditions $\mathbf{r} = 0, \theta = 0$ at the clamped edge $s = 0$ and $\kappa = \kappa' = 0$ at the free tip $s = 1$. The non-dimensional relative velocity is given by $U_\tau \boldsymbol{\tau} + U_n \mathbf{n} = \dot{\mathbf{r}} - u/\sqrt{\beta} \mathbf{e}_x$. This system is ruled by three non-dimensional parameters that are

$$\beta = \frac{m_a}{m_a + m}, \quad u = UL\sqrt{\frac{m_a}{EI}} \quad \text{and} \quad \lambda = \frac{\rho C_D WL}{2m_a} = \left(\frac{2}{\pi} C_D \right) \frac{L}{W}. \quad (2.8)$$

The mass ratio β represents the amount of fluid inertia within the total inertia of the system. It takes values between 0 and 1. For instance, $\beta \rightarrow 0$ for a very dense structure, $\beta = 0.5$ for a neutrally buoyant cylinder with circular cross section and $\beta \rightarrow 1$ for very thin plates ($D \ll W$). The reduced velocity u compares the relative magnitude of the fluid inertial (or reactive) load with the internal elasticity forces. Both are classically used in studies about the flutter of slender beams in axial flow, as in [49] or [28], while the third parameter $\lambda = O(L/W)$ is mostly a slenderness parameter specific to the geometry of the structure. It can also be seen as the ratio of the resistive drag to the reactive force. Because our model is only valid for elongated structures, we are restricted to $\lambda \gg 1$.

As already mentioned, the flutter instability results from the competition between the destabilizing effect of the reactive force and the stabilizing effect of the rigidity of the structure. The reduced velocity u is therefore the natural parameter that governs this phenomenon. On the other hand, the static reconfiguration of the beam is primarily due to the resistive drag overcoming the bending stiffness of the structure. The classical non-dimensional parameter that compares these two forces is the Cauchy number C_Y [52–54]. In the case of a slender structure bending in transverse flow, we define the Cauchy number following [4] as $C_Y = \rho C_D WL^3 U^2 / 2EI$. These two non-dimensional parameters are redundant as they both provide scaling of the flow velocity with respect to the structural stiffness. They are related via the slenderness parameter by $C_Y = \lambda u^2$. However, the Cauchy number is more relevant to describe reconfiguration, while the reduced velocity is more relevant to discuss features of the flutter instability.

3. Stability of the static reconfiguration

To discuss the joint effect of flutter and reconfiguration, we first need to identify the domain in which flutter may happen, and that in which the structure will reconfigure without flapping. To do so, let us first look for the stationary equilibrium solutions of the governing equation (2.7). Removing all unsteady terms in equation (2.7) yields the static equation

$$\kappa'' + \frac{1}{2}\kappa^3 + \frac{C_Y}{\lambda} \left(\sin^2 \theta - \frac{1}{2} \cos^2 \theta \right) \kappa - C_Y \cos^2 \theta = 0, \quad (3.1)$$

with boundary conditions $\theta = 0$ at $s = 0$ and $\kappa = \kappa' = 0$ at $s = 1$. This equation is independent of the mass ratio β , and depends exclusively on the Cauchy number C_Y and the slenderness parameter λ . In the limit of infinite slenderness $\lambda \rightarrow +\infty$, we recover the model in [4,6] based on the equilibrium between the elastic forces and the resistive drag to describe static reconfiguration. The numerical results in [55] have proved that the static contribution of the reactive force $O(C_Y/\lambda)$ is negligible as soon as the slenderness $\lambda \gtrsim 10$ so that the results of [4,6] remain valid for slender structures, regardless of their actual aspect ratio. However, by analogy with beams in axial flow, we expect the static shape solution of equation (3.1) to become unstable to some flutter instability as the flow velocity exceeds some threshold and the structure aligns with the flow.

To determine the stability threshold, we make use of Lyapunov's indirect method as advocated in [56] and applied in [57] regarding the stability of cantilever fluid-conveying pipes with an inclined terminal nozzle. Namely, for each value of the parameters, we perform a global linear stability analysis of the dynamic governing equation (2.7) with the corresponding boundary conditions, about the stationary equilibrium solution of equation (3.1) for that particular set of parameters. Thus, we expand the instantaneous position vector and angle θ as

$$\mathbf{r}(s, t) = \mathbf{r}_0(s) + \xi(s, t) \boldsymbol{\tau}_0(s) + \eta(s, t) \mathbf{n}_0(s) \quad \text{and} \quad \theta(s, t) = \theta_0(s) + \delta\theta(s, t), \quad (3.2)$$

where the subscript '0' refers to quantities related to the stationary solution, and ξ , η and $\delta\theta$ are small-amplitude time-dependent perturbations of the same order. At the linear order, the tangential and normal vectors read

$$\boldsymbol{\tau}(s, t) = \boldsymbol{\tau}_0(s) + \delta\theta(s, t) \mathbf{n}_0(s) \quad \text{and} \quad \mathbf{n}(s, t) = \mathbf{n}_0(s) - \delta\theta(s, t) \boldsymbol{\tau}_0(s). \quad (3.3)$$

Linearization of the inextensibility condition $\mathbf{r}' = \boldsymbol{\tau}$ provides two relations between the small variables

$$\xi' - \kappa_0 \eta = 0 \quad \text{and} \quad \delta\theta = \eta' + \kappa_0 \xi. \quad (3.4)$$

Making use of the boundary condition $\xi = 0$ at $s = 0$, we may rewrite the tangential perturbation as

$$\xi = \int_0^s \kappa_0 \eta \, ds. \quad (3.5)$$

Finally, injecting the expansion (3.2) in equation (2.7) and making use of (3.3)–(3.5), we obtain the governing equation for the small-amplitude normal perturbation

$$\begin{aligned} \ddot{\eta} - (1 - \beta) \kappa_0 \int_1^s ds \int_0^s \kappa_0 \ddot{\eta} \, ds + 2u\sqrt{\beta} \left[S_0 \dot{\eta}' + \left(\frac{1}{2} \kappa_0 + \lambda \right) C_0 \dot{\eta} \right] \\ + \left(\left[u^2 \left(S_0^2 - \frac{1}{2} C_0^2 \right) + \frac{5}{2} \kappa_0^2 \right] \eta' \right)' + \eta^{(4)} + \left[\frac{3}{2} (\kappa_0^2)'' + \kappa_0^4 \right] \eta \\ + 2\lambda u^2 C_0 \left[S_0 \eta' + \frac{1}{2} C_0 \kappa_0 \eta \right] = 0, \end{aligned} \quad (3.6)$$

where the notations $C_0 = \cos \theta_0$ and $S_0 = \sin \theta_0$ have been used for brevity, and with the boundary conditions $\eta = \eta' = 0$ at $s = 0$ and $\eta'' = \eta''' = 0$ at $s = 1$. This equation is consistent with previous

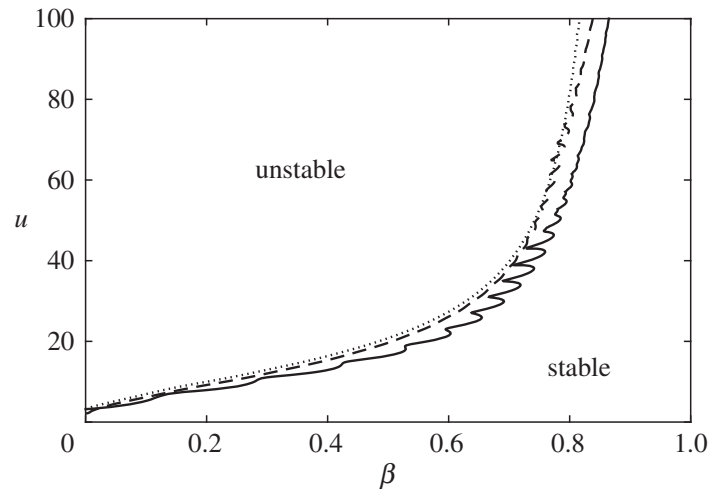


Figure 2. Critical velocity u_c as a function of the mass ratio β , for $\lambda = 10$ (solid line), $\lambda = 10^2$ (dashed line) and $\lambda = 10^3$ (dotted line).

work on slender beams in axial flow. Indeed, for $\theta_0(s) = \pi/2$ and $\kappa_0(s) = 0$ (structure parallel to the flow in the static equilibrium configuration), equation (3.6) reduces to

$$\ddot{\eta} + 2u\sqrt{\beta}\dot{\eta}' + u^2\eta'' + \eta^{(4)} = 0, \quad (3.7)$$

which is the classical small-amplitude flutter equation for an undamped beam in axial flow with no friction or gravity that is used, for instance, in [27,49] or [25].

Following [28], we then assume a perturbation of the form $\eta(s, t) = \phi(s)e^{i\omega t}$ so that equation (3.6) turns into the quadratic eigenvalue problem

$$\begin{aligned} & -\omega^2 \left[\phi - (1 - \beta)\kappa_0 \int_1^s ds \int_0^s \kappa_0 \phi ds \right] + 2iu\sqrt{\beta}\omega \left[S_0\phi' + \left(\frac{1}{2}\kappa_0 + \lambda \right) C_0\phi \right] \\ & + \phi^{(4)} + \left(\left[u^2(S_0^2 - \frac{1}{2}C_0^2) + \frac{5}{2}\kappa_0^2 \right] \phi' \right)' + 2\lambda u^2 C_0 S_0 \phi' + \left[\frac{3}{2}(\kappa_0^2)'' + \kappa_0^4 + \lambda u^2 C_0^2 \kappa_0 \right] \phi = 0, \end{aligned} \quad (3.8)$$

with the boundary conditions $\phi = \phi' = 0$ at $s = 0$ and $\phi'' = \phi''' = 0$ at $s = 1$.

To solve this numerically, the beam is discretized using $N = 100$ Gauss–Lobatto points $s_k = \frac{1}{2}(1 - \cos((k-1)/(N-1)\pi))$, and the derivatives and integrals are computed, respectively, by Chebyshev collocation and using the Clenshaw–Curtis quadrature formulae. For a given slenderness λ and mass ratio β , we first compute the static solution of equation (3.1) iteratively by increasing the Cauchy number from the upright case $C_Y = 0$. After each increment, we solve equation (3.1) with a pseudo-Newton solver (method of Broyden [58]) using the solution at the previous step as an initial guess. Then, for each value of C_Y (equivalently of u), we compute the eigenmodes $\phi(s)$ and eigenfrequencies ω by solving equation (3.8) with the Matlab function `quadeig` [59]. To check convergence of the results with respect to the mesh, computations with twice the number of points $N = 200$ were conducted and led to no significant modification of the results. For instance, the static angle at the tip of the structure $\theta_0(s = 1)$ (solution of equation (3.1)) varied by less than 10^{-10} for any Cauchy number C_Y between 10^{-1} and 10^5 and for the three values of λ considered (10, 10^2 or 10^3).

The stability thresholds are shown in figure 2 in the $\beta - u$ plane for different values of the slenderness λ . Similar to the axial case, the critical velocity increases with the mass ratio, hence making the structure heavier or the fluid lighter has a destabilizing effect. For instance, a given structure is much more likely to flap in air than in water, and neutrally buoyant structures are always stable if they are close to flat ($\beta \rightarrow 1$), while they lose stability between around $u \sim 16$ and 21 if they have a circular cross section ($\beta = 0.5$). For a given mass ratio, the critical velocity depends very little on the slenderness. Therefore, it is indeed the relative magnitude of the

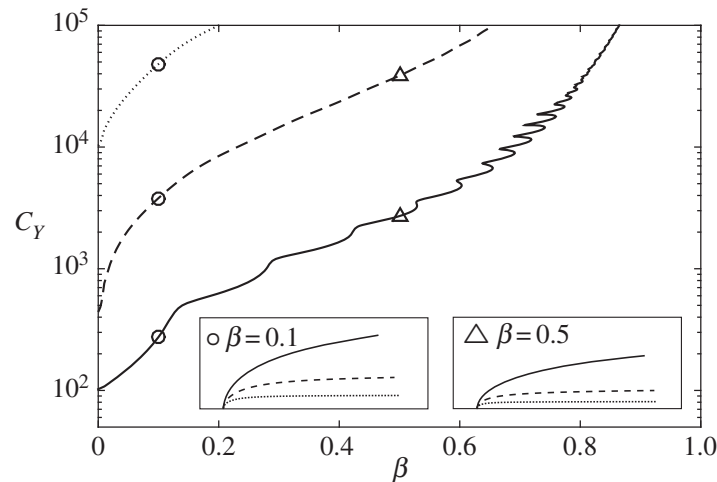


Figure 3. Critical Cauchy number $C_{Y,c}$ as a function of the mass ratio β and static equilibrium shape at the stability threshold for two specific values of the mass ratio, for $\lambda = 10$ (solid line), $\lambda = 10^2$ (dashed line) and $\lambda = 10^3$ (dotted line).

reactive fluid force and the structural stiffness that determines the onset of flutter regardless of the magnitude of the resistive drag.

On the other hand, the same stability thresholds redrawn in terms of the Cauchy number in figure 3 are obviously shifted with respect to one another as $C_Y \propto \lambda$ for a given u . Consequently, the static equilibrium shapes at the critical velocity (also shown on figure 3) are more and more deflected as slenderness is increased. Thus, we may deduce that the critical velocity does not depend on the pre-existing curvature distribution in the static equilibrium shape. More importantly, we may conclude that elongation stabilizes reconfiguration. Indeed, the more slender a structure is, the larger its critical Cauchy number $C_{Y,c}$, and so the more it may reconfigure statically before it loses stability and starts fluttering. Note finally that the critical Cauchy number is always much larger than 1. Consequently, flutter may only occur on highly reconfigured structures.

Note that, even for the most deflected cases (corresponding to $\lambda \rightarrow +\infty$) that are almost parallel to the flow, the critical velocity does not converge to that of slender beams in axial flow. This point is discussed in appendix B.

4. Post-critical kinematics

When the stability threshold is exceeded, the static solution of equation (3.1) cannot physically exist anymore. The static reconfiguration models are not valid in the unstable domain and we ought to account for the self-triggered dynamics to properly assess the drag. In this section, we start by analysing the kinematics that takes place in the post-critical regime in order to discuss its consequences in terms of drag in §5.

Hence, we now solve the full time-dependent nonlinear equation (2.7) using a time-stepping method. The time derivatives are computed using implicit second-order accurate finite differences. The time step is tuned for each case using the period T_{lin} and growth rate σ_{lin} of the most unstable eigenmode found in the linear stability analysis. It is chosen so that 100 iterations are performed over T_{lin} or $1/\sigma_{\text{lin}}$, whichever is the shortest. At $t = 0$, we combine a small contribution of the most unstable eigenmode with the static solution to initialize the system. Then, at each time step, the boundary value problem is solved with the pseudo-Newton solver used in the static case [58]. Computations are carried on a horizon such that $120 T_{\text{lin}}$ has passed, and the amplitude of the most unstable eigenmode would have had time to grow by a factor of 10^{10} in the linear framework, whichever lasts the longest.

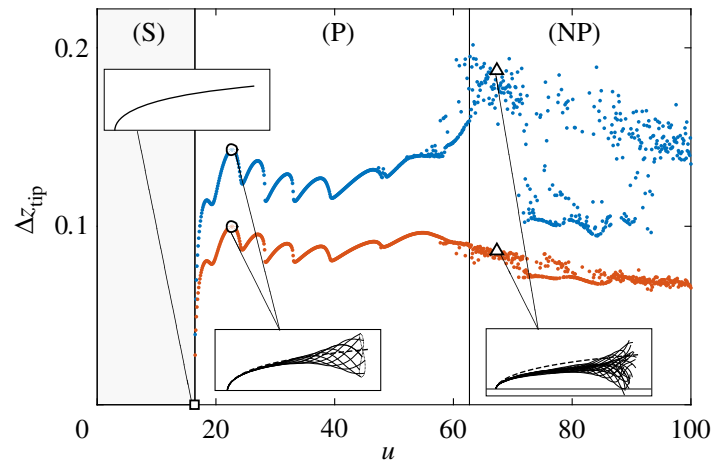


Figure 4. Vertical amplitude of flapping at the tip (blue) and standard deviation (orange) versus the reduced velocity u , for $\beta = 0.5$, $\lambda = 10$. Examples of deformation modes are shown in the thumbnails for $u = 16.4$ (square, static regime (S)), $u = 22.7$ (circle, periodic regime (P)) and $u = 67.3$ (triangle, non-periodic regime (NP)). Static equilibrium shape superimposed (dashed lines).

(a) Kinematic regimes

For the sake of clarity, let us first focus on the reference case of a neutrally buoyant circular cylinder ($\beta = 0.5$) with moderately large aspect ratio ($\lambda = 10$), before discussing the influence of varying slenderness or mass ratio in §4b. We analyse both the average and the extreme features of the dynamics, respectively, through the standard deviation and the amplitude (defined as half of the peak-to-peak amplitude measured over the simulation horizon) of the tip vertical displacement on figure 4. As is classical in flag flutter studies, three distinct regimes are identified depending on the value of u [20,21,60,61]. Each regime is illustrated in figure 4 for particular values of u in the thumbnails. Below the critical velocity $u_c = 16.5$, the structure is statically stable, so the amplitude of flapping is null. Right above the stability threshold, periodic flapping takes place. The amplitude and standard deviation both sharply increase from zero, then decrease very slowly for increasing u . The bumpy shape of these curves is most probably associated with flapping mode switches [21,61]. The amplitude is continuous at the onset of the flutter, thus indicating that the instability is supercritical. Periodic flapping is observed until $u \sim 62.7$. Above that threshold, no limit cycle can be identified in most cases and the motion is generally either quasi-periodic or chaotic. In this non-periodic regime, the standard deviation of the tip displacement remains rather continuous and of the same order of magnitude as in the periodic regime. On the other hand, the amplitude of flapping measured over the simulation horizon is rather erratic, due to the random nature of the dynamics. Overall, our results indicate that the amplitude jumps from being of the order of 0.12 to approximately 0.2. In fact, if the loss of periodicity preserves the flapping amplitude on average, it is also associated with the random occurrence of isolated, short, extreme events characterized by violent accelerations. These so-called ‘snapping events’ have also been reported in the axial configuration [20,60] and are known to be responsible for drag peaks probably at the origin of the tearing of flags [36]. Note that, owing to the random occurrence of these peaks, their magnitude may actually depend on the horizon of the simulation. Longer simulations would allow more of the most extreme events to occur and would consequently lead most probably to a larger, and smoother, amplitude. The precise features of the non-periodic dynamics such as its frequency spectrum or the probability distribution of the magnitude of the snapping events are, however, outside the scope of this article. Note also that regular flapping is still observed for some values of reduced velocity between $u \sim 72$ and $u \sim 93$, corresponding to the lower flapping amplitudes in figure 4. These occurrences are disseminated among irregular flapping cases without a clear separation, so the boundary of the periodic regime

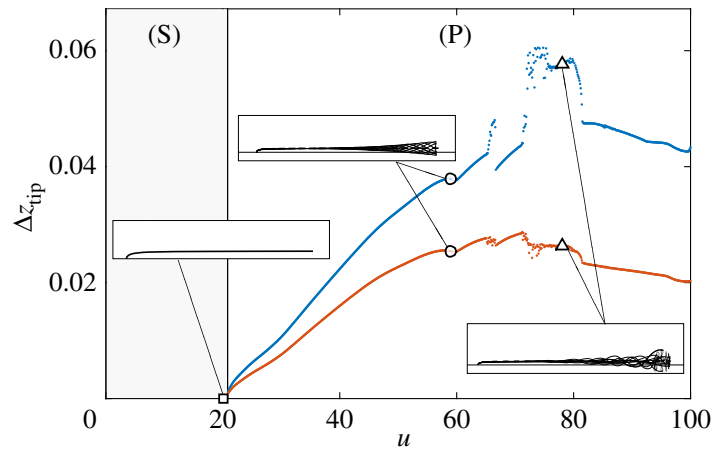


Figure 5. Vertical amplitude of flapping at the tip (blue) and standard deviation (orange) versus the reduced velocity u , for $\beta = 0.5$, $\lambda = 10^3$. Examples of deformation modes are shown in the thumbnails for $u = 20.0$ (square, static regime (S)), $u = 59.0$ (circle, periodic regime (P)) and $u = 78.0$ (triangle, periodic regime also). Static equilibrium shape superimposed (dashed lines).

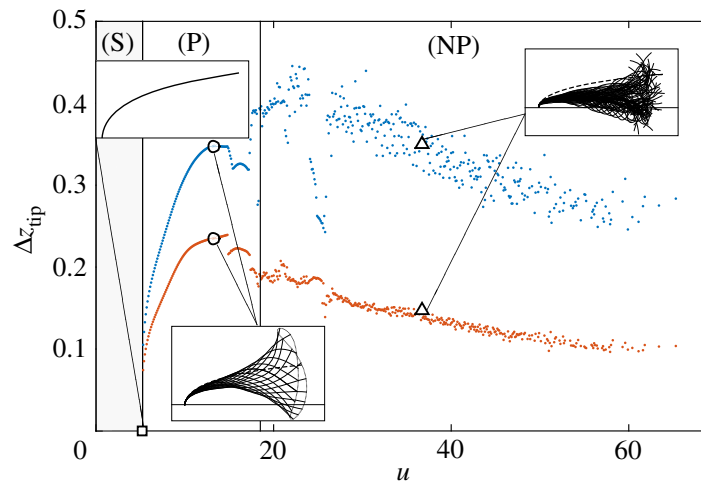


Figure 6. Vertical amplitude of flapping at the tip (blue) and standard deviation (orange) versus the reduced velocity u , for $\beta = 0.1$, $\lambda = 10$. Examples of deformation modes are shown in the thumbnails for $u = 5.2$ (square, static regime (S)), $u = 13.2$ (circle, periodic regime (P)) and $u = 36.7$ (triangle, non-periodic regime (NP)). Static equilibrium shape superimposed (dashed lines).

drawn on figure 4 is actually more of a threshold above which non-periodic motion is observed, but not exclusively.

(b) Influence of the slenderness and mass ratio

The kinematic regimes described above are affected if the slenderness or mass ratio is varied.

For instance, the same data as in figure 4 are displayed in figure 5 for a structure 100 times more elongated $\lambda = 10^3$. First, the order of magnitude of the non-dimensional amplitude of flapping is drastically decreased. Actually, it even seems that $\lambda \Delta z_{\text{tip}} = O(1)$ so that the dimensional amplitude of flapping would scale with the width of the structure, independently of its length. Similarly to the previous case, limit-cycle flapping takes place above the critical velocity $u_c = 20.8$. But, contrary to the previous case, the motion remains periodic for the whole range of reduced velocities tested. As u is increased, period multiplications and divisions successively take place, leading to more complex flapping dynamics illustrated in the thumbnail for $u = 78.0$ in figure 5. The trajectory of the tip makes several loops within a single period of the system while it simply

follows an eight-shaped trajectory in the simpler case $u = 59.0$. These flapping modes are elaborate but remain nonetheless regular and no snapping event is observed. Slenderness thus has a stabilizing effect on the nonlinear dynamics as it saturates the flapping amplitude and prevents irregular motion from taking place at large flow velocities.

The mass ratio also has an influence on the post-critical dynamics. We show in figure 6 the case of a flat plate with smaller mass ratio $\beta = 0.1$, and moderate slenderness similar to the first situation $\lambda = 10$. Similar to the reference case, periodic flapping is triggered right above the critical velocity $u_c = 5.24$ until periodicity is lost above some other threshold $u \sim 18.5$. The amplitude of flapping is, however, larger and the domain of regular flapping is reduced. Thus, reducing the mass ratio has a destabilizing effect on the nonlinear dynamics, as it enhances the flapping amplitude and favours the early transition towards irregular motion.

5. Drag reduction in the post-critical regime

The very occurrence of flutter, be it periodic or not, is known to be responsible for a significant additional drag force. Besides, its magnitude is strongly related not only to the amplitude of the flapping motion but also to its regularity as the violent accelerations associated with snapping events are responsible for enhanced drag peaks [36]. We thus expect the drag reduction abilities of the three structures introduced in §4 to be at least mitigated above the stability threshold. In this section, we discuss the modulation of drag due to flexibility for the same three structures, based on the computational results of the previous section, and in the light of the observations regarding the post-critical kinematics.

To quantify drag reduction by reconfiguration, the reconfiguration number is defined in [4] as the ratio of the drag force on the deflected structure to that on the similar but upright beam $\mathcal{R} = F/F_{\text{rigid}}$. The total drag force F is equal to the internal shear force at the base $Q(s=0) = -EI\kappa'(s=0)$, while the rigid drag is the integral of the resistive drag on the vertical structure of length L , $F_{\text{rigid}} = 1/2\rho C_D WLU^2$, so that the reconfiguration number reads in terms of the non-dimensional quantities $\mathcal{R} = -\kappa'(s=0)/C_Y$. When $\mathcal{R} < 1$, flexibility is responsible for lowering the drag, while it enhances it when $\mathcal{R} > 1$. Because the drag force F on the deflected structure is time dependent when flutter occurs, we will focus in the following on the time-averaged and maximum values of \mathcal{R} . The variations in the maximum and average reconfiguration numbers are related, respectively, to those of the amplitude and standard deviation of flapping.

First, figure 7 displays the variations of these two quantities with the Cauchy number C_Y in the reference case ($\beta = 0.5$, $\lambda = 10$), along with the corresponding static reconfiguration curve. The maximum and average reconfiguration numbers diverge from the static curve at the critical Cauchy number $C_{Y,c} = \lambda u_c^2 = 2.71 \times 10^3$, because of the triggering of flutter. Further increasing C_Y , the average reconfiguration number remains always larger than the static one. The self-induced dynamics is therefore responsible for an additional drag that significantly contributes to the total drag on average. However, the average reconfiguration number is decreasing with increasing C_Y so that a larger flexibility is still associated with an enhanced drag reduction above the stability threshold, on average. This trend carries on in the non-periodic as well as in the periodic regime. On the other hand, similarly to the flapping amplitude, the maximum drag sharply increases when periodicity is lost due to the occurrence of snapping events, as will be discussed in further detail later in the low mass ratio case. But, most importantly, the maximum reconfiguration number remains inferior to 1 for all values of C_Y . Therefore, no matter how large the flow velocity, the drag force remains at all times inferior to what it would be if the structure were rigid and standing upright. In other words, the additional drag due to flapping is not large enough in this case so as to completely offset the drag reduction due to reconfiguration.

This conclusion holds also for more stable structures, such as the more slender structure ($\beta = 0.5$, $\lambda = 10^3$) in §4b. In fact, we have shown in §4b that the amplitude of regular flapping is reduced compared with the reference case, so that the associated flutter-induced drag contribution is smaller. Besides, the results of §3 indicate that the instability is restricted to more deflected structures (the critical Cauchy number $C_{Y,c} = 4.33 \times 10^5$ is higher), associated

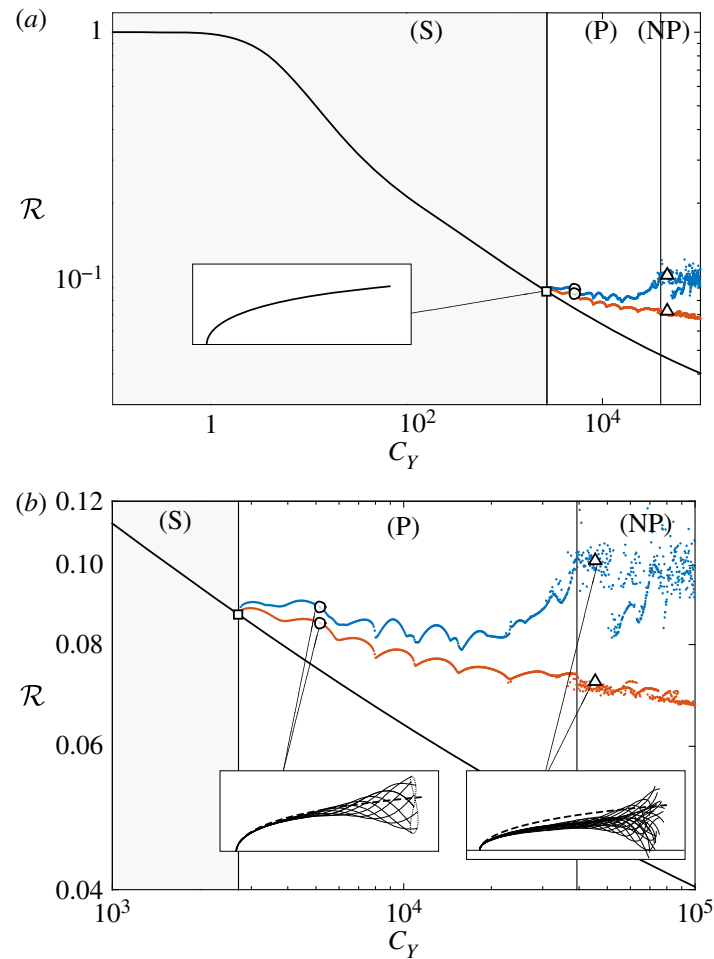


Figure 7. Reconfiguration number \mathcal{R} versus the Cauchy number C_Y , time average (orange) and maximum (blue), for $\beta = 0.5$, $\lambda = 10$. Static reconfiguration number (black). The same examples of deformation modes as in figure 4 are shown in the thumbnails, corresponding, respectively, to $C_Y = 2.69 \times 10^3$ (square, static regime (S)), $C_Y = 5.15 \times 10^3$ (circle, periodic regime (P)) and $C_Y = 4.53 \times 10^4$ (triangle, non-periodic regime (NP)). Static equilibrium shape superimposed (dashed line). (b) Simply a zoom of the lower right corner of (a).

with larger static drag. Consequently, the relative contribution of flutter-induced drag to the total drag is now almost negligible, and the reconfiguration numbers displayed in figure 8 are almost superimposed on the static curve.

The situation of a less stable structure such as the low mass ratio plate ($\beta = 0.1$, $\lambda = 10$) of §4b is actually more intricate. As for the two previous cases, the average \mathcal{R} displayed in figure 9 keeps decreasing slowly (or remains almost constant) above the stability threshold, regardless of the regularity of the flapping motion. Thus, a larger flexibility is still responsible for an alleviation (or at least no enhancement) of the drag on average even when flutter is triggered at an early stage of reconfiguration, when the amplitude of flapping is large, and in spite of the early loss of periodicity. On the other hand, the sharp increase in the flapping amplitude in the non-periodic regime may induce large enough flutter-induced drag forces so as to increase the total drag in excess of its static value. The maximum reconfiguration number increases above 1 in these cases, as, for instance, in the case $C_Y = 1.35 \times 10^4$ in figure 9. The variations of \mathcal{R} through time for this case in figure 10 confirm that this peak of drag is related to a very brief, rare, snapping event. If the peak value of the drag during one of those snapping events exceeds the largest load, the structure may endure; flexibility may in this particular case and at this particular moment be responsible for structural failure. Nonetheless, the rareness and brevity of these events make their contribution negligible on average, and flexibility remains responsible for a large overall reduction in drag, at almost any moment, in spite of flapping.

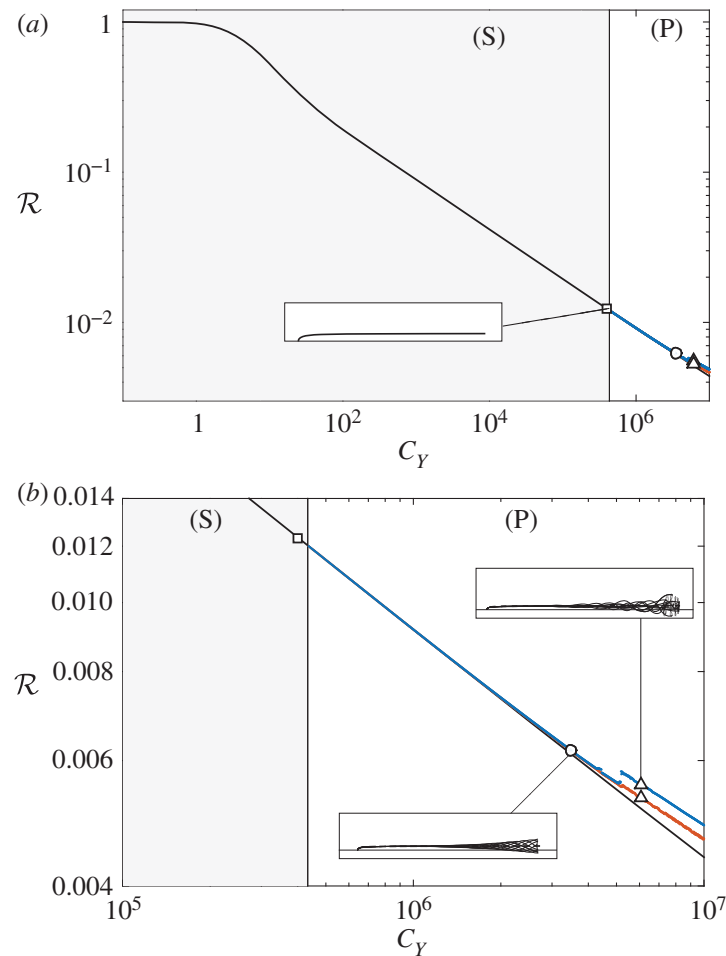


Figure 8. Reconfiguration number \mathcal{R} versus the Cauchy number C_Y , time average (orange) and maximum (blue), for $\beta = 0.5$, $\lambda = 10^3$. Static reconfiguration number (black). The same examples of deformation modes as in figure 5 are shown in the thumbnails, corresponding, respectively, to $C_Y = 4.00 \times 10^5$ (square, static regime (S)), $C_Y = 3.48 \times 10^6$ (circle, periodic regime (P)) and $C_Y = 6.08 \times 10^6$ (triangle, periodic regime also). Static equilibrium shape superimposed (dashed line). (b) Simply a zoom of the lower right corner of (a).

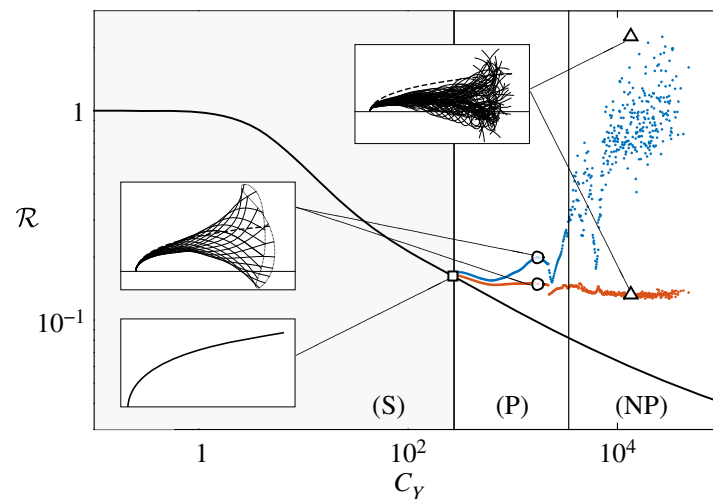


Figure 9. Reconfiguration number \mathcal{R} versus the Cauchy number C_Y , time average (orange) and maximum (blue), for $\beta = 0.1$, $\lambda = 10$. Static reconfiguration number (black). The same examples of deformation modes as in figure 6 are shown in the thumbnails, corresponding, respectively, to $C_Y = 2.70 \times 10^2$ (square, static regime (S)), $C_Y = 1.74 \times 10^3$ (circle, periodic regime (P)) and $C_Y = 1.35 \times 10^4$ (triangle, non-periodic regime (NP)). Static equilibrium shape superimposed (dashed line).

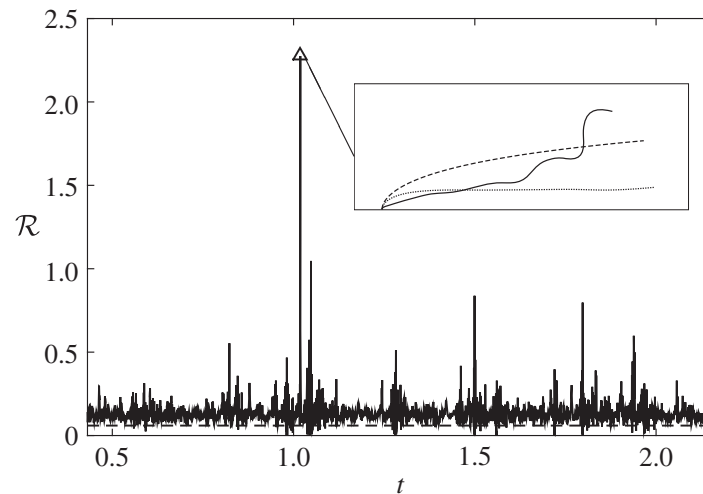


Figure 10. Time series of the reconfiguration number in the non-periodic regime of case $\beta = 0.1$, $\lambda = 10$, $C_Y = 1.35 \times 10^4$ (equivalently $u = 36.7$) corresponding to the thumbnail shown in figures 6 and 9. Level of the static reconfiguration number drawn for comparison (dashed line). The time interval displayed corresponds to the whole simulation, apart from the transient regime. Largest snapping event at $t_{\text{snap}} = 1.019$ (triangle). The shape of the structure at t_{snap} is shown in the thumbnail (solid line), along with the static shape (dashed line) and the average shape (dotted line).

6. Discussion

In this study, we have addressed the question of how flexibility may affect the drag of structures exposed to transverse flows, when the competing influences of reconfiguration and flutter are simultaneously considered. First, we performed a linear stability analysis to determine the domain in which dynamics comes into play. Then we performed nonlinear simulations in the time domain to analyse how the occurrence of dynamics alters the total drag force in the post-critical domain.

We may finally draw the following conclusions. First, it appears that, in spite of an additional flutter-induced drag contribution, the total drag of flexible structures is still reduced overall in comparison with rigid structures. Flutter may only occur when the structure reaches an advanced level of reconfiguration, so that the drag associated with the flapping motion is never large enough to fully offset the already significant reduction due to bending. Thus, flutter does not prevent drag reduction by reconfiguration.

However, the triggering of dynamics does lower the extent to which the drag of flexible structures is reduced, depending on the slenderness λ and mass ratio β of the structure. Increasing either of these parameters has a threefold stabilizing effect that tends to abate the flutter-induced contribution to drag. Firstly, both parameters are positively correlated with the stability threshold in terms of the Cauchy number $C_{Y,c}$, so the level of reconfiguration reachable before losing stability is enhanced when any of the two parameters is increased. Secondly, the amplitude of flapping is negatively correlated with β and λ , and so is the magnitude of the additional drag force. Thirdly, both parameters have a regularizing effect on the post-critical dynamics in the sense that the larger β and λ are, the larger the flow velocity may get before periodicity of the dynamics is lost. This last point is particularly important because, when flapping is irregular, very large inertial forces may transiently raise the total drag in excess of the rigid value during short snapping events. In that case, flexibility may possibly be the cause of structural damage if the failure threshold is reached. But this situation may only happen for heavy structures with moderate slenderness, and only during rare and very brief occurrences. The order of magnitude of the drag remains otherwise comparable to its mean value, which is much reduced compared with the rigid case in any situation. Therefore, we may finally conclude that the ability of flexible structures to alleviate drag by reconfiguration, albeit lessened by the flapping motion, generally prevails nonetheless in spite of flutter.

Data accessibility. This work has no additional data.

Authors' contributions. T.L., N.P. and E.d.L. conceived the project. T.L. performed the computations. All the authors contributed to the paper.

Competing interests. We declare we have no competing interests.

Funding. The authors acknowledge financial support from the DGA/DSTL grant no. 2014.60.0005.

Appendix A. Simplification of the reactive force

In the particular case of an inextensible structure, the reactive force (2.2) is purely normal and may be simplified in (2.3). Indeed, developing and sorting the terms in equation (2.2) yields

$$\mathbf{q}_{\text{am}} = -m_{\text{a}}[(\dot{U}_{\text{n}} - U'_{\text{n}}U_{\tau} - U_{\text{n}}U'_{\tau} + \frac{1}{2}\kappa U_{\text{n}}^2)\mathbf{n} + (U'_{\text{n}} + \kappa U_{\tau} - \dot{\theta})\boldsymbol{\tau}]. \quad (\text{A } 1)$$

Differentiating the relative velocity equation $U_{\tau}\boldsymbol{\tau} + U_{\text{n}}\mathbf{n} = \dot{\mathbf{r}} - \mathbf{U}$ with respect to s and using the inextensibility condition $\mathbf{r}' = \boldsymbol{\tau}$ provides

$$(U'_{\tau} - \kappa U_{\text{n}})\boldsymbol{\tau} + (U'_{\text{n}} + \kappa U_{\tau})\mathbf{n} = \dot{\mathbf{r}}' = \dot{\mathbf{t}} = \dot{\theta}\mathbf{n}, \quad (\text{A } 2)$$

so that the tangential component of equation (A 1) vanishes and $U'_{\tau} = \kappa U_{\text{n}}$ and $U'_{\text{n}} = \dot{\theta} - \kappa U_{\tau}$. Using these expressions, equation (A 1) further simplifies in

$$\mathbf{q}_{\text{am}} = -m_{\text{a}}[\dot{U}_{\text{n}} - \dot{\theta}U_{\tau} + \kappa(U_{\tau}^2 - \frac{1}{2}U_{\text{n}}^2)]\mathbf{n}. \quad (\text{A } 3)$$

Differentiating the relative velocity with respect to time now provides

$$(\dot{U}_{\tau} - \dot{\theta}U_{\text{n}})\boldsymbol{\tau} + (\dot{U}_{\text{n}} + \dot{\theta}U_{\tau})\mathbf{n} = \ddot{\mathbf{r}}, \quad (\text{A } 4)$$

so that projection on the normal vector gives $\dot{U}_{\text{n}} = \ddot{\mathbf{r}} \cdot \mathbf{n} - \dot{\theta}U_{\tau}$. Making use of that expression in equation (A 3) finally yields equation (2.3).

Appendix B. Comparison with the stability of the axial configuration

For asymptotically large slenderness $\lambda \rightarrow +\infty$, the structure aligns with the flow, and one might expect it to behave similarly to the classical axial configuration. However, figure 11 shows that the critical velocity for large slenderness does not converge to the threshold expected for an elongated beam in axial flow. In fact, even though $\theta_0 \rightarrow \pi/2$ almost everywhere, the product λC_0 remains of order $O(1)$ so that the contribution of the resistive drag remains significant even on the part of the structure that is nearly parallel to the flow. Consequently, in the limit of infinite slenderness,

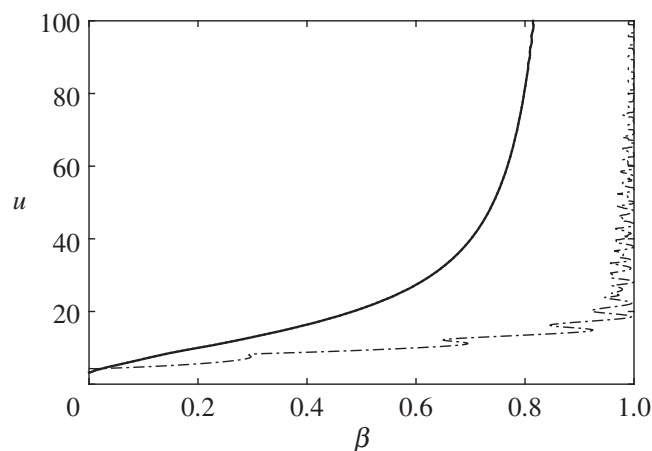


Figure 11. Linear stability thresholds obtained with the full equation (3.6) for $\lambda = 10^3$ (dotted line), with the equation relative to the axial configuration (3.7) (dashed dotted line) and with the asymptotic equation (B 1) for $\lambda = 10^3$ (solid line).

equation (3.6) actually reduces to the classical elongated small-amplitude equation in axial flow equation (3.7), but supplemented by the non-vanishing resistive drag contribution

$$\ddot{\eta} + 2u\sqrt{\beta}\dot{\eta}' + u^2\eta'' + \eta^{(4)} + 2\lambda C_0 \left(u\sqrt{\beta}\dot{\eta} + u^2\eta' \right) = 0. \quad (\text{B } 1)$$

The stability curve found for $\lambda = 10^3$ with this asymptotic equation on figure 11 is indistinguishable from that obtained with the full equation (3.6). Quite understandably, this persistent drag term introduces some additional damping that stabilizes the system compared with the axial configuration, as soon as $\beta \gtrsim 0.024$.

References

1. Vogel S. 1984 Drag and flexibility in sessile organisms. *Am. Zool.* **24**, 37–44. (doi:10.1093/icb/24.1.37)
2. Harder DL, Speck O, Hurd CL, Speck T. 2004 Reconfiguration as a prerequisite for survival in highly unstable flow-dominated habitats. *J. Plant. Growth. Regul.* **23**, 98–107. (doi:10.1007/s00344-004-0043-1)
3. Alben S, Shelley M, Zhang J. 2004 How flexibility induces streamlining in a two-dimensional flow. *Phys. Fluids* **16**, 1694–1713. (doi:10.1063/1.1668671)
4. Gosselin F, de Langre E, Machado-Almeida BA. 2010 Drag reduction of flexible plates by reconfiguration. *J. Fluid Mech.* **650**, 319–341. (doi:10.1017/S0022112009993673)
5. Luhar M, Nepf HM. 2011 Flow-induced reconfiguration of buoyant and flexible aquatic vegetation. *Limnol. Oceanogr.* **56**, 2003–2017. (doi:10.4319/lo.2011.56.6.2003)
6. Leclercq T, de Langre E. 2016 Drag reduction by elastic reconfiguration of non-uniform beams in non-uniform flows. *J. Fluids Struct.* **60**, 114–129. (doi:10.1016/j.jfluidstructs.2015.10.007)
7. Hassani M, Mureithi NW, Gosselin F. 2016 Large coupled bending and torsional deformation of an elastic rod subjected to fluid flow. *J. Fluids Struct.* **62**, 367–383. (doi:10.1016/j.jfluidstructs.2015.12.009)
8. Zhu L, Peskin CS. 2007 Drag of a flexible fiber in a 2D moving viscous fluid. *Comput. Fluids* **36**, 398–406. (doi:10.1016/j.compfluid.2006.02.002)
9. Zhu L. 2008 Scaling laws for drag of a compliant body in an incompressible viscous flow. *J. Fluid Mech.* **607**, 387–400. (doi:10.1017/S0022112008002103)
10. Alvarado J, Comtet J, de Langre E, Hosoi AE. 2017 Nonlinear flow response of soft hair beds. *Nat. Phys.* **13**, 1014–1019. (doi:10.1038/nphys4225)
11. Zhu L. 2007 Viscous flow past a flexible fibre tethered at its centre point: vortex shedding. *J. Fluid Mech.* **587**, 217–234. (doi:10.1017/S002211200700732X)
12. Yang X, Liu M, Peng S. 2014 Smoothed particle hydrodynamics and element bending group modeling of flexible fibers interacting with viscous fluids. *Phys. Rev. E* **90**, 063011. (doi:10.1103/PhysRevE.90.063011)
13. Vogel S. 1989 Drag and reconfiguration of broad leaves in high winds. *J. Exp. Bot.* **40**, 941–948. (doi:10.1093/jxb/40.8.941)
14. Miller LA, Santhanakrishnan A, Jones S, Hamlet C, Mertens K, Zhu L. 2012 Reconfiguration and the reduction of vortex-induced vibrations in broad leaves. *J. Exp. Biol.* **215**, 2716–2727. (doi:10.1242/jeb.064501)
15. Tadriss L, Julio K, Saudreau M, de Langre E. 2015 Leaf flutter by torsional galloping: experiments and model. *J. Fluids Struct.* **56**, 1–10. (doi:10.1016/j.jfluidstructs.2015.04.001)
16. Kim D, Gharib M. 2011 Flexibility effects on vortex formation of translating plates. *J. Fluid Mech.* **677**, 255–271. (doi:10.1017/jfm.2011.82)
17. Kornecki A, Dowell EH, O'Brien J. 1976 On the aeroelastic instability of two-dimensional panels in uniform incompressible flow. *J. Sound. Vib.* **47**, 163–178. (doi:10.1016/0022-460X(76)90715-X)
18. Huang L. 1995 Flutter of cantilevered plates in axial flow. *J. Fluids Struct.* **9**, 127–147. (doi:10.1006/jfls.1995.1007)
19. Watanabe Y, Suzuki S, Sugihara M, Sueoka Y. 2002 An experimental study of paper flutter. *J. Fluids Struct.* **16**, 529–542. (doi:10.1006/jfls.2001.0435)
20. Connell BSH, Yue DKP. 2007 Flapping dynamics of a flag in a uniform stream. *J. Fluid Mech.* **581**, 33–67. (doi:10.1017/S0022112007005307)

21. Michelin S, Llewellyn Smith SG, Glover BJ. 2008 Vortex shedding model of a flapping flag. *J. Fluid Mech.* **617**, 1–10. (doi:10.1017/S0022112008004321)
22. Shelley MJ, Zhang J. 2011 Flapping and bending bodies interacting with fluid flows. *Annu. Rev. Fluid Mech.* **43**, 449–465. (doi:10.1146/annurev-fluid-121108-145456)
23. Datta SK, Gottenberg WG. 1975 Instability of an elastic strip hanging in an airstream. *J. Appl. Mech.* **42**, 195–198. (doi:10.1115/1.3423515)
24. Yadykin Y, Tenetov V, Levin D. 2001 The flow-induced vibration of a flexible strip hanging vertically in a parallel flow. Part 1: temporal aeroelastic instability. *J. Fluids Struct.* **15**, 1167–1185. (doi:10.1006/jfls.2001.0400)
25. Paidoussis MP, Grinevich E, Adamovic D, Semler C. 2002 Linear and nonlinear dynamics of cantilevered cylinders in axial flow. Part 1: physical dynamics. *J. Fluids Struct.* **16**, 691–713. (doi:10.1006/jfls.2002.0447)
26. Semler C, Lopes JL, Augu N, Paidoussis MP. 2002 Linear and nonlinear dynamics of cantilevered cylinders in axial flow. Part 3: nonlinear dynamics. *J. Fluids Struct.* **16**, 739–759. (doi:10.1006/jfls.2002.0445)
27. Lemaitre C, Hémon P, de Langre E. 2005 Instability of a long ribbon hanging in axial air flow. *J. Fluids Struct.* **20**, 913–925. (doi:10.1016/j.jfluidstructs.2005.04.009)
28. de Langre E, Paidoussis MP, Doaré O, Modarres-Sadeghi Y. 2007 Flutter of long flexible cylinders in axial flow. *J. Fluid Mech.* **571**, 371–389. (doi:10.1017/S002211200600317X)
29. Moretti PM. 2003 Tension in fluttering flags. *Int. J. Acoustics Vibration* **8**, 227–230. (doi:10.20855/ijav.2003.8.4148)
30. Fairthorne RA. 1930 Drag of flags. In *Aeronautical Research Committee Reports and Memoranda*, no. 1345, pp. 887–891. London, UK: HM Stationery Office.
31. Hoerner SF. 1965 *Fluid dynamic drag*. Bricktown, NJ: SF Hoerner.
32. Taneda S. 1968 Waving motions of flags. *J. Phys. Soc. Japan* **24**, 392–401. (doi:10.1143/JPSJ.24.392)
33. Carruthers AC, Filippone A. 2005 Aerodynamic drag of streamers and flags. *J. Aircr.* **42**, 976–982. (doi:10.2514/1.9754)
34. Morris-Thomas MT, Steen S. 2009 Experiments on the stability and drag of a flexible sheet under in-plane tension in uniform flow. *J. Fluids Struct.* **25**, 815–830. (doi:10.1016/j.jfluidstructs.2009.02.003)
35. Wilk A, Skuta M. 2009 Laboratory tests of the aerodynamic drag coefficient of the flag as a body with low stiffness. *Task Quarterly* **13**, 5–14.
36. Virost E, Amandolese X, Hémon P. 2013 Fluttering flags: an experimental study of fluid forces. *J. Fluids Struct.* **43**, 385–401. (doi:10.1016/j.jfluidstructs.2013.09.012)
37. Ni Q, Li M, Tang M, Wang Y, Luo Y, Wang L. 2014 In-plane and out-of-plane free vibration and stability of a curved rod in flow. *J. Fluids Struct.* **49**, 667–686. (doi:10.1016/j.jfluidstructs.2014.06.008)
38. Gurugubelli PS, Jaiman RK. 2015 Self-induced flapping dynamics of a flexible inverted foil in a uniform flow. *J. Fluid Mech.* **781**, 657–694. (doi:10.1017/jfm.2015.515)
39. Tang C, Liu N-S, Lu X-Y. 2015 Dynamics of an inverted flexible plate in a uniform flow. *Phys. Fluids* **27**, 073601. (doi:10.1063/1.4923281)
40. Sader JE, Cossé J, Kim D, Fan B, Gharib M. 2016 Large-amplitude flapping of an inverted flag in a uniform steady flow—a vortex-induced vibration. *J. Fluid Mech.* **793**, 524–555. (doi:10.1017/jfm.2016.139)
41. Schouveiler L, Eloy C, Le Gal P. 2005 Flow-induced vibrations of high mass ratio flexible filaments freely hanging in a flow. *Phys. Fluids* **17**, 047104. (doi:10.1063/1.1878292)
42. Audoly B, Pomeau Y. 2010 *Elasticity and geometry: from hair curls to the non-linear response of shells*. Oxford, UK: Oxford University Press.
43. Eloy C, Kofman N, Schouveiler L. 2012 The origin of hysteresis in the flag instability. *J. Fluid Mech.* **691**, 583–593. (doi:10.1017/jfm.2011.494)
44. Singh K, Michelin S, de Langre E. 2012 Energy harvesting from axial fluid-elastic instabilities of a cylinder. *J. Fluids Struct.* **30**, 159–172. (doi:10.1016/j.jfluidstructs.2012.01.008)
45. Singh K, Michelin S, de Langre E. 2012 The effect of non-uniform damping on flutter in axial flow and energy-harvesting strategies. *Proc. R. Soc. A* **468**, 3620–3635. (doi:10.1098/rspa.2012.0145)
46. Michelin S, Doaré O. 2013 Energy harvesting efficiency of piezoelectric flags in axial flows. *J. Fluid Mech.* **714**, 489–504. (doi:10.1017/jfm.2012.494)

47. Lighthill MJ. 1971 Large-amplitude elongated-body theory of fish locomotion. *Proc. R. Soc. Lond. B* **179**, 125–138. (doi:10.1098/rspb.1971.0085)
48. Candelier F, Boyer F, Leroyer A. 2011 Three-dimensional extension of Lighthill's large-amplitude elongated-body theory of fish locomotion. *J. Fluid Mech.* **674**, 196–226. (doi:10.1017/S002211201000649X)
49. Païdoussis MP. 1998 *Fluid-structure interactions: slender structures and axial flow*, vol. 2. London, UK: Academic Press.
50. Eloy C, Souilliez C, Schouveiler L. 2007 Flutter of a rectangular plate. *J. Fluids. Struct.* **23**, 904–919. (doi:10.1016/j.jfluidstructs.2007.02.002)
51. Taylor GI. 1952 Analysis of the swimming of long and narrow animals. *Proc. R. Soc. Lond. A* **214**, 158–183. (doi:10.1098/rspa.1952.0159)
52. Tickner EG, Sacks AH. 1969 Engineering simulation of the viscous behavior of whole blood using suspensions of flexible particles. *Circ. Res.* **25**, 389–400. (doi:10.1161/01.RES.25.4.389)
53. Chakrabarti SK. 2002 *The theory and practice of hydrodynamics and vibration*, vol. 20. Hackensack, NJ: World Scientific.
54. de Langre E. 2008 Effects of wind on plants. *Annu. Rev. Fluid Mech.* **40**, 141–168. (doi:10.1146/annurev.fluid.40.111406.102135)
55. Leclercq T, de Langre E. In press. Reconfiguration of elastic blades in oscillatory flow. *J. Fluid Mech.*
56. Dupuis C, Rousselet J. 1992 The equations of motion of curved pipes conveying fluid. *J. Sound Vib.* **153**, 473–489. (doi:10.1016/0022-460X(92)90377-A)
57. Lundgren TS, Sethna PR, Bajaj AK. 1979 Stability boundaries for flow induced motions of tubes with an inclined terminal nozzle. *J. Sound. Vib.* **64**, 553–571. (doi:10.1016/0022-460X(79)90804-6)
58. Broyden CG. 1965 A class of methods for solving nonlinear simultaneous equations. *Math. Comput.* **19**, 577–593. (doi:10.1090/S0025-5718-1965-0198670-6)
59. Hammarling S, Munro CJ, Tisseur F. 2013 An algorithm for the complete solution of quadratic eigenvalue problems. *ACM Trans. Math. Software (TOMS)* **39**, 18. (doi:10.1145/2450153.2450156)
60. Alben S, Shelley MJ. 2008 Flapping states of a flag in an inviscid fluid: bistability and the transition to chaos. *Phys. Rev. Lett.* **100**, 074301. (doi:10.1103/PhysRevLett.100.074301)
61. Alben S. 2008 The flapping-flag instability as a nonlinear eigenvalue problem. *Phys. Fluids* **20**, 104106. (doi:10.1063/1.3000670)

Vortex-induced vibrations of cylinders bent by the flow

Tristan LECLERCQ^{a,*}, Emmanuel DE LANGRE^a

^a*Department of Mechanics, LadHyX, CNRS, École Polytechnique, 91128 Palaiseau, France*

Abstract

Flexible cylinders exposed to transverse flows may undergo transverse vortex-induced vibrations due to the oscillating lift force imposed by their wake. But the drag on such structures often leads to large in-line deflections that may significantly affect the dynamics through the combined effects of the curvature-induced tension, the local inclination of the cylinder, the non-uniformity of the normal flow profile, and the large axial flow component. In this paper, we investigate the consequences of flow-induced bending on the vortex-induced dynamics of slender cantilever cylinders, by means of numerical simulations. We combine a distributed wake oscillator approach to model the dynamics of the wake with Lighthill's large-amplitude elongated body theory to account for the effect of the axial flow in the reactive (added mass) force. The use of such reduced order models facilitates the identification of the physical mechanisms at play, including through the linear analysis of the coupled fluid-structure system. We find that the primary consequence of flow-induced bending is the inhibition of single mode lock-in, replaced by a multi-frequency response of the structure, and the reduction of the vibration amplitude, as a result of the broadening of the wake excitation spectrum and of the localization of the energy transfer due to the variations induced in the normal flow profile. We also find that the curvature-induced tension is of negligible influence, but that the axial flow component may on the other hand significantly alter the dynamics owing to the destabilizing effect of the reactive force on the structural modes.

Keywords: vortex-induced vibrations, wake oscillator, curved cylinder, linear stability analysis

1. Introduction

The vortex-induced vibrations (VIVs) of slender cylindrical structures has been a prominent subject of research for many years. Originally, a better understanding of this phenomenon was sought in the civil and marine engineering community mostly because of the damage it may cause on a number of flow-exposed structures such as buildings, power transmission lines, marine risers, towing cables, or mooring lines. For extensive reviews regarding VIVs, the reader is referred to Williamson and

*Corresponding author: tristan.leclercq@polytechnique.edu

Govardhan (2004); Sarpkaya (2004); Williamson and Govardhan (2008); Bearman (2011); Wu et al. (2012). More recently, a renewed interest for the VIVs has arisen from the potential they bear as an alternative source of energy (Bernitsas et al., 2008).

The large majority of existing studies focus on the VIVs of straight cylinders in a variety of configurations: rigid or flexible, perpendicular to the flow or slanted, exposed to a uniform or a sheared flow. However, most of the off-shore flexible structures such as those cited above are actually greatly deformed in the direction of the flow under the effect of the free-stream. This configuration differs from the case of a straight cylinder on several aspects. First, the deflection in the plane of the free-stream of a cylinder is responsible for a curvature-induced tension inside the structure. The tensioning of the cylinder may affect its natural frequencies, and consequently its dynamic response to the wake excitation. Secondly, deflected structures are not locally perpendicular to the flow, which modifies the features of vortex shedding in the wake and the associated forces on the structure. Besides, a curved structure experiences a spanwise variation of its angle with the free-stream. Finally, the reconfiguration of the structure leads to a large axial component of the flow on the most inclined portion of the structure that may even become dominant when the deflection is significant. The consequences of some of these specificities have been individually studied, see for instance Srinil et al. (2009); Srinil (2010) for the structural effect of the curvature, Lucor and Karniadakis (2003); Facchinetti et al. (2004b); Franzini et al. (2009); Jain and Modarres-Sadeghi (2013); Bourguet et al. (2015) for the effect of the inclination, or Vandiver (1993); Chaplin et al. (2005); Trim et al. (2005); Lucor et al. (2006); Violette et al. (2010); Bourguet et al. (2013) for the effect of non-uniform normal flow profiles, but their combined effects may lead to a significant alteration of the wake-structure interaction that has not yet been fully investigated.

As a first step towards the understanding of VIVs of bent cylinders, Miliou et al. (2007) and de Vecchi et al. (2008) numerically explored the vortex shedding process in the wake of a rigid cylinder in the shape of a convex or concave quarter of a ring, when the structure is respectively fixed or forced into an oscillatory motion. Building on these results, Assi et al. (2014) and Seyed-Aghazadeh et al. (2015) experimentally investigated the free vibrations of similar structures and found that the amplitude of the oscillations is much reduced compared to the straight configuration. Two studies provided experimental observations regarding the VIVs of flexible structures about a curvy shape: the experimental work of Zhu et al. (2016) considered the vibrations of a naturally concave-shaped cylinder subjected to a shear flow, while that of Morooka and Tsukada (2013) tested a model riser deformed in the shape of a concave catenary under the effect of a uniform free-stream. Finally, Bourguet et al. (2012) and Bourguet et al. (2015) numerically investigated the VIVs of tensioned flexible beams respectively exposed to a normal sheared flow and an inclined uniform flow. Both studies considered the influence of a small average in-line deformation and noted the transition from a mono-frequency to a multi-frequency response associated with a modification of the normal flow profile due to the bending.

A reduction of the amplitude of the VIVs was also reported in Bourguet et al. (2015). At this point however, a theoretical study is still missing to clarify the consequences of flow-induced bending on the VIVs of slender cylinders in large deformations and identify the physical mechanisms at play. One may for instance wonder how the bending-induced shear in the normal flow might impact the vibration spectrum, whether lock-in may or may not still occur, or furthermore how the amplitude of vibration might be affected?

But the flow-induced bending of the structure may have even more dramatic consequences. Indeed, slender structures in axial flows are liable to a flutter instability (Datta and Gottenberg, 1975; Yadykin et al., 2001; Païdoussis et al., 2002; Semler et al., 2002). This self-induced dynamics results from the destabilizing effect of the inviscid pressure forces associated with the deformation of the structure in a free-stream with a significant axial component (Eloy et al., 2007; Singh et al., 2012a). When a cylinder deflects in a transverse flow, the increasing spanwise component of the free-stream may thus be the cause of such instability. More generally, the influence of the inviscid pressure forces on the structural modes may have consequences on the vortex-induced dynamics even in a domain of the parameter space where the system does not flutter.

The purpose of the present paper is to provide an analysis of the small-amplitude vibrations of slender cylinders bent by the flow by means of reduced order models to identify the physical mechanisms at play. In particular, a formulation of the inviscid pressure forces based on Lighthill's large-amplitude elongated body theory (Lighthill, 1971) will be used to account for the destabilizing effect of the axial component of the free-stream. We will also make use of a wake oscillator to describe the lift resulting from vortex shedding. This class of models was originally derived to represent the dynamics of the free wake behind a fixed structure (Birkhoff and Zarantonello, 1957; Bishop and Hassan, 1964), and they have been proved able to capture some characteristic features of the vortex shedding mechanism, such as the formation of cells in shear flow (Noack et al., 1991; Mathelin and de Langre, 2005). Such models have also been proved useful in qualitatively describing the physics of VIVs when coupled with a structural oscillator (Hartlen and Currie, 1970; Skop and Balasubramanian, 1997; Balasubramanian et al., 2000; Mukundan et al., 2009; Srinil and Zanganeh, 2012), and they have been validated against experimental and numerical results (Violette et al., 2007). In this regard, the work of Facchinetti et al. (2004a) demonstrated that features such as the boundaries of the lock-in range, the amplitude of the vibrations or the phase between the structure and the wake are correctly predicted when a coupling term proportional to the structural acceleration is used. The subsequent work of de Langre (2006) and Violette et al. (2010) further demonstrated that many features of the nonlinear limit-cycle dynamics can be interpreted through the linear analysis of the coupled wake-structure oscillators.

In Section 2, the model for the flow-structure interactions and its specific adaptations to the problem in question are detailed. The consequences of the flow-induced bending on the VIVs are then discussed

in Section 3 based on the results of numerical simulations.

2. Model

2.1. Theoretical modeling

We consider the model system represented on Fig. 1. A circular cylinder of length L , diameter D and mass per unit length m is clamped perpendicular to a uniform and steady flow of velocity $U\mathbf{e}_x$ of a fluid of density ρ . We assume the cylinder is slender ($D \ll L$) and we model it as an inextensible Euler-Bernoulli beam of bending stiffness EI (see more details about the structural model in Appendix A.1). We note s the curvilinear coordinate along the span from the clamped end to the free end, and $\mathbf{r}(s, t)$ the location of the centerline. In this paper we focus on the small-amplitude transverse oscillations so we consider that the structure is primarily deflected in the xz -plane under the effect of the flow into a leading order configuration $\mathbf{r}_0(s)$ (broken black line on Fig. 1, specifically shown on Fig. 1(c)). Vortex shedding in the wake of the bent structure is then responsible for an oscillatory lift force in the y -direction that induces small-amplitude transverse vibrations (solid grey line on Fig. 1, specifically shown on Fig. 1(d)) such that $\mathbf{r}(s, t) = \mathbf{r}_0(s) + Y(s, t)\mathbf{e}_y$.

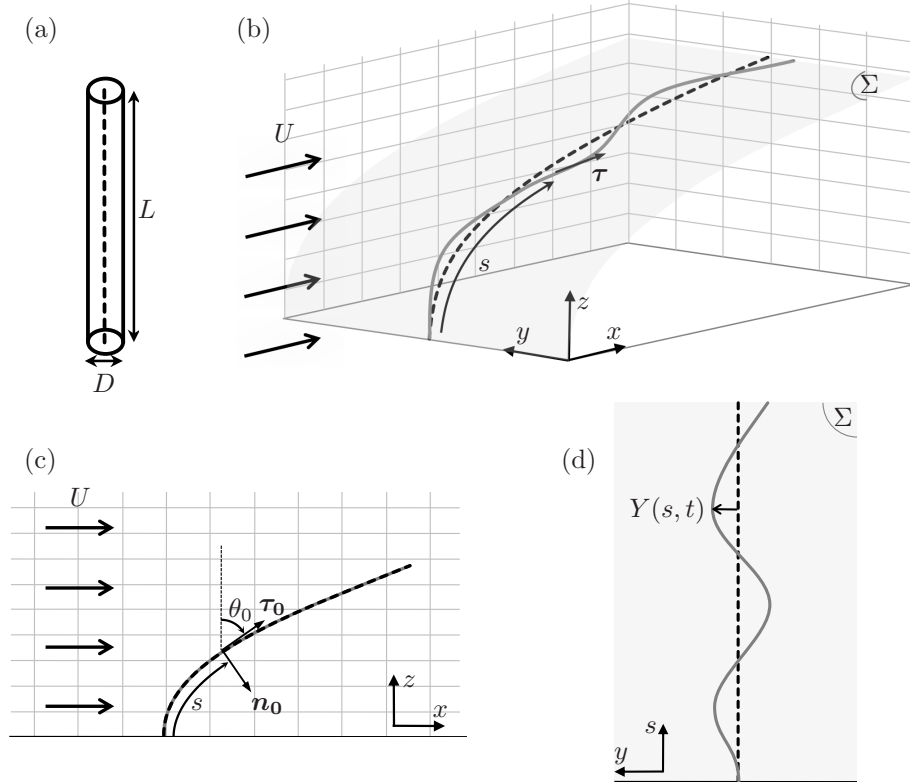


Figure 1: (a) Dimensions of the undeformed cylinder and centerline (broken line). (b) 3D view of the centerline of the vibrating cylinder, static deflection $\mathbf{r}_0(s)$ (broken black line), fully deformed shape $\mathbf{r}(s, t)$ (solid grey line). The π -plane in grey indicates the surface upon which the vibration occurs. (c) Projection of the deformation on the plane of static deflection (xz -plane). (d) Projection of the deformation on the surface of vibration (π -surface or sy -surface).

We disregard the influence of gravity and buoyancy, and we restrict our study to large Reynolds number flows so that friction forces are neglected. Following Mukundan et al. (2009) and Violette et al. (2010), we model the effect of the fluid as the combination of three load distributions along the span $\mathbf{p} = \mathbf{p}_{am} + \mathbf{p}_d + \mathbf{p}_w$, where \mathbf{p}_{am} is the reactive or added mass force, \mathbf{p}_d is the resistive drag due to flow separation in the plane of the cross-section, and \mathbf{p}_w is the oscillating lift force due to the vorticity wake. The expressions of these forces involve the projections (U_τ, U_N) on the direction tangent to the structure and on the plane normal to it, of the relative velocity between the cylinder and the fluid $\mathbf{U}_{rel} = \dot{Y}\mathbf{e}_y - U\mathbf{e}_x = U_\tau\boldsymbol{\tau} + U_N\mathbf{N}$, where the overdot stands for time differentiation.

Firstly, in the case of an elongated body such as those considered in this study, the expression of the added mass force stemming from the pressure field associated with the potential component of the flow has originally been derived by Lighthill (1971) for large-amplitude planar motions. Its extension to 3D deformations has been derived by Candelier et al. (2011) and reads

$$\mathbf{p}_{am} = -m_a \left[\partial_t(U_N\mathbf{N}) - \partial_s(U_\tau U_N\mathbf{N}) + \frac{1}{2}\partial_s(U_N^2\boldsymbol{\tau}) \right] \quad (1)$$

with the added mass $m_a = 1/4\rho\pi D^2$. This expression differs from the usual added mass force used in VIV studies because it is designed to account for the effects of the curvature as well as a large axial flow component. The additional terms thus introduced cancel in the specific case of a straight structure so this choice is nonetheless consistent with the usual expression used in previous works on the topic. On the other hand, this expression has been widely used in studies of the flutter instability of slender beams in axial flow (Païdoussis, 1998; de Langre et al., 2007; Eloy et al., 2012; Singh et al., 2012b; Michelin and Doaré, 2013).

Secondly, following Taylor (1952), we express the resistive drag force as

$$\mathbf{p}_d = -\frac{1}{2}\rho C_D D |U_N| U_N \mathbf{N} \quad (2)$$

with C_D the cross-section drag coefficient. Due to the transverse vibrations, this coefficient may be dynamically enhanced by an amplitude-dependent factor classically of the order of 2 (Vandiver, 1983; Blevins, 1990; Chaplin et al., 2005). The exact value of the drag coefficient should however have only a limited impact on the qualitative features of the VIVs. For the sake of simplicity, we hereafter take $C_D = 2$ for a vibrating cylinder (Blevins, 1990; Chaplin et al., 2005; Mathelin and de Langre, 2005). The resistive drag term is responsible for the leading order static deflection of the beam in the xz -plane (see Gosselin et al., 2010; Leclercq and de Langre, 2016) and acts as hydrodynamic damping for the transverse vibrations.

Finally, following Antoine et al. (2016) the local effect of vortex shedding is modeled as an oscillating lift force orthogonal to the cylinder axis and to the component of the free-stream normal to the still

cylinder

$$\mathbf{p}_w = \frac{1}{4} \rho C_L^0 D U^2 \cos^2 \theta_0 q \mathbf{e}_y \quad (3)$$

where the fixed cylinder lift coefficient C_L^0 is multiplied by a local magnification factor $q(s, t)$ that satisfies a nonlinear Van der Pol equation forced by the transverse acceleration of the structure

$$\ddot{q} + \varepsilon \left(2\pi \frac{S_t U}{D} \cos \theta_0 \right) (q^2 - 1) \dot{q} + \left(2\pi \frac{S_t U}{D} \cos \theta_0 \right)^2 q = A \frac{\ddot{Y}}{D}. \quad (4)$$

We assume in this study the classical values $S_t = 0.2$, $C_L^0 = 0.3$ in the sub-critical range $300 < Re < 1.5 \times 10^5$ (Blevins, 1990; Facchinetti et al., 2004a). Following Facchinetti et al. (2004a), we further assume $A = 12$, $\varepsilon = 0.3$. Even though these parameters were derived from experiments on rigid cylinders, this approach was validated in the case of flexible structures in Facchinetti et al. (2004b) and Violette et al. (2007). It was then successfully used in subsequent theoretical studies (Mathelin and de Langre, 2005; Violette et al., 2010; Meng and Chen, 2012; Dai et al., 2013, 2014). No direct spanwise coupling between the wake oscillators is considered in Eq. (4) as the work of Mathelin and de Langre (2005) has demonstrated that the coupling with the structural oscillator is the main source of synchronisation in the wake. Similar observations have been reported by de Vecchi et al. (2008) from direct numerical simulations that showed parallel vortex shedding in the wake of a curved cylinder in forced oscillations, in contrast with the spanwise phase shift reported by Miliou et al. (2007) in the wake behind a fixed cylinder. Moreover, this local modeling is based on the so-called *independence principle* that states that the physics of vortex shedding is primarily governed by the component of the free-stream normal to the structure only (see Lucor and Karniadakis, 2003; Franzini et al., 2009; Jain and Modarres-Sadeghi, 2013). The work of Bourguet et al. (2015) has demonstrated the validity of that principle when applied locally at each location along the span in the case of the VIVs of flexible cylinders inclined at 60° of incidence. In this case, due to the in-line deformation of the structure, the local incidence of the cylinder could reach values as large as 75° . The local lift force (3) is thus taken quadratic in the locally normal projection of the free-stream velocity $U \cos \theta_0$ and the local natural shedding frequency that appears in (4) satisfies the Strouhal law expressed in terms of that normal component as well $f_w = S_t U \cos \theta_0 / D$ (Williamson, 1996; Facchinetti et al., 2004b).

Note that vortex shedding in the wake is also responsible for an oscillating drag term that creates slight temporal variations of the in-line deflection. Besides, recent studies have shown that the coupling between the in-line and transverse vibrations may considerably affect the transverse dynamics (Jauvtis and Williamson, 2003, 2004; Marcollo and Hinwood, 2006; Srinil and Zanganeh, 2012; Srinil et al., 2013). However, for the sake of simplicity and given the leading-order nature of the resistive drag term considered here, we choose to disregard the influence of the in-line fluctuations in this study.

2.2. Governing equations

We non-dimensionalize all variables but the transverse displacement using the length L of the cylinder as characteristic length, and the inverse of the natural shedding frequency on the undeformed straight cylinder $f_w^0 = S_t U/D$ as characteristic time scale. Because the amplitude of the VIVs classically scales with the diameter of the structure, we non-dimensionalize the transverse displacement Y using D instead of L . We also define the following non-dimensional parameters: the Cauchy number C_Y , the reduced velocity u , the aspect ratio Λ , the mass ratio β

$$C_Y = \frac{\rho C_D D U^2 L^3}{2EI} \quad , \quad u = \frac{S_t U}{D} L^2 \sqrt{\frac{m + m_a}{EI}} \quad , \quad \Lambda = \frac{L}{D} \quad , \quad \beta = \frac{m_a}{m + m_a} \quad (5)$$

and rescaled drag and lift coefficients $c_d = 2C_D/\pi$ and $c_l = C_L^0/\pi$. The Cauchy number measures the level of static in-plane deflection. The definition of the Cauchy number used here is classical in studies of the static deflection of slender structures (Gosselin et al., 2010; Leclercq and de Langre, 2016; Hassani et al., 2016). More details about the significance of this number will be provided in Section 2.3. Note that the reduced velocity used here is consistent with the classical definition used in VIV studies of systems with only one degree of freedom (see for instance Khalak and Williamson, 1999; Païdoussis et al., 2010), in the sense that it compares the characteristic scale of the natural period of the structure $T_s = L^2 \sqrt{(m + m_a)/EI}$ to the reference vortex shedding period $1/f_w^0 = D/S_t U$. Our definition of the mass ratio on the other hand differs from the more classical ratio $m^* = m/(\rho\pi D^2/4)$ (Païdoussis et al., 2010) and they are related by $m^* = 1/\beta - 1$. The proper linearization of the model presented in Section 2.1 is detailed in Appendix A, and its appropriateness for the modelling of VIVs is discussed in Appendix B. Note that, for the sake of simplicity we do not introduce different notations for the non-dimensional variables and in the rest of this paper, the notations Y , κ , s and t always refer to the non-dimensional quantities. In terms of the non-dimensional variables, the governing equation for the leading order static deflection in the xz -plane then reads

$$\kappa_0'' + \frac{1}{2}\kappa_0^3 + \frac{C_Y}{c_d \Lambda} \left(S_0^2 - \frac{1}{2}C_0^2 \right) \kappa_0 - C_Y C_0^2 = 0 \quad (6)$$

where the prime notation stands for curvilinear differentiation, the notations $S_0 = \sin \theta_0$ and $C_0 = \cos \theta_0$ have been used for brevity, and with the curvature $\kappa_0 = \theta_0'$. The corresponding boundary conditions are $\theta_0 = 0$ at the clamped edge $s = 0$ and $\kappa_0 = \kappa_0' = 0$ at the free tip $s = 1$. At the linear order, the equation for the non-dimensional vibration $Y(s, t)$ is

$$u^2 \ddot{Y} + \frac{\beta u^2}{S_t \Lambda} \left[2S_0 \dot{Y}' + C_0 (\kappa_0 + c_d \Lambda) \dot{Y} \right] + \left(\left[\frac{\beta u^2}{S_t^2 \Lambda^2} \left(S_0^2 + \frac{1}{2}C_0^2 \right) + \frac{3}{2}\kappa_0^2 \right] Y' \right)' + c_d \frac{\beta u^2}{S_t^2 \Lambda} C_0 S_0 Y' + Y^{(4)} = c_l \frac{\beta u^2}{S_t^2} C_0^2 q \quad (7)$$

with $Y = Y' = 0$ at the clamped edge $s = 0$ and $Y'' = Y''' = 0$ at the free tip $s = 1$. The lift magnification factor $q(s, t)$ then satisfies the Van der Pol equation

$$\ddot{q} + \varepsilon (2\pi C_0) (q^2 - 1) \dot{q} + (2\pi C_0)^2 q = A\dot{Y}. \quad (8)$$

2.3. On the governing parameters

Within the four non-dimensional parameters defined above (C_Y, u, Λ, β), only three are necessary to fully characterize the problem. In fact, for a given structure with a fixed mass and aspect ratios, the Cauchy number and the reduced velocity are redundant parameters that are related by $C_Y = (c_d \beta / S_t^2 \Lambda) u^2$. Both quantities scale the influence of the flow to the rigidity of the structure, but from different perspectives. The Cauchy number expresses the ratio between the leading order drag force and the restoring structural stiffness (Tickner and Sacks, 1969; Chakrabarti, 2002; de Langre, 2008). Consequently, it controls the level of static deflection in the xz -plane. For small $C_Y < 1$, deflection is negligible and the structure stands upright in the flow, while for $C_Y \gg 1$ the cylinder is highly deformed in the direction of the free-stream (Gosselin et al., 2010). On the other hand, the reduced velocity compares the natural shedding frequency f_w^0 (on the straight structure) to the scale of the natural period of the structure T_s , so it controls the dynamic behaviour of the coupled wake-structure system.

The mass ratio β represents the amount of fluid inertia within the total inertia of the system. We do not expect the precise value of β should significantly influence the qualitative features of the VIVs presented in this article. We also expect the influence of the gravity and buoyancy forces on the static deflection due to the flow to remain small (Luhar and Nepf, 2011). Thus, for the sake of simplicity, we restrict this study to the case of a neutrally buoyant cylinder $\beta = 0.5$. Finally, the aspect ratio $\Lambda = L/D$ scales the relative contributions of the resistive and reactive terms. In the case of slender structures $\Lambda \gg 1$ as those considered in this paper, the contribution of the reactive force $O(C_Y/\Lambda)$ to the static equilibrium shape in Eq. (6) is in fact negligible. On the other hand, as will be shown in Section 3.3, the reactive force may be responsible for triggering the large-amplitude flutter instability, and its influence on the vortex-induced dynamics may still be significant near the critical threshold when the deflection is large. Thus we may not neglect a priori the terms originating from the reactive force in Eq. (7).

Our main interest in this study is the effect of the flow-induced bending on the properties of the vortex-induced vibrations. In other words, we wish to compare the dynamics of structures with varying levels of deflection in the direction of the free-stream (varying Cauchy numbers C_Y), at a given reduced velocity u . However, as explained above, for a given fluid-structure system of fixed mass and aspect ratios (β, Λ), the Cauchy number and the reduced velocity vary together as $C_Y \propto \beta u^2 / \Lambda$. Therefore,

increasing the Cauchy number *with a fixed reduced velocity* requires to change the structure to lower the aspect ratio Λ . This may seem counter-intuitive, as a lower aspect ratio is classically associated with lower deflections. Indeed, the Cauchy number is an increasing function of the aspect ratio $C_Y \propto \Lambda^3$ when the dimensional flow velocity, fluid density, and Young's modulus of the solid material are kept constant. In our case however, we allow these dimensional quantities to vary in order to keep the reduced velocity u constant instead, and consequently the Cauchy number becomes a decreasing function of the aspect ratio. In the limit of an infinitely slender structure $\Lambda \rightarrow +\infty$, the Cauchy number remains much smaller than 1 even for arbitrarily large reduced velocities. This asymptotic case is therefore equivalent to considering a structure that remains straight in the free-stream. For this benchmark case, the dynamic system (7)-(8) reduces to

$$u^2 \ddot{Y} + c_d \frac{\beta u^2}{S_t} \dot{Y} + Y^{(4)} = c_l \frac{\beta u^2}{S_t^2} q \quad (9)$$

$$\ddot{q} + \varepsilon (2\pi) (q^2 - 1) \dot{q} + (2\pi)^2 q = A \ddot{Y} \quad (10)$$

which is the standard system of equations for the modeling of VIVs by means of a wake oscillator, in the case of a straight slender cylinder with flexural stiffness and hydrodynamic damping (Mukundan et al., 2009).

3. Numerical results

In order to analyse the vibration behaviour, we solve the problem defined by equations (6),(7),(8) numerically. The beam is discretized using $N = 100$ Gauss-Lobatto points $s_k = \frac{1}{2}(1 - \cos((k-1)/(N-1)\pi))$, and the curvilinear derivatives are computed by Chebyshev collocation. For a given aspect ratio Λ , we first compute the static solution of Eq. (6) iteratively by increasing the Cauchy number from the upright case $C_Y = 0$. After each increment, we solve Eq. (6) with a pseudo-Newton solver (method of Broyden, 1965) using the solution at the previous step as initial guess. Then, for each value of C_Y (corresponding to a given u), we solve the nonlinear system (7)-(8) using a time-stepping method, with time step $dt = 10^{-2}$. The time derivatives are computed using implicit second order accurate finite differences. At each time step, the nonlinear boundary value problem involving the unknown spanwise distributions (Y, q) is solved thanks to the pseudo-Newton solver. The simulations are run for 200 periods and the last 100 periods are considered for the analysis in order to cut the transient.

3.1. Wake excitation bandwidth and inhibition of single mode lock-in

First, we discuss the influence of the deflection on the modal content of the dynamics. To do so, we compare the vibrations of a structure that bends (finite aspect ratio $\Lambda = 10^3$) to that of a structure

that remains straight ($\Lambda \rightarrow +\infty$), on the same range of reduced velocities. For the structure with finite aspect ratio $\Lambda = 10^3$, the variations of u within the range considered will be associated with variations in the Cauchy number $C_Y \propto u^2/\Lambda$ leading to varying levels of deflections. On the other hand, the infinitely slender cylinder will remain straight because the Cauchy number will remain asymptotically small in the same finite range of u . We recall here that the cylinder with the finite aspect ratio is the one that deflects while the infinitely slender one remains unbent because we compare the dynamics of the two structures *on the same range of reduced velocities* (see Section 2.3 for more details).

As explained in Section 2.1, the independence principle states that the natural frequency of vortex shedding $f_w(s)$ decreases along the span when the structure is deformed because of the projection of the free-stream on the normal direction $f_w(s)/f_w^0 = U_{n_0}/U = \cos \theta_0(s)$. The deforming structure is therefore subjected to a forcing by the wake on a continuum of frequencies that broadens when the deflection is enhanced with increasing Cauchy numbers, as shown on Fig. 2.

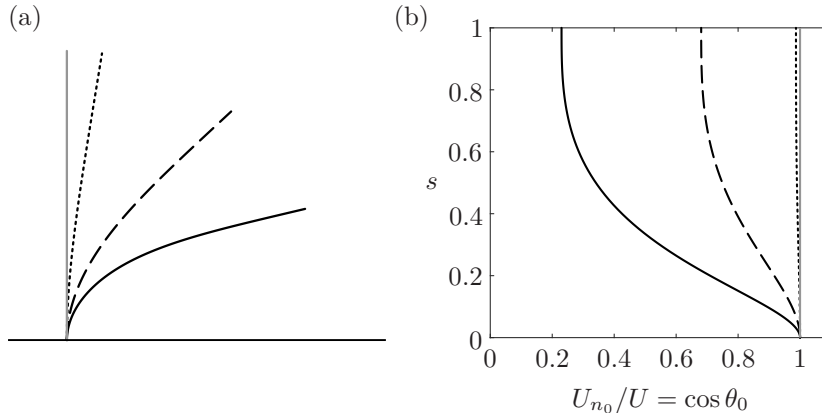


Figure 2: (a) Deflection in the xz -plane and (b) normal velocity profile normalized by the horizontal velocity, in the straight case (grey —), and in deflected cases $C_Y = 10^0$ ($\cdot \cdot \cdot$), $C_Y = 10^1$ ($- - -$), and $C_Y = 10^2$ (black —) for $\Lambda = 10^3$.

The enrichment of the excitation spectrum significantly alters the modal content of the structural response. This is illustrated on Fig. 3 for the vibration spectrum and Fig. 4 for the spanwise localization of the vibration. In the straight case, the structure is subject to a forcing by the wake at a single frequency along the whole span. The frequency of the vibration remains close to the Strouhal law ($f \simeq 1$ on Fig. 3(a)), but slightly deviates to follow an evolution closer to that of the nearest structural mode. As u varies, lock-in with the successive structural modes occurs in turn and frequency discontinuities mark the transitions between consecutive lock-ins. This phenomenon is a well-known feature of the VIVs of flexible structures perpendicular to the flow (King, 1995; Chaplin et al., 2005; Violette et al., 2010). As expected, this behaviour remains unchanged for as long as the deflection is negligible ($C_Y < 1$ on Fig. 3(b)) in the case $\Lambda = 10^3$. However, at the early stages of reconfiguration ($C_Y \lesssim 10^1$ on Fig. 3(b)), the ranges of reduced velocities within which lock-in with a given mode

occurs are slightly widened and increasingly shifted towards larger reduced velocities (see Table 1). For instance, lock-in with mode 4 persists on a slightly larger range $u \in [16.3, 29.9]$ when the structure is bent compared to $u \in [15.2, 27.0]$ when it is not. The modal shapes in both configurations remain on the other hand almost identical, as illustrated for $u = 19.8$ in Fig. 4(c), which proves that the curvature of the structure in the xz -plane only has a very limited impact on the transverse deformation.

Following the method of Violette et al. (2010), we may interpret these results by comparing the spectrum of the nonlinear dynamics to the frequencies of the eigenmodes found by a linear stability analysis (see Fig. 5). The details of the linear stability analysis can be found in Appendix C. The eigenmodes thus found can be classified in 3 distinct types. Firstly, a series of N unstable modes (where N is the number of discretization points s_k) with eigenvalues matching almost exactly the eigenvalues of the linearized wake oscillator without structural coupling $\omega_k \simeq \cos \theta_0(s_k)(2\pi\sqrt{1 - (\varepsilon/2)^2} - i\pi\varepsilon)$ are observed. They have no significant structural component ($\phi_k(s) \simeq 0$), and their wake components are localized respectively at each discretization point ($|\psi_k(s)| \simeq \delta(s - s_k)$ with δ the Dirac function). These modes thus correspond to the naturally unstable free wake modes. For the sake of clarity, the continuous spectrum of the free wake oscillator itself is represented in grey on Fig. 5(b) instead of the N individual eigenmodes spanning the area. Secondly, the modes in blue correspond closely to the eigenmodes of the structural equation (7) without coupling with the wake. These modes may thus be designated as the free structural modes. Finally, the four modes in black are coupled modes that each arise from lock-in with one of the structural modes. They are all unconditionally unstable and will be referred to as the lock-in modes. Following Violette et al. (2010), we expect lock-in with a given mode to persist in the nonlinear limit-cycle if the corresponding linear lock-in mode is the most unstable. The comparison of the linear and nonlinear lock-in ranges in Table 1 confirms these findings and we may thus lean on the linear analysis to interpret the dynamics observed in the limit-cycle. In particular, as deflection increases, we notice on Fig. 5 that the broadening of the free wake spectrum allows the structural frequencies to remain within the excitation bandwidth on a larger range of reduced velocities. Lock-in with these modes may consequently occur on these larger ranges as well. Hence, it appears that the primary consequence of the deflection is the broadening of the free wake spectrum due to the increased shear in the normal component of the free-stream. At leading order, a bending structure in a uniform flow is therefore equivalent to a straight structure in a sheared flow whose profile varies, depending on the Cauchy number, according to that of the normal flow shown on Fig. 2(b).

When bending is more pronounced ($C_Y > 10^1$), not only one but several frequencies are involved in the spectrum of the nonlinear limit-cycle Fig. 3(b), and the localization of the transverse vibration significantly deviates from the single-mode shape on Fig. 4. Indeed, when the wake spectrum becomes large enough, several structural modes are excited simultaneously at different locations along the span

	straight case (nonlinear)	bent case $\Lambda = 10^3$ (nonlinear)	bent case $\Lambda = 10^3$ (linear)
mode 1	0 – 2.3	0 – 2.3	0 – 2.16
mode 2	2.4 – 6.8	2.4 – 6.9	2.16 – 6.80
mode 3	6.9 – 15.1	7 – 16.2	6.80 – 15.86
mode 4	15.2 – 27.0	16.3 – 29.9	15.86 – 28.70

Table 1: Reduced velocity ranges for lock-in in the straight and bent cases (nonlinear and linear ranges).

(several structural modes appear within the wake excitation bandwidth on Fig. 5). Consequently, single mode lock-in is replaced by a multi-frequency response of the whole structure associated with the spatial fragmentation of the wake into multiple cells of locally uniform frequency. As illustrated on Fig. 6, the frequency within each wake cell matches that of the structural mode that is closest (in the frequency space) from the Strouhal law, so that it might be said that single mode lock-in is actually replaced by multiple occurrences of lock-in along the span. It is however noteworthy that the local wake dynamics is essentially monochromatic, while the structural dynamics involves comparable contributions from all the excited modes at any location along the span. Besides, the linear analysis shows that, past $u > 28.7$, the most unstable mode is not one of the coupled lock-in modes anymore, but is found instead within one of the free wake modes. No fifth coupled mode that would appear because of lock-in with the fifth structural mode is observed. It thus appears that the large shear in the normal flow hinders single mode lock-in, but leads to the simultaneous excitation of multiple structural modes that all participate in the dynamics.

We may finally conclude that bending primarily affects the dynamics through its influence on the component of the free-stream normal to the cylinder. More specifically, the growing shear in the normal flow is responsible for broadening the wake spectrum. When the deflection remains moderate, the wake excitation bandwidth remains narrow enough so that single-mode lock-in still prevails, but on a slightly larger range of reduced frequencies. On the other hand, when the deflection is large, several structural modes may be simultaneously excited, leading to the inhibition of single mode lock-in replaced by a multi-frequency response to the broadband excitation. These conclusions are consistent with the observations of Bourguet et al. (2012), Bourguet et al. (2015) for a pinned-pinned cylinder experiencing small in-line deformations, as well as those of Vandiver (1993); Ge et al. (2011); Srinil (2011) for straight pinned-pinned cylinders in shear flow.

3.2. Localization of the excitation and VIV mitigation

As emphasized in the introduction, the experimental work of Assi et al. (2014) and Seyed-Aghazadeh et al. (2015) has shown that the amplitude of the vibrations of rigid cylinders is much reduced under the effect of the curvature. The same observation was made by Bourguet et al. (2015) regarding the VIVs of pinned-pinned flexible cylinders. Similarly, the works of Trim et al. (2005); Ge et al. (2011); Srinil (2011) have also shown that sheared incoming flows entailed lower structural responses than

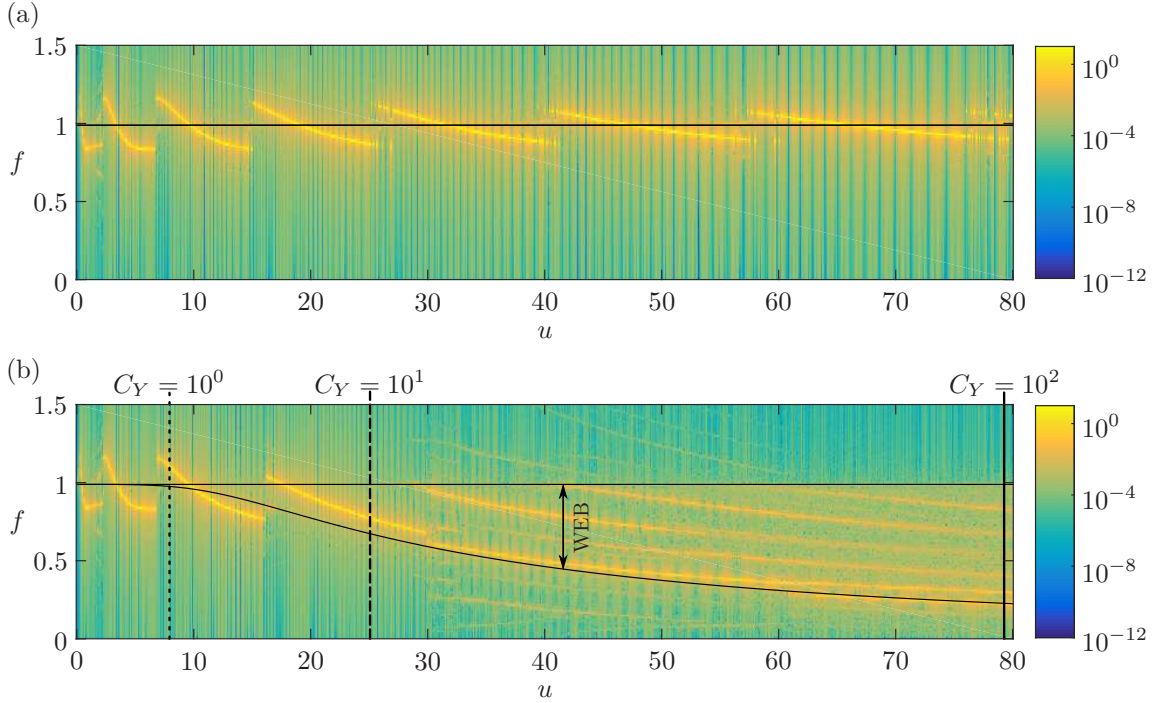


Figure 3: Comparison between the power spectral densities of the motion at the tip $Y(s=1, t)$ in (a) the straight case and (b) the deflected case $\Lambda = 10^3$, for varying reduced velocities u . The natural wake excitation bandwidth (WEB) is superimposed. The particular values of the reduced velocity u corresponding to Fig. 2 are indicated as well.

uniform flows. Our numerical simulations indicate that this observation holds true as well for flexible cantilever cylinders curved by the flow. Indeed, the amplitude of the VIVs of the deflecting cylinder ($\Lambda = 10^3$) reduces progressively on Fig. 7(a) compared to the straight case above the bending threshold $C_Y > 1$. For large deflections $C_Y > 10$, the amplitude settles around approximately $1/3$ of the amplitude of the straight case.

We may explain this reduction of amplitude by considering the energy transferred to the structure from the wake oscillator. In non-dimensional form, the work of the oscillating lift force at a given location along the span reads $e = \dot{Y} \cdot q \cos^2 \theta_0$, so that the total energy E transferred to the structure over one cycle of oscillations is the temporal mean of e , integrated over the whole span. The evolution of E with the reduced velocity on Fig. 7(b) proves that deflection drastically mitigates the transfer. A more detailed look at the spanwise distribution of the mean energy transfer on Fig. 8 indicates that the excitation by the wake, which is equally distributed in the straight case, concentrates around $s \sim 0.2$ as the deflection increases. This is actually quite intuitive, because the lift force varies with the square of the normal component of the free-stream $\propto \cos^2 \theta_0$. When deflection is important, only the small region close to the clamping point remains close enough to the vertical so as to significantly contribute to the excitation. As the Cauchy number increases and the cylinder bends more and more, the size of that region reduces progressively. The amount of energy transferred overall is consequently

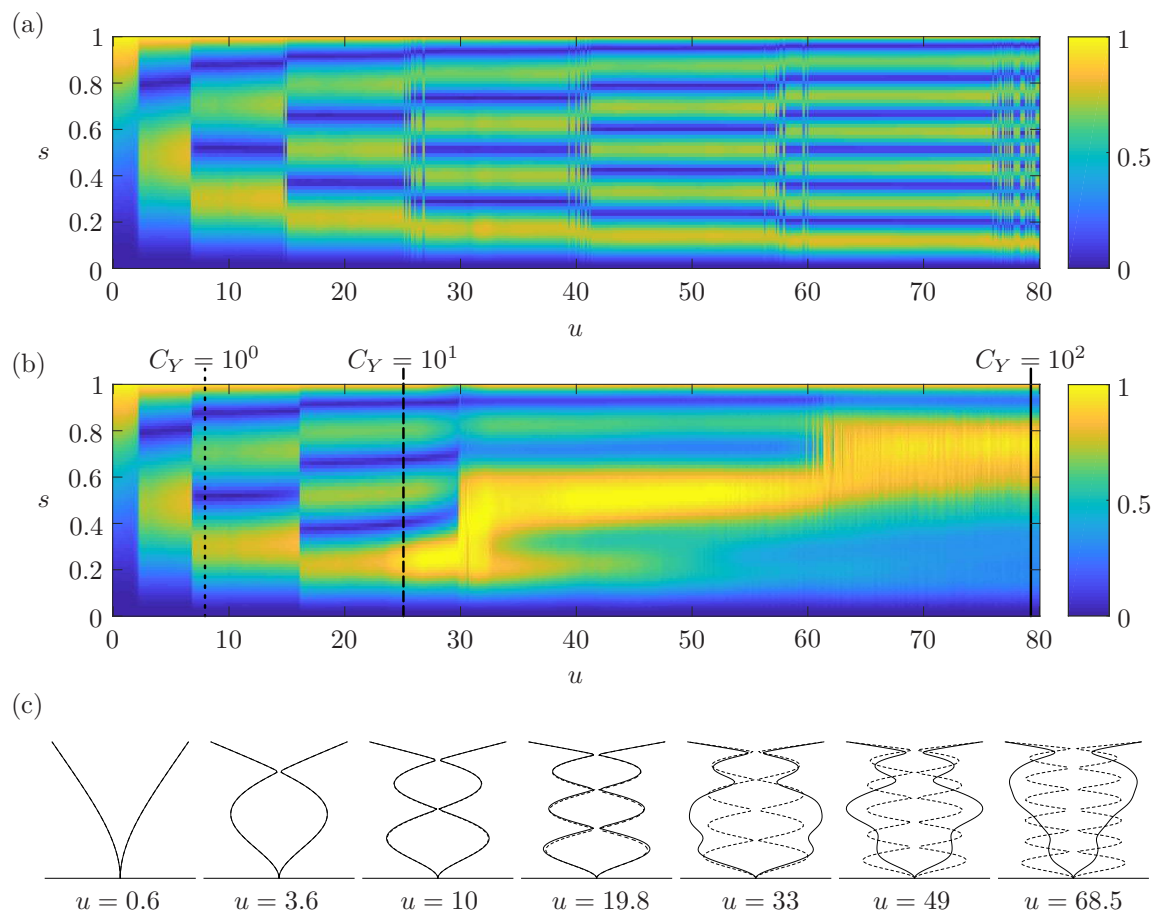


Figure 4: Comparison between the spanwise localizations of the transverse deformation in (a) the straight case and (b) the deflected case $\Lambda = 10^3$, for varying reduced velocities u . The colorplots show the temporal RMS of $Y(s,t)$, normalized to 1 along the span. The particular values of the reduced velocity u corresponding to Fig. 2 are indicated as well. (c) Comparison of the envelopes of the transverse deformation in the straight case (---) and deflected case $\Lambda = 10^3$ (—), for particular values of u corresponding to successive structural modes in the straight case.

reduced, and the amplitude of the vibrations accordingly mitigated.

Note that the discontinuities observed in the straight and low-deflection cases on Fig. 7 correspond to mode switches. The disappearance of these jumps above $u > 30$ in the deflected case is consistent with the continuous evolution of the spectrum and vibration shape reported in Figs. 3(b) and 4(b).

3.3. Influence of the reactive force

Finally, we discuss the influence of the large axial component of the free-stream when the structure is highly reconfigured. Indeed, as the flow velocity increases, the inclination of the structure switches from perpendicular to mostly parallel to the flow. As explained in Section 2.3, the level of deflection is controlled by the Cauchy number $C_Y \propto u^2/\Lambda$. We focus here on a case where the deflection increases more rapidly with the reduced velocity than before, that is to say a structure with a smaller aspect ratio $\Lambda = 10$.

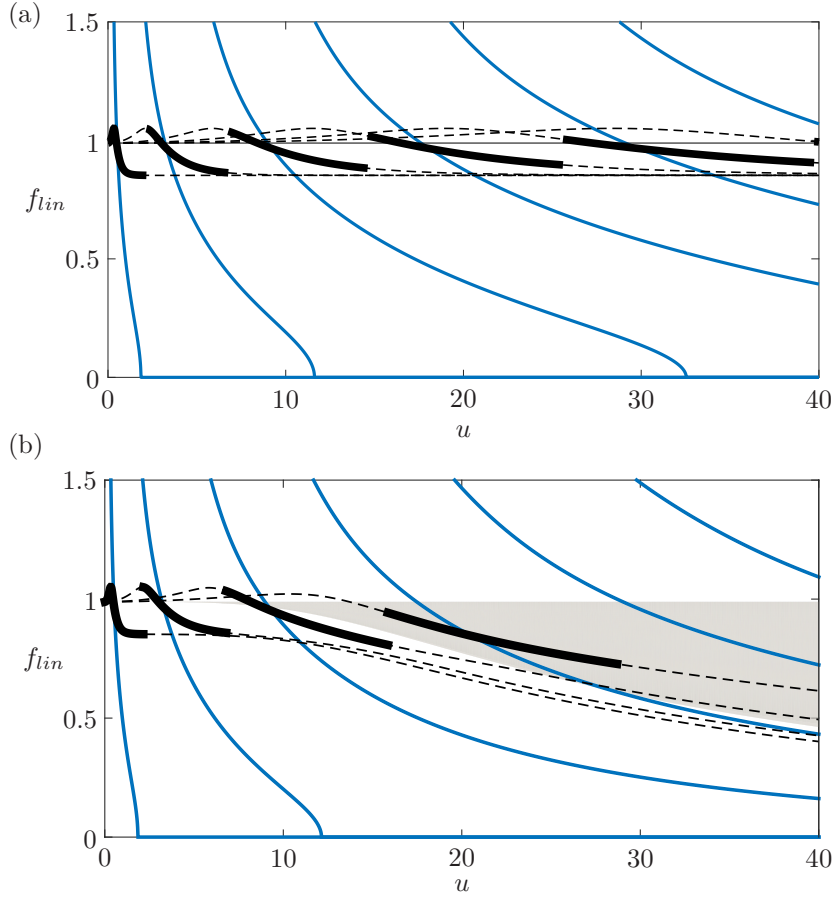


Figure 5: Evolution of the linear frequencies of the coupled wake-structure system with the reduced velocity u , for (a) the straight case and (b) the deflected case $\Lambda = 10^3$. The unconditionally unstable free wake spectrum is represented by the grey area. The structural modes in blue are always stable. The coupled modes, displayed in black, are always unstable. The most unstable mode for a given range of u is emphasized in bold.

At first, the amplitude of vibrations on Fig. 9(a) follows the same trend as in the previous case: below $C_Y < 1$, the effect of bending is unnoticeable, while it results in a constant amplitude much reduced compared to the straight case when bending is significant. The amplitude is even reduced as low as 1/10–th of the straight case. But conversely to the previous case, the vibrations start growing again slowly past $u \sim 20$ and they even exceed the amplitude of the straight case for $u \gtrsim 33.5$. Above some critical threshold $u \sim 35$, the amplitude finally grows continuously during the whole time of the simulation. The VIVs are by nature a self-initiated and self-limited phenomenon. In the model, the onset of the VIVs is ensured by the negative damping of the Van der Pol wake oscillator when the amplitude of q is small, while the limitation of the amplitude is ensured by the nonlinear saturation of that same term. This unbounded growth is therefore not related to the VIVs, but is instead the consequence of the onset of a flutter instability caused by the destabilizing influence of the hydrodynamic reactive force on the large portion of the cylinder that is aligned with the free-stream

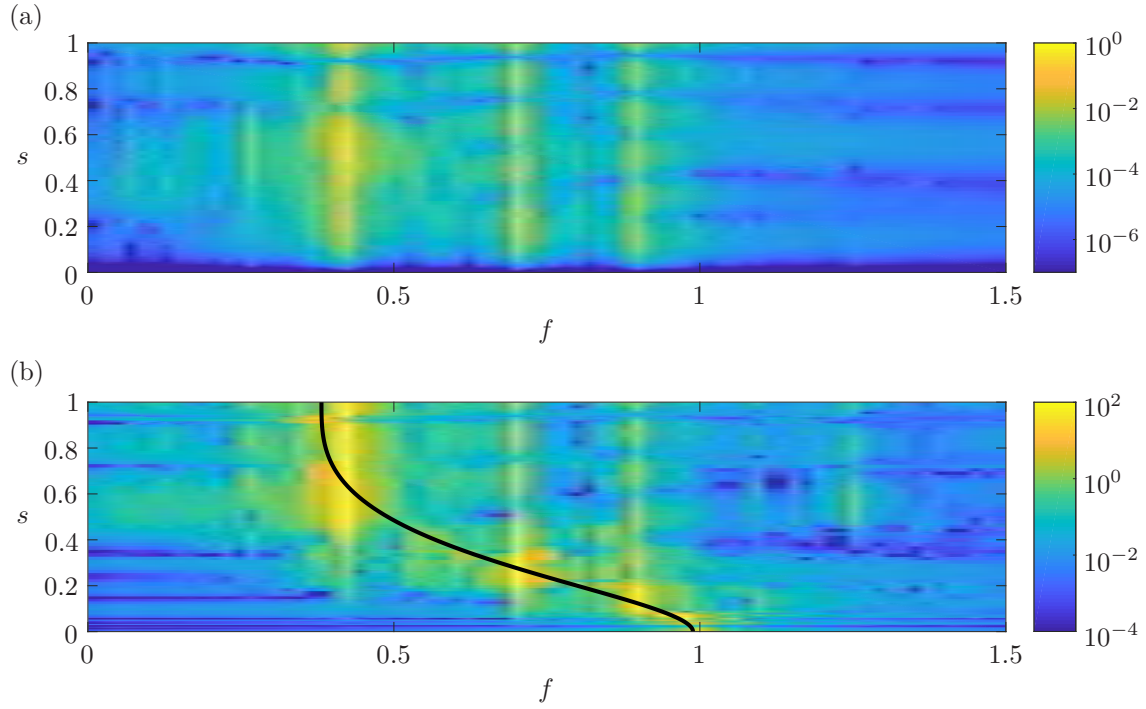


Figure 6: Spanwise distribution of power spectral density of (a) the structural motion Y and (b) the wake oscillator q , for $\Lambda = 10^3$ and $u = 49.0$. The natural shedding frequency $f_w^0(s)$ given by the Strouhal law is superimposed in (b) (—).

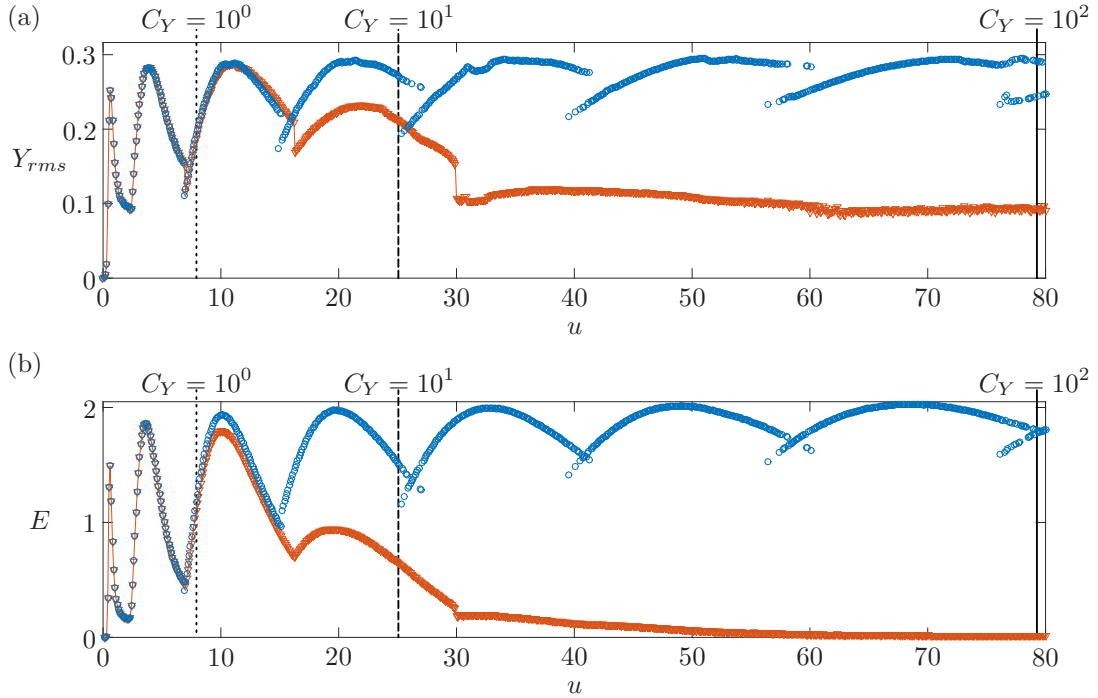


Figure 7: Comparison of (a) the RMS amplitude of vibration Y_{rms} and (b) the total energy transfer E from the wake to the structure, between the straight case (blue \circ) and the deflected case $\Lambda = 10^3$ (orange ∇) for varying reduced velocities u . The particular values of the reduced velocity u corresponding to Fig. 2 are indicated as well.

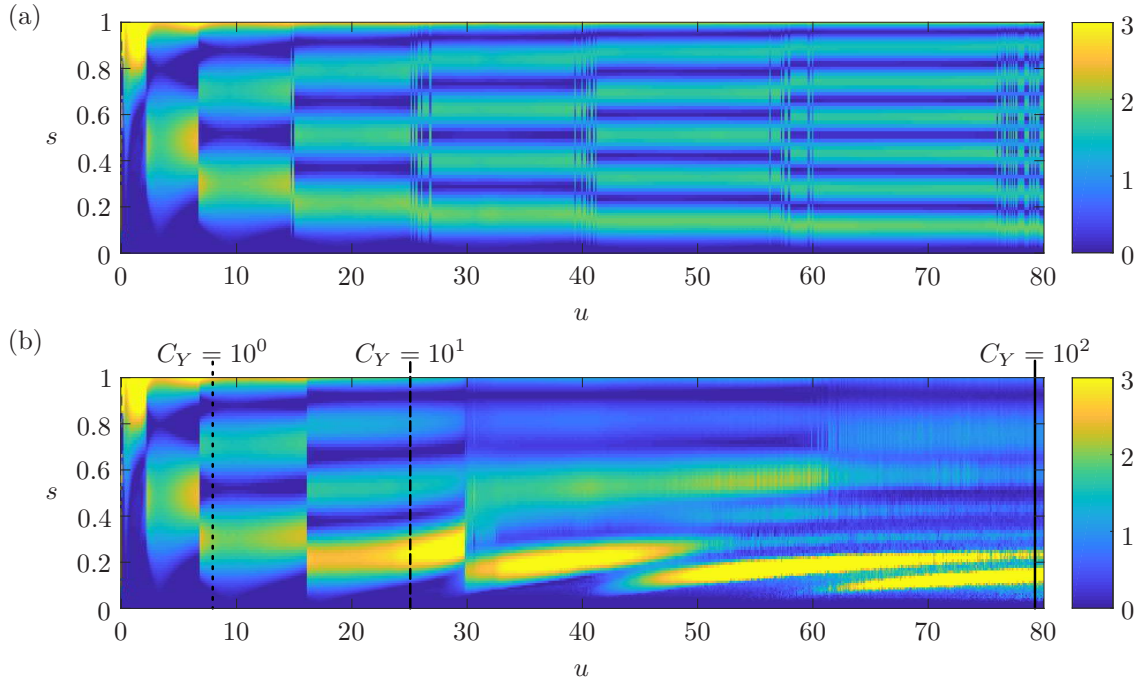


Figure 8: Comparison of the spanwise distributions of energy transfer from the wake to the structure between (a) the straight case and (b) the deflected case $\Lambda = 10^3$, for varying reduced velocities u . The colorplots show the mean work of the oscillating lift force $\langle e \rangle$ normalized by the total energy transfer E . The particular values of the reduced velocity u corresponding to Fig. 2 are indicated as well.

(Eloy et al., 2007; Singh et al., 2012a).

This is confirmed by the results of the linear stability analysis presented on Fig. 9(b) and (c). Lock-in with structural mode 1 occurs for the smallest reduced velocities (the coupled linear mode is the most unstable as long as $u < 2.30$), when flow-induced bending is still small. When deflection becomes significant ($C_Y \gg 1$), several structural modes are simultaneously excited by the wake on Fig. 9(b). But in this case, one of the structural modes (mode 3) is progressively destabilized as u increases. Above $u \gtrsim 20$, the growth rate of this mode starts increasing on Fig. 9(c) until it finally becomes unstable at the critical threshold $u_c = 34.9$ (marked by the orange cross on Fig. 9(b) and (c)). If the effect of the curvature on the structural modes has been proved negligible in Section 3.1, these observations prove on the other hand that the influence of the reactive force may be very significant in the vicinity of the critical threshold. The progressive increase of the vibration amplitude from $u \sim 20$ until the actual onset of the instability $u_c = 34.9$ is indeed concomitant with the destabilization of structural mode 3. Hence, the larger vibration amplitudes observed in this range of reduced velocities are most likely attributable to the growing influence of the gradually destabilizing structural mode 3.

The flow-induced bending thus has competing consequences on the amplitude of the vibrations. On the one hand, we have shown in Section 3.2 that the shrinkage of the wake excitation zone considerably mitigates the VIVs. We demonstrate here that on the other hand, the reorientation of the structure

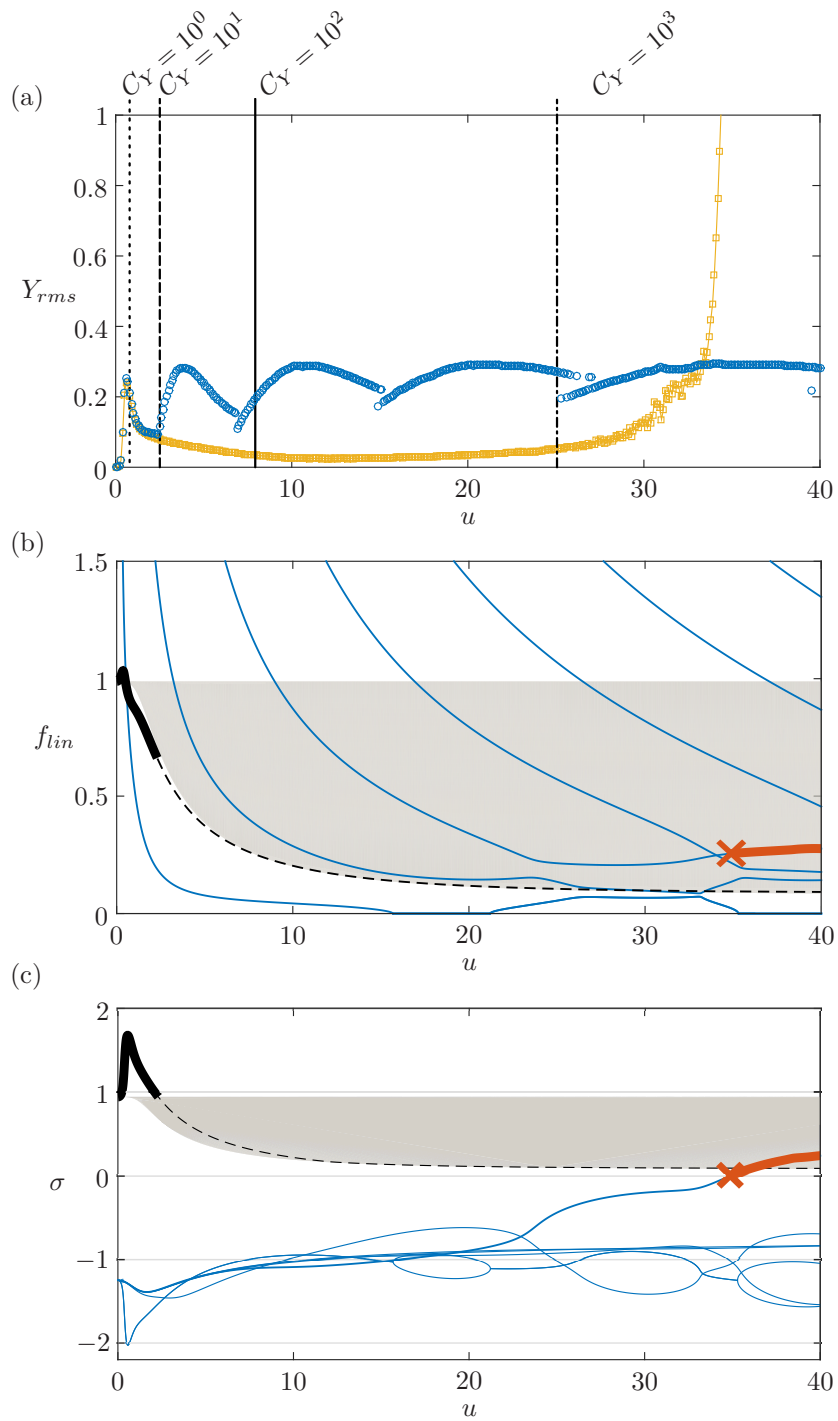


Figure 9: (a) Comparison of the RMS amplitude of vibration between the straight case (blue \circ) and the deflected case $\Lambda = 10$ (yellow \square). (b) and (c) Linear frequencies f_{lin} and growth rates σ of the coupled wake-structure system, for $\Lambda = 10$. The unconditionally unstable free wake spectrum is represented by the grey area. The structural modes are in blue when stable, and in bold orange when unstable. The orange cross marks the stability threshold for structural mode 3. The coupled mode, displayed in black, is always unstable. It is emphasized when it is the most unstable mode.

in the direction of the free-stream may amplify the vibrations because of the destabilizing effect of the reactive force on the structural modes. This last effect becomes significant in the vicinity of the structural stability threshold. As explained in Appendix D, the structural stability threshold in terms of either the reduced velocity u or the Cauchy number C_Y is close to proportional to the aspect ratio Λ . More slender structures may consequently reach much higher modes and larger deflections before feeling the destabilizing influence of the reactive force.

4. Discussion and conclusion

In this paper, we have provided a qualitative analysis of the consequences of flow-induced bending on the vortex-induced dynamics of slender flexible cylinders based on reduced order models. Overall, the effects of the deflection may impact the features of the vibrations on two levels.

Firstly, the deformation of the cylinder changes the spanwise profile of the component of the free-stream normal to the structure. We have shown that the increasing non-uniformity of the normal flow leads to the spreading of the wake excitation spectrum and the localization of the energy transfer from the wake to the structure, owing to the independence principle. These two effects result in a strong mitigation of the amplitude of the vibrations coupled with the inhibition of single mode lock-in replaced by the simultaneous excitation of multiple structural modes. These mechanisms were indeed evidenced in several experimental and numerical studies about the VIVs of straight cylinders in shear incoming flow, such as Vandiver (1993); Trim et al. (2005); Srinil (2011); Ge et al. (2011); Bourguet et al. (2013) for instance. As any deformation of a straight cylinder in the direction of the free-stream would induce shear in the normal flow, we expect that these conclusions are independent of the initial structural configuration, boundary conditions, or the features of the in-plane deformation. For instance, similar observations have been reported by Bourguet et al. (2015) for a pinned-pinned cylinder initially inclined and slightly deformed by the flow. Similarly, the smaller amplitudes of vibrations reported in Assi et al. (2014) and Seyed-Aghazadeh et al. (2015) for rigid curved cylinders compared to straight ones is likely also the consequence of the difference in the normal flow profiles between the two configurations. The loss of harvesting efficiency reported in Antoine et al. (2016) when increasing the sag (and consequently the deformation) in the in-flow catenary configuration also results from the induced shear in the normal flow.

Secondly, the deformation of the structure is responsible for a modification of the structural modes resulting from both the flow-induced tension and the axial component of the flow through the reactive forcing term.

The effect of the tension is negligible in our case, but it should be noted that it may be of significant importance in other situations. Indeed, the structural frequencies depend on the total stiffness of the system, which can be decomposed in the natural bending stiffness EI specific to the structure, and an additional tension-induced stiffness. In our case, the structural tension $T = -1/2EI\kappa_0^2$ itself is the physical consequence of the structural stiffness EI , and so it is understandable that the influence of the tension-induced stiffness on the natural frequencies of the structure be small compared to that of the natural stiffness that originated it. However, in the rather common case of tensioned cables, the structural tension is either externally controlled or flow-induced but it is in any case independent of the usually small bending stiffness. Its influence on the structural frequencies and thus on the vortex-induced dynamics may then be totally dominant (see for instance the study of Antoine et al., 2016), but this effect is out of the scope of the present work as the tension in this case is not related to the flow-induced deformation of the structure.

The effect of the axial flow component may on the other hand be dramatic in the configuration chosen in this article. When the deflection is very large, the axial flow may become the dominant component, and the added damping and stiffness stemming from the reactive forcing on the inclined portion of the cylinder may significantly alter the structural modes. Above some critical velocity threshold, the cylinder might undergo some large-amplitude oscillations originating from a flutter instability. It should be noted that only the transverse stability along the y -direction has been considered in this article, but flutter may also be initiated in the xz -plane (see Leclercq et al., 2018). However, we do not expect the in-plane destabilization to have consequences on the vortex-induced dynamics below the stability threshold. Indeed, the geometrical linearization performed in Appendix A.2 results in the decoupling of the small-amplitude dynamics in the two directions. There should consequently be no interactions between the in-plane structural modes and the transverse vibrations as long as the amplitude of vibration remains small $Y/L \ll 1$. On the other hand, we have shown that the progressive destabilization of the transverse structural modes may enhance the amplitude of the VIVs even in the stable domain. These conclusions may not easily be generalized to other structural configurations as the stability of the structural modes is highly dependent on the boundary conditions of the structure. The choice of the cantilever configuration in our work merely demonstrates the potentially large consequences the axial flow may bear through the reactive force, and neglecting the terms originating from it must only be done with great care. Nonetheless, we also found that the magnification of the vibrations due to the reactive force becomes significant for higher modes of vibrations and larger levels of deflection as the structure is made more slender. In this regard, it may thus be considered as a secondary effect that sets a limit to the strong abatement of the vortex-induced vibrations more commonly observed.

We may thus conclude that the primary consequence of flow-induced deformations on the vortex-induced dynamics of flexible cylinders is the hindrance of single mode lock-in, replaced by a multi-frequency response of the structure, and the strong mitigation of the vibrations that rest on the modification of the spanwise profile of the normal component of the free-stream. Neglecting the in-line deformation when assessing the features of the VIVs should therefore generally result in an overestimation of the severity of the vibrations.

Acknowledgment

The authors would like to acknowledge financial support from the DGA/DSTL grant 2014.60.0005.

Appendix A Derivation of the governing equations

A.1 Details about the structural model

Following Audoly and Pomeau (2010), we define a local direct orthonormal frame $\mathbf{e}_{i=1,2,3} = (\mathbf{n}, \mathbf{w}, \boldsymbol{\tau})$, materially attached to the structure and such that $(\mathbf{n}, \mathbf{w}, \boldsymbol{\tau})|_{s=0} = (\mathbf{e}_x, \mathbf{e}_y, \mathbf{e}_z)$. We also define the Darboux vector $\boldsymbol{\Omega} = \kappa_n \mathbf{n} + \kappa_w \mathbf{w} + \gamma \boldsymbol{\tau}$ where κ_n and κ_w are the material curvatures and γ is the twist of the cylinder. By definition, the Darboux vector is such that $\mathbf{e}_i' = \boldsymbol{\Omega} \times \mathbf{e}_i$. For an Euler-Bernoulli beam of bending stiffness EI in both (\mathbf{n}, \mathbf{w}) -directions, torsional stiffness GJ , and subjected to an external force \mathbf{q} and no external torque, the Kirchhoff equations governing the dynamics of the structure read

$$m\ddot{\mathbf{r}} = \mathbf{F}' + \mathbf{q} \quad , \quad \mathbf{0} = \mathbf{M}' + \boldsymbol{\tau} \times \mathbf{F} \quad (11)$$

with the internal force vector $\mathbf{F} = T\boldsymbol{\tau} + Q\mathbf{n} + P\mathbf{w}$ and the constitutive law for the internal bending moment $\mathbf{M} = GJ\gamma\boldsymbol{\tau} + EI\kappa_n\mathbf{n} + EI\kappa_w\mathbf{w}$. The inextensibility condition reads $\mathbf{r} = \boldsymbol{\tau}$, and for a cantilever beam, the boundary conditions read $\mathbf{r} = 0$ and $\mathbf{r}' = \mathbf{e}_z$ at the clamped edge $s = 0$, and $\mathbf{F} = \mathbf{M} = 0$ at the free end $s = L$. Using the second Kirchhoff law (11) and the boundary conditions for the twist, we find that

$$\gamma = 0 \quad , \quad Q = -EI\kappa_w' \quad , \quad P = EI\kappa_n' \quad (12)$$

so that finally the curvilinear derivatives of the material frame simplify in

$$\boldsymbol{\tau}' = \kappa_w\mathbf{n} - \kappa_n\mathbf{w} \quad , \quad \mathbf{n}' = -\kappa_w\boldsymbol{\tau} \quad , \quad \mathbf{w}' = \kappa_n\boldsymbol{\tau} \quad (13)$$

and the curvilinear derivative of the internal force vector that appears on the right hand side of the first Kirchhoff equation (11) reads

$$\mathbf{F}' = \left(T + \frac{1}{2}EI(\kappa_n^2 + \kappa_w^2) \right)' \boldsymbol{\tau} + \left(\kappa_w T - EI\kappa_w'' \right) \mathbf{n} - \left(\kappa_n T - EI\kappa_n'' \right) \mathbf{w}. \quad (14)$$

The boundary conditions read $\mathbf{r} = \boldsymbol{\tau} = \mathbf{0}$ at $s = 0$ and $T = \kappa_n = \kappa_n' = \kappa_w = \kappa_w' = 0$ at $s = 1$.

A.2 Linearization of the structural model

As explained in Section 2, we expand $\mathbf{r}(s, t) = \mathbf{r}_0(s) + Y(s, t)\mathbf{e}_y$ where the transverse displacement Y is taken as a first order perturbation to the static shape \mathbf{r}_0 . At the leading order the deformation is contained exclusively in the xz -plane so κ_n is a first order perturbation as well and we also expand $\kappa_w = \kappa_0 + \delta\kappa$ and the frame vectors

$$\boldsymbol{\tau} = \boldsymbol{\tau}_0 + \delta\boldsymbol{\tau} \quad , \quad \mathbf{n} = \mathbf{n}_0 + \delta\mathbf{n} \quad , \quad \mathbf{w} = \mathbf{e}_y + \delta\mathbf{w}. \quad (15)$$

Using (13), the inextensibility condition and all the expansions above mentioned, we obtain after some calculations the expansions of the material frame

$$\boldsymbol{\tau} = \boldsymbol{\tau}_0 + Y'\mathbf{e}_y \quad , \quad \mathbf{n} = \mathbf{n}_0 + \alpha\mathbf{e}_y \quad , \quad \mathbf{w} = \mathbf{e}_y - Y'\boldsymbol{\tau}_0 - \alpha\mathbf{n}_0 \quad (16)$$

where the small angle α and the small curvature κ_n satisfy

$$\alpha' = -\kappa_0 Y' \quad , \quad \kappa_n = \kappa_0 \alpha - Y'' \quad (17)$$

and $\delta\kappa_w = 0$. Besides, expanding all the terms in (14), we obtain up to the linear order

$$\mathbf{F}' = \left(T + \frac{1}{2}EI\kappa_0^2 \right)' \boldsymbol{\tau}_0 + \left(\kappa_0 T - EI\kappa_0'' \right) \mathbf{n}_0 + \left((T - EI\kappa_0^2) Y'' - \frac{3}{2}EI(\kappa_0^2)' Y' - EII Y^{(4)} \right) \mathbf{e}_y. \quad (18)$$

A.3 Linearization of the fluid forces

The oscillating lift force \mathbf{p}_w defined in (3) is a linear order term by assumption. On the other hand, the resistive and reactive forces (1),(2) both include a leading order and a linear order term. First, the expansion of the relative velocity up to the linear order in Y gives $\mathbf{U}_{rel} = \dot{Y}\mathbf{e}_y - U\mathbf{e}_x = \dot{Y}\mathbf{e}_y - US_0\boldsymbol{\tau}_0 - UC_0\mathbf{n}_0$ so that projection on the tangent direction and its orthogonal plane using (16) yields

$$U_\tau\boldsymbol{\tau} = -US_0\boldsymbol{\tau}_0 - US_0Y'\mathbf{e}_y \quad , \quad U_N\mathbf{N} = -UC_0\mathbf{n}_0 + \left(\dot{Y} + US_0Y' \right) \mathbf{e}_y. \quad (19)$$

Making use of that decomposition in (1) and (2), we obtain the linearized fluid loads

$$\mathbf{p}_{am} = -m_a U^2 \left(S_0^2 - \frac{1}{2}C_0^2 \right) \kappa_0 \mathbf{n}_0 - m_a \left(\ddot{Y} + 2US_0\dot{Y}' + UC_0\kappa_0 Y' + U^2 \left(\left[S_0^2 + \frac{1}{2}C_0^2 \right] Y' \right)' \right) \mathbf{e}_y \quad (20)$$

$$\mathbf{p}_d = \frac{1}{2}\rho C_D DU^2 |C_0| C_0 \mathbf{n}_0 - \frac{1}{2}\rho C_D DU |C_0| \left(\dot{Y} + US_0 Y' \right) \mathbf{e}_y. \quad (21)$$

A.4 Governing equations

Finally, the linearized structural acceleration reads $\ddot{\mathbf{r}} = \ddot{Y} \mathbf{e}_y$ so that substitution of (18),(20),(21) and (3) in the first Kirchhoff equation (11) provides, after projection along $\boldsymbol{\tau}_0$ and \mathbf{n}_0 , the leading order system of equation

$$\left(T + \frac{1}{2} EI \kappa_0^2 \right)' = 0 \quad , \quad \left(\kappa_0 T - EI \kappa_0'' \right) + \frac{1}{2} \rho C_D DU^2 |C_0| C_0 - m_a U^2 \left(S_0^2 - \frac{1}{2} C_0^2 \right) \kappa_0 = 0 \quad (22)$$

with leading order boundary conditions $\theta_0 = 0$ at $s = 0$ and $T = \kappa_0 = \kappa_0' = 0$ at $s = L$. The first equation provides the expression of the tension $T = -1/2 EI \kappa_0^2$. Replacing T in the second equation yields the static equilibrium equation (6) after non-dimensionalization. Similarly, projection of (11) on \mathbf{e}_y yields

$$\begin{aligned} m \ddot{Y} = & \left((T - EI \kappa_0^2) Y'' - \frac{3}{2} EI (\kappa_0^2)' Y' - EI Y^{(4)} \right) \\ & - m_a \left(\ddot{Y} + 2US_0 \dot{Y}' + UC_0 \kappa_0 Y' + U^2 \left(\left[S_0^2 + \frac{1}{2} C_0^2 \right] Y' \right)' \right) \\ & - \frac{1}{2} \rho C_D DU |C_0| \left(\dot{Y} + US_0 Y' \right) + \frac{1}{4} \rho C_L^0 DU^2 C_0^2 q \end{aligned} \quad (23)$$

which gives the VIV equation (7) after replacement of the tension and non-dimensionalization.

Appendix B Validity of the linearization

The model used throughout this study is based on the assumption that the only relevant source of nonlinearity in the dynamics comes from the damping term in the Van der Pol wake oscillator. This term is indeed sufficient to ensure the saturation of the vibration amplitude in the limit-cycle to a magnitude consistent with physical observations. However, the linearization leading to the governing equation for the structure (7) relies on the assumption that the transverse displacement Y is a small perturbation to the leading order deformation $\mathbf{r}_0(s)$, while the amplitude of the limit-cycle oscillations due to VIVs is not infinitesimal. Thus, the adequacy of the linearization detailed in Appendix A for modeling VIVs requires verification.

The linearization of the structural model performed in Appendix A.2 is purely geometrical and holds as long as $Y \ll L$. The numerical results displayed on Fig. 7(a) and 9(a) indicate that the amplitude of the transverse perturbation does not exceed $Y \lesssim 0.5D$ in the case of VIVs. The geometrical

linearization thus still holds in the limit-cycle for the slender structures considered in this work $\Lambda = L/D \gg 1$.

On the other hand, the linearization of the fluid forces performed in Appendix A.3 relies on the additional assumption that the transverse velocity is small compared to the free-stream $\dot{Y} \ll U$. The frequency of the VIVs is approximately equal to $f_w^0 = S_t U/D$ as shown on Fig. 3. Assuming an amplitude $Y \sim 0.5D$ and with $S_t = 0.2$, the order of magnitude of the transverse velocity scales as $\dot{Y} \sim 2\pi f_w^0 Y \sim 0.6U$, which is at the mathematical limit of validity of the linearization. Nonetheless, considering only the linear contribution of the fluid forces in the dynamic equation is consistent with the leading-order nature of the models generally used in VIV studies involving wake oscillator models (Skop and Luo, 2001; Facchinetti et al., 2004b; Mathelin and de Langre, 2005; Mukundan et al., 2009). A more detailed discussion about the appropriateness of such an approximation can be found in Skop and Balasubramanian (1997). If the nonlinearity in the Van der Pol wake oscillator is critical in the limitation of the amplitude of the vibrations in the limit-cycle, we expect that the influence of other nonlinearities should be less significant on a qualitative point of view. More details about the influence of nonlinearities arising from the structure, the fluid forces, or the coupling between them can be found in Srinil and Zanganeh (2012).

Finally, when the system becomes unstable to flutter, the amplitude of the oscillations becomes too large for the geometrical linearization of Appendix A.2 to remain valid. In this case, nonlinear coupling between the transverse and in-plane directions in the structural equation would eventually lead to a complex large-amplitude 3D motion.

Appendix C Linear stability analysis

To perform the linear stability analysis of the coupled system (7)-(8), we neglect the nonlinear term in Eq. (8) and assume a perturbation of the form $(Y, q)(s, t) = (\phi(s), \psi(s)) e^{i\omega t}$. The coupled system (7)-(8) then yields

$$-u^2\omega^2\phi + i\omega\frac{\beta u^2}{S_t\Lambda} [2S_0\phi' + C_0(\kappa_0 + c_d\Lambda)\phi] + \left(\left[\frac{\beta u^2}{S_t^2\Lambda^2} \left(S_0^2 + \frac{1}{2}C_0^2 \right) + \frac{3}{2}\kappa_0^2 \right] \phi' \right)' + c_d\frac{\beta u^2}{S_t^2\Lambda} C_0 S_0 \phi' + \phi^{(4)} - c_l\frac{\beta u^2}{S_t^2} C_0^2 \psi = 0 \quad (24)$$

$$-\omega^2(\psi - A\phi) - i\omega\varepsilon(2\pi C_0)\psi + (2\pi C_0)^2\psi = 0 \quad (25)$$

with boundary conditions $\phi = \phi' = 0$ at $s = 0$ and $\phi'' = \phi''' = 0$ at $s = 1$. We then solve the coupled quadratic eigenvalue problem (24)-(25) at the discretization points with the MatLab function `quadeig`

of Hammarling et al. (2013). The linear frequency f_{lin} and growth rate σ of the linear modes are then related to the eigenvalues thus found by $\omega = 2\pi f_{lin} - i\sigma$.

Appendix D Structural stability thresholds

The destabilization of the structural modes is due to the influence of the reactive force in the structural equation (7), and the effect of the oscillatory lift force due to the wake is most likely negligible in this regard. To compute the stability threshold for the structural modes only, we may thus neglect the coupling between equations (7)-(8) and consider exclusively the left-hand side of (7). Besides, the frequency of shedding f_w^0 is irrelevant in this case and we rescale the dimensional time with respect to the characteristic structural time $T_s = L^2 \sqrt{(m + m_a)/EI}$ instead of f_w^0 . The governing equation then reduces to

$$\ddot{Y} + v\sqrt{\beta} \left[2S_0 \dot{Y}' + C_0 (\kappa_0 + c_d \Lambda) \dot{Y} \right] + \left(\left[v^2 \left(S_0^2 + \frac{1}{2} C_0^2 \right) + \frac{3}{2} \kappa_0^2 \right] Y' \right)' + c_d \Lambda v^2 C_0 S_0 Y' + Y^{(4)} = 0 \quad (26)$$

where the flutter-specific reduced velocity $v = UL \sqrt{m_a/EI}$ is related to the VIV-specific reduced velocity used throughout this article through $u = (S_t/\sqrt{\beta}) \Lambda v$, and to the Cauchy number through $C_Y = c_d \Lambda v^2$. The stability thresholds found by linear stability analysis of Eq. (26) for $\beta = 0.5$ and three different aspect ratios are provided in Table 2 in terms of the three parameters v , u and C_Y .

The threshold for $\Lambda = 10$ in terms of the VIV-specific reduced velocity $u_c = 35.8$ is very close to that found in Section 3.3 for the coupled system (7)-(8), $u_c = 34.9$. This confirms the very limited influence of the wake coupling on the structural stability. Besides, the thresholds expressed in term of the flutter-specific reduced velocity v seems almost insensitive to the aspect ratio Λ . Consequently, according to the scalings of the VIV-specific reduced velocity $u \propto \Lambda v$ and Cauchy number $C_Y \propto \Lambda v^2$ provided here, the stability thresholds in terms of both these parameters is close to proportional to the aspect ratio Λ .

	critical velocity v_c	critical velocity u_c	critical Cauchy number $C_{Y,c}$
$\Lambda = 10$	12.7	3.58×10^1	2.04×10^3
$\Lambda = 10^2$	16.1	4.55×10^2	3.30×10^4
$\Lambda = 10^3$	17.1	4.85×10^3	3.74×10^5

Table 2: Structural stability thresholds in terms of the flutter-specific reduced velocity v , VIV-specific reduced velocity u , and Cauchy number C_Y .

References

- G.O. Antoine, E. de Langre, and S. Michelin. Optimal energy harvesting from vortex-induced vibrations of cables. *Proceedings of the Royal Society of London A: Mathematical, Physical and Engineering Sciences*, 468(2147), 2016.
- G.R.S. Assi, N. Srinil, C.M. Freire, and I. Korkischko. Experimental investigation of the flow-induced vibration of a curved cylinder in convex and concave configurations. *Journal of Fluids and Structures*, 44:52–66, 2014.
- B. Audoly and Y. Pomeau. *Elasticity and geometry: from hair curls to the non-linear response of shells*. Oxford University Press, Oxford, UK, 2010.
- S. Balasubramanian, R.A. Skop, F.L. Haan, and A.A. Szewczyk. Vortex-excited vibrations of uniform pivoted cylinders in uniform and shear flow. *Journal of Fluids and Structures*, 14(1):65–85, 2000.
- P.W. Bearman. Circular cylinder wakes and vortex-induced vibrations. *Journal of Fluids and Structures*, 27(5):648–658, 2011.
- M.M. Bernitsas, K. Raghavan, Y. Ben-Simon, and E.M. Garcia. Vivace (vortex induced vibration aquatic clean energy): A new concept in generation of clean and renewable energy from fluid flow. *Journal of Offshore Mechanics and Arctic Engineering*, 130(4):041101, 2008.
- G. Birkhoff and E.H. Zarantonello. *Jets, wakes and cavities*. New York: Academic Press, 1957.
- R.E.D. Bishop and A.Y. Hassan. The lift and drag forces on a circular cylinder in a flowing fluid. *Proceedings of the Royal Society of London A: Mathematical, Physical and Engineering Sciences*, 277(1368):32–50, 1964.
- R.D. Blevins. *Flow-induced vibration*. Van Nostrand Reinhold Company, New York, NY, USA, 1990.
- R. Bourguet, D. Lucor, and M.S. Triantafyllou. Mono-and multi-frequency vortex-induced vibrations of a long tensioned beam in shear flow. *Journal of Fluids and Structures*, 32:52–64, 2012.
- R. Bourguet, G.E. Karniadakis, and M.S. Triantafyllou. Multi-frequency vortex-induced vibrations of a long tensioned beam in linear and exponential shear flows. *Journal of Fluids and Structures*, 41:33–42, 2013.
- R. Bourguet, G.E. Karniadakis, and M.S. Triantafyllou. On the validity of the independence principle applied to the vortex-induced vibrations of a flexible cylinder inclined at 60° . *Journal of Fluids and Structures*, 53:58–69, 2015.

- C.G. Broyden. A class of methods for solving nonlinear simultaneous equations. *Mathematics of computation*, 19(92):577–593, 1965.
- F. Candelier, F. Boyer, and A. Leroyer. Three-dimensional extension of Lighthill’s large-amplitude elongated-body theory of fish locomotion. *Journal of Fluid Mechanics*, 674:196–226, 2011.
- S.K. Chakrabarti. *The theory and practice of hydrodynamics and vibration*. World scientific, NJ, USA, 2002.
- J.R. Chaplin, P.W. Bearman, F.J. Huera Huarte, and R.J. Pattenden. Laboratory measurements of vortex-induced vibrations of a vertical tension riser in a stepped current. *Journal of Fluids and Structures*, 21(1):3–24, 2005.
- H.L. Dai, L. Wang, Q. Qian, and Q. Ni. Vortex-induced vibrations of pipes conveying fluid in the subcritical and supercritical regimes. *Journal of Fluids and Structures*, 39:322–334, 2013.
- H.L. Dai, L. Wang, Q. Qian, and Q. Ni. Vortex-induced vibrations of pipes conveying pulsating fluid. *Ocean Engineering*, 77:12–22, 2014.
- S.K. Datta and W.G. Gottenberg. Instability of an elastic strip hanging in an airstream. *Journal of Applied Mechanics*, 42(1):195–198, 1975.
- E. de Langre. Frequency lock-in is caused by coupled-mode flutter. *Journal of Fluids and Structures*, 22(6):783–791, 2006.
- E. de Langre. Effects of wind on plants. *Annual Review of Fluid Mechanics*, 40:141–168, 2008.
- E. de Langre, M.P. Païdoussis, O. Doaré, and Y. Modarres-Sadeghi. Flutter of long flexible cylinders in axial flow. *Journal of Fluid Mechanics*, 571:371–389, 2007.
- A. de Vecchi, S.J. Sherwin, and J.M.R. Graham. Wake dynamics of external flow past a curved circular cylinder with the free-stream aligned to the plane of curvature. *Journal of Fluids and Structures*, 24(8):1262–1270, 2008.
- C. Eloy, C. Souilliez, and L. Schouveiler. Flutter of a rectangular plate. *Journal of Fluids and Structures*, 23(6):904–919, 2007.
- C. Eloy, N. Kofman, and L. Schouveiler. The origin of hysteresis in the flag instability. *Journal of Fluid Mechanics*, 691:583–593, 2012.
- M.L. Facchinetti, E. de Langre, and F. Biolley. Coupling of structure and wake oscillators in vortex-induced vibrations. *Journal of Fluids and Structures*, 19(2):123–140, 2004a.

- M.L. Facchinetti, E. de Langre, and F. Biolley. Vortex-induced travelling waves along a cable. *European Journal of Mechanics-B/Fluids*, 23(1):199–208, 2004b.
- G.R. Franzini, A.L.C. Fajarra, J.R. Meneghini, I. Korkischko, and R. Franciss. Experimental investigation of vortex-induced vibration on rigid, smooth and inclined cylinders. *Journal of Fluids and Structures*, 25(4):742–750, 2009.
- F. Ge, W. Lu, L. Wang, and Y.-S. Hong. Shear flow induced vibrations of long slender cylinders with a wake oscillator model. *Acta Mechanica Sinica*, 27(3):330, 2011.
- F. Gosselin, E. de Langre, and B.A. Machado-Almeida. Drag reduction of flexible plates by reconfiguration. *Journal of Fluid Mechanics*, 650:319–341, 2010.
- S. Hammarling, C.J. Munro, and F. Tisseur. An algorithm for the complete solution of quadratic eigenvalue problems. *ACM Transactions on Mathematical Software (TOMS)*, 39(3):18, 2013.
- R.T. Hartlen and I.G. Currie. Lift-oscillator model of vortex-induced vibration. *Journal of the Engineering Mechanics Division*, 96(5):577–591, 1970.
- M. Hassani, N.W. Mureithi, and F. Gosselin. Large coupled bending and torsional deformation of an elastic rod subjected to fluid flow. *Journal of Fluids and Structures*, 62:367–383, 2016.
- A. Jain and Y. Modarres-Sadeghi. Vortex-induced vibrations of a flexibly-mounted inclined cylinder. *Journal of Fluids and Structures*, 43:28–40, 2013.
- N. Jauvtis and C.H.K. Williamson. Vortex-induced vibration of a cylinder with two degrees of freedom. *Journal of Fluids and Structures*, 17(7):1035–1042, 2003.
- N. Jauvtis and C.H.K. Williamson. The effect of two degrees of freedom on vortex-induced vibration at low mass and damping. *Journal of Fluid Mechanics*, 509:23–62, 2004.
- A. Khalak and C.H.K. Williamson. Motions, forces and mode transitions in vortex-induced vibrations at low mass-damping. *Journal of Fluids and Structures*, 13(7-8):813–851, 1999.
- R. King. An investigation of vortex-induced vibrations of sub-sea communications cables. In *Proceedings of the 6th International Conference on Flow-Induced Vibration, London, UK*, pages 443–454, 1995.
- T. Leclercq and E. de Langre. Drag reduction by elastic reconfiguration of non-uniform beams in non-uniform flows. *Journal of Fluids and Structures*, 60:114–129, 2016. doi:10.1016/j.jfluidstructs.2015.10.007.

- T. Leclercq, N. Peake, and E. de Langre. Does flutter prevent drag reduction by reconfiguration? *Proceedings of the Royal Society of London A: Mathematical, Physical and Engineering Sciences*, 474:20170678, 2018. doi: 10.1098/rspa.2017.0678.
- M.J. Lighthill. Large-amplitude elongated-body theory of fish locomotion. *Proceedings of the Royal Society of London. Series B. Biological Sciences*, 179(1055):125–138, 1971.
- D. Lucor and G.E. Karniadakis. Effects of oblique inflow in vortex-induced vibrations. *Flow, Turbulence and Combustion*, 71(1-4):375–389, 2003.
- D. Lucor, H. Mukundan, and M.S. Triantafyllou. Riser modal identification in CFD and full-scale experiments. *Journal of Fluids and Structures*, 22(6):905–917, 2006.
- M. Luhar and H.M. Nepf. Flow-induced reconfiguration of buoyant and flexible aquatic vegetation. *Limnology and Oceanography*, 56(6):2003–2017, 2011.
- H. Marcollo and J.B. Hinwood. On shear flow single mode lock-in with both cross-flow and in-line lock-in mechanisms. *Journal of Fluids and structures*, 22(2):197–211, 2006.
- L. Mathelin and E. de Langre. Vortex-induced vibrations and waves under shear flow with a wake oscillator model. *European Journal of Mechanics-B/Fluids*, 24(4):478–490, 2005.
- D. Meng and L. Chen. Nonlinear free vibrations and vortex-induced vibrations of fluid-conveying steel catenary riser. *Applied Ocean Research*, 34:52–67, 2012.
- S. Michelin and O. Doaré. Energy harvesting efficiency of piezoelectric flags in axial flows. *Journal of Fluid Mechanics*, 714:489–504, 2013.
- A. Miliou, A. de Vecchi, S.J. Sherwin, and J.M.R. Graham. Wake dynamics of external flow past a curved circular cylinder with the free stream aligned with the plane of curvature. *Journal of Fluid Mechanics*, 592:89–115, 2007.
- C.K. Morooka and R.I. Tsukada. Experiments with a steel catenary riser model in a towing tank. *Applied Ocean Research*, 43:244–255, 2013.
- H. Mukundan, Y. Modarres-Sadeghi, J.M. Dahl, F.S. Hover, and M.S. Triantafyllou. Monitoring VIV fatigue damage on marine risers. *Journal of Fluids and Structures*, 25(4):617–628, 2009.
- B.R. Noack, F. Ohle, and H. Eckelmann. On cell formation in vortex streets. *Journal of Fluid Mechanics*, 227:293–308, 1991.
- M.P. Paidoussis. *Fluid-structure interactions: slender structures and axial flow*, volume 2. Academic Press, London, 1998.

- M.P. Païdoussis, E. Grinevich, D. Adamovic, and C. Semler. Linear and nonlinear dynamics of cantilevered cylinders in axial flow. part 1: physical dynamics. *Journal of Fluids and Structures*, 16(6): 691–713, 2002.
- M.P. Païdoussis, S.J. Price, and E. de Langre. *Fluid-structure interactions: cross-flow-induced instabilities*. Cambridge University Press, 2010.
- T. Sarpkaya. A critical review of the intrinsic nature of vortex-induced vibrations. *Journal of Fluids and Structures*, 19(4):389–447, 2004.
- C. Semler, J.L. Lopes, N. Augu, and M.P. Païdoussis. Linear and nonlinear dynamics of cantilevered cylinders in axial flow. part 3: Nonlinear dynamics. *Journal of Fluids and Structures*, 16(6):739–759, 2002.
- B. Seyed-Aghazadeh, C. Budz, and Y. Modarres-Sadeghi. The influence of higher harmonic flow forces on the response of a curved circular cylinder undergoing vortex-induced vibration. *Journal of Sound and Vibration*, 353:395–406, 2015.
- K. Singh, S. Michelin, and E. de Langre. Energy harvesting from axial fluid-elastic instabilities of a cylinder. *Journal of Fluids and Structures*, 30:159–172, 2012a.
- K. Singh, S. Michelin, and E. de Langre. The effect of non-uniform damping on flutter in axial flow and energy-harvesting strategies. *Proceedings of the Royal Society of London A: Mathematical, Physical and Engineering Sciences*, 468(2147):3620–3635, 2012b.
- R.A. Skop and S. Balasubramanian. A new twist on an old model for vortex-excited vibrations. *Journal of Fluids and Structures*, 11(4):395–412, 1997.
- R.A. Skop and G. Luo. An inverse-direct method for predicting the vortex-induced vibrations of cylinders in uniform and nonuniform flows. *Journal of Fluids and Structures*, 15(6):867–884, 2001.
- N. Srinil. Multi-mode interactions in vortex-induced vibrations of flexible curved/straight structures with geometric nonlinearities. *Journal of Fluids and Structures*, 26(7):1098–1122, 2010.
- N. Srinil. Analysis and prediction of vortex-induced vibrations of variable-tension vertical risers in linearly sheared currents. *Applied Ocean Research*, 33(1):41–53, 2011.
- N. Srinil and H. Zanganeh. Modelling of coupled cross-flow/in-line vortex-induced vibrations using double duffing and van der pol oscillators. *Ocean Engineering*, 53:83–97, 2012.
- N. Srinil, M. Wiercigroch, and P. O’Brien. Reduced-order modelling of vortex-induced vibration of catenary riser. *Ocean Engineering*, 36(17):1404–1414, 2009.

- N. Srinil, H. Zanganeh, and A. Day. Two-degree-of-freedom VIV of circular cylinder with variable natural frequency ratio: Experimental and numerical investigations. *Ocean Engineering*, 73:179–194, 2013.
- G.I. Taylor. Analysis of the swimming of long and narrow animals. *Proceedings of the Royal Society of London. Series A. Mathematical and Physical Sciences*, 214(1117):158–183, 1952.
- E.G. Tickner and A.H. Sacks. Engineering simulation of the viscous behavior of whole blood using suspensions of flexible particles. *Circulation research*, 25(4):389–400, 1969.
- A.D. Trim, H. Braaten, H. Lie, and M.A. Tognarelli. Experimental investigation of vortex-induced vibration of long marine risers. *Journal of Fluids and Structures*, 21(3):335–361, 2005.
- J.K. Vandiver. Drag coefficients of long flexible cylinders. In *Offshore Technology Conference*. Offshore Technology Conference, 1983.
- J.K. Vandiver. Dimensionless parameters important to the prediction of vortex-induced vibration of long, flexible cylinders in ocean currents. *Journal of Fluids and Structures*, 7(5):423–455, 1993.
- R. Violette, E. de Langre, and J. Szydlowski. Computation of vortex-induced vibrations of long structures using a wake oscillator model: comparison with DNS and experiments. *Computers & Structures*, 85(11):1134–1141, 2007.
- R. Violette, E. de Langre, and J. Szydlowski. A linear stability approach to vortex-induced vibrations and waves. *Journal of Fluids and Structures*, 26(3):442–466, 2010.
- C.H.K. Williamson. Vortex dynamics in the cylinder wake. *Annual Review of Fluid Mechanics*, 28(1):477–539, 1996.
- C.H.K. Williamson and R. Govardhan. Vortex-induced vibrations. *Annual Review of Fluid Mechanics*, 36:413–455, 2004.
- C.H.K. Williamson and R. Govardhan. A brief review of recent results in vortex-induced vibrations. *Journal of Wind Engineering and Industrial Aerodynamics*, 96(6-7):713–735, 2008.
- X. Wu, F. Ge, and Y. Hong. A review of recent studies on vortex-induced vibrations of long slender cylinders. *Journal of Fluids and Structures*, 28:292–308, 2012.
- Y. Yadykin, V. Tenetov, and D. Levin. The flow-induced vibration of a flexible strip hanging vertically in a parallel flow part 1: Temporal aeroelastic instability. *Journal of Fluids and Structures*, 15(8):1167–1185, 2001.

H. Zhu, P. Lin, and J. Yao. An experimental investigation of vortex-induced vibration of a curved flexible pipe in shear flows. *Ocean Engineering*, 121:62–75, 2016.

Titre : Déformations induites par l'écoulement et réduction d'efforts par la flexibilité

Mots clefs : Interactions fluide-structure, Reconfiguration, Réduction de traînée, Efforts internes, Instabilité de flottement, Vibrations induites par vortex

Résumé : La déflexion statique d'une structure flexible exposée à un écoulement transverse permet classiquement de réduire la traînée à laquelle elle est soumise. Dans le domaine de la biomécanique, la déformation induite par l'écoulement d'éléments végétaux flexibles conduisant à une réduction du chargement est désignée par le terme 'reconfiguration' pour souligner le caractère avantageux de ce processus adaptatif. Dans cette thèse, nous examinons les mécanismes qui sous-tendent le processus de reconfiguration, dans des systèmes fluide-structure présentant une variabilité spatiale, ou de la dynamique provenant au choix de l'instationnarité de l'écoulement de base, d'un couplage fluide-structure conduisant à une instabilité, ou de vibrations induites par vortex. Nous montrons que l'aptitude des structures flexibles à réduire l'intensité du chargement imposé par l'écoulement est préservée en présence de non-uniformités ou de dynamique, à condition que le design de la structure soit tel que la traînée résistive domine les forces inertielles. Nous montrons de plus que la capacité à se déformer présente l'avantage supplémentaire de permettre la réduction des vibrations induites par vortex. Notre travail indique également que des structures légères et élancées sont les mieux adaptées pour supporter les chargements induits par l'écoulement en se reconfigurant, et que l'efficacité de la réduction du chargement par reconfiguration élastique dépend faiblement de la distribution spatiale des propriétés du système. Finalement, la réduction des chargements résulte toujours, indépendamment du régime de reconfiguration, de la concentration de la déformation sur une longueur caractéristique inférieure à la longueur réelle de la structure.

Title : Flow-induced deformations and stress reduction by flexibility

Keywords : Fluid-structure interactions, Reconfiguration, Drag reduction, Internal stress, Flutter instability, Vortex-induced vibrations

Abstract : The static deflection of a flexible structure exposed to a transverse flow is classically known to reduce the drag it has to withstand. In the field of biomechanics, the flow-induced deformation of flexible plant elements leading to a reduction of the loads is referred to as 'reconfiguration', in order to highlight the alleged benefits of such adaptive process. In this thesis, we investigate the mechanisms underpinning the reconfiguration in flow-structure systems featuring some spatial variability, or some dynamics arising either from the unsteadiness of the free-stream, from a flow-structure coupling leading to an instability, or from vortex-induced vibrations. We show that the ability of flexible structures to reduce the magnitude of the flow-induced loads is preserved in the presence of non-uniformities or dynamics, provided that the design of the structure is such that resistive drag dominates over inertial forces. We also show that the ability to deform has the added benefit of reducing the magnitude of the vortex-induced vibrations. Our work further indicates that light, slender structures are better suited to accommodate the flow-induced loads by reconfiguring, and that the efficiency of the process of load reduction by elastic reconfiguration is weakly sensitive to the spatial distribution of the system properties. Finally, regardless of the regime of reconfiguration, the reduction of the load always results from the concentration of the deformation on a characteristic bending length smaller than the actual length of the structure.